THE UNIVERSITY
OF BIRMINGHAM

Synthesis of Coupled Resonator Circuits with Multiple Outputs using Coupling Matrix Optimization

Talal F. Skaik

A thesis submitted to the University of Birmingham for the degree of Doctor of Philosophy

School of Electronic, Electrical and Computer Engineering
The University of Birmingham

March 2011

Abstract

Design techniques used for two-port coupled resonator circuits are extended in this thesis to multi-port coupled resonator circuits. Three-port coupled resonator power dividers and diplexers are demonstrated in particular. The design approach is based on coupling matrix optimization, and it allows synthesis of coupled resonator power dividers with arbitrary power division, and diplexers with contiguous and non-contiguous bands. These components have been synthesised with novel topologies that can achieve Chebyshev and Quasi-elliptic filtering responses.

To verify the design methodology, some components with Chebyshev filtering response have been designed, fabricated and tested. X-band coupled resonator devices have been realized using waveguide cavities: 3-dB power divider, unequal power divider, 4-resonator diplexer, and 12-resonator diplexer. An E-band 12-resonator coupled resonator diplexer has been designed to be used as a front end component in the transceiver of a wireless communications system. An H-band coupled resonator diplexer with embedded bends has been designed and realized using micromachining technology.

Acknowledgements

I would like to express deep gratitude to my supervisor Professor Mike Lancaster for his guidance and support. His encouragement and inspiring suggestions have been a great value for my PhD research. I am also extremely grateful to Dr. Fred Huang for his thoughtful guidance and useful advice throughout my study. Special thanks go to Dr. Mao Ke for the fabrication of the micromachined devices, and to Dr. Yi Wang for his advice and help during the measurements. Many thanks as well to Clifford Ansell and Adnan Zentani for the fabrication of the waveguide devices.

My acknowledgement also goes to the UK Overseas Research Student (ORS) scholarship and to the department of Electronic, Electrical and Computer Engineering at the University of Birmingham for the financial support. Finally, I would like to thank my family and friends for their invaluable encouragement and support.

Table of Contents

Chapter 1

Introduction

1.1 Overview of Power Dividers and their Applications

Power dividers are passive components used to divide an input signal into a number of signals with smaller amounts of power. The simplest forms of power dividers are three-port networks, and they can be extended to N-way power dividers by forming multi-stage structures. Power dividers are employed in many microwave and RF applications. They are widely used in balanced power amplifiers, mixers, phase shifters, and antenna arrays. Wilkinson power dividers [1] and T-junctions [2] are examples of power dividers that are commonly used in many microwave circuits and subsystems. Four-port devices such as hybrids and directional couplers are also used for power splitting with a phase shift between the output ports of either 90^{o} (branch-line hybrids) or an 180^{o} (magic-T) [2].

In power amplifier systems, power dividing/combining networks are used when high output power is required [3-5]. Figure 1.1 shows a general diagram of such systems, where the output powers from large number of power amplifiers are required to be combined. Input power is first divided by the power splitter to provide drive signals to the power amplifiers. The amplifiers outputs are then combined by the power combiner into a single output with high power. It is usually required for power dividing/combining networks in these systems to have low loss and high inter-port isolation.

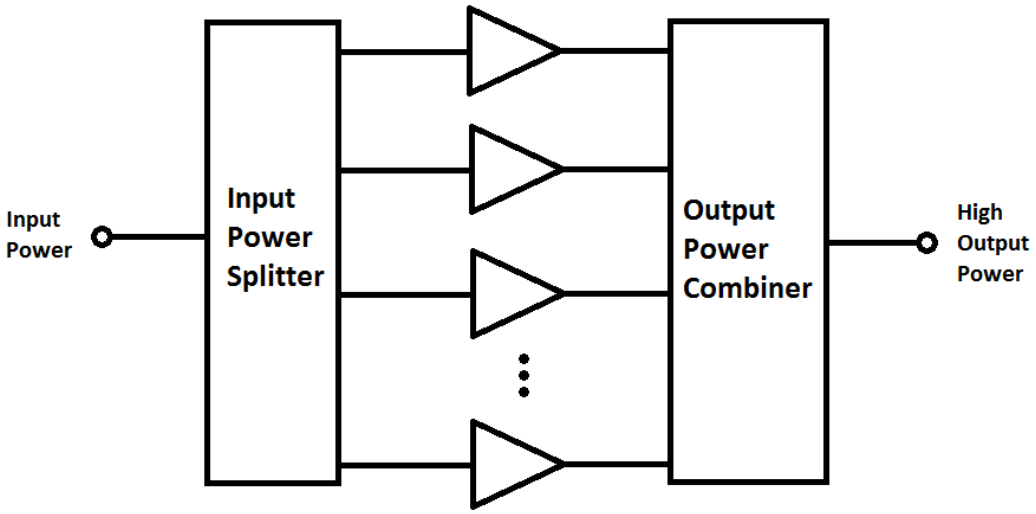

Figure 1.1: Diagram of Amplifier System

Power dividers are also used as feeding networks in beam-steering antennas. Phased array antennas are usually used in beam-steering applications that require changing the direction of the beam's main lobe with time. This is achieved by using phase shifters that vary the phases of the signals feeding the antennas in such a way that the radiation pattern is moved in a desired direction. Figure 1.2 depicts a phased array antenna system that consists of antenna elements, phase shifters, and power distribution network [6].

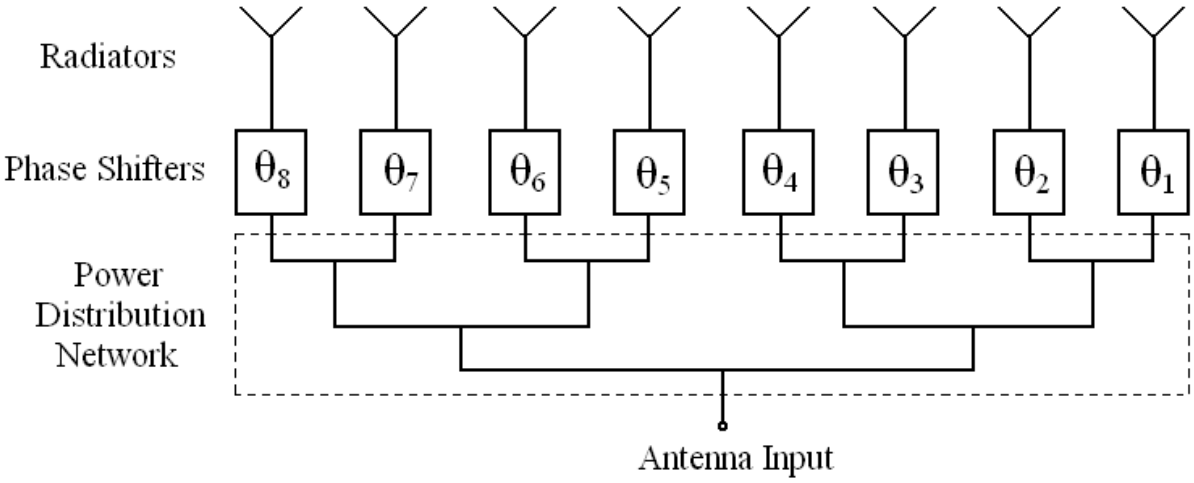

Figure 1.2: Phased Array Antenna System

There has been extensive research to develop power dividers that are compatible with the requirements of beam forming/steering systems. Several power dividers such as Wilkinson power divider, T-junctions, and branch-line couplers have been developed to be used in these systems for feeding purposes [7-9].

1.2 Overview of Diplexers and their Applications

Multiplexers and diplexers are key components in a huge variety of communication systems, including radio transmission, cellular radio, satellite-communication systems, and broadband wireless communications. They are frequency selective components that are used to combine or separate signals with different frequencies in multiport networks. Multiplexers are usually formed of a set of filters, known as channel filters, and a common junction.

A diplexer is the simplest form of a multiplexer. It is a passive three-port device that connects two networks operating at different frequencies to a common terminal. Diplexers allow two transmitters on different frequencies to use a common antenna at the same time. Also, they may be used as forms of duplexers, which allow a transmitter and a receiver operating on different frequencies to share one common antenna with a minimum interaction between the transmitted and received signals. Therefore, reduction in volume and mass is possible due to the use of a single antenna.

Both base stations and radio handsets in cellular radio systems have driven towards various innovations in filter/diplexer technology for numerous system standards. Figure 1.3 shows a block diagram of the RF front end of a cellular base station [10]. The diplexer is a key component in the overall system, and it consists of a power divider and two channel filters with stringent requirements on selectivity and isolation. Such filters operate in different frequency bands. Diplexers are used in cellular base stations to allow simultaneous transmission and reception using a single antenna. Generally, the transmitter generates signals

with relatively high power, and hence the TX filter should have high power handling capability, and the receiver needs to detect very weak signals.

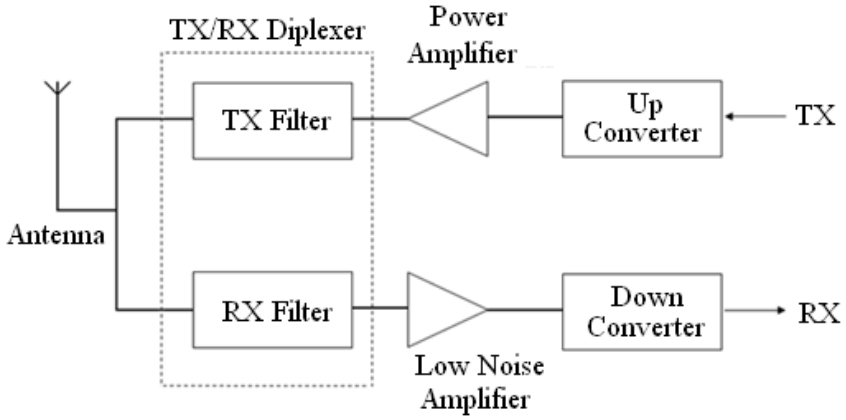

Figure 1.3: RF front end of a cellular base station

The RX filter is required to have high attenuation in the transmit band in order to protect the low-noise amplifier in the receiver from the transmitter high power signals. Similarly, the TX filter is required to have high level of stopband attenuation in order to reject the out-of-band noise generated by the power amplifier. Thus, the isolation between the receive and transmit channels is a crucial parameter in the diplexer design.

Broadband wireless access communications systems commonly employ diplexers in their transceivers. The rapid expansion of these systems increased the demand for compact size and low cost diplexers, which are used as front end components to separate the inbound and outbound transmissions. Several approaches of design of diplexers have been proposed in literature for WiMAX systems by employing various technologies to meet the current trends of low-cost and compactness [11-13]. The WiMAX systems provide wireless broadband internet services within large coverage areas to the end users without needing direct line of sight with base stations, and they have great potential in leading positions in the wireless broadband market. Here, diplexers are employed to separate subbands in the frequency range 2-11 GHz.

Diplexers are also used as front-end components in the transceivers of the broadband wireless E-band systems that provide access to high data rate internet [14]. The 71-76 and 81-86 GHz bands, known as the E-band, are allocated for gigabit-wireless point-to-point communication systems, providing up to 10 GHz of bandwidth, and enabling transmission rates of 1 Gbps and higher [15]. These wireless point-to-point links can be realised over distances of several miles, and they can provide bridges for the gaps in fibre networks [14]. In this thesis, a novel diplexer that has been designed for E-band systems will be proposed.

1.3 Thesis Motivation

There has been a tremendous increasing demand in miniaturization and reducing design complexity of microwave components and subsystems. This thesis addresses development of novel compact topologies for filter integrated power dividers and diplexers with reduced complexity in the design. Conventionally, power dividers and bandpass filters are cascaded to be used for example in image reject mixers or other circuits to produce two duplicate signals of an input signal filtered within a desired frequency range [16-17]. Figure 1.4 shows a power divider cascaded to two identical bandpass filters [18]. However, this configuration may require a considerable area in implementation. Novel networks that can do the same functions of filtering and power division are addressed in this thesis. Such networks are based on coupled resonator structures and they may be miniaturised in comparison to the conventional configurations.

Conventional diplexers consist of two channel filters connected to a junction for energy distribution. Extensive work has been reported in literature on miniaturization of diplexers by using specific types of compact resonators or using folded structures. However, the use of external junctions in the structures of these diplexers might involve design complexity. Design techniques for multiplexers/diplexers based on coupled resonator structures without

external junctions have also been presented in literature. These structures are miniaturised since there are no external junctions. Coupled resonator circuits with multiple outputs are addressed in this thesis to synthesise compact novel topologies for diplexers with reduced design complexity and with no practical constraints in realisation.

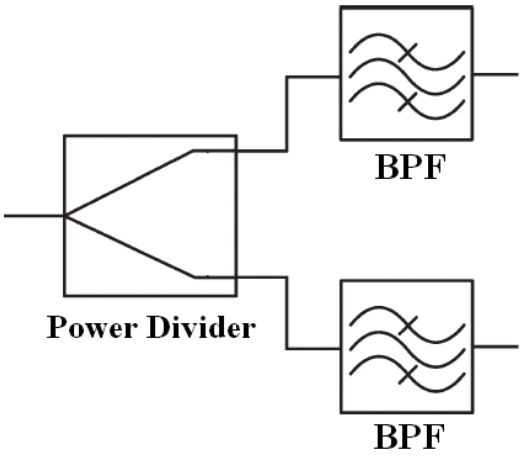

Figure 1.4: Configuration of power divider cascaded with filters

1.4 Thesis Overview

The objective of this research work is synthesis of coupled-resonator circuits with multiple outputs by extending the design techniques used for two-port coupled resonator circuits. Figure 1.5 (a) shows a topology for a two-port coupled resonator filter, where the black dots represent resonators and the lines linking the resonators represent couplings. Synthesis methods of coupled resonator filters have been extensively presented in literature. The work in this thesis extends the theory of two-port coupled resonator filters to multi-port coupled resonator circuits, such as the general network shown in figure 1.5 (b). This enables synthesis of other passive microwave components made of coupled resonators such as *N*-way power dividers and multiplexers. Three-port components such as coupled resonator power dividers and diplexers are the main focus in this thesis. The design approach allows the synthesis of

filtering power dividers with arbitrary power division, as well as diplexers with novel topologies.

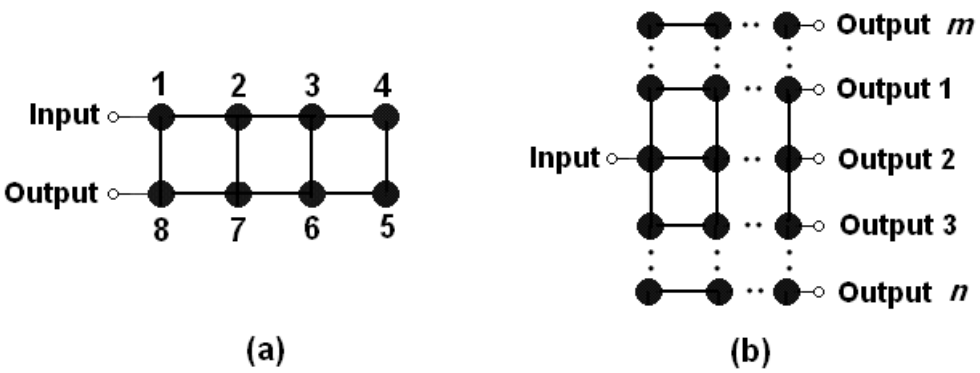

Figure 1.5: (a) two-port coupled resonator filter, (b) multi-port coupled resonator circuit

The rest of chapter 1 introduces the background theory of coupled resonator filters. The coupling matrix of a two-port circuit with multiple coupled resonators is given, and the scattering parameters in terms of the coupling matrix are presented. The theory presented here will be generalised to multi-port coupled resonator circuits in the next chapters.

A detailed derivation of the coupling matrix of multiple coupled resonators with multiple outputs is presented in Chapter 2. The relations between the scattering parameters and the general coupling matrix are also derived. The derived equations are used as a basis to the synthesis of three-port components such as power dividers and diplexers in the next chapters.

Chapter 3 looks into the synthesis of coupled resonator power dividers. The synthesis of polynomial functions of the filtering dividers is presented, and a cost function that is used in the optimisation of the coupling matrix is derived. Numerical examples of coupled resonator power dividers with different topologies are illustrated.

The synthesis of coupled resonator diplexers using coupling matrix optimisation is presented in Chapter 4. Novel diplexer topologies based on multiple coupled resonators are proposed. These topologies are different from the conventional diplexers since they do not include any

external junctions for distribution of energy. Numerical examples of diplexers with T-topologies and canonical topologies are presented, and a comparison between the proposed diplexers and a conventional diplexer in terms of isolation performance is carried out.

Chapter 5 presents coupled resonator power dividers and diplexers that are designed and realised using waveguide cavity resonators to verify the new design methodology. The devices are as follows: (1) X-band 3-dB power divider. (2) X-band unequal power divider. (3) X-band 4-resonator diplexer. (4) X-band 12-resonator diplexer. (5) E-band 12-resonator diplexer for a point-to-point wireless communication system that offers Gigabit Ethernet connectivity.

In chapter 6, an H-band (220-325 GHz) coupled resonator diplexer is presented. The diplexer structure is made of 4 layers of metal coated SU-8 using micromachining technology. An SU-8 micromachining process using photolithography is outlined, and a novel micromachined waveguide bend operating in the H-band is presented. The bend is designed to be integrated in the diplexer structure, so that the measurement can be done with direct and accurate connection with standard waveguide flanges. The measurement results of a structure of two back-to-back bends with a straight through waveguide, and the H-band micromachined diplexer are presented. The final chapter provides summary and conclusions drawn from this work.

1.5 Overview of Coupled Resonator Filters

Coupled resonator filters have been extensively presented in literature for many applications. There is a general technique for designing these filters that can be applied to any type of resonator regardless of its physical structure [19]. Such a technique is based on coupling matrix for coupled resonators arranged in a two-port network. It is worthwhile introducing some fundamental concepts in coupled-resonator filter theory that relate to the current work.

The general coupling matrix and its relation to the scattering parameters is given in the next section.

1.5.1 Coupling matrix representation

The derivation of the general coupling matrix of a coupled resonator filter has been presented in [19]. Electric and magnetic couplings have been considered separately in the derivation of the coupling matrix, and a solution has been generalised for both types of coupling. In the case of magnetically coupled resonators, using Kirchoff's voltage law, the loop equations are derived from the equivalent circuit shown in figure 1.6 (a), and represented in impedance matrix form. Similarly, for electrically coupled resonators, using Kirchoff's current law, node equations are derived from the equivalent circuit in figure 1.6 (b), and represented in admittance matrix form. The derivations show that the normalised admittance matrix has identical form to the normalised impedance matrix [19]. Accordingly, regardless of the type of coupling, a general normalised matrix [*A*] in terms of coupling coefficients and external quality factors is derived as given in equation (1.1).

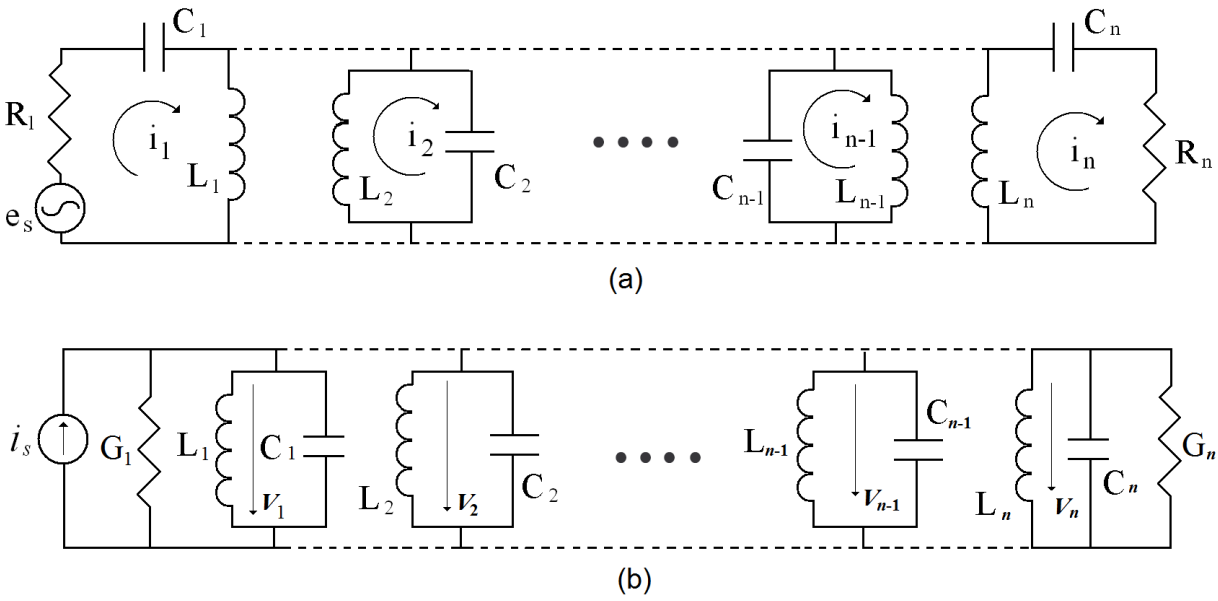

Figure 1.6: (a) Equivalent circuit of magnetically *n*-coupled resonators, (b) Equivalent circuit of electrically *n*-coupled resonators.

$$[A]=\begin{bmatrix} \frac{1}{q_{e1}} & 0 & \cdots & \\ 0 & \ddots & & \vdots \\ \vdots & & & 0 \\ 0 & \cdots & & \frac{1}{q_{en}} \end{bmatrix}+P\begin{bmatrix} 1 & 0 & \cdots & \\ & 1 & & \vdots \\ \vdots & & \ddots & \\ 0 & \cdots & & \end{bmatrix}-j\begin{bmatrix} m_{11} & m_{12} & \cdots & \\ & \ddots & & \vdots \\ \vdots & & & \\ m_{1n} & \cdots & & m_{nn} \end{bmatrix} \tag{1.1}$$

where q_{ei} is the scaled external quality factor (q_{ei}=Q_{ei}.FBW) of resonator i, P is the complex lowpass frequency variable, m_{ij} is the normalised coupling coefficient (m_{ij}=M_{ij}/FBW), FBW is the fractional bandwidth, and the diagonal entries m_{ii} account for asynchronous tuning, so that resonators can have different self-resonant frequencies.

The transmission and reflection scattering parameters are expressed in terms of the coupling matrix and the external quality factors as follows [19],

$$\begin{aligned} S_{21} &= \frac{2}{\sqrt{q_{e1}.q_{en}}}[A]^{-1}_{n1} \\ S_{11} &= \pm\left(1-\frac{2}{q_{e1}}[A]^{-1}_{11}\right) \end{aligned} \tag{1.2}$$

Equations and tables have been presented in many filter design reference books for lowpass prototype filters, which are lumped-element circuits with cut-off frequency of 1 Rad/s and input/output impedance of 1Ω [19-21]. The design equations are given for the so called *g*-values that represent the circuit elements of the lowpass prototype filter, such as the inductance, capacitance, resistance, and conductance. The *g*-values of lowpass prototype filters are used to calculate the coupling coefficients and the external quality factors of coupled resonator bandpass filters. The *g*-values for an *N*th order Chebyshev lowpass prototype filter with a passband ripple of L_{Ar} dB may be extracted from the following formulae [19],

$$
\begin{aligned}
g_0 &= 1 \\
g_1 &= \frac{2}{\gamma}\sin\left(\frac{\pi}{2N}\right) \\
g_i &= \frac{1}{g_{i-1}}\frac{4\sin\left[\frac{(2i-1)\pi}{2N}\right].\sin\left[\frac{(2i-3)\pi}{2N}\right]}{\gamma^2+\sin^2\left[\frac{(i-1)\pi}{N}\right]} \qquad for \quad i=2,3,...N \\
g_{N+1} &= \begin{cases} 1 & for \quad N \quad odd \\ \coth^2\left(\frac{\beta}{4}\right) & for \quad N \quad even \end{cases}
\end{aligned}
\tag{1.3}
$$

where

$$
\begin{aligned}
\beta &= \ln\left[\coth\left(\frac{L_{Ar}}{17.37}\right)\right] \\
\gamma &= \sinh\left(\frac{\beta}{2N}\right)
\end{aligned}
$$

The coupling matrix values and the external quality factors for a coupled resonator bandpass filter with centre frequency of ω_0 and passband edges of ω_1 and ω_2 may be found from the g-values of the lowpass prototype filter as follows [19],

$$
\begin{aligned}
M_{i,i+1} &= \frac{FBW}{\sqrt{g_i g_{i+1}}}, \qquad for \quad i=1,...,N-1 \\
Q_{e1} &= \frac{g_0 g_1}{FBW}, \qquad Q_{eN} = \frac{g_N g_{N+1}}{FBW}
\end{aligned}
\tag{1.4}
$$

where *FBW* is the fractional bandwidth given by [19]

$$
FBW = \frac{\omega_2 - \omega_1}{\omega_0} \tag{1.5}
$$

1.5.2 Filter transfer and reflection functions

For a two port lossless filter composed of *N* coupled resonators, the transfer and reflection functions may be defined as a ratio between two polynomials,

$$S_{11}(\omega)=\frac{F_N(\omega)}{E_N(\omega)},\qquad S_{21}(\omega)=\frac{P_{NZ}(\omega)}{\varepsilon E_N(\omega)} \tag{1.6}$$

where ω is the real frequency variable, and ε is a ripple constant and it can be expressed in terms of the prescribed return loss RL in decibels as,

$$\varepsilon=\frac{1}{\sqrt{10^{RL/10}-1}}.\left|\frac{P_{NZ}(\omega)}{F_N(\omega)}\right|_{\omega=\pm 1} \tag{1.7}$$

It is assumed that all polynomials are normalised so that their highest degree coefficients are 1. The roots of $F(\omega)$ correspond to the reflection zeros, and the roots of $P(\omega)$ correspond to the prescribed transmission zeros. The number of reflection zeros is N, whereas the number of the transmission zeros is assumed to be NZ. $E(\omega)$ is Nth degree polynomial and has its roots corresponding to the poles of the filter.

Applying the conservation of energy formula of a two-port losses system $|S_{11}|^2+|S_{21}|^2=1$, and using equation (1.6), the transfer function can be expressed in terms of the Chebyshev filtering function as follows,

$$|S_{21}(\omega)|^2=\frac{1}{1+\varepsilon^2 C_N^2(\omega)},\quad C_N(\omega)=\frac{F_N(\omega)}{P_N(\omega)} \tag{1.8}$$

$C_N(\omega)$ is Nth degree filtering function, and it has a form of general Chebyshev characteristic,

$$C_N(\omega)=\cosh\left(\sum_{k=1}^{N}\cosh^{-1}(x_k)\right) \tag{1.9}$$

where

$$x_k=\frac{\omega-1/\omega_k}{1-\omega/\omega_k}$$

and $j\omega_k=s_k$ is the position of the kth transmission zero in the complex frequency domain.

In order to find the roots of $F_N(\omega)$, the expression of $C_N(\omega)$ in (1.9) should be rearranged in a form of numerator and denominator, so that the numerator zeros will be equal to the roots of

$F_N(\omega)$ as in (1.8). Cameron's recursive technique [22] that is used to evaluate the coefficients of the polynomial $F_N(\omega)$ is described in Appendix A.

Since the polynomial $P(\omega)$ is constructed from the prescribed transmission zeros, and the polynomial $F(\omega)$ is found using Cameron's technique, it remains to determine the polynomial $E(\omega)$ to fully characterise the filter response. The polynomial $E(\omega)$ may be derived by applying the conservation of energy formula as follows,

$$F(\omega)F(\omega)^* + \frac{P(\omega)P(\omega)^*}{\varepsilon^2} = E(\omega)E(\omega)^* \tag{1.10}$$

The polynomial $E(\omega)E(\omega)^*$ is of the order $2N$ and it is formulated from the left hand side of equation (1.10). Its roots are symmetric about the imaginary axis in the complex s-plane. The roots of the polynomial $E(\omega)$ must be those that lie in the left half of the s-plane since it is strictly Hurwitz.

References

[1] E.J. Wilkinson, "An N-way hybrid power divider," *IRE Transactions on Microwave Theory and Techniques*, vol. 8, no. 1, pp. 116-118, 1960.

[2] D.M. Pozar, *Microwave Engineering*. 2nd edition, John Wiley & Sons, 1998.

[3] X. Zhang, Q. Wang, A. Liao, Y. Xiang, "Millimeter-wave integrated waveguide power dividers for power combiner and phased array applications," *Proc. International Conference on Microwave and Millimeter Wave Technology (ICMMT)*, China, 8-11 May 2010, pp.233-235.

[4] Y-O. Tam and C-W. Cheung, "High Efficiency Power Amplifier with Traveling-Wave Combiner and Divider," *International Journal of Electronics*, Vol 82, No. 2, pp 203-218, 1997.

[5] P. Jia, L-Y Chen, A. Alexanian, and R.A. York, "Broad-band high-power amplifier using spatial power-combining technique," *IEEE Transactions on Microwave Theory and Techniques*, vol.51, no.12, pp. 2469- 2475, Dec. 2003.

[6] J. Ehmouda, Z. Briqech, and A. Amer, "Steered Microstrip Phased Array Antennas," *World Academy of Science, Engineering and Technology*, vol. 49, pp. 319-323, 2009.

[7] S. Lee, J-M. Kim, J-M. Kim, Y-K. Kim, C. Cheon, Y. Kwon, "V-band Single-Platform Beam Steering Transmitters Using Micromachining Technology," *IEEE MTT-S International Microwave Symposium*, USA, June 2006, pp.148-151.

[8] L. Yang, N. Ito, C. W. Domier, N.C. Luhmann, and A. Mase, "18–40-GHz Beam-Shaping/Steering Phased Antenna Array System Using Fermi Antenna," *IEEE Transactions on Microwave Theory and Techniques* , vol.56, no.4, pp.767-773, April 2008.

[9] E. Colin-Beltran, A. Corona-Chavez, R. Torres-Torres, I. Llamas-Garro, "A wideband antenna array with novel 3dB branch-line power dividers as feeding network," *Proc. International Workshop on Antenna Technology (iWAT): Small Antennas and Novel Metamaterials*, Japan, March 2008, pp.267-270.

[10] I. Hunter, *Theory and Design of Microwave Filters*. London, UK: IEE, 2001.

[11] D. Zayniyev, D. Budimir, G. Zouganelis, "Microstrip filters and diplexers for WiMAX applications," *IEEE Antennas and Propagation Society International Symposium*, USA, June 2007, pp.1561-1564.

[12] D-H. Kim, D. Kim, J-I. Ryu, J-C, Kim, J-C. Park, C-D. Park, "A novel integrated Tx-Rx diplexer for dual-band WiMAX system," *IEEE MTT-S International Microwave Symposium*, USA, May 2010, pp.1736-1739.

[13] A. Yatsenko, W. Wong, J. Heyen, M. Nalezinski, G. Sevskiy, M. Vossiek, and P. Heide, "System-in-Package solutions for WiMAX applications based on LTCC technology," *IEEE Radio and Wireless Symposium*, USA, Jan. 2009. pp. 470-473.

[14] M-S. Kang, B-S. Kim, K-S. Kim, W-J Byun, M-S. Song, and S-H. Oh, "Wireless PtP system in E-band for gigabit ethernet," *Proc. 12th International Conference on Advanced Communication Technology (ICACT)*, Feb. 2010, pp.733-736.

[15] http://www.ebandcom.com/

[16] S.E Gunnarsson, C. Karnfelt, H. Zirath, R. Kozhuharov, D. Kuylenstierna, A. Alping, and C. Fager, "Highly integrated 60 GHz transmitter and receiver MMICs in a GaAs pHEMT technology," *IEEE Journal of Solid-State Circuits*, vol. 40, no. 11, pp. 2174- 2186, Nov. 2005.

[17] S. Llorente-Romano, A. Garcia-Lamperez, M. Salazar-Palma, A.I. Daganzo-Eusebio, J.S. Galaz-Villasante, and M.J. Padilla-Cruz, "Microstrip filter and power divider with improved out-of-band rejection for a Ku-band input multiplexer," *in Proc. 33rd European Microwave Conference,* Germany, Oct. 2003, pp. 315- 318.

[18] X. Tang and K. Mouthaan, "Filter integrated Wilkinson power dividers," *Microwave and Optical Technology letters*, vol. 52, no. 12, pp. 2830-2833, Dec. 2010.

[19] J.S. Hong and M.J. Lancaster, *Microstrip filters for RF/microwave applications*. New York: Wiley, 2001.

[20] R. Cameron, C. Kudsia, and R. Mansour, *Microwave filters for communication systems*. Wiley, 2007.
[21] G.L. Matthei, E.M.T Jones, and L. Young, *Microwave Filters, Impedance-matching Networks and Coupling Structures*. Artech House, 1980.
[22] R.J. Cameron, "General coupling matrix synthesis methods for Chebyshev filtering functions," *IEEE Transactions on Microwave Theory and Techniques*, vol.47, no.4, pp.433-442, Apr. 1999.

Chapter 2

N-Port Coupled Resonator Circuits

2.1 Introduction

Coupled resonator circuits are the basis for the design of microwave filters. Design techniques are extended in this thesis to multiple output circuits such as power dividers and diplexers. The general coupling matrix of a two-port *n*-coupled resonator filter was outlined in chapter 1. It is generalised in this chapter to *N*-port circuit with *n*-coupled resonators, and a detailed derivation of the general coupling matrix and its relation to the scattering parameters is presented in the next sections. The derived coupling matrix is fundamental to the current work, and it will be used as a basis for the synthesis of three-port coupled resonator power dividers in Chapter 3, and diplexers in Chapter 4.

2.2 Deriving Coupling Matrix of *N*-port Networks

In a coupled resonator circuit, energy may be coupled between adjacent resonators by a magnetic field or an electric field or both. The coupling matrix can be derived from the equivalent circuit by formulation of impedance matrix for magnetically coupled resonators or admittance matrix for electrically coupled resonators [1]. This approach has been used to derive the coupling matrix of coupled resonator filters, and it is adopted here in the derivation of general coupling matrix of an *N*-port *n*-coupled resonators circuit. Magnetic coupling and Electric coupling will be considered separately and later a solution will be generalised for both types of couplings.

2.2.1 Circuits with magnetically coupled resonators

Considering only magnetic coupling between adjacent resonators, the equivalent circuit of magnetically coupled *n*-resonators with multiple ports is shown in figure 2.1, where *i* represents loop current, *L*, *C* denote the inductance and capacitance, and *R* denotes the resistance (represents a port). It is assumed that all the resonators are connected to ports, and the signal source is connected to resonator 1. It is also assumed that the coupling exists between all the resonators. This is extension of section 8.1 in [1] by considering multiple outputs here.

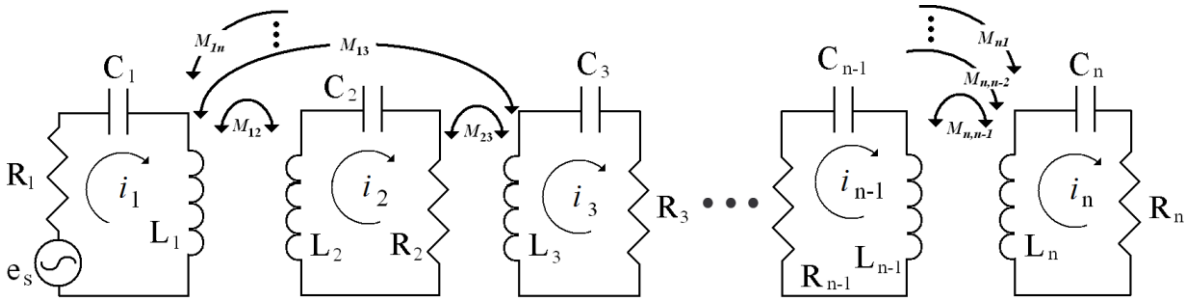

Figure 2.1: Equivalent circuit of magnetically *n*-coupled resonators in *N*-port network

Using Kirchoff's voltage law, the loop equations are derived as follows,

$$\left(R_1 + j\omega L_1 + \frac{1}{j\omega C_1}\right) i_1 - j\omega L_{12} i_2 \ldots \quad {}_{\ldots(n-1)} i_{(n-1)} - j\omega L_{1n} i_n = e_s$$

$$-j\omega L_{21} i_1 + \left(R_2 + j\omega L_2 + \frac{1}{j\omega C_2}\right) i_2 \ldots \quad {}_{-(n-1)} i_{(n-1)} - j\omega L_{2n} i_n = 0$$

$$\vdots \qquad (2.1)$$

$$-j\omega L_{(n-1)1} i_1 - j\omega L_{(n-1)2} i_2 + \ldots \left(\quad + j\omega L_{n-1} + \frac{1}{j\omega C_{n-1}}\right) i_{n-1} - j\omega L_{(n-1)n} i_n = 0$$

$$-j\omega L_{n1} i_1 - j\omega L_{n2} i_2 + \ldots \quad {}_{\ldots(n-1)} i_{n-1} + \left(R_n + j\omega L_n + \frac{1}{j\omega C_n}\right) i_n = 0$$

where $L_{ab}=L_{ba}$ denotes the mutual inductance between resonators *a* and *b*. The matrix form representation of these equations is as follows,

$$\begin{bmatrix} R_1+j\omega L_1+\frac{1}{j\omega C_1} & -j\omega L_{12} & \cdots & -j\omega L_{1(n-1)} & -j\omega L_{1n} \\ -j\omega L_{21} & R_2+j\omega L_2+\frac{1}{j\omega C_2} & \cdots & -j\omega L_{2(n-1)} & -j\omega L_{2n} \\ \vdots & \vdots & \vdots & \vdots & \vdots \\ -j\omega L_{(n-1)1} & -j\omega L_{(n-1)2} & \cdots & j\omega L_{n-1}+\frac{1}{j\omega C_{n-1}} & -j\omega L_{(n-1)n} \\ -j\omega L_{n1} & -j\omega L_{n2} & \cdots & -j\omega L_{n(n-1)} & R_n+j\omega L_n+\frac{1}{j\omega C_n} \end{bmatrix} \begin{bmatrix} i_1 \\ i_2 \\ \\ i_{n-1} \\ i_n \end{bmatrix} = \begin{bmatrix} e_s \\ 0 \\ 0 \\ 0 \\ 0 \end{bmatrix} \tag{2.2}$$

or equivalently $[Z].[i]=[e]$, where $[Z]$ is the impedance matrix. Assuming all resonators are synchronized at the same resonant frequency $\omega_0=1/\sqrt{LC}$, where $L=L_1=L_2=\ldots=L_{n-1}=L_n$ and $C=C_1=C_2=\ldots=C_{n-1}=C_n$, the impedance matrix $[Z]$ can be expressed by $[Z]=\omega_0 L.FBW.[\overline{Z}]$, where $FBW=\Delta\omega/\omega_0$ is the fractional bandwidth, and $[\overline{Z}]$ is the normalized impedance matrix, given by,

$$[\overline{Z}]=\begin{bmatrix} \frac{R_1}{\omega_0 L(FBW)}+P & \frac{-j\omega L_{12}}{\omega_0 L}\frac{1}{FBW} & \cdots & \frac{-j\omega L_{1(n-1)}}{\omega_0 L}\frac{1}{FBW} & \frac{-j\omega L_{1n}}{\omega_0 L}\frac{1}{FBW} \\ \frac{-j\omega L_{21}}{\omega_0 L}\frac{1}{FBW} & \frac{R_2}{\omega_0 L(FBW)}+P & \cdots & \frac{-j\omega L_{2(n-1)}}{\omega_0 L}\frac{1}{FBW} & \frac{-j\omega L_{2n}}{\omega_0 L}\frac{1}{FBW} \\ \vdots & \vdots & \vdots & \vdots & \vdots \\ \frac{-j\omega L_{(n-1)1}}{\omega_0 L(FBW)} & \frac{-j\omega L_{(n-1)2}}{\omega_0 L}\frac{1}{FBW} & \cdots & \frac{R_{n-1}}{\omega_0 L(FBW)}+P & \frac{-j\omega L_{(n-1)n}}{\omega_0 L}\frac{1}{FBW} \\ \frac{-j\omega L_{n1}}{\omega_0 L}\frac{1}{FBW} & \frac{-j\omega L_{n2}}{\omega_0 L}\frac{1}{FBW} & \cdots & \frac{-j\omega L_{n(n-1)}}{\omega_0 L}\frac{1}{FBW} & \frac{R_n}{\omega_0 L(FBW)}+P \end{bmatrix} \tag{2.3}$$

where $P=\frac{j}{FBW}\left(\frac{\omega}{\omega_0}-\frac{\omega_0}{\omega}\right)$ is the complex lowpass frequency variable.

Defining the external quality factor for resonator i as $Q_{ei}= \omega_0 L/R_i$, and the coupling coefficient as $M_{ij}=L_{ij}/L$, and assuming $\omega / \omega_0 \approx 1$ for narrow band approximation, $[\overline{Z}]$ is simplified to,

$$[\overline{Z}] = \begin{bmatrix} \frac{1}{q_{e1}} + P & -jm_{12} & \cdots & -jm_{1(n-1)} & -jm_{1n} \\ -jm_{21} & \frac{1}{q_{e2}} + P & \cdots & -jm_{2(n-1)} & -jm_{2n} \\ \vdots & \vdots & \vdots & \vdots & \vdots \\ -jm_{(n-1)1} & -jm_{(n-1)2} & \cdots & \frac{1}{q_{e(n-1)}} + P & -jm_{(n-1)n} \\ -jm_{n1} & -jm_{n2} & \cdots & -jm_{n(n-1)} & \frac{1}{q_{en}} + P \end{bmatrix} \tag{2.4}$$

where q_{ei} is the scaled external quality factor ($q_{ei}=Q_{ei}.FBW$) and m_{ij} is the normalized coupling coefficient ($m_{ij}=M_{ij}/FBW$).

The network representation for the circuit in figure 2.1, considering only three-ports, is shown in figure 2.2, where a_1, b_1, a_2, b_2 and a_3, b_3 are the wave variables, V_1, I_1, V_2, I_2 and V_3, I_3 are the voltage and current variables and i is the loop current. It is assumed that port 1 is connected to resonator 1, port 2 is connected to resonator x, and port 3 is connected to resonator y.

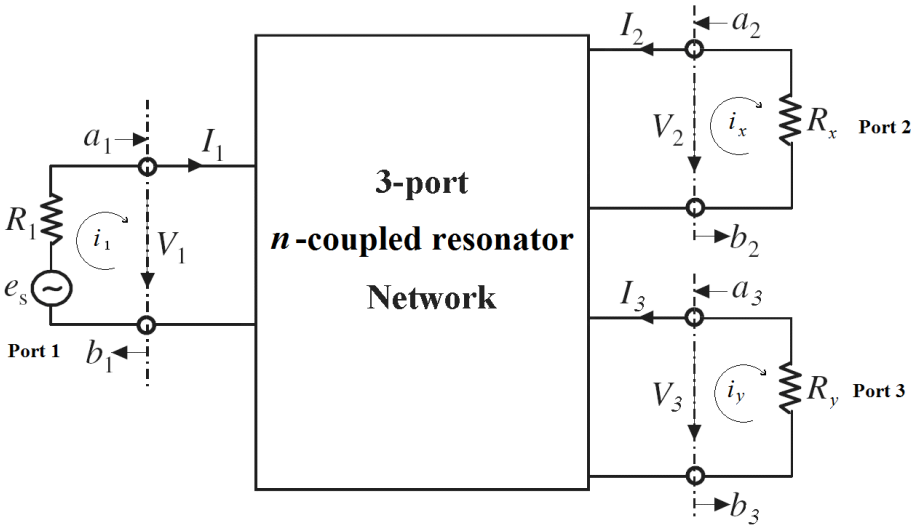

Figure 2.2: Network representation of 3-port circuit in figure 2.1.

Three ports have been considered at this point since three-port devices such as power dividers and diplexers are the main focus in this thesis. However, this does not lose generality, and more ports may be considered for *N*-way power dividers and multiplexers.

The relationships between the voltage and current variables and the wave variables are defined as follows [2],

$$V_N = \sqrt{R}\left(a_N + b_N\right) \quad and \quad I_N = \frac{1}{\sqrt{R}}\left(a_N - b_N\right) \tag{2.5}$$

Solving the equations (2.5) for a_N and b_N, the wave parameters are defined as follows,

$$a_N = \frac{1}{2}\left(\frac{V_N}{\sqrt{R}} + \sqrt{R}I_N\right) \quad and \quad b_N = \frac{1}{2}\left(\frac{V_N}{\sqrt{R}} - \sqrt{R}I_N\right) \tag{2.6}$$

where N is the port number, and R corresponds to R_1 for port 1, R_x for port 2, and R_y for port 3. It is noticed in the circuit in figure 2.2 that $I_1=i_1$, $I_2= - I_x$, $I_3= - I_y$, and $V_1=e_s-i_1R_1$. Accordingly, the wave variables may be rewritten as follows,

$$\begin{aligned} a_1 &= \frac{e_s}{2\sqrt{R_1}} & b_1 &= \frac{e_s - 2i_1R_1}{2\sqrt{R_1}} \\ a_2 &= 0 & b_2 &= i_x\sqrt{R_x} \\ a_3 &= 0 & b_3 &= i_x\sqrt{R_y} \end{aligned} \tag{2.7}$$

The S-parameters are found from the wave variables as follows,

$$\begin{aligned} S_{11} &= \left.\frac{b_1}{a_1}\right|_{a_2=a_3=0} = 1 - \frac{2R_1i_1}{e_s} \\ S_{21} &= \left.\frac{b_2}{a_1}\right|_{a_2=a_3=0} = \frac{2\sqrt{R_1R_x}i_x}{e_s} \\ S_{31} &= \left.\frac{b_3}{a_1}\right|_{a_2=a_3=0} = \frac{2\sqrt{R_1R_y}i_y}{e_s} \end{aligned} \tag{2.8}$$

Solving (2.2) for i_1, i_x and i_y,

$$i_1 = \frac{e_s}{\omega_0 L.FBW}\left[\overline{Z}\right]_{11}^{-1}$$

$$i_x = \frac{e_s}{\omega_0 L.FBW}\left[\overline{Z}\right]_{x1}^{-1} \tag{2.9}$$

$$i_y = \frac{e_s}{\omega_0 L.FBW}\left[\overline{Z}\right]_{y1}^{-1}$$

and by substitution of equations (2.9) into equations (2.8), we have,

$$S_{11} = 1 - \frac{2R_1}{\omega_0 L.FBW}\left[\overline{Z}\right]_{11}^{-1}$$

$$S_{21} = \frac{2\sqrt{R_1 R_x}}{\omega_0 L.FBW}\left[\overline{Z}\right]_{x1}^{-1} \tag{2.10}$$

$$S_{31} = \frac{2\sqrt{R_1 R_y}}{\omega_0 L.FBW}\left[\overline{Z}\right]_{y1}^{-1}$$

In terms of external quality factors $q_{ei} = \omega_0 L.FBW / R_i$, the S-parameters become,

$$S_{11} = 1 - \frac{2}{q_{e1}}\left[\overline{Z}\right]_{11}^{-1}$$

$$S_{21} = \frac{2}{\sqrt{q_{e1} q_{ex}}}\left[\overline{Z}\right]_{x1}^{-1} \tag{2.11}$$

$$S_{31} = \frac{2}{\sqrt{q_{e1} q_{ey}}}\left[\overline{Z}\right]_{y1}^{-1}$$

Where q_{e1}, q_{ex} and q_{ey} are the normalised external quality factors at resonators 1, x, and y, respectively. In case of asynchronously tuned coupled-resonator circuit, resonators may have

different resonant frequencies, and extra entries m_{ii} are added to the diagonal entries in $[\overline{Z}]$ to account for asynchronous tuning as follows,

$$[\overline{Z}] = \begin{bmatrix} \frac{1}{q_{e1}} + P - jm_{11} & \cdots & -jm_{1(n-1)} & -jm_{1n} \\ \vdots & \vdots & \vdots & \vdots \\ -jm_{(n-1)1} & \cdots & \frac{1}{q_{e(n-1)}} + P - jm_{(n-1)(n-1)} & -jm_{(n-1)n} \\ -jm_{n1} & \cdots & -jm_{n(n-1)} & \frac{1}{q_{en}} + P - jm_{nn} \end{bmatrix} \tag{2.12}$$

2.2.2 Circuits with electrically coupled resonators

The coupling coefficients introduced in the previous section are based on magnetic coupling. This section presents the derivation of coupling coefficients for electrically coupled resonators in an *N*-port circuit, where the electric coupling is represented by capacitors. The normalised admittance matrix $[\overline{Y}]$ will be derived here in an analogous way to the derivation of the $[\overline{Z}]$ matrix in the previous section.

Shown in figure 2.3 is the equivalent circuit of electrically coupled *n*-resonators in an *N*-port network, where i_s represents the source current, v_i denotes the node voltage, and *G* represents port conductance. This is extension to node equation formulation of electrically coupled two-port resonator filter in [1] by considering multiple ports here.

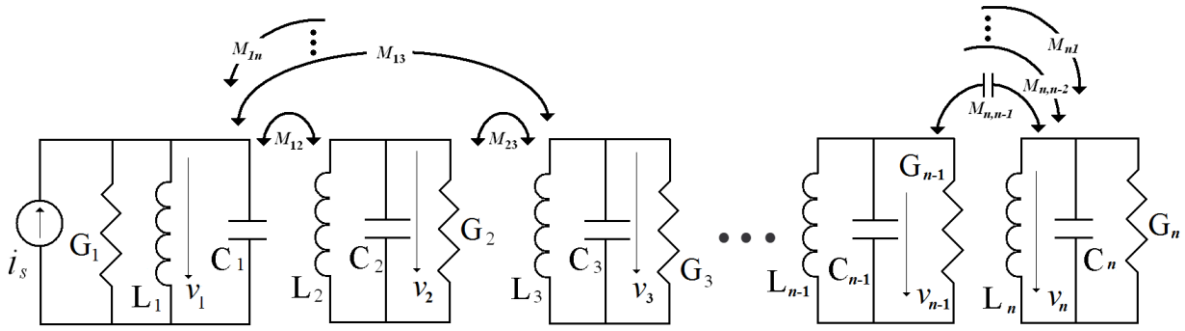

Figure 2.3: Equivalent circuit of electrically *n*-coupled resonators in *N*-port network

It is assumed here that all resonators are connected to ports, and the current source is connected to resonator 1. Also, it is assumed that all resonators are coupled to each other. The solution of this network is found by using Kirchhoff's current law, which states that the algebraic sum of the currents leaving a node is zero. Using this law, the node voltage equations are formulated as follows,

$$\begin{aligned}
&\left(G_1 + j\omega C_1 + \frac{1}{j\omega L_1}\right)v_1 - j\omega C_{12}v_2 \cdots - j\omega C_{1(n-1)}v_{n-1} - j\omega C_{1n}v_n = i_s \\
&-j\omega C_{21}v_1 + \left(G_2 + j\omega C_2 + \frac{1}{j\omega L_2}\right)v_2 \cdots - j\omega C_{2(n-1)}v_{n-1} - j\omega C_{2n}v_n = 0 \\
&\qquad\qquad \vdots \qquad\qquad (2.13) \\
&-j\omega C_{(n-1)1}v_1 - j\omega C_{(n-1)2}v_2 + \cdots + \left(G_{(n-1)} + j\omega C_{n-1} + \frac{1}{j\omega L_{(n-1)}}\right)v_{n-1} - j\omega C_{(n-1)n}v_n = 0 \\
&-j\omega C_{n1}v_1 - j\omega C_{n2}v_2 + \cdots - j\omega C_{n(n-1)}v_{n-1} + \left(G_n + j\omega C_n + \frac{1}{j\omega L_n}\right)v_n = 0
\end{aligned}$$

where $C_{ab}=C_{ba}$ denotes the mutual capacitance between resonators a and b. The previous equations are represented in matrix form as follows,

$$\begin{bmatrix}
G_1 + j\omega C_1 + \frac{1}{j\omega L_1} & -j\omega C_{12} & \cdots & -j\omega C_{1(n-1)} & -j\omega C_{1n} \\
-j\omega C_{21} & G_2 + j\omega C_2 + \frac{1}{j\omega L_2} & \cdots & -j\omega C_{2(n-1)} & -j\omega C_{2n} \\
\vdots & \vdots & \vdots & \vdots & \vdots \\
-j\omega C_{(n-1)1} & -j\omega C_{(n-1)2} & \cdots & G_{n-1} + j\omega C_{n-1} + \frac{1}{j\omega L_{n-1}} & -j\omega C_{(n-1)n} \\
-j\omega C_{n1} & -j\omega C_{n2} & \cdots & -j\omega C_{n(n-1)} & G_n + j\omega C_n + \frac{1}{j\omega L_n}
\end{bmatrix}
\begin{bmatrix} v_1 \\ v_2 \\ \vdots \\ v_{n-1} \\ v_n \end{bmatrix} =
\begin{bmatrix} i_s \\ 0 \\ \vdots \\ 0 \\ 0 \end{bmatrix}$$

(2.14)

or equivalently $[Y].[v]=[i]$, where $[Y]$ is the admittance matrix.

Assuming all resonators are synchronized at the same resonant frequency $\omega_0 = 1/\sqrt{LC}$, where $L=L_1=L_2=...=L_{n-1}=L_n$ and $C=C_1=C_2=...=C_{n-1}=C_n$, the admittance matrix $[Y]$ can be expressed by,

$$[Y] = \omega_0 C.FBW.[\overline{Y}] \tag{2.15}$$

where FBW is the fractional bandwidth, and $[\overline{Y}]$ is the normalized admittance matrix, given by,

$$[\overline{Y}] = \begin{bmatrix} \frac{G_1}{\omega_0 C.FBW} + P & \frac{-j\omega C_{12}}{\omega_0 C}\frac{1}{FBW} & \cdots & \frac{-j\omega C_{1(n-1)}}{\omega_0 C}\frac{1}{FBW} & \frac{-j\omega C_{1n}}{\omega_0 C}\frac{1}{FBW} \\ \frac{-j\omega C_{21}}{\omega_0 C}\frac{1}{FBW} & \frac{G_2}{\omega_0 C.FBW} + P & \cdots & \frac{-j\omega C_{2(n-1)}}{\omega_0 C}\frac{1}{FBW} & \frac{-j\omega C_{2n}}{\omega_0 C}\frac{1}{FBW} \\ \vdots & \vdots & \vdots & \vdots & \vdots \\ \frac{-j\omega C_{(n-1)1}}{\omega_0 C}\frac{1}{FBW} & \frac{-j\omega C_{(n-1)2}}{\omega_0 C}\frac{1}{FBW} & \cdots & \frac{G_{n-1}}{\omega_0 C.FBW} + P & \frac{-j\omega C_{(n-1)n}}{\omega_0 C}\frac{1}{FBW} \\ \frac{-j\omega C_{n1}}{\omega_0 C}\frac{1}{FBW} & \frac{-j\omega C_{n2}}{\omega_0 C}\frac{1}{FBW} & \cdots & \frac{-j\omega C_{n(n-1)}}{\omega_0 C}\frac{1}{FBW} & \frac{G_n}{\omega_0 C.FBW} + P \end{bmatrix} \tag{2.16}$$

where P is the complex lowpass frequency variable.

By defining the coupling coefficient as $M_{ij}=C_{ij}/C$, and the external quality factor for resonator i as $Q_{ei}=\omega_0 C/G_i$, and assuming $\omega / \omega_0 \approx 1$ for narrow band approximation, the normalised admittance matrix $[\overline{Y}]$ may be simplified to,

$$[\overline{Y}] = \begin{bmatrix} \frac{1}{q_{e1}} + P & -jm_{12} & \cdots & -jm_{1(n-1)} & -jm_{1n} \\ -jm_{21} & \frac{1}{q_{e2}} + P & \cdots & -jm_{2(n-1)} & -jm_{2n} \\ \vdots & \vdots & \vdots & \vdots & \vdots \\ -jm_{(n-1)1} & -jm_{(n-1)2} & \cdots & \frac{1}{q_{e(n-1)}} + P & -jm_{(n-1)n} \\ -jm_{n1} & -jm_{n2} & \cdots & -jm_{n(n-1)} & \frac{1}{q_{en}} + P \end{bmatrix} \tag{2.17}$$

where $q_{ei}=Q_{ei}.FBW$ is the scaled external quality factor, and $m_{ij}=M_{ij}/FBW$ is the normalized coupling coefficient.

A 3-port network with n-coupled resonators is considered here, with port 1 connected to resonator 1, port 2 connected to resonator x, and port 3 connected to resonator y. The network representation is shown in figure 2.4, where all wave and voltage and current variables at the network ports are the same as those in figure 2.2.

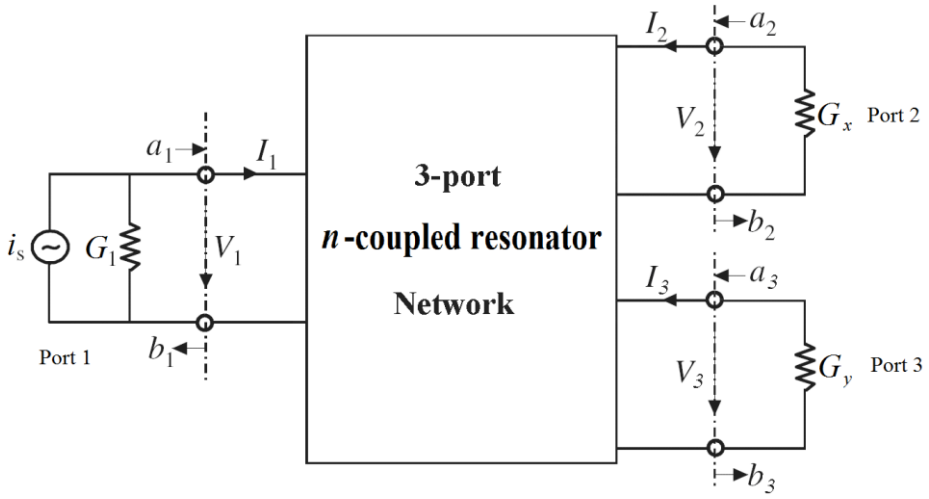

Figure 2.4: Network representation of 3-port circuit in figure 2.3.

By comparing the variables at the ports in the circuit in figure 2.3 and the network representation in figure 2.4, it is identified that $V_1=v_1$, $V_2=v_x$, $V_3= v_y$, and $I_1=i_s-v_1G_1$, where v_x and v_y are node voltages at resonators x and y, respectively. Accordingly, the wave parameters may be expressed as follows,

$$a_1 = \frac{i_s}{2\sqrt{G_1}} \qquad b_1 = \frac{2v_1G_1 - i_s}{2\sqrt{G_1}}$$

$$a_2 = 0 \qquad b_2 = v_x\sqrt{G_x} \tag{2.18}$$

$$a_3 = 0 \qquad b_3 = v_y\sqrt{G_y}$$

The scattering parameters are found from the wave variables as,

$$S_{11} = \left.\frac{b_1}{a_1}\right|_{a_2=a_3=0} = \frac{2v_1G_1}{i_s} - 1$$

$$S_{21} = \left.\frac{b_2}{a_1}\right|_{a_2=a_3=0} = \frac{2\sqrt{G_1G_x}v_x}{i_s} \tag{2.19}$$

$$S_{31} = \left.\frac{b_3}{a_1}\right|_{a_2=a_3=0} = \frac{2\sqrt{G_1G_y}v_y}{i_s}$$

The node voltage variables v_1, v_x and v_y are found from (2.14) and (2.15) as follows,

$$v_1 = \frac{i_s}{\omega_0 C.FBW}\overline{[Y]}^{-1}_{11}$$

$$v_x = \frac{i_s}{\omega_0 C.FBW}\overline{[Y]}^{-1}_{x1} \tag{2.20}$$

$$v_y = \frac{i_s}{\omega_0 C.FBW}\overline{[Y]}^{-1}_{y1}$$

By substitution of equations (2.20) into equations (2.19), the S-parameters are found,

$$S_{11} = \frac{2G_1}{\omega_0 C.FBW}\overline{[Y]}^{-1}_{11} - 1$$

$$S_{21} = \frac{2\sqrt{G_1G_x}}{\omega_0 C.FBW}\overline{[Y]}^{-1}_{x1} \tag{2.21}$$

$$S_{31} = \frac{2\sqrt{G_1G_y}}{\omega_0 C.FBW}\overline{[Y]}^{-1}_{y1}$$

The S-parameters can now be expressed in terms of the normalised external quality factors, $q_{ei}=\omega_0 C.FBW/G_i$ as follows,

$$S_{11} = \frac{2}{q_{e1}}\overline{[Y]}_{11}^{-1} - 1$$

$$S_{21} = \frac{2}{\sqrt{q_{e1}q_{ex}}}\overline{[Y]}_{x1}^{-1} \tag{2.22}$$

$$S_{31} = \frac{2}{\sqrt{q_{e1}q_{ey}}}\overline{[Y]}_{y1}^{-1}$$

To account for asynchronous tuning, the normalised admittance matrix will have extra terms m_{ii} in the principal diagonal, and it will be identical to the normalised impedance matrix in equation (2.12).

2.2.3 General coupling matrix

The derivations in the previous sections show that the normalized admittance matrix of electrically coupled resonators is identical to the normalized impedance matrix of magnetically coupled resonators. Accordingly, a unified solution may be formulated regardless of the type of coupling. In consequence, the S parameters of a three-port coupled resonator circuit may be generalised as,

$$S_{11} = 1 - \frac{2}{q_{e1}}[A]_{11}^{-1},$$

$$S_{21} = \frac{2}{\sqrt{q_{e1}q_{ex}}}[A]_{x1}^{-1} \tag{2.23}$$

$$S_{31} = \frac{2}{\sqrt{q_{e1}q_{ey}}}[A]_{y1}^{-1}$$

where it is assumed that port 1 is connected to resonator 1, ports 2 and 3 are connected to resonators x and y respectively. The matrix $[A]$ is given below,

$$[A]=\begin{bmatrix} 1/q_{e1} & \cdots & 0 \\ \vdots & \vdots & \vdots \\ 0 & \cdots & 1/q_{e(n-1)} \\ 0 & \cdots & 1/q_{en} \end{bmatrix}+P\begin{bmatrix} 1 & \cdots & \\ \vdots & \vdots & \vdots \\ 0 & \cdots & \\ 0 & \cdots & \end{bmatrix}-J\begin{bmatrix} m_{11} & \cdots & m_{1n} \\ \vdots & \vdots & \vdots \\ m_{(n-1)1} & \cdots & m_{(n-1)n} \\ m_{n1} & \cdots & m_{nn} \end{bmatrix} \tag{2.24}$$

The formulae in (2.23) and (2.24) will be used as a basis to synthesise 3-port coupled resonator power dividers and diplexers in the next chapters. For completeness, the formulae of the remaining scattering parameters S_{22}, S_{33}, and S_{32} can be derived analogously to the previous derivations, and they are given by,

$$\begin{aligned} S_{22} &= 1-\frac{2}{q_{ex}}[A]^{-1}_{xx} \\ S_{33} &= 1-\frac{2}{q_{ey}}[A]^{-1}_{yy} \\ S_{32} &= \frac{2}{\sqrt{q_{ex}q_{ey}}}[A]^{-1}_{yx} \end{aligned} \tag{2.25}$$

The proposed coupled resonator components may be synthesised using different ways: analytic solution to calculate the coupling coefficients, or full synthesis using EM simulation tools, whereby the dimensions of the physical structure are optimized, or optimization techniques to synthesise the coupling matrix [m]. The use of full-wave EM simulation is very time consuming when compared to coupling matrix optimization that requires significantly less computational time. Coupling matrix optimisation techniques similar to those used to synthesise coupled-resonator filters will be utilised in the current work to produce the coupling matrix entries of the proposed coupled resonator devices. The entries of the coupling matrix [m] are modified at each iteration in the optimization process until an optimal solution

is found such that a scalar cost function is minimised. Optimization techniques and cost function formulation will be discussed in Chapter 3.

2.3 Conclusion

The derivation of the coupling matrix of multiple coupled resonators with multiple outputs has been presented. A unified solution has been found for both electrically and magnetically coupled resonators. The relationships between the scattering parameters and the coupling matrix of a 3-port coupled resonator circuit have been formulated. The derived equations in this chapter will be used as a basis in the synthesis of coupled resonator power dividers and diplexers in the next chapters.

References

[1] J.S. Hong and M.J. Lancaster, Microstrip filters for RF/microwave applications. New York: Wiley, 2001.
[2] M. Radmanesh, *RF & Microwave Design Essentials*, Authorhouse, 2007.

Chapter 3

Synthesis of Coupled Resonator Power Dividers

3.1 Introduction

Power dividers are passive microwave components used to divide input signal into two or more signals of less power [1]. They are widely used in antenna arrays, balanced power amplifiers, mixers, and phase shifters. Examples of widely used power dividers are T-junctions [2], and Wilkinson power dividers [3]. These devices are three-port networks in their simplest form, and they can be generalised to N-way power dividers by constructing multi-stage structures. Four-port components such as directional couplers and hybrids are also used for power division with a phase shift of either 90^{o} (branch-line hybrids) or an 180^{o} (magic-T) between the output ports [2].

In this chapter, an approach to design three-port power dividers with arbitrary power division is proposed. It is based on multiple coupled resonators arranged in a three-port structure, and resonator realization is possible including microstrip resonators or waveguide cavities or other types of resonators. The synthesis of the proposed power dividers employs coupling matrix optimization techniques similar to those used to synthesise coupled resonator filters. The equations of the scattering parameters in terms of the general coupling matrix that were derived in chapter 2 will be utilised in the synthesis.

The general properties of a three-port network will be discussed first, and then the synthesis of polynomial functions for the power divider will be presented. A cost function that is used

in the optimization of the coupling matrix will be then derived. Examples of power dividers with different topologies with Chebyshev and Quasi-Elliptic filtering responses will be finally illustrated.

3.2 Three-Port Networks

A power divider that is represented as a three-port network will have the general scattering matrix,

$$[S]=\begin{bmatrix} S_{11} & S_{12} & S_{13} \\ S_{21} & S_{22} & S_{23} \\ S_{31} & S_{32} & S_{33} \end{bmatrix} \tag{3.1}$$

If the network is passive and contains only isotropic materials, then it must be reciprocal (S_{ij}=S_{ji}). It is desired for power dividers to be lossless and matched at all ports. However, it is impossible to create a three-port network that is reciprocal, lossless and matched at all ports, as will be shown.

If the network is reciprocal, and if all ports are matched (S_{ii}=0), then the scattering matrix in (3.1) is reduced to,

$$[S]=\begin{bmatrix} 0 & S_{12} & S_{13} \\ S_{12} & 0 & S_{23} \\ S_{13} & S_{23} & 0 \end{bmatrix} \tag{3.2}$$

For a lossless network, the scattering matrix must be unitary [2], that is,

$$\begin{aligned} &\sum_{k=1}^{N} S_{ki}S_{ki}^{*} = 1 \\ &\sum_{k=1}^{N} S_{ki}S_{kj}^{*} = 0, \qquad for \qquad i \neq j \end{aligned} \tag{3.3}$$

By applying the unitary condition on the scattering matrix in (3.2), the following equations are obtained [2],

$$\begin{aligned} |S_{12}|^2 + |S_{13}|^2 &= 1 \\ |S_{12}|^2 + |S_{23}|^2 &= 1 \\ |S_{13}|^2 + |S_{23}|^2 &= 1 \\ S_{12}S_{13}^* &= 0 \\ S_{12}S_{23}^* &= 0 \\ S_{13}S_{23}^* &= 0 \end{aligned} \tag{3.4}$$

The last three equations in (3.4) are inconsistent with the first three equations, since they show that at least two of the three parameters S_{12}, S_{13}, S_{23} must be zero. This implies that a three-port network can never be lossless, reciprocal and matched at all ports. However, it is possible to physically realize the three-port component if one of these three conditions is abandoned.

3.3 Insertion and Reflection Loss

For a 3-port power divider with n coupled resonators, the insertion and reflection loss parameters may be defined in (dB) as follows:

$$L_{A1} = -20\log|S_{21}|, \quad L_{A2} = -20\log|S_{31}|, \quad L_R = 20\log|S_{11}| \tag{3.5}$$

where L_{A1} corresponds to insertion loss between ports 1 and 2, L_{A2} corresponds to the to insertion loss between ports 1 and 3, and L_R represents the return loss at port 1 in decibels. By employing the conservation of energy formula, we have:

$$L_R = 10\log[1 - |S_{21}|^2 - |S_{31}|^2] \tag{3.6}$$

If the input power is to be divided between the output ports such that,

$$|S_{31}|^2 = \alpha|S_{21}|^2 \tag{3.7}$$

then by substitution (3.7) into (3.6) and solving for $|S_{21}|^2$ and $|S_{31}|^2$, we have:

$$\begin{aligned} |S_{21}|^2 &= \frac{1}{1+\alpha}\left(1-10^{0.1L_R}\right) \\ |S_{31}|^2 &= \frac{\alpha}{1+\alpha}\left(1-10^{0.1L_R}\right) \end{aligned} \tag{3.8}$$

and by substitution of (3.8) into (3.5), we obtain L_{A1} and L_{A2} as follows,

$$\begin{aligned} L_{A1} &= -10\log\left(\frac{1}{1+\alpha}\right) - 10\log\left(1-10^{0.1L_R}\right) \\ L_{A2} &= -10\log\left(\frac{\alpha}{1+\alpha}\right) - 10\log\left(1-10^{0.1L_R}\right) \end{aligned} \tag{3.9}$$

Note that the terms $10\log\left(1/1+\alpha\right)$ and $10\log\left(\alpha/1+\alpha\right)$ correspond to the maximum values of $|S_{21}|$ and $|S_{31}|$ in dB respectively, whereas the term $10\log\left(1-10^{0.1L_R}\right)$ correspond to the ripple value in dB, as illustrated in figure 3.1.

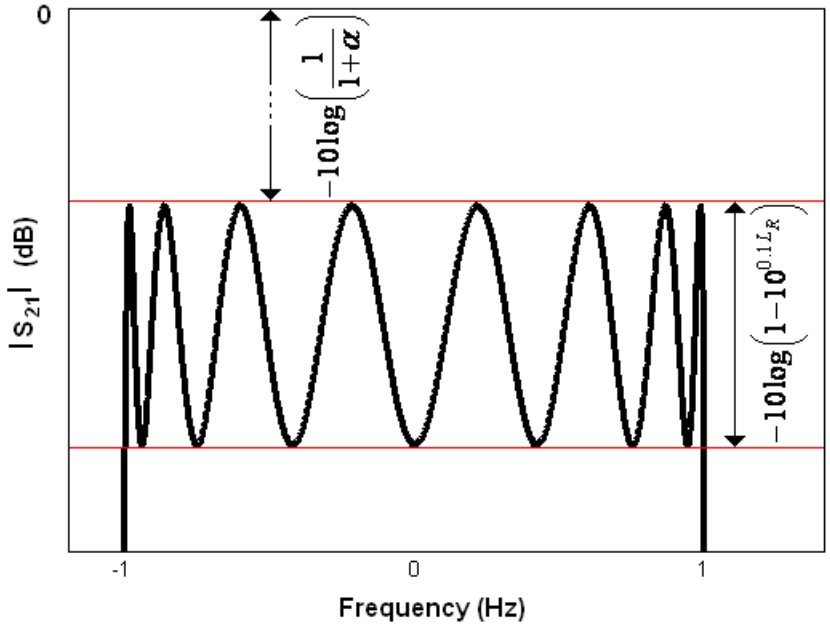

Figure 3.1: Insertion loss S_{21} (dB)

3.4 Power Divider Polynomials

Since the proposed divider is based on filtering functions, its response can be described by polynomial transfer functions. This section presents the synthesis of the polynomial characteristics of a coupled-resonator power divider. An example of a power divider with 8th order filtering function and unequal power division will be illustrated.

3.4.1 Polynomials synthesis

For a 3-port power divider consisting of *n* coupled resonators, the reflection and transmission functions may be defined as ratio of two polynomials as follows:

$$S_{11}(s)=\frac{F(s)}{E(s)},\ S_{21}(s)=\frac{P(s)/\varepsilon_1}{E(s)},\ S_{31}(s)=\frac{P(s)/\varepsilon_2}{E(s)} \tag{3.10}$$

where $s=j\omega$ is the complex frequency variable, the polynomials $F(s)$, $P(s)$ and $E(s)$ are assumed to be normalized so that their highest degree coefficients are unity. $F(s)$ and $E(s)$ are N^{th} order polynomials, where N is the order of the filtering function, whereas $P(s)$ has an order equal to the number of prescribed transmission zeros. The roots of $F(s)$ correspond to the reflection zeros and can be found by a recursive technique [4], whereas the roots of $P(s)$ correspond to the frequency positions of transmission zeros. For a Chebyshev function, the constants ε_1 and ε_2 normalize $S_{21}(s)$ and $S_{31}(s)$ to the specified insertion loss levels at $\omega=\pm1$ respectively. The polynomial $E(s)$ has its complex roots corresponding to the filter pole positions and can be constructed if the polynomials $F(s)$, $P(s)$ and the constants ε_1 and ε_2 are known. Expressions for ε_1 and ε_2 will be derived next, follows by a discussion on determining $E(s)$.

In a lossless 3-port system, conservation of energy formula is defined as,

$$S_{11}(s)S_{11}(s)^*+S_{21}(s)S_{21}(s)^*+S_{31}(s)S_{31}(s)^*=1 \tag{3.11}$$

By applying (3.7) into (3.11), the following equation is obtained,

$$|S_{11}(s)|^2 + (1+\alpha)|S_{21}(s)|^2 = 1 \tag{3.12}$$

From (3.10) and (3.12), the constant ε_1 is evaluated as:

$$\varepsilon_1 = \left|\frac{S_{11}(s)}{S_{21}(s)}\right| \cdot \left|\frac{P(s)}{F(s)}\right| = \frac{\sqrt{1+\alpha}\,|S_{11}(s)|}{\sqrt{1-|S_{11}(s)|^2}} \cdot \left|\frac{P(s)}{F(s)}\right| \tag{3.13}$$

when $s=\pm j$, $|S_{11}|$ is equal to the maximum passband reflection coefficient, whose value is known from the specification. ε_1 can be expressed in terms of the polynomials $F(s)$ and $P(s)$, and the prescribed return loss level in dB, L_R, in the passband as follows,

$$\varepsilon_1 = \sqrt{\frac{1+\alpha}{10^{-L_R/10}-1}} \cdot \left|\frac{P(s)}{F(s)}\right|_{s=\pm j} \tag{3.14}$$

Similarly, ε_2 can be expressed as,

$$\varepsilon_2 = \sqrt{\frac{1+\alpha}{\alpha\left(10^{-L_R/10}-1\right)}} \cdot \left|\frac{P(s)}{F(s)}\right|_{s=\pm j} \tag{3.15}$$

Once the polynomials F and P, and the constants ε_1 and ε_2 are known, the denominator polynomial E can be derived by substitution of $F(s)$, $P(s)$ and $E(s)$, into the conservation of energy formula, as follows,

$$F(s)F(s)^* + \frac{P(s)P(s)^*}{\varepsilon_1^2} + \frac{P(s)P(s)^*}{\varepsilon_2^2} = E(s)E(s)^* \tag{3.16}$$

$E(s)E(s)^*$ is constructed by polynomials multiplications in the left hand side of equation (3.16), which must be polynomial of the order $2N$ with real coefficients. The roots of $E(s)E(s)^*$ will be symmetric about the imaginary axis in the complex plane as shown in figure 3.2, and they can be found using numerical analysis software such as MATLAB. Since $E(s)$ is strictly Hurwitz, then its roots are those in the left half plane, whereas the roots of $E(s)^*$ are those in the right half plane. The polynomial $E(s)$ is then constructed by choosing the N roots in the left half plane [5].

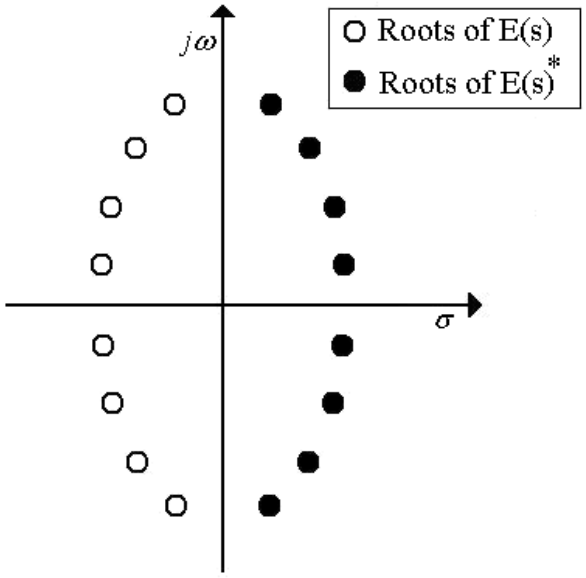

Figure 3.2: Pattern of the roots of $E(s)E(s)^*$

3.4.2 Example A: polynomials synthesis of coupled resonator power divider

The polynomials of a power divider with 8th order filtering response with finite transmission zeros located at ±1.23*j* Hz are synthesised here. It has a return loss of 20 dB, and an unequal power division with α=1/3. The polynomial *F* is found by applying the recursive technique presented in Appendix A. The recursive process starts by substitution of ω_1=1.23 into equation (A.14), which results to

$$U_1 = -0.813 + \omega \quad \text{and} \quad V_1 = \omega'(0.5823)$$

The recursive procedure continues to find U_2 and V_2 by using equations (A.16) for ω_2=-1.23 as follows,

$$U_2 = 1.339\omega^2 - 1 \text{ and } V_2 = 1.1645\omega\omega'$$

The process continues by substitution of $\omega_k=\infty$ for *k*=3,…,8 into equations (A.17) and the highest degree polynomials U_8 and V_8 are found as,

$$U_8 = 80.1127\omega^8 - 170.8012\omega^6 + 116.3535\omega^4 - 26.3260\omega^2 + 1$$

$$V_8 = \left(80.1127\omega^7 - 130.7448\omega^5 + 60.9952\omega^3 - 7.1645\omega\right)\omega'$$

Normalizing the polynomial U_8 gives the polynomial $F(\omega)$, and finding its roots yields the N reflection zeroes, where N is the order of the filtering function. The roots of V_8 are the N-1 frequency locations of the reflection maxima. The polynomial P is constructed from its prescribed roots, and the constants ε_1 and ε_2 are calculated from (3.14) and (3.15) and found to be ε_1=14.0658 and ε_2=24.3626. The polynomial E can now be constructed as shown in section 3.4.1. Table 3.1 shows the prescribed transmission zeros, the reflection zeros, the reflection maxima locations and the poles of the filtering power divider and figure 3.3 depicts its pole-zero diagram. The normalised coefficients of the polynomials $P(s)$, $F(s)$ and $E(s)$ are shown in table 3.2.

The scattering parameters are constructed using equations (3.10) and they are shown in figure 3.4. The parameters L_{A1} and L_{A2} have been calculated using equation (3.9) as L_{A1}=1.2930 and L_{A2}=6.0642. Figure 3.5 depicts the passband ripple and L_{A1} and L_{A2}.

Table 3.1: zero and pole locations of the filtering power divider

TZs	RZs	Refl. maxima	Poles
-1.23*j*	-0.9860*j*	-0.9424*j*	-0.0497 - 1.0380*j*
1.23*j*	-0.8655*j*	-0.7523*j*	-0.1778 - 0.9340*j*
	-0.603*j*	-0.4218*j*	-0.3248 - 0.6635*j*
	-0.2171*j*	0*j*	-0.4199 - 0.2407*j*
	0.2171*j*	0.4218*j*	-0.4199 + 0.2407*j*
	0.603*j*	0.7523*j*	-0.3248 + 0.6635*j*
	0.8655*j*	0.9424*j*	-0.1778 + 0.9340*j*
	0.9860*j*		-0.0497 + 1.0380*j*

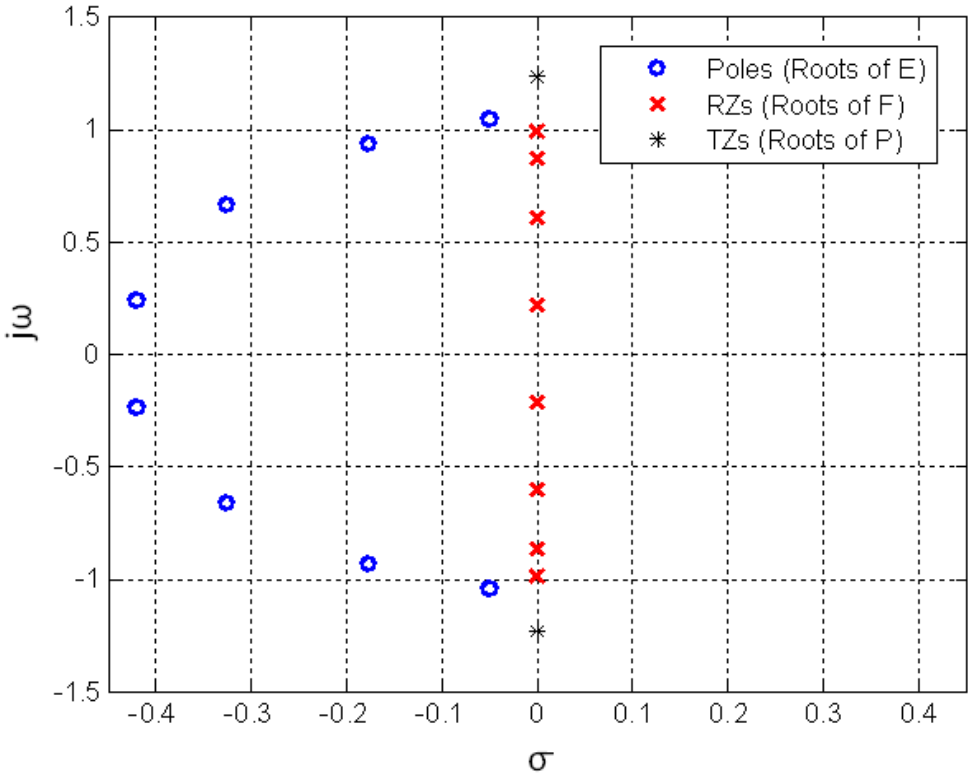

Figure 3.3: Pole-zero diagram of the filtering power divider

Table 3.2: Polynomial coefficients of the filtering power divider

s^n, n=	$P(s)$	$F(s)$	$E(s)$
0	1.5129	0.0125	0.1248
1	0	0	0.6566
2	1	0.3286	1.8416
3		0	3.3732
4		1.4524	4.7645
5		0	4.6953
6		2.1320	4.0226
7		0	1.9445
8		1	1

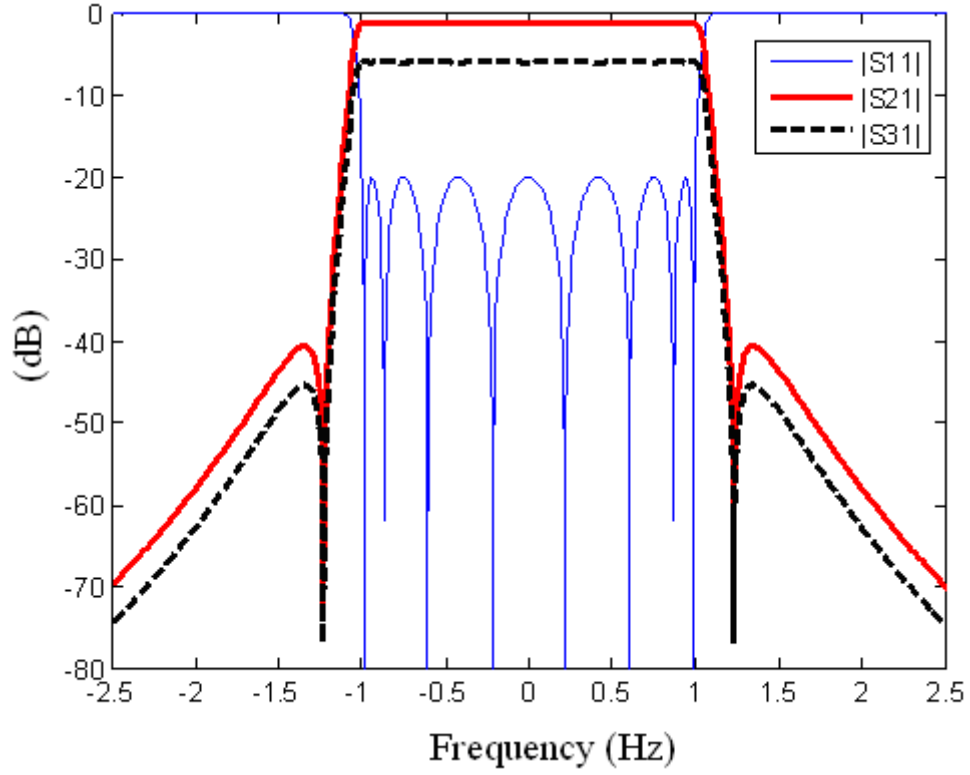

Figure 3.4: The magnitudes of S_{11}, S_{21} and S_{31} of the filtering power divider

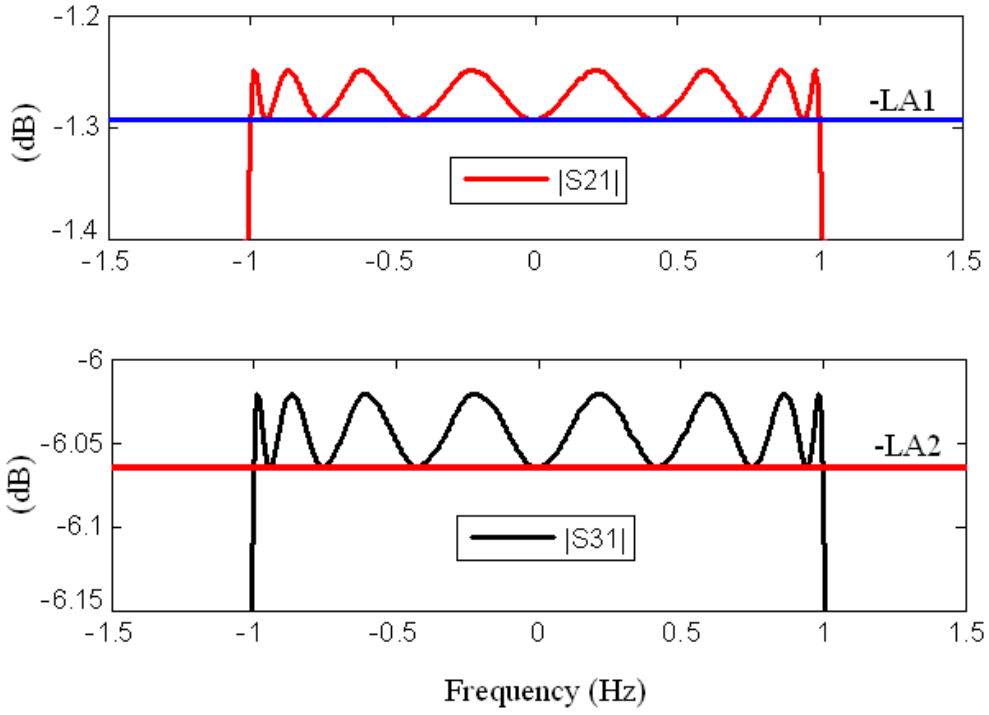

Figure 3.5: Passband details for S_{21} and S_{31}

3.5 Power Divider Coupling Matrix Optimization

The coupling matrix of multiple coupled resonators with multiple outputs has been derived in chapter 2. This section presents the production of the coupling matrix of a three-port coupled resonator power divider using an optimisation technique, whereby a cost function is minimised. An overview of optimisation techniques will be presented, and a cost function will be formulated in this section. Examples of coupled resonator power dividers with different topologies will be illustrated in the next sections.

3.5.1 Optimization techniques

Numerous optimisation techniques have been developed to synthesise coupled resonator filters. These techniques can be based either on optimisation of the dimensions of the physical structure of the filter using EM simulations [6], or on optimisation of the coupling coefficients in a coupling matrix. A main advantage of coupling matrix optimisation approach is that it requires significantly less computational time than full scale EM simulations to complete the synthesis process.

Optimisation techniques, despite their diversity, generally share a common aim of minimisation of a scalar cost function $\Omega(x)$, where x is a set of parameters known as control variables. At each iteration in the optimisation process, some or all values of x are modified, and the cost function is evaluated. This is repeated till an optimal solution is found such that the cost function is minimised.

In case of optimisation of the coupling matrix of a coupled resonator circuit, the control variables correspond to the values of the direct/cross coupling coefficients and external quality factors. The control variables may be either unconstrained, so that the search space is unbounded, or constrained by lower and upper limits to prevent the optimisation algorithm from giving an unfeasible solution.

In microwave coupled resonator optimisation problems, as well as real world optimisation problems, the cost function of many variables will have several local minima, one of them is the global minimum. Local optimisation methods are used to find an arbitrary local minimum, which is relatively straightforward. However, finding the global minimum is more challenging and global optimisation methods can be used.

Local optimisation algorithms strongly depend on the initial values of the control parameters. The initial guess should be given as an input to the algorithm that will seek a local minimum within the local neighbourhood of the initial guess. However, this local minimum is not guaranteed to be the global minimum.

Global optimisation algorithms generally do not require initial guess for the control variables, as they generate their own initial values, and they seek the global minimum within the entire search space. In comparison to local methods, global optimisation methods are much slower and may take hours or even days to find the optimal solution for problems with tens of variables. Global algorithms tend to be utilised when the local algorithms are not adequate, or when it is of great importance to find the global solution.

A large number of optimisation methods have been reported in the literature. Gradient based local optimisation techniques have been reported for the design of coupled resonator filters [7-9], where in case of optimising the coupling matrix, the gradient of the cost function is evaluated with respect to all coupling coefficients. Genetic algorithms, inspired by the natural biological evolution, provide a global search mechanism. They have been utilised to design microwave circuits as reported in [10-12]. Hybrid optimisation methods that combine a genetic algorithm with a local search method have been also reported for the synthesis of coupled resonator filters [13-14].

A gradient based local optimisation method has been used in the current work to produce coupling matrices of coupled resonator power dividers. The method has been successful and efficient for all of the examples illustrated in this chapter, and the convergence of the algorithm was very fast. A cost function will be formulated and examples of synthesised power dividers will be demonstrated in the next sections.

3.5.2 Cost function formulation

Several cost functions have been reported in literature for synthesis of coupling matrices of coupled resonator filters [7-9],[13],[15]. The cost function adopted in the current work is a modified version of that used in [8]. It has been selected since it depends on minimum set of characteristics that fully identify the desired response, which makes the algorithm requires less iterations and converges faster. The modification here is addition of an extra term to the cost function given in [8] to satisfy the power division ratio requirement. The formulation of the cost function used in the current work is presented next.

The initial cost function is written in terms of the polynomials F and P and it is evaluated at the frequency locations of transmission and reflection zeros as follows,

$$\Omega = \sum_{i=1}^{T} \left| P(s_{ti}) \right|^2 + \sum_{j=1}^{R} \left| F(s_{rj}) \right|^2 + \sum_{j=1}^{R} \left(\left| \frac{P(s_{rj})}{\varepsilon_1 E(s_{rj})} \right| - \sqrt{\frac{1}{1+\alpha}} \right)^2 \tag{3.17}$$

Where T is the number of transmission zeros, R is the number of reflection zeros, s_{ti} and s_{rj} are the complex lowpass prototype transmission and reflection zeros respectively. The lowpass prototype frequency positions of reflection zeros are found using Cameron's recursive technique in Appendix A. The last term in the cost function is used to achieve the required power division ratio, and is evaluated at the frequency locations of the peaks of $|S_{21}|=|P/\ \varepsilon_1 E|$, which coincide with the frequency locations of reflection zeros s_{rj}. The constant α is the

power ratio as given in equation (3.7), and $\sqrt{1/(1+\alpha)}$ is the peak value of $|S_{21}|$. Alternatively, the last term in the cost function can be evaluated at the frequency locations of the peaks of $|S_{31}|=|P/\varepsilon_2 E|$, with $\sqrt{\alpha/(1+\alpha)}$ is the peak value of $|S_{31}|$. This cost function does not involve the ripple in the optimization parameters, and hence the external quality factors have to be calculated analytically at the desired return loss, as shown in section (1.4.1). The calculations of the external quality factors and the right locations of the return zeros enforce the peaks of $|S_{11}|$ to be at the required return loss level.

The polynomials P and F can be evaluated in terms of the coupling matrix by equating the scattering parameters in equations (3.10) to their equivalent in equations (2.23) that relate the scattering parameters to the matrix $[A]$. Recalling equations (2.23), and assuming that port 1 is connected to resonator 1, and ports 2 and 3 are connected to resonators a and b respectively:

$$S_{11} = 1 - \frac{2}{q_{e1}}[A]^{-1}_{11}, \qquad S_{21} = \frac{2}{\sqrt{q_{e1}q_{ea}}}[A]^{-1}_{a1}, \qquad S_{31} = \frac{2}{\sqrt{q_{e1}q_{eb}}}[A]^{-1}_{b1} \tag{3.18}$$

The inverse of the matrix $[A]$ can be described in terms of the adjugate and determinant by employing Cramer's rule for the inverse of a matrix,

$$[A]^{-1} = \frac{adj([A])}{\Delta_A}, \qquad \Delta_A \neq 0 \tag{3.19}$$

where $adj([A])$ is the adjugate of the matrix $[A]$, and Δ_A is its determinant. Noting that the adjugate is the transpose of the matrix cofactors, the $(x,1)$ element of the inverse of matrix $[A]$ is:

$$[A]^{-1}_{x1} = \frac{cof_{1x}([A])}{\Delta_A} \tag{3.20}$$

where $cof_{1x}([A])$ is the $(1,x)$ element of the cofactor matrix of $[A]$. By substitution of (3.20) into (3.18), the following equations are obtained,

$$
\begin{aligned}
S_{11} &= 1 - \frac{2}{q_{e1}} \frac{cof_{11}\left(\left[A\right]\right)}{\Delta_A} \\
S_{21} &= \frac{2}{\sqrt{q_{e1} q_{ea}}} \frac{cof_{1a}\left(\left[A\right]\right)}{\Delta_A} \\
S_{31} &= \frac{2}{\sqrt{q_{e1} q_{eb}}} \frac{cof_{1b}\left(\left[A\right]\right)}{\Delta_A}
\end{aligned}
\tag{3.21}
$$

by equating the S-parameters in (3.21) to their equivalent in (3.10), the polynomials $F(s)$, $P(s)$ and $E(s)$ are expressed in terms of the general matrix $[A]$ as follows,

$$
\begin{aligned}
F(s) &= \Delta_A(s) - \frac{2.cof_{11}\left(\left[A(s)\right]\right)}{q_{e1}}, \\
\frac{P(s)}{\varepsilon_1} &= \frac{2.cof_{1a}\left(\left[A(s)\right]\right)}{\sqrt{q_{e1} q_{ea}}}, \\
\frac{P(s)}{\varepsilon_2} &= \frac{2.cof_{1b}\left(\left[A(s)\right]\right)}{\sqrt{q_{e1} q_{eb}}} \\
E(s) &= \Delta_A(s)
\end{aligned}
\tag{3.22}
$$

The cost function in equation (3.17) can now be expressed in terms of the general matrix $[A]$ and the external quality factors as follows,

$$
\begin{aligned}
\Omega = \sum_{i=1}^{T} \left| \frac{2}{\sqrt{q_{e1} q_{ea}}} .cof_{1a}([A(S_{ti})]) \right|^2 + \sum_{j=1}^{R} \left| \Delta_A(S_{rj}) - \frac{2.cof_{11}([A(S_{rj})])}{q_{e1}} \right|^2 \\
+ \sum_{j=1}^{R} \left| \frac{2}{\sqrt{q_{e1} q_{ea}}} . \frac{cof_{1a}([A(S_{rj})])}{\Delta_A(S_{rj})} - \sqrt{\frac{1}{1+\alpha}} \right|^2
\end{aligned}
\tag{3.23}
$$

where $[A]$ is the matrix derived and given in (2.24), $\Delta_A(S_{rj})$ is the determinant of the matrix $[A]$ evaluated at the frequency variable S_{rj}, and $cof_{mn}([A(s=a)])$ is the cofactor of matrix $[A]$ evaluated by removing the m^{th} row and the n^{th} column of $[A]$ and finding the determinant of the resulting matrix at the frequency variable $s=a$.

The cost function in (3.23) has been used in a gradient based optimization algorithm to synthesize coupling matrices of coupled resonator power dividers. The initial values of

control variables, which correspond to coupling coefficients, were set to 0.5 for direct coupling, and to -0.5 for cross coupling. Alternatively, the initial coupling coefficients may be set to values corresponding to Chebyshev response, which can be calculated from the g-values given in section 1.5.1.

3.5.3 Optimization algorithm flowchart

The flowchart of the algorithm is given in figure 3.6. The frequency locations of the prescribed transmission zeros and the frequency locations of the reflection zeros that are calculated using Cameron's technique are set at the beginning of the optimization algorithm.

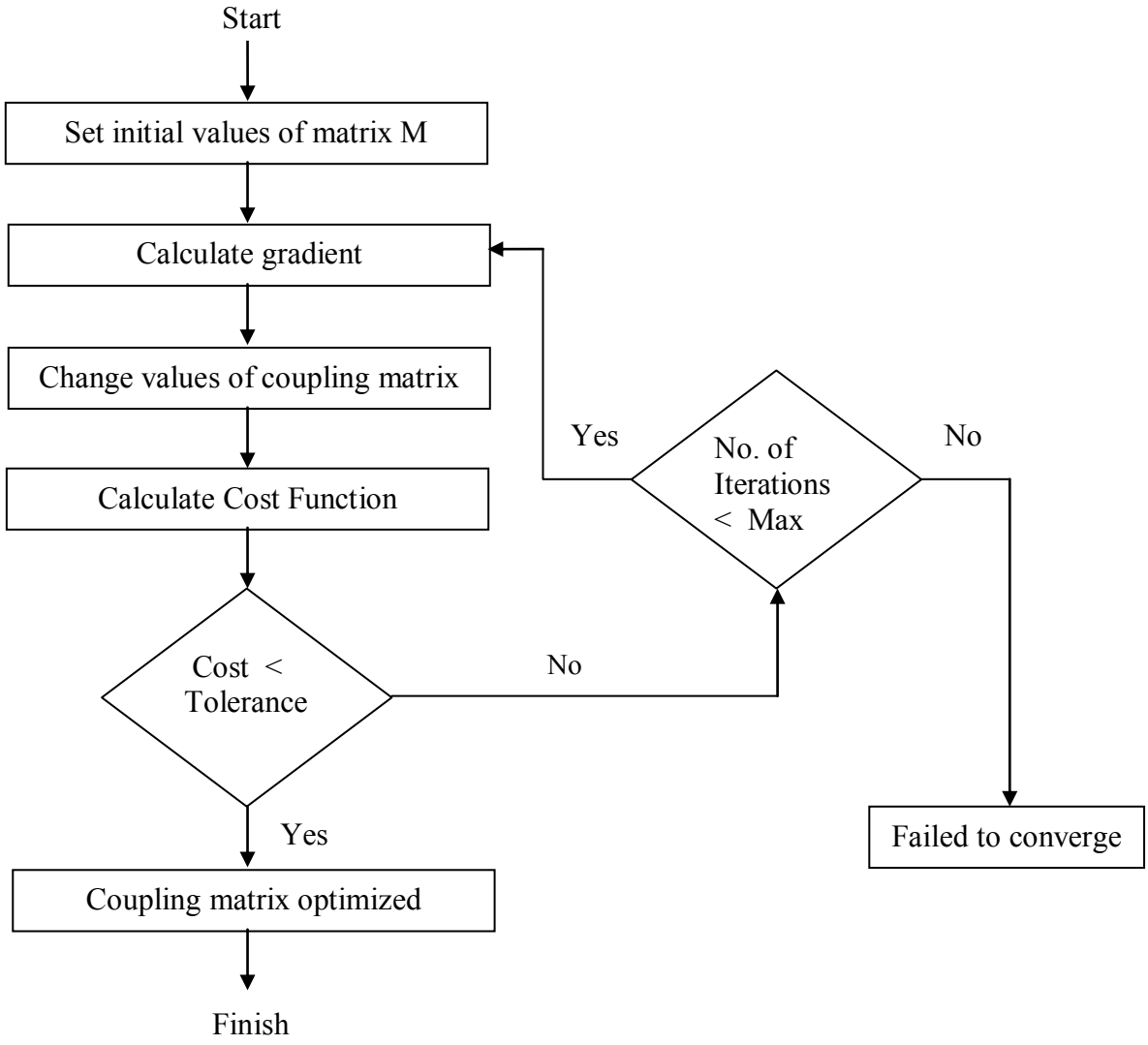

Figure 3.6: Flowchart of optimization algorithm

Also, the specified power ratio (α) and the calculated external quality factors are set at the outset of the algorithm. The divider topology is enforced in the algorithm such that the coupling coefficients that do not exist are set to zero. The algorithm starts with initial values of coupling coefficients as described earlier. The cost function is calculated at every iteration and compared to a specified tolerance value that is selected based on the desired accuracy of the optimisation. The gradient is calculated to determine the direction of the maximum decrease of the cost function, and the values of the coupling coefficients are changed accordingly. The process is repeated until the value of the cost function is smaller than the specified tolerance, or the number of iterations exceeds a specified maximum value.

The optimisation has been successful in producing coupling matrices for power dividers with Chebyshev and Quasi-Elliptic filtering responses. The next sections present examples of power dividers with different topologies to demonstrate the design approach.

3.6 Topology with Chebyshev Response

There are many possible topologies for *n*-coupled resonators that can achieve a Chebyshev response. For example, for 8-coupled resonators, the three topologies in figure 3.7 can achieve power division with Chebyshev filtering response. However, the order of the filtering function at the outputs is different when these topologies are compared. For example, topology 1 can achieve 7^{th} order filtering function at the outputs, whereas topology 2 can achieve 6^{th} order, and topology 3 can achieve 5^{th} order. The order of the filtering function is equal to the number of resonators that exist in the signal path between the input and the output. Hence, topology 1 is preferred since it has more shared resonators that contribute to the filter transfer function. Consequently, a general T-Topology for a 3-port power divider with *n* coupled resonators with Chebyshev filtering response is proposed in figure 3.8.

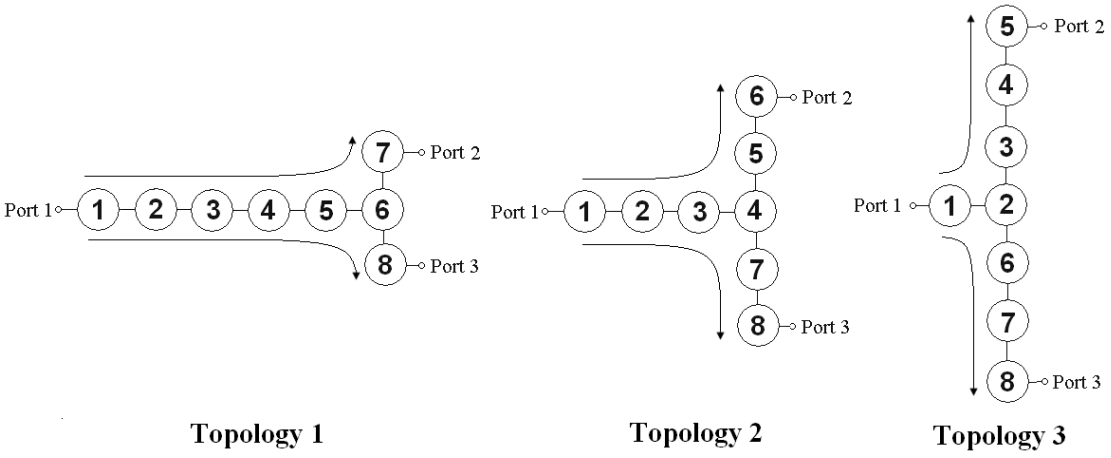

Figure 3.7: Topologies of power dividers with 8 coupled resonators

The topology shown has been suggested since it has large number of shared resonators, so that the order of the filtering function at each output is equal to (n-1), where n is the total number of resonators. This is due to the existence of two signal paths with (n-1) resonators in each; the first contains the resonators (1,2,3,…,n-2,n-1) and the second contains the resonators (1,2,3,…,n-2,n).

The coupling coefficients $m_{(n-2),(n-1)}$ and $m_{(n-2),n}$ will have equal values in case of 3-dB power division, and differing values for arbitrary power division.

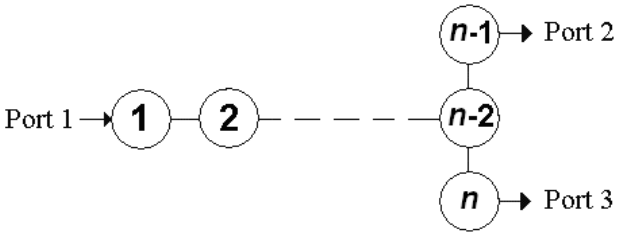

Figure 3.8: General power divider T-topology with Chebyshev response

3.6.1 Example B: 3-dB power divider with T-Topology and Chebyshev response

A 3-dB power divider with Chebyshev filtering response and a return loss of 20 dB is synthesised. The divider consists of 12 resonators in a T-Topology as shown in figure 3.9.

The reflection zeros and the external quality factors have been evaluated for 11th order filter, which is the order of the filtering function at each output, and their values have been set in the optimization algorithm.

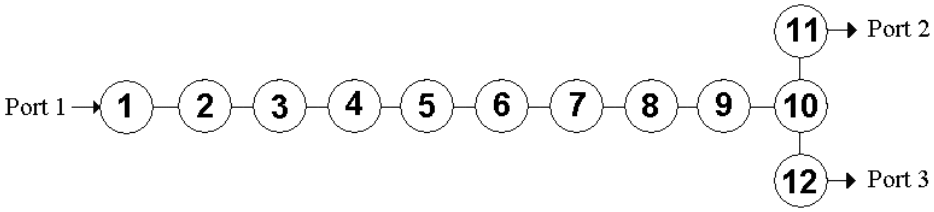

Figure 3.9: Topology of power divider in example B.

The reflection zeros have been calculated using Cameron's recursive technique as follows, s_{rj}=0, ±0.2817i, ±0.5406i, ±0.7557i, ±0.9096i and ±0.9898i Hz, and the values of normalized external quality factors are q_{e1}=q_{e11}=q_{e12}=1.0331. The cost function in equation (3.23) has been used in an unconstrained gradient based local optimisation algorithm, and the initial values of coupling coefficients have been set to 0.5. The synthesised normalized coupling coefficients are shown in table 3.3 and the power divider response is shown in figure 3.10. The algorithm converged after 65 iterations with final error of 6.39 x 10^{-12}.

It is noticed from the coupling matrix that $m_{10,11}$=$m_{10,12}$=0.573. These coefficients are equal due to the equal power division criteria (α=1). However, for unequal power division, with α=2 for example, these coefficients are unequal and their optimised values are $m_{10,11}$=0.4679 and $m_{10,12}$=0.6616, and the rest of the coupling coefficients m_{12},…,$m_{9,10}$ are the same as those in table 3.3.

It should be noted that this power divider is not matched at all ports, i.e. matching is only achieved at port 1, and that the output ports are not isolated (around 6 dB in the passband). This is a typical problem of lossless reciprocal 3-port junctions, as discussed in section 3.2.

Table 3.3: Coupling matrix of power divider in example B

	1	2	3	4	5	6	7	8	9	10	11	12
1	0	0.8103	0	0	0	0	0	0	0	0	0	0
2	0.8103	0	0.5817	0	0	0	0	0	0	0	0	0
3	0	0.5817	0	0.5419	0	0	0	0	0	0	0	0
4	0	0	0.5419	0	0.5289	0	0	0	0	0	0	0
5	0	0	0	0.5289	0	0.5245	0	0	0	0	0	0
6	0	0	0	0	0.5245	0	0.5244	0	0	0	0	0
7	0	0	0	0	0	0.5244	0	0.5290	0	0	0	0
8	0	0	0	0	0	0	0.5290	0	0.5418	0	0	0
9	0	0	0	0	0	0	0	0.5418	0	0.5817	0	0
10	0	0	0	0	0	0	0	0	0.5817	0	0.5730	0.5730
11	0	0	0	0	0	0	0	0	0	0.5730	0	0
12	0	0	0	0	0	0	0	0	0	0.5730	0	0

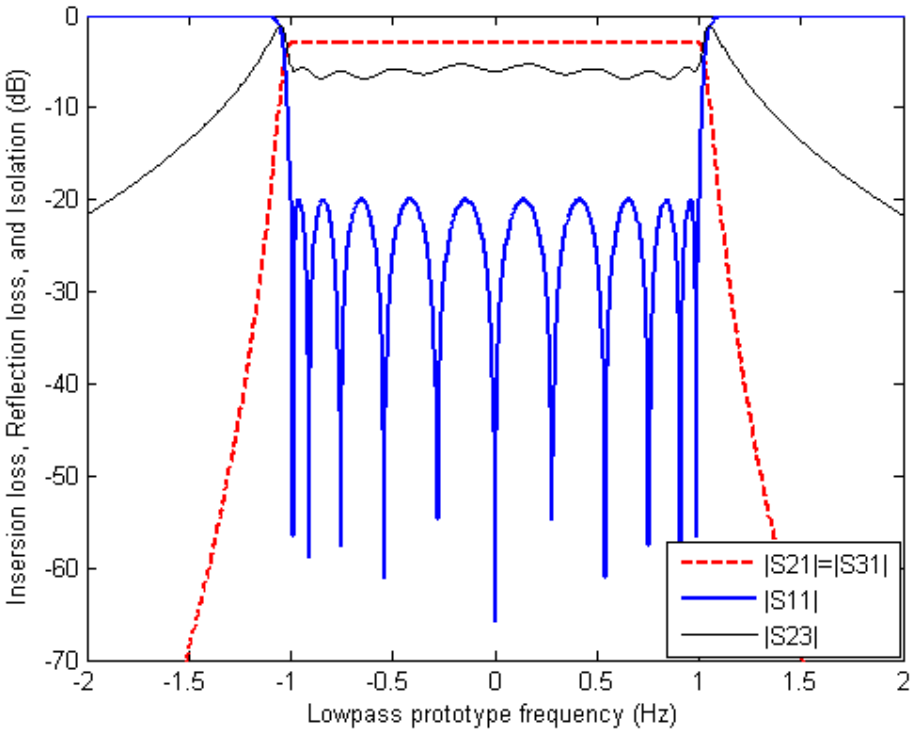

Figure 3.10: Response of Power Divider in example B

3.7 General Topology with Quasi-Elliptic Response

Shown in figure 3.11 is a proposed topology for a 3-port power divider with *n* coupled resonators with a Quasi-Elliptic filtering response. It is possible to achieve cross coupling with the suggested structure, and hence transmission zeros can be generated in the power divider filtering response.

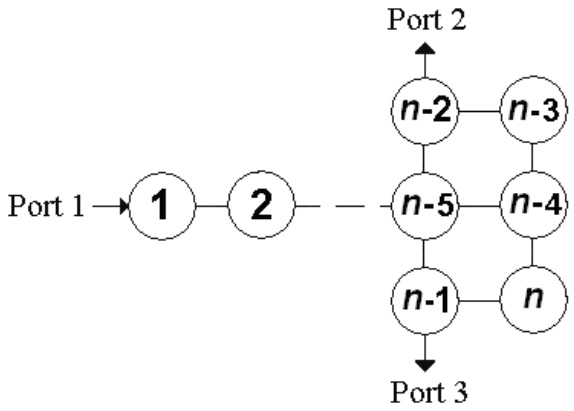

Figure 3.11: General power divider topology with Quasi-Elliptic response.

The order of the filtering function at each output is equal to (*n*-2), where *n* is the total number of resonators. There are two signal paths with (*n*-2) resonators in each; the first contains the resonators (1,2, …,*n*-5,*n*-4, *n*-3,*n*-2) and the second contains the resonators (1,2, …,*n*-5,*n*-4,*n*,*n*-1).

The coupled-resonator filtering power dividers proposed in this thesis may be used to replace the configuration of cascaded power divider and two identical filters in figure 1.4, and thus miniaturization can be achieved. However, unlike the cascaded structure, the order of the filtering function in the proposed filtering power dividers is less than the number of resonators *n*, and it depends on the topology. For example, the general T-topology in figure 3.8 can achieve filtering functions of order of (*n*-1), whereas the general topology in figure 3.11 can achieve filtering function of order (*n*-2). Thus, the proposed filter integrated power dividers exhibit a trade-off between the reduction in size and the order of the filtering function.

3.7.1 Example C: 3-dB power divider with Quasi-Elliptic response

A 3-dB (α=1) power divider with a 20 dB return loss and a Quasi-Elliptic response with finite transmission zeros located at ±1.23*j* Hz is synthesized. The structure of the divider is shown in figure 3.12. The frequency locations of return zeros have been evaluated using Cameron's technique for 5th order filtering function as follows, s_{rj}=0, ±0.6221*i*, and ±0.9591*i* Hz, and the values of the normalized external quality factors are calculated as follows: $q_{e1}=q_{e11}=q_{e12}=0.99$.

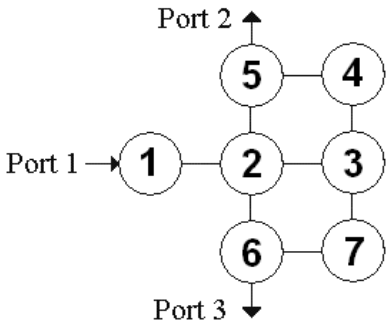

Figure 3.12: Topology for divider in example C

The normalized coupling matrix is shown below and the corresponding response is shown in figure 3.13. The algorithm converged after 45 iterations with final error of 1.202 x 10^{-10}. The negative coupling between resonators 2 and 3 generates two transmission zeros in the response at both output ports. It is noticed that the isolation between ports 2 and 3 within the passband is around 6 dB.

$$M = \begin{bmatrix} 0 & 0.8483 & 0 & 0 & 0 & 0 & 0 \\ 0.8483 & 0 & -0.5978 & 0 & 0.1168 & 0.1168 & 0 \\ 0 & -0.5978 & 0 & 0.5149 & 0 & 0 & 0.5149 \\ 0 & 0 & 0.5149 & 0 & 0.8321 & 0 & 0 \\ 0 & 0.1168 & 0 & 0.8321 & 0 & 0 & 0 \\ 0 & 0.1168 & 0 & 0 & 0 & 0 & 0.8321 \\ 0 & 0 & 0.5149 & 0 & 0 & 0.8321 & 0 \end{bmatrix}$$

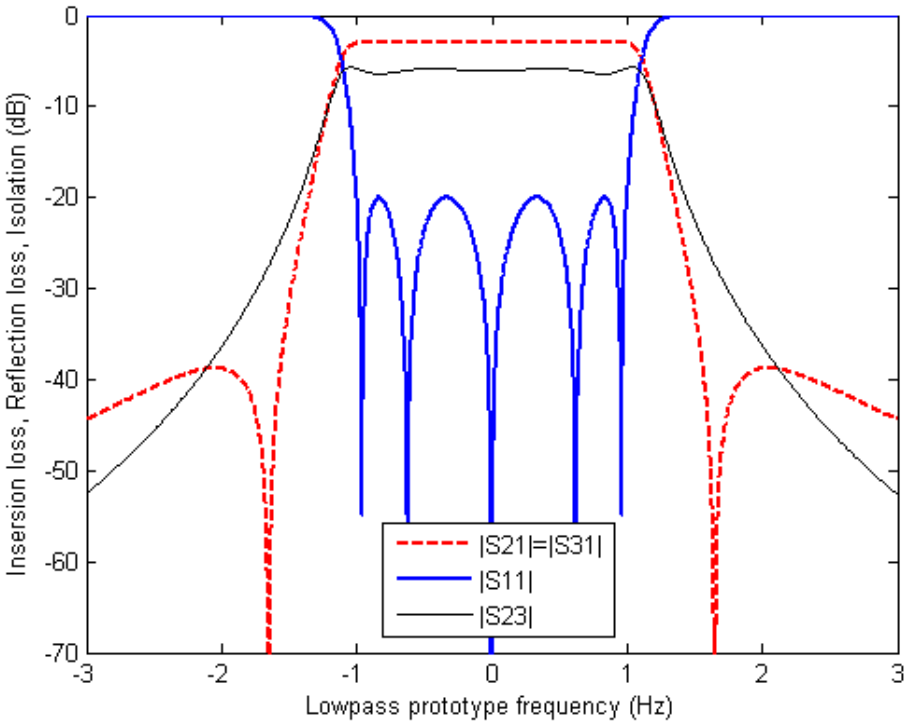

Figure 3.13: Response of Power Divider in example C

3.7.2 Example D: Unequal power divider with Quasi-Elliptic response

An unequal power divider (α=1/3) that has 8th order filtering function with two transmission zeros located at ±1.23j Hz, and a return loss of 20 dB, is synthesized here. These specifications are recalled from power divider in example A, whereby the power divider polynomials have been synthesised. In this example, a coupling matrix will be optimized so that the given specifications are met. The structure of the divider has 10 resonators and it is shown in figure 3.14. The locations of reflection zeros are found in example A (section 3.4.2) as s_{rj}=±0.9860i, ±0.8655i, ±0.603i, ±0.2171i and the values of the normalized external quality factors are evaluated as: q_{e1}=q_{e8}=q_{e9}=1.029. The normalized coupling matrix is given below and the corresponding response is shown in figure 3.15. The algorithm converged after 84 iterations with final error of 3.152 x 10^{-10}.

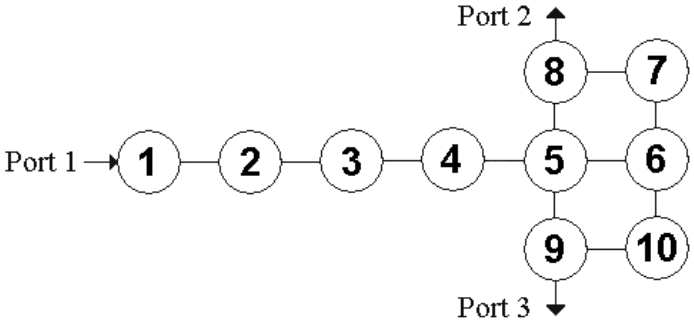

Figure 3.14: Topology for divider in example D

$$M = \begin{bmatrix} 0 & 0.8140 & 0 & 0 & 0 & 0 & 0 & 0 & 0 & 0 \\ 0.8140 & 0 & 0.5846 & 0 & 0 & 0 & 0 & 0 & 0 & 0 \\ 0 & 0.5846 & 0 & 0.5451 & 0 & 0 & 0 & 0 & 0 & 0 \\ 0 & 0 & 0.5451 & 0 & 0.5338 & 0 & 0 & 0 & 0 & 0 \\ 0 & 0 & 0 & 0.5338 & 0 & -0.4668 & 0 & 0.2638 & 0.1523 & 0 \\ 0 & 0 & 0 & 0 & -0.4668 & 0 & 0.6763 & 0 & 0 & 0.3905 \\ 0 & 0 & 0 & 0 & 0 & 0.6763 & 0 & 0.7547 & 0 & 0 \\ 0 & 0 & 0 & 0 & 0.2638 & 0 & 0.7547 & 0 & 0 & 0 \\ 0 & 0 & 0 & 0 & 0.1523 & 0 & 0 & 0 & 0 & 0.7547 \\ 0 & 0 & 0 & 0 & 0 & 0.3905 & 0 & 0 & 0.7547 & 0 \end{bmatrix}$$

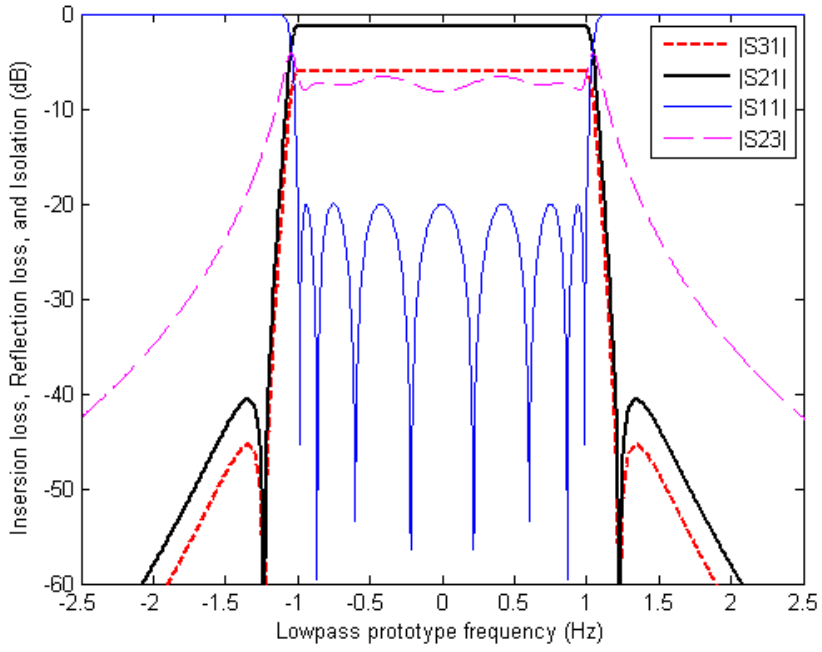

Figure 3.15: Response of Power Divider in example C

3.8 Conclusion

Coupled resonator power dividers have been proposed. The design procedure is based on optimisation of the coupling matrix of a 3-port circuit with multiple coupled resonators. The realisation of the dividers is possible using waveguide cavities, microstrip resonators or other types of resonators. The synthesis of the polynomial characteristics of the filtering power divider has been presented. A cost function has been formulated to be minimised in the optimisation algorithm, and a gradient based local optimisation search method has been utilised to synthesise the coupled resonator dividers. The optimisation has been successful in the synthesis of dividers with arbitrary power division with both Chebyshev and Quasi-Elliptic filtering responses.

The proposed divider is not matched at all ports, and the output ports are not isolated, which is a typical problem of lossless reciprocal 3-port junctions. The design, fabrication, and measurement of 3-dB and unequal power dividers will be presented in Chapter 5.

References

[1] R.E. Collin, *Foundations for Microwave Engineering*. 2nd edition, John Wiley & Sons, 2001.

[2] D.M. Pozar, Microwave Engineering. 2nd edition, Wiley, 1998.

[3] E.J. Wilkinson, "An N-way hybrid power divider," *IRE Transactions on Microwave Theory and Techniques*, vol. 8, no. 1, pp. 116-118, 1960.

[4] R.J. Cameron, "General coupling matrix synthesis methods for Chebyshev filtering functions," *IEEE Transactions on Microwave Theory and Techniques*, vol. 47, no. 4, pp. 433-442, April 1999.

[5] R. Cameron, C. Kudsia, and R. Mansour, *Microwave filters for communication systems*. Wiley, 2007.

[6] J.W. Bandler, R.M. Biernacki, S.H. Chen, D.G. Swanson, and S. Ye, "Microstrip filter design using direct EM Field simulation," *IEEE Transactions on Microwave Theory and Techniques*, vol. 42, pp. 1353-1359, July 1994.

[7] S. Amari, "Synthesis of cross-coupled resonator filters using an analytical gradient-based optimization technique," *IEEE Transactions on Microwave Theory and Techniques*, vol. 48, no. 9, pp. 1559-1564, 2000.

[8] A.B. Jayyousi and M.J. Lancaster, "A gradient-based optimization technique employing determinants for the synthesis of microwave coupled filters," *IEEE MTT-S International Microwave Symposium*, USA, 2004, pp 1369-1372.

[9] W.A. Atia, K. A. Zaki, and A.E. Atia, "Synthesis of general topology multiple coupled resonator filters by optimization," *IEEE MTTS Int. Microw. Symp.*, Baltimore, USA, June 1998, pp. *821-824.*

[10] M. Lecouve, N. Boutheiller, P. Jarry, and E. Kerherve,"Genetic algorithm based CAD of microwave waveguide filters with resonating bend," in *Proc. European Microwave Conference*, Paris, Oct. 2000, pp. 1-4.

[11] S. Chakravarty and R. Mittra, "Design Of Microwave Filters Using A Binary Coded Genetic Algorithm," *IEEE Antennas and Propagation Society International Symposium*, USA, July 2000, vol. 1, pp. 144 – 147.

[12] A. Takacs, A. Serbanescu, G. Leu, H. Aubert, P. Pons, T. Parra, and R. Plana, "On layout optimization of the microwave diplexor filter using genetic algorithms," *in proc. International Semiconductor Conference,* Oct. 2004, pp. 133-136.

[13] G.L. Nicholson, M.J. Lancaster, "Coupling matrix synthesis of cross-coupled microwave filters using a hybrid optimisation algorithm," *IET journal of Microwaves, Antennas & Propagation,* vol.3, no.6, pp.950-958, September 2009.

[14] Manseok Uhm, Sangho Nam, and Jeongphill Kim, "Synthesis of Resonator Filters With Arbitrary Topology Using Hybrid Method," *IEEE Transactions on Microwave Theory and Techniques*, vol.55, no.10, pp. 2157-2167, Oct. 2007.

[15] P. Kozakowski, and M. Mrozowski, "Automated synthesis of coupled resonator filters with a given topology," *14th International Conference on Microwaves, Radar and Wireless Communications,* Poland, 2002, vol.2, pp. 373- 376.

Chapter 4

Synthesis of Coupled Resonator Diplexers

4.1 Introduction

This chapter presents the synthesis of coupled resonator diplexers using coupling matrix optimization. The synthesis employs the theory presented in chapter 2 for multiple coupled resonators with multiple outputs.

A general review about conventional multiplexers and diplexers will be firstly presented, and then diplexers with novel topologies based on multiple coupled resonators will be proposed. These novel diplexers can be implemented using any type of resonators and they can be miniaturised in comparison to the conventional ones.

The synthesis of the proposed diplexers employs a similar coupling matrix optimization technique to that of coupled resonator filters. A cost function that is used in optimization will be derived, and examples of diplexers with different topologies will be illustrated throughout this chapter. A comparison between three diplexers with the same specification and different topologies in terms of isolation performance will be carried out.

4.2 Multiplexers

Multiplexers are generally used in communications systems to selectively separate a wideband signal into narrowband signals, for example, or to combine a number of narrowband signals into a wideband signal to be transmitted via a common antenna [1]. This is conventionally achieved by using a set of bandpass filters (usually known as channel filters), and an energy distribution network. The channel filters pass frequencies within a

specified range, and reject frequencies outside the specified boundaries, and the distribution network divides the signal going into the filters, or combines the signals coming from the filters [2]. The most commonly used distribution configurations are *E*- or *H*-plane *n*-furcated power dividers [3,4], circulators [5] and manifold structures [6-9].

Figure 4.1 shows the configuration of *n*-channel multiplexer with a 1:*n* divider multiplexing network, and figure 4.2 depicts a circulator configuration, where each channel consists of a bandpass filter and a channel-dropping circulator [1]. In manifold configurations, channel filters are connected by transmission lines: microstrip, coaxial, waveguide, etc. and T-junctions. The configuration of the manifold multiplexer is shown in figure 4.3 [1].

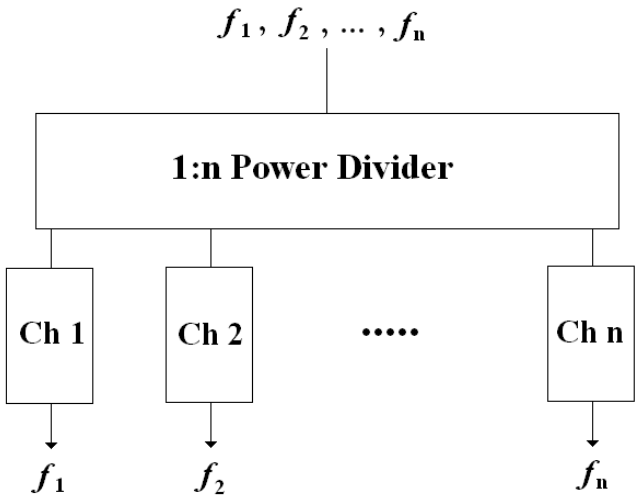

Figure 4.1: Configuration of multiplexer with a 1:*n* divider multiplexing network.

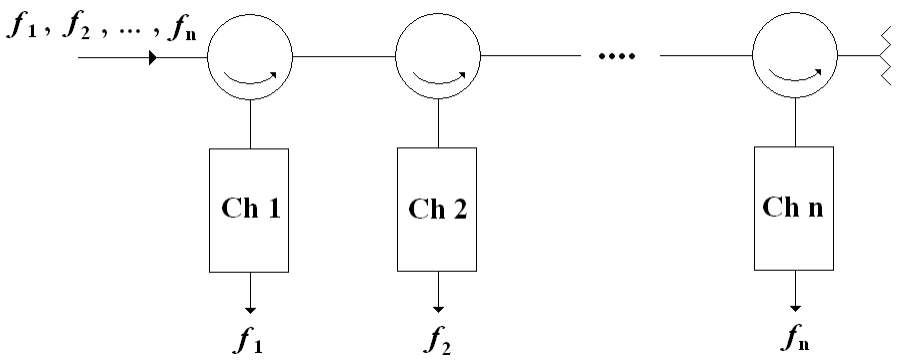

Figure 4.2: Configuration of circulator-coupled multiplexer.

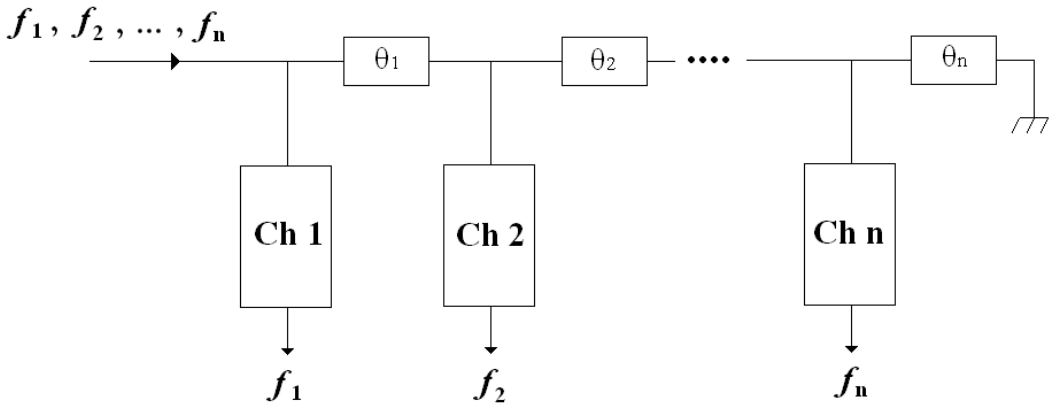

Figure 4.3: Configuration of manifold-coupled multiplexer.

The power divider configurations can be designed for multiplexers with wideband channels or large channel separation [3]. The circulator configurations have no interaction between channel filters and they are simple to tune. They provide flexibility in adding new channels or replacing the channel filters by different filters without disrupting the whole design. However, they exhibit relatively higher losses since signals pass through the circulators in succession, causing extra loss per trip. Manifold configurations provide low insertion loss and high power handling capability. However, they have complex design, and they do not have the flexibility in adding channels to an existing multiplexer, or changing a channel since this requires a new design. Also, tuning the whole multiplexer can be time consuming [1].

Multiplexers without distribution networks have been reported in literature [10]-[13]. These multiplexers/diplexers are based on inter-coupled resonators with multiple outputs, without using the distribution networks mentioned earlier. In [10], some coupled resonator circuits with multiple outputs were patented. In [11]-[12], the design of multiport microwave coupled-resonator networks based on coupling matrix synthesis has been presented. In [13], the design and implementation of a novel Ku-Band dielectric resonator triplexer without external junctions has been presented.

4.3 Conventional Diplexers

Conventional diplexers consist of two channel filters connected to an energy distribution network. Such a network can be a waveguide manifold [14,15], a T-junction [16]-[18], a Y-junction [19], or a circulator [20]. An approach for the diplexer synthesis is based on firstly designing the channel filters independently of the diplexer, and then using numerical optimization for the whole diplexer structure. This approach can be very time consuming for large diplexer structures and the convergence of the cost function might be problematic. In [21,22], an approach to the synthesis of diplexers that takes into account a three-port junction in the initial synthesis of the two channel filters was presented. This approach provides a very good starting point for the optimization of the whole structure, so the convergence can be achieved with very few iterations.

Miniaturised diplexers have been reported extensively in literature. Compact microstrip diplexers have been designed using specific types of compact resonators such as stepped impedance resonators [23,24], dual loop resonators [25], and hybrid resonators [26]. Compact waveguide diplexers have been also realised using folded structures as reported in [27,28].

4.3.1 Configuration of a conventional diplexer

This section presents equivalent circuit and design equations of a conventional diplexer, that will be used later in this chapter for comparison with the proposed coupled-resonator diplexers.

The equivalent circuit of a diplexer consisting of two bandpass filters with a rectangular *H*-Plane waveguide T-junction is shown in figure 4.4 [21], where the transformer ratio n and the susceptance b_0 can be calculated using formulas in [29].

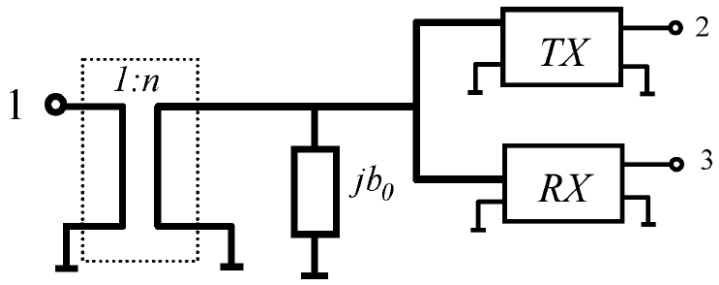

Figure 4.4: Architecture of diplexer with *H*-plane waveguide T-junction

The diplexer in figure 4.4 has input admittance at port 1 as follows [21],

$$y_{in} = n^2 \left(jb_0 + y_{in}^{TX} + y_{in}^{RX} \right) \tag{4.1}$$

Where y_{in}^{TX} is the admittance at input port of the TX filter with the other port terminated with the reference load, and similarly, y_{in}^{RX} is the admittance at the input port of the RX filter with the other port matched. These admittances are expressed in terms of S_{11} parameters of the individual TX and RX filters as follows,

$$y_{in}^{TX} = \frac{1 - S_{11}^{TX}}{1 + S_{11}^{TX}} \tag{4.2}$$

$$y_{in}^{RX} = \frac{1 - S_{11}^{RX}}{1 + S_{11}^{RX}} \tag{4.3}$$

The S_{11} parameter of the diplexer is expressed in terms of the input admittance y_{in} as follows,

$$S_{11} = \frac{1 - y_{in}}{1 + y_{in}} \tag{4.4}$$

The transmission parameters S_{21} and S_{31} of the diplexer are expressed as follows [21],

$$S_{21} = \frac{S_{21}^{TX} \left(1 + y_{in}^{TX} \right)}{\frac{1}{n} + jnb_0 + n.y_{in}^{TX} + n.y_{in}^{RX}} \tag{4.5}$$

$$S_{31} = \frac{S_{21}^{RX} \left(1 + y_{in}^{RX} \right)}{\frac{1}{n} + jnb_0 + n.y_{in}^{TX} + n.y_{in}^{RX}} \tag{4.6}$$

4.4 Coupled Resonator Diplexer Design

The synthesis procedure of the proposed diplexer in this thesis is based on optimization of coupling matrix of multiple coupled resonators representing a three-port network, and it is performed in the normalized frequency domain. The proposed diplexers do not contain any of the energy distribution junctions presented earlier, and hence the structure can be miniaturised in comparison to conventional diplexers.

In this section, formulas for frequency transformation from bandpass to lowpass frequency domain will be derived, and a cost function will be formulated to be used in the optimization algorithm. The next sections will present examples of diplexers with different topologies, synthesised using coupling matrix optimization.

4.4.1 Frequency transformation

The specifications of a diplexer are usually given in the bandpass frequency domain, in which the real diplexer operates. As mentioned earlier, the design of the proposed diplexers takes place in the normalized frequency domain as a lowpass prototype. Therefore, a frequency transformation from bandpass frequency domain to normalized frequency domain is needed. This section presents frequency transformation formulas of bandpass diplexer with given specification to a lowpass prototype. This enables finding critical lowpass prototype parameters such as inner edges x_1, x_2 and bandwidth BW_{LP} that are used in the synthesis of the lowpass prototype diplexer. An illustration of the frequency mapping is shown in figure 4.5.

The frequency edges of the bands of the diplexer are (ω_1, ω_a) and (ω_b, ω_2). These frequencies are mapped into lowpass prototype frequencies (Ω) using the following transformation formula [30],

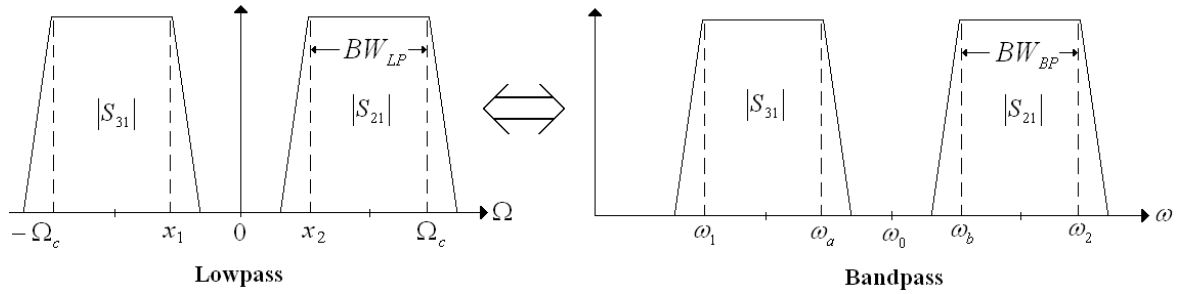

Figure 4.5: Lowpass to bandpass transformation

$$\Omega = \alpha\left(\frac{\omega}{\omega_0} - \frac{\omega_0}{\omega}\right) \tag{4.7}$$

To map the band edges $\Omega = -\Omega_c$ to $\omega = \omega_1$, and $\Omega = \Omega_c$ to $\omega = \omega_2$,

$$-\Omega_c = \alpha\left(\frac{\omega_1}{\omega_0} - \frac{\omega_0}{\omega_1}\right) \tag{4.8}$$

$$\Omega_c = \alpha\left(\frac{\omega_2}{\omega_0} - \frac{\omega_0}{\omega_2}\right) \tag{4.9}$$

Solving equations (4.8) and (4.9) yields,

$$\omega_0 = \sqrt{\omega_1\omega_2} \tag{4.10}$$

$$\alpha = \frac{\Omega_c}{FBW}, \qquad where \quad FBW = \frac{\omega_2 - \omega_1}{\omega_0} \tag{4.11}$$

To map the inner edge $\Omega = x_1$ to $\omega = \omega_a$, and the edge $\Omega = x_2$ to $\omega = \omega_b$,

$$x_1 = \alpha\left(\frac{\omega_a}{\omega_0} - \frac{\omega_0}{\omega_a}\right) \tag{4.12}$$

$$x_2 = \alpha\left(\frac{\omega_b}{\omega_0} - \frac{\omega_0}{\omega_b}\right) \tag{4.13}$$

The value of the lowpass cutoff frequency Ω_c is normally taken as 2π radian/sec, and the values of x_1, x_2 can now be found from equations (4.12) and (4.13) since all other variables are known from the diplexer bandpass specification.

4.4.2 Derivation of cost function

A cost function that is used in the optimization of the coupling matrix of coupled resonator diplexer is formulated here. For a coupled resonator diplexer, the reflection and transmission functions may be defined in terms of polynomials as follows,

$$S_{11}(s)=\frac{F(s)}{E(s)},\qquad S_{21}(s)=\frac{P_1(s)/\varepsilon}{E(s)},\qquad S_{31}(s)=\frac{P_2(s)/\varepsilon}{E(s)} \tag{4.14}$$

where the roots of $F(s)$ correspond to the reflection zeros, the roots of $P_1(s)$, and $P_2(s)$ correspond to the transmission zeros of the filter frequency response at ports 2, and 3 respectively, ε is a ripple constant, and $E(s)$ roots correspond to the pole positions of the filtering function. The initial cost function may be written in terms of the characteristic polynomials as follows,

$$\Omega=\sum_{i=1}^{T_1}\left|P_1(s_{ti})\right|^2+\sum_{k=1}^{T_2}\left|P_2(s_{tk})\right|^2+\sum_{j=1}^{R}\left|F(s_{rj})\right|^2+\sum_{v=1}^{R-2}\left|\left|\frac{F(s_{pv})}{E(s_{pv})}\right|-10^{\frac{L_R}{20}}\right|^2 \tag{4.15}$$

where s_{ti}, s_{tk} are the frequency locations of transmission zeros of S_{21}, S_{31} respectively, T_1, T_2 are the numbers of the transmission zeros of S_{21}, S_{31} respectively, R is the total number of resonators in the diplexer, L_R is the desired return loss in dB (L_R<0), and s_{rj} and s_{pv} are the frequency locations of the reflection zeros and the peaks' frequency values of $|S_{11}|$ in the passband. The last term in the cost function is used to set the peaks of $|S_{11}|=|F/E|$ to the required return loss level. It is assumed here that both channels of the diplexer have the same return loss level.

Recall from section (3.5.2), that for a 3-port network of multiple coupled resonators, the scattering parameters are expressed the in terms of the general matrix [A] (equation (2.24)) as follows,

$$
\begin{aligned}
S_{11} &= 1 - \frac{2}{q_{e1}} \frac{cof_{11}\left([A]\right)}{\Delta_A} \\
S_{21} &= \frac{2}{\sqrt{q_{e1} q_{ea}}} \frac{cof_{1a}\left([A]\right)}{\Delta_A} \\
S_{31} &= \frac{2}{\sqrt{q_{e1} q_{eb}}} \frac{cof_{1b}\left([A]\right)}{\Delta_A}
\end{aligned}
\tag{4.16}
$$

where it is assumed that the common port is connected to resonator 1, port 2 is connected to resonator *a*, and port 3 is connected to resonator *b*.

By equating (4.14) and (4.16), the polynomials $P_1(s)$, $P_2(s)$, $F(s)$ and $E(s)$ are expressed in terms of the general matrix $[A]$ as follows,

$$
\begin{aligned}
\frac{P_1(s)}{\varepsilon} &= \frac{2.cof_{1a}\left([A(s)]\right)}{\sqrt{q_{e1} q_{ea}}} \\
\frac{P_2(s)}{\varepsilon} &= \frac{2.cof_{1b}\left([A(s)]\right)}{\sqrt{q_{e1} q_{eb}}} \\
F(s) &= \Delta_A(s) - \frac{2.cof_{11}\left([A(s)]\right)}{q_{e1}} \\
E(s) &= \Delta_A(s)
\end{aligned}
\tag{4.17}
$$

By substitution of the polynomials in equation (4.17) into equation (4.15), the cost function is now expressed in terms of determinants and cofactors of the matrix $[A]$ and the external quality factors as follows,

$$
\begin{aligned}
\Omega = &\sum_{i=1}^{T_1} \left| \frac{2}{\sqrt{q_{e1} q_{ea}}} .cof_{1a}([A(s_{ti})]) \right|^2 + \sum_{k=1}^{T_2} \left| \frac{2}{\sqrt{q_{e1} q_{eb}}} .2.cof_{1b}([A(s_{tk})]) \right|^2 \\
&+ \sum_{j=1}^{R} \left| \Delta_A(s_{rj}) - \frac{2.cof_{11}([A(s_{rj})])}{q_{e1}} \right|^2 + \sum_{v=1}^{R-2} \left| \left| 1 - \frac{2.cof_{11}([A(s_{pv})])}{q_{e1}.\Delta_A(s_{pv})} \right| - 10^{\frac{L_R}{20}} \right|^2
\end{aligned}
\tag{4.18}
$$

where q_{e1}, q_{ea}, and q_{eb} are the external quality factors at ports 1, 2 and 3 respectively, $\Delta_A(S{=}x)$ is the determinant of the matrix $[A]$ evaluated at the frequency variable x, and $cof_{mn}([A(s{=}v)])$

is the cofactor of matrix [*A*] evaluated by removing the m^{th} row and the n^{th} column of [*A*] and finding the determinant of the resulting matrix at the frequency variable $s=v$.

The first two terms in the cost function are used if the diplexer characteristics contain transmission zeros. However, for a Chebyshev response, these terms may be used to minimize the transmission of each channel at the passband of the other channel, thus increasing the isolation between channel ports. Consequently, the frequency locations s_{ti} are chosen to be the band edges of the channel at port 3, and similarly the frequency locations s_{tk} are chosen to be the band edges of the channel at port 2.

The lowpass frequency positions of the reflection zeros of the diplexer are initially set to be equally spaced in the optimization algorithm, and later these positions are moved until equiripple level at specified insertion loss is achieved. Alternatively, the initial values of the frequency locations of reflection zeros may be scaled from standard low-pass prototype Chebyshev filters, but these locations still need to be moved until equiripple is achieved. The frequency locations of the peaks of $|S_{11}|$ are found using numerical differentiation at each iteration in the optimization algorithm. The values of the external quality factors are numerically calculated, as will be shown in the next section, and their values are set at the beginning of the algorithm. This reduces the optimization parameters set and improves the convergence time. The variables that need to be optimized in the optimization algorithm are the coupling coefficients and also the frequency locations of the reflection zeros. The initial values of the coefficients of the coupling matrix can be set to 0.5 for the coupling coefficients between adjacent resonators (m_{ij}) and for the coefficients that represent positive frequency offsets ($m_{ii}>0$), and to -0.5 for the coefficients that represent negative frequency offsets ($m_{ii}<0$). The optimization usually converges with these initial values. However, in some cases, the initial values are changed to obtain a better starting point for the optimization algorithm to

converge. Moreover, it has been found useful for optimization to weight the third term in the cost function in equation (4.18) that is used to minimise the cost function at the frequency locations of the reflection zeros.

Coupling matrices of symmetrical diplexers have been successfully optimized using gradient based technique. Two general diplexer topologies are proposed in the next sections, the first is a T-Topology that can achieve a Chebyshev response at both channels, and the second is a general canonical topology that can achieve a Quasi-Elliptic filtering response. Numerical examples for both topologies will be presented and isolation comparison will be discussed.

4.4.3 Calculation of external quality factor

The responses of two lowpass prototype filters with the same order and filtering function but different bandwidth are shown in figure 4.6. The first is with frequency edges of ±1 Hz and a bandwidth of $BW_{\pm 1}$, and the second is with frequency edges of x and 1 Hz and a bandwidth of BW_{x1}.

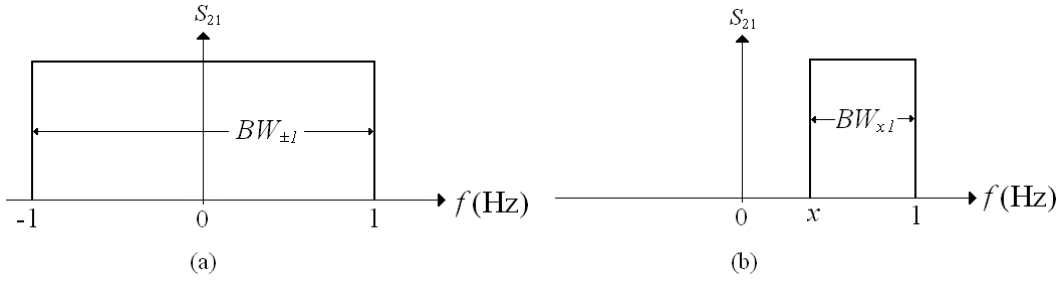

Figure 4.6: Lowpass prototype filters (a) passband edges of ±1 Hz, (b) passband edges of *x* and 1 Hz.

The normalised external quality factors of these filters are related by,

$$q_{ex1} = \frac{BW_{\pm 1}}{BW_{x1}} q_{e\pm 1} = \frac{2}{1-x} q_{e\pm 1} \tag{4.19}$$

where q_{ex1} is the normalized external quality factor of the filter with edges of x and +1, and $q_{e\pm1}$ is the normalized external quality factor of the filter with edges of ±1, that can be calculated from the g-values as shown in section (1.5.1).

Accordingly, for a symmetrical diplexer with channel edges of (-1,-x) and (x,1), the normalised external quality factors at ports 2 and 3 are calculated from equation (4.19), and the normalized external quality factor at the common port is equal to $q_{ex1}/2$. This works for all the examples of symmetrical diplexers presented throughout this chapter.

4.4.4 Initial spacing of reflection zeros

The initial guess of the locations of reflection zeros within a diplexer channel is presented here. For a diplexer channel with edges of (x, f_c) Hz, the leftmost reflection zero is located at (x+0.02)i Hz, and the rightmost reflection zero is located at (f_c-0.02)i Hz. The other reflection zeros are equally spaced between (x+0.02)i and (f_c-0.02)i with frequency spacing as follows,

$$\frac{\left(f_c - x - 0.04\right)}{m-1}$$

Where m is the total number of reflection zeros within a diplexer channel. Consider, for example, a symmetrical diplexer with m=5, x=0.333 Hz, f_c=1 Hz, will have equally spaced initial values of reflection zeros as follows,

$$\pm 0.3533i,\ \pm 0.510i,\ \pm 0.6667i,\ \pm 0.8234i,\ \pm 0.98i$$

Figure 4.7 shows the diplexer response produced using the initial guess of the reflection zeros and with a target of return loss of -20 dB. It is noticed that the peaks of $|S_{11}|$ deviate from -20 dB. Hence, the locations of the reflection zeros should be moved throughout the optimization so that the peaks are level at -20 dB.

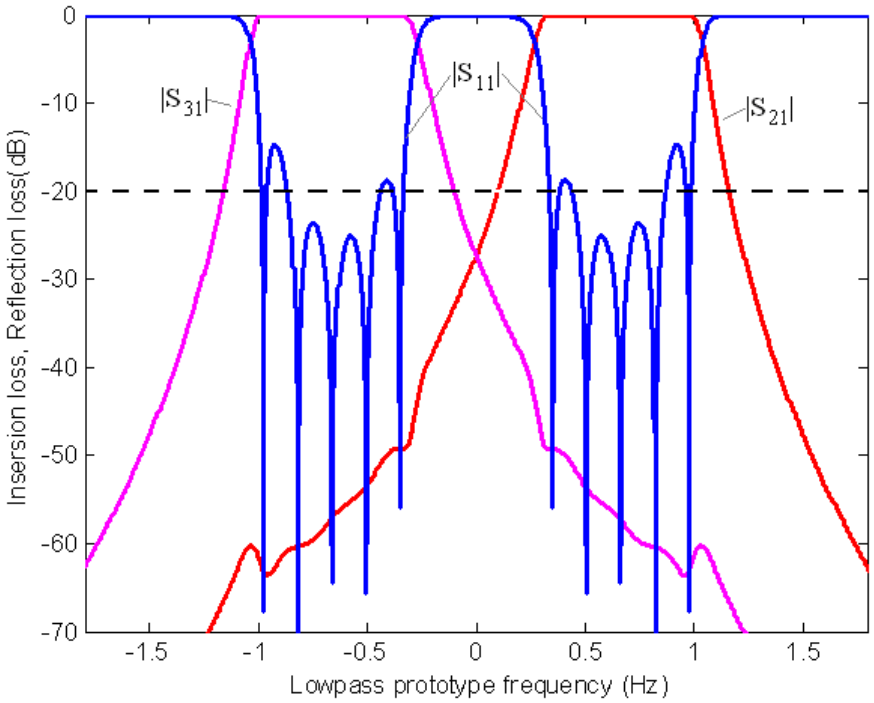

Figure 4.7: Response of diplexer with initial equal spacing of reflection zeros.

4.5 Diplexers with T-Topology

A proposed general T-Topology for a symmetrical diplexer is shown in figure 4.8, where n is the total number of resonators, $\pm x$ define the inner edges of the two channels, and r is the number of resonators located between either output port, and the junction resonator. Resonators in each arm should have different self-resonant frequencies to separate the diplexer channels from each other.

In this particular T-topology, the resonators are directly coupled (no cross coupling), and hence only Chebyshev response can be obtained. The resonators in the vertical branch, apart from the junction resonator, should have different self-resonant frequencies; this is to achieve disjoint frequency bands at the ports 2 and 3. Consequently, for the high frequency channel to be at port 2, the resonators above the junction resonator should have positive frequency offsets ($M_{ii}>0$), and for the low frequency channel to be at port 3, the resonators below the junction resonator should have negative frequency offsets ($M_{ii}<0$).

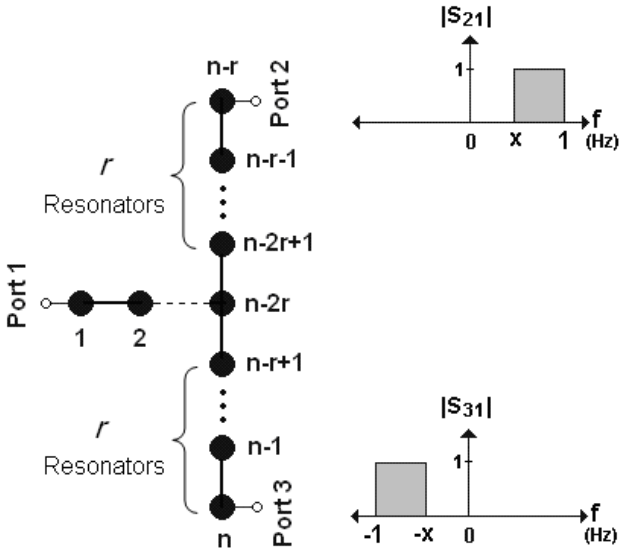

Figure 4.8: Diplexer T-Topology

It should be noted that the work on novel diplexer topologies started from a simple 4-resonator structure, with n=4 and r=1, followed by many experiments on adding resonators to the horizontal and vertical branches until arriving to the generalised topology given in figure 4.8. The junction resonator takes important part in power distribution and also it contributes to the filter transfer function.

The topology of the diplexer has been enforced in the optimization algorithm, and the following conditions for coupling coefficients have been applied to simplify the optimization problem,

$$m_{n-2r,n-2r+1} = m_{n-2r,n-r+1}, \ldots, m_{n-r-1,n-r} = m_{n-1,n}$$

$$m_{n-r+1,n-r+1} = -m_{n-2r+1,n-2r+1}, \ldots, m_{n-1,n-1} = -m_{n-r-1,n-r-1}, \ldots, m_{nn} = -m_{n-r,n-r}$$

4.5.1 Examples of diplexers with T-Topology

Examples of diplexers with symmetrical Chebyshev response will be shown in this section. Diplexers A-E have the T-topology shown in figure 4.8, with different values of n, x and r, and diplexer F is a conventional diplexer synthesised for the purpose of comparison with the proposed coupled resonator diplexers, as will be discussed later in this chapter.

4.5.1.1 Example A: Non-contiguous band diplexer with n=8, x=0.5, and r=2

A non-contiguous diplexer, where the channels are separated in frequency by a guard band, is synthesised with symmetrical Chebyshev response. The diplexer has a total number of resonators of n=8, a return loss of 20 dB for both channels, and inner edges for both channels of ±0.5 Hz. The value of r is taken as **2** in this example, which means 2 resonators should be located between the junction resonator and either of the output ports. The diplexer topology is shown in figure 4.9.

The normalized external quality factors are numerically calculated using equation (4.19) as q_{e6}=q_{e8}=3.726 and q_{e1}=1.863.

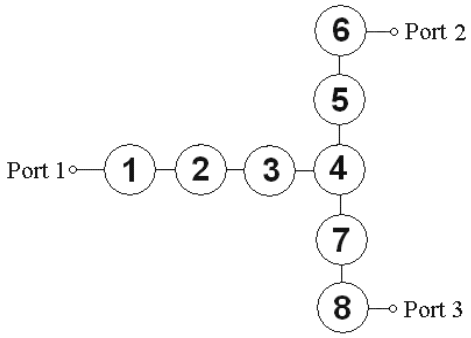

Figure.4.9: Topology of Diplexer A

The coupling coefficients between any adjacent resonators are initially set to 0.5 in the initial coupling matrix, and the couplings that do not exist between resonators are set to zero. The coefficients m_{ii} that represent frequency offsets are initially set to 0.5 for resonators 5 and 6, and to -0.5 for resonators 7 and 8. Since the desired response of the diplexer has symmetrical frequency bands, the coupling coefficients m_{47} and m_{78} are set equal to the coefficients m_{45} and m_{56} respectively. Furthermore, m_{77} is set equal to $-m_{55}$, and similarly, m_{88} is set equal to $-m_{66}$. An unconstrained local optimization algorithm using the cost function in equation (4.18) has been utilized. The cost function is evaluated at the return zeros locations s_{rj}, S_{11} peaks' frequency locations s_{pv}, and the locations of transmission coefficients at passband edges s_{ti}= [-

0.5i, -i], and s_{tk}= [0.5i, i]. The initial values of return zeros locations s_{rj} have been set with equal spacing as explained in section (4.4.4), with lower channel edges of -1 and -0.5 Hz, and upper channel edges of 0.5 and 1 Hz, as follows: ±0.52i, ±0.6733i, ±0.8267i, ±0.98i. These values are then allowed to be moved in the optimization algorithm until the peaks of $|S_{11}|$ in the passband are equal to the specified return loss. The final locations of return zeros are: ±0.523i, ±0.673i, ±0.862i, ±0.984i. The optimized normalized coupling matrix is shown below, and the response of diplexer A is shown in figure 4.10. The algorithm converged after 50 iterations with final error of 6.267 x 10^{-6}.

$$M = \begin{bmatrix} 0 & 0.8218 & 0 & 0 & 0 & 0 & 0 & 0 \\ 0.8218 & 0 & 0.4224 & 0 & 0 & 0 & 0 & 0 \\ 0 & 0.4224 & 0 & 0.7117 & 0 & 0 & 0 & 0 \\ 0 & 0 & 0.7117 & 0 & 0.2553 & 0 & 0.2553 & 0 \\ 0 & 0 & 0 & 0.2553 & 0.7112 & 0.2315 & 0 & 0 \\ 0 & 0 & 0 & 0 & 0.2315 & 0.7414 & 0 & 0 \\ 0 & 0 & 0 & 0.2553 & 0 & 0 & -0.7112 & 0.2315 \\ 0 & 0 & 0 & 0 & 0 & 0 & 0.2315 & -0.7414 \end{bmatrix}$$

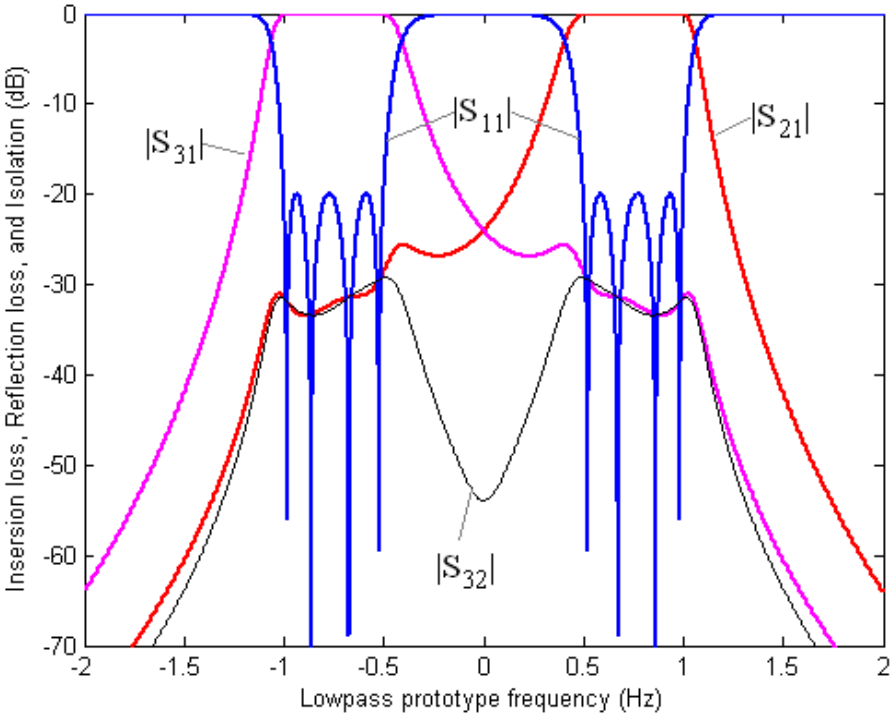

Figure 4.10: Response of Diplexer A

4.5.1.2 Example B: Non-contiguous band diplexer with n=8, x=0.5, and r=3

A non-contiguous symmetrical diplexer that has the T-Topology in figure 4.8 with r=3 is synthesised. The diplexer has a Chebyshev response with a return loss of 20 dB at both channels, a total number of resonators of n=8, and inner edges for both channels of ±0.5 Hz. The diplexer topology is shown in figure 4.11. A comparison between this diplexer and diplexer *A* will be shown later.

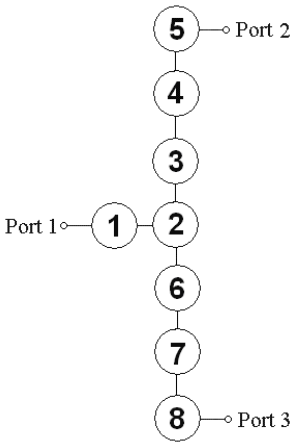

Figure 4.11: Topology of Diplexer B

The normalized external quality factors are found using equation (4.19) as q_{e5}=q_{e8}=3.726 and q_{e1}=1.863. The following conditions for coupling coefficients have been set in the optimization algorithm to achieve symmetrical channels: m_{26}=m_{23}, m_{67}=m_{34}, m_{78}=m_{45}, m_{66}=-m_{33}, m_{77}=-m_{44}, m_{88}=-m_{55}. The initial values of the coupling coefficients between adjacent resonators are set to 0.5, and to 0.7 for coefficients m_{33}, m_{44} and m_{55}, and the initial values of return zeros s_{rj} and the locations of transmission coefficients s_{ti} and s_{tk} are the same as those of diplexer *A*. The optimization has been done in two stages. In the first stage, the optimization was carried out by using the cost function in (4.18) without the last term, and with equally spaced reflection zeros. In the second stage, the full cost function in (4.18) was used, and the resulting coupling coefficients from the first stage are used as initial values, and the locations of the reflections zeros are allowed to move until the peaks of $|S_{11}|$ in the passband are equal

to the desired return loss. An unconstrained local optimization algorithm has been used in both stages, and the final locations of return zeros are,

$$\pm 0.521i,\ \pm 0.663i,\ \pm 0.854i,\ \pm 0.982i$$

The optimized normalized coupling matrix is shown below, and the response of diplexer B is shown in figure 4.12. The algorithm converged after 63 iterations with final error of 2.434 x 10^{-8} in the first stage and after 93 iterations with final error of 6.438 x 10^{-8} in the second stage.

$$M = \begin{bmatrix} 0 & 0.8256 & 0 & 0 & 0 & 0 & 0 & 0 \\ 0.8256 & 0 & 0.2981 & 0 & 0 & 0.2981 & 0 & 0 \\ 0 & 0.2981 & 0.6963 & 0.1786 & 0 & 0 & 0 & 0 \\ 0 & 0 & 0.1786 & 0.7428 & 0.2284 & 0 & 0 & 0 \\ 0 & 0 & 0 & 0.2284 & 0.7462 & 0 & 0 & 0 \\ 0 & 0.2981 & 0 & 0 & 0 & -0.6963 & 0.1786 & 0 \\ 0 & 0 & 0 & 0 & 0 & 0.1786 & -0.7428 & 0.2284 \\ 0 & 0 & 0 & 0 & 0 & 0 & 0.2284 & -0.7462 \end{bmatrix}$$

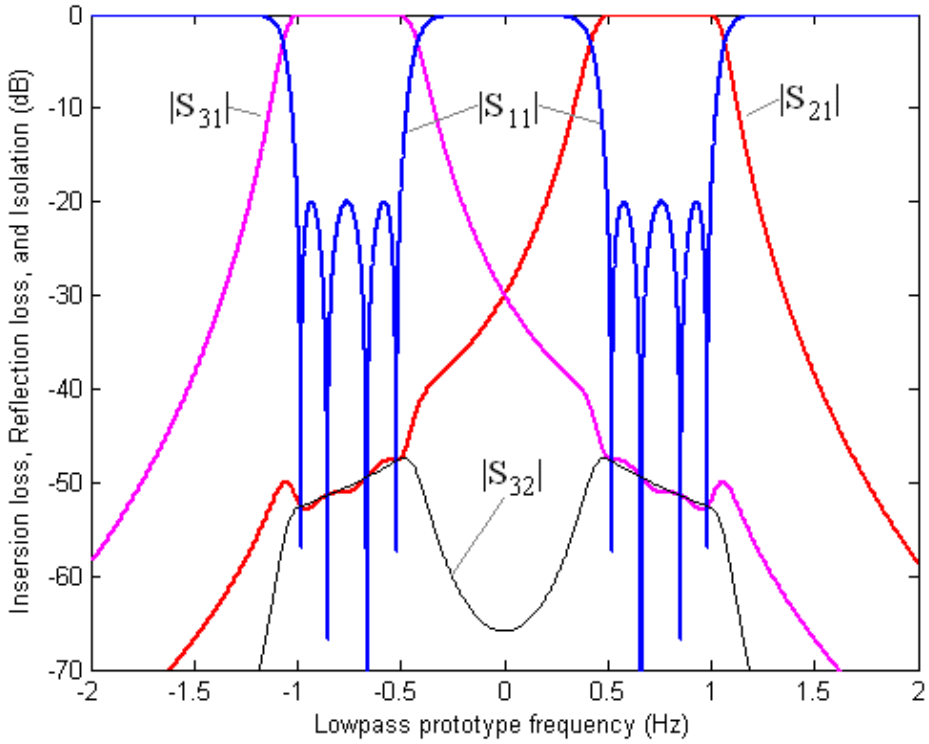

Figure 4.12: Response of Diplexer B

4.5.1.3 Example C: Non-contiguous band diplexer with n=10, x=0.333, and r=4

Diplexer C has non-contiguous symmetrical bands and a Chebyshev response. It has the topology in figure 4.8 with r=4, a total number of resonators of n=10, inner edges for both channels of ±0.333 Hz, and a return loss of 20 dB for both channels. The diplexer topology is shown in figure 4.13.

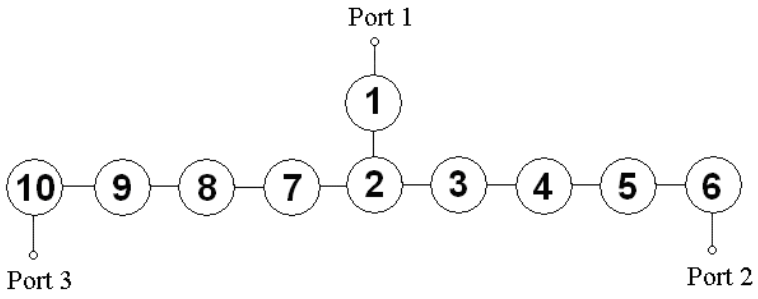

Figure 4.13: Topology of Diplexer C

The values of normalized external quality factors are calculated using equation (4.19) as q_{e6}=q_{e10}=2.914 and q_{e1}=1.457. The following conditions for coupling coefficients have been forced in the optimization algorithm to achieve symmetrical channels: m_{27}= m_{23}, m_{78}= m_{34}, m_{89}= m_{45}, $m_{9,10}$= m_{56}, m_{77}= -m_{33}, m_{88}= -m_{44}, and m_{99}= -m_{55}, $m_{10,10}$= -m_{66}. The initial values of the coupling coefficients between adjacent resonators are set to 0.5, and those of the coefficients m_{33}, m_{44}, m_{55}, m_{66} are set to 0.6. The cost function in equation (4.18) has been used and the optimization has been done in two stages as described earlier with an unconstrained gradient-based local optimization method. The frequency locations s_{ti} and s_{tk} in the first two terms in the cost function have been taken as s_{ti}= [-0.333i, -i, 0], and s_{tk}= [0.333i, i, 0].

The initial values of return zeros locations s_{rj} are equally spaced as follows,

$$\pm 0.3533i,\ \pm 0.510i,\ \pm 0.6667i,\ \pm 0.8234i,\ \pm 0.98i$$

The final locations of return zeros are

$$\pm 0.351i,\ \pm 0.482i,\ \pm 0.682i,\ \pm 0.872i,\ \pm 0.985i$$

The optimized normalized coupling matrix is given below, and the response of diplexer C is shown in figure 4.14. The algorithm converged after 23 iterations with final error of 3.160 x 10^{-7} in the first stage and after 200 iterations with final error of 4.757 x 10^{-7} in the second stage.

$$M = \begin{bmatrix}
0 & 0.8010 & 0 & 0 & 0 & 0 & 0 & 0 & 0 & 0 \\
0.8010 & 0 & 0.3536 & 0 & 0 & 0 & 0.3536 & 0 & 0 & 0 \\
0 & 0.3536 & 0.5928 & 0.2179 & 0 & 0 & 0 & 0 & 0 & 0 \\
0 & 0 & 0.2179 & 0.6553 & 0.2131 & 0 & 0 & 0 & 0 & 0 \\
0 & 0 & 0 & 0.2131 & 0.6619 & 0.2892 & 0 & 0 & 0 & 0 \\
0 & 0 & 0 & 0 & 0.2892 & 0.6635 & 0 & 0 & 0 & 0 \\
0 & 0.3536 & 0 & 0 & 0 & 0 & -0.5928 & 0.2179 & 0 & 0 \\
0 & 0 & 0 & 0 & 0 & 0 & 0.2179 & -0.6553 & 0.2131 & 0 \\
0 & 0 & 0 & 0 & 0 & 0 & 0 & 0.2131 & -0.6619 & 0.2892 \\
0 & 0 & 0 & 0 & 0 & 0 & 0 & 0 & 0.2892 & -0.6635
\end{bmatrix}$$

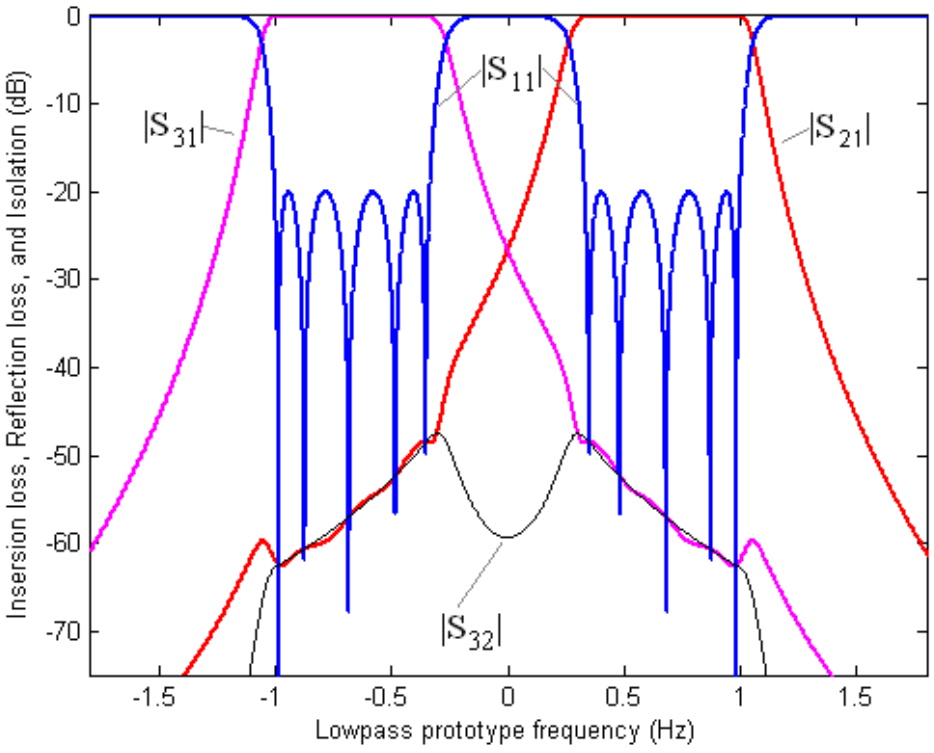

Figure 4.14: Response of diplexer C

4.5.1.4 Example D: Non-contiguous band diplexer with n=12, x=0.3, and r=3

A symmetrical diplexer with non-contiguous bands and a Chebyshev response is synthesised. It has a total number of resonators of n=12, inner edges for both channels of ±0.3 Hz, and a return loss of 20 dB for both channels. The number of resonators between the junction resonator and either of the output ports is taken as r=3. The diplexer topology is shown in figure 4.15.

The values of normalized external quality factors are calculated using equation (4.19) as q_{e9}=q_{e12}=2.84 and q_{e1}=1.42. The initial values of the coupling coefficients between adjacent resonators are set to 0.8 for m_{12} and to 0.5 for other coefficients, and the coefficients m_{ii} that represent frequency offsets are initially set to 0.6 for resonators 7, 8 and 9, and to -0.6 for resonators 10, 11, and 12.

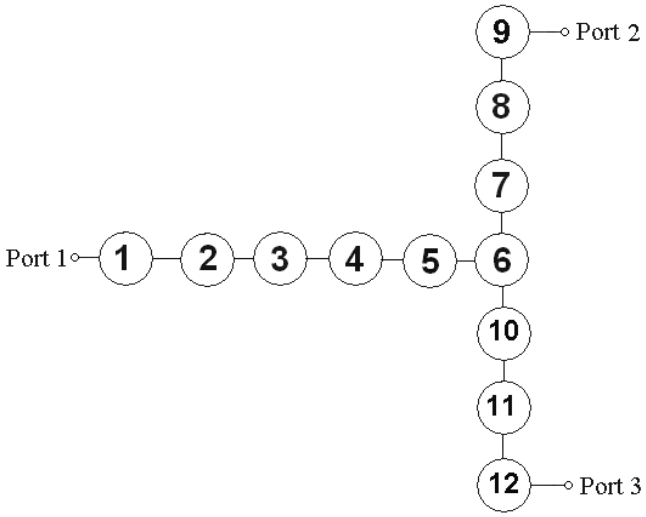

Figure 4.15: Topology of Diplexer D

To achieve symmetrical channels, the following conditions for coupling coefficients have been forced in the optimization algorithm: $m_{6,10}$= m_{67}, $m_{10,11}$= m_{78}, $m_{11,12}$= m_{89}, $m_{10,10}$= -m_{77}, $m_{11,11}$= -m_{88}, and $m_{12,12}$= -m_{99}.

The optimization has been done in two stages as explained earlier with unconstrained local optimization in the first stage and with constrained optimization in the second stage. The frequency locations s_{ti} and s_{tk} in the first two terms in the cost function (4.18) are s_{ti}= [-0.3i, -i] and s_{tk}= [0.3i, i]. The values of return zeros locations s_{rj} have been initially equally spaced between lower channel edges of -1 and -0.3 Hz, and upper channel edges of 0.3 and 1 Hz, as follows,

$$\pm 0.32i,\ \pm 0.4520i,\ \pm 0.5840i,\ \pm 0.7160i,\ \pm 0.8480i,\ \pm 0.98i$$

In the second stage, some constraints have been applied on the control variables to prevent the optimization algorithm from giving an unfeasible solution for the coupling coefficients, and also to prevent the locations of reflection zeros from moving outside the passband. The variables in the optimization algorithm are:

$$\{m_{12}, m_{23}, m_{34}, m_{45}, m_{56}, m_{67}, m_{78}, m_{89}, m_{77}, m_{88}, m_{99}, s_{r1}, s_{r2}, s_{r3}, s_{r4}, s_{r5}, s_{r6}\}$$

The last 6 variables represent the reflection zeros of the upper band, and the reflection zeros of the lower band are equal to -s_{rj}. The lower and upper bounds of the variables are as follows,

$$\begin{cases} 0.6,\ 0.0,\ 0.0,\ 0.0,\ 0.0,\ 0.0,\ 0.0,\ 0.0,\ 0.5,\ 0.5,\ 0.5,\ 0.300,\ 0.402,\ 0.544,\ 0.686,\ 0.808,\ 0.940, & \textit{lower bounds} \\ 1.5,\ 1.5,\ 1.5,\ 1.5,\ 1.5,\ 1.5,\ 1.5,\ 1.5,\ 1.5,\ 1.5,\ 1.5,\ 0.360,\ 0.492,\ 0.614,\ 0.756,\ 0.888,\ 0.980, & \textit{upper bounds} \end{cases}$$

The final locations of return zeros are

$$\pm 0.316i,\ \pm 0.432i,\ \pm 0.606i,\ \pm 0.78i,\ \pm 0.917i,\ \pm 0.99i$$

The optimized normalized coupling matrix is shown in table 4.1, and the response of diplexer D is shown in figure 4.16. The algorithm converged after 97 iterations with final error of 1.218×10^{-7} in the first stage. In the second stage, the third term in the cost function (4.18) has been weighted and the algorithm converged after 50 iterations.

Table 4.1: Coupling matrix of diplexer D

	1	2	3	4	5	6	7	8	9	10	11	12
1	0	0.7927	0	0	0	0	0	0	0	0	0	0
2	0.7927	0	0.5062	0	0	0	0	0	0	0	0	0
3	0	0.5062	0	0.6114	0	0	0	0	0	0	0	0
4	0	0	0.6114	0	0.4408	0	0	0	0	0	0	0
5	0	0	0	0.4408	0	0.6176	0	0	0	0	0	0
6	0	0	0	0	0.6176	0	0.2989	0	0	0.2989	0	0
7	0	0	0	0	0	0.2989	0.5935	0.2212	0	0	0	0
8	0	0	0	0	0	0	0.2212	0.6376	0.2975	0	0	0
9	0	0	0	0	0	0	0	0.2975	0.6407	0	0	0
10	0	0	0	0	0	0.2989	0	0	0	-0.5935	0.2212	0
11	0	0	0	0	0	0	0	0	0	0.2212	-0.6376	0.2975
12	0	0	0	0	0	0	0	0	0	0	0.2975	-0.6407

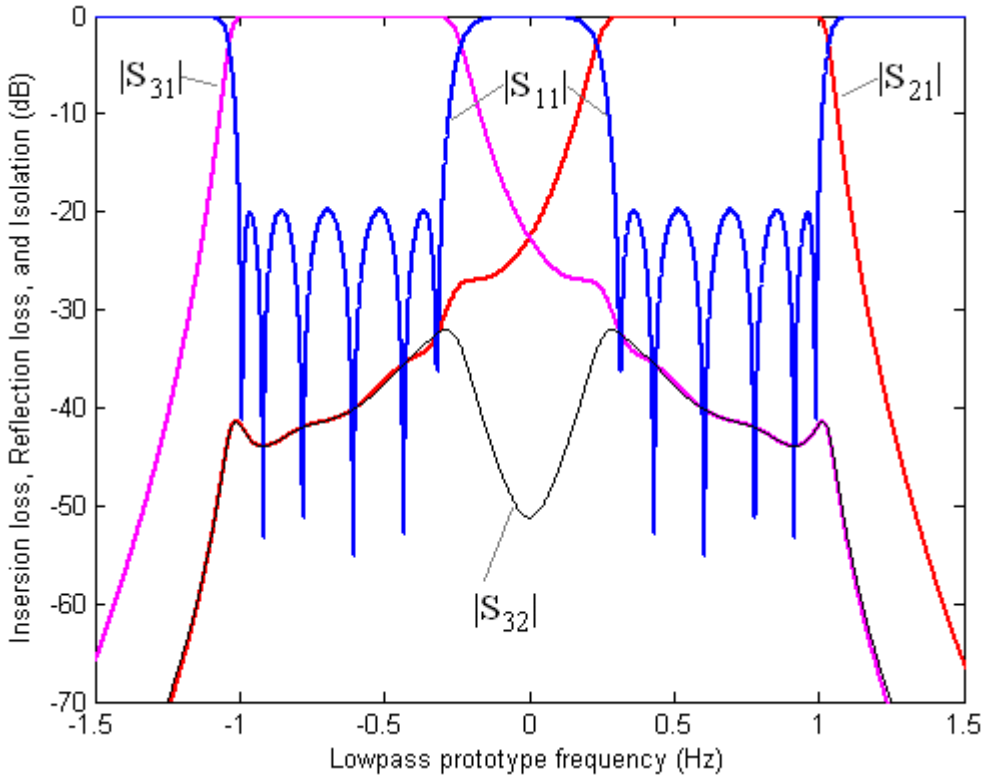

Figure 4.16: Response of Diplexer D

4.5.1.5 Example E: Contiguous band diplexer with *n*=12, x=0.1, and *r*=5

Diplexer E has symmetrical bands with x=0.1 Hz, r=5, and a return loss of 20 dB at both channels. The response of the diplexer is Chebyshev and it consists of 12 resonators directly coupled together. The diplexer topology is shown in figure 4.17.

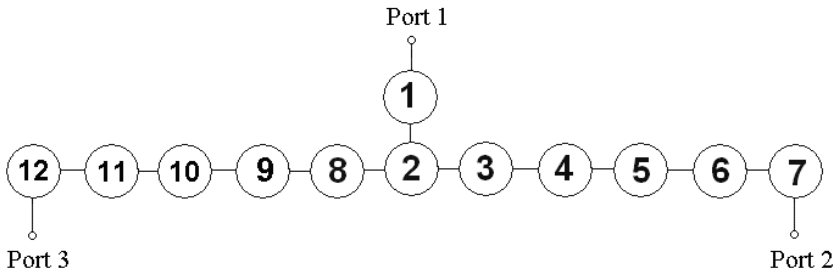

Figure 4.17: Topology of diplexer E

The normalized external quality factors are calculated using equation (4.19) as $q_{e7}=q_{e12}$=2.209 and q_{e1}=1.1045. To obtain symmetrical bands as specified, The following conditions for coupling coefficients have been set in the optimization algorithm: $m_{28}= m_{23}$, $m_{89}= m_{34}$, $m_{9,10}= m_{45}$, $m_{10,11}= m_{56}$, $m_{11,12}= m_{67}$, $m_{88}= -m_{33}$, $m_{99}= -m_{44}$, and $m_{10,10}= -m_{55}$, $m_{11,11}= -m_{66}$, $m_{12,12}= -m_{77}$. The initial values of the coupling coefficients for adjacent resonators are set to 0.6 for m_{12}, and to 0.5 for other coefficients, and the initial values of the coefficients m_{ii} (i=3,…7) have been set to 0.6. The cost function in equation (4.18) has been used and the optimization has been done in two stages as explained earlier with an unconstrained local optimization technique. The initial values of return zeros locations s_{rj} are set with equal spacing as follows,

$$\pm 0.12i,\ \pm 0.292i,\ \pm 0.464i,\ \pm 0.636i,\ \pm 0.808i,\ \pm 0.98i$$

The realised locations of return zeros are

$$\pm 0.118i,\ \pm 0.248i,\ \pm 0.46i,\ \pm 0.69i,\ \pm 0.88i,\ \pm 0.986i$$

The optimized normalized coupling matrix is shown in table 4.2, and the response of diplexer E is shown in figure 4.18.

It has been found useful for optimization in the first stage to weight the first two terms in the cost function (4.18) by 100, and the algorithm converged after 70 iterations with final error of 1.171×10^{-7}. In the second stage, the third term in the cost function (4.18) has been weighted by 100 and the algorithm converged after 192 iterations.

Table 4.2: Coupling matrix of diplexer E

	1	2	3	4	5	6	7	8	9	10	11	12
1	0	0.8052	0	0	0	0	0	0	0	0	0	0
2	0.8052	0	0.4051	0	0	0	0	0.4051	0	0	0	0
3	0	0.4051	0.4827	0.2757	0	0	0	0	0	0	0	0
4	0	0	0.2757	0.5396	0.2623	0	0	0	0	0	0	0
5	0	0	0	0.2623	0.5440	0.2759	0	0	0	0	0	0
6	0	0	0	0	0.2759	0.5447	0.3806	0	0	0	0	0
7	0	0	0	0	0	0.3806	0.5459	0	0	0	0	0
8	0	0.4051	0	0	0	0	0	-0.4827	0.2757	0	0	0
9	0	0	0	0	0	0	0	0.2757	-0.5396	0.2623	0	0
10	0	0	0	0	0	0	0	0	0.2623	-0.5440	0.2759	0
11	0	0	0	0	0	0	0	0	0	0.2759	-0.5447	0.3806
12	0	0	0	0	0	0	0	0	0	0	0.3806	-0.5459

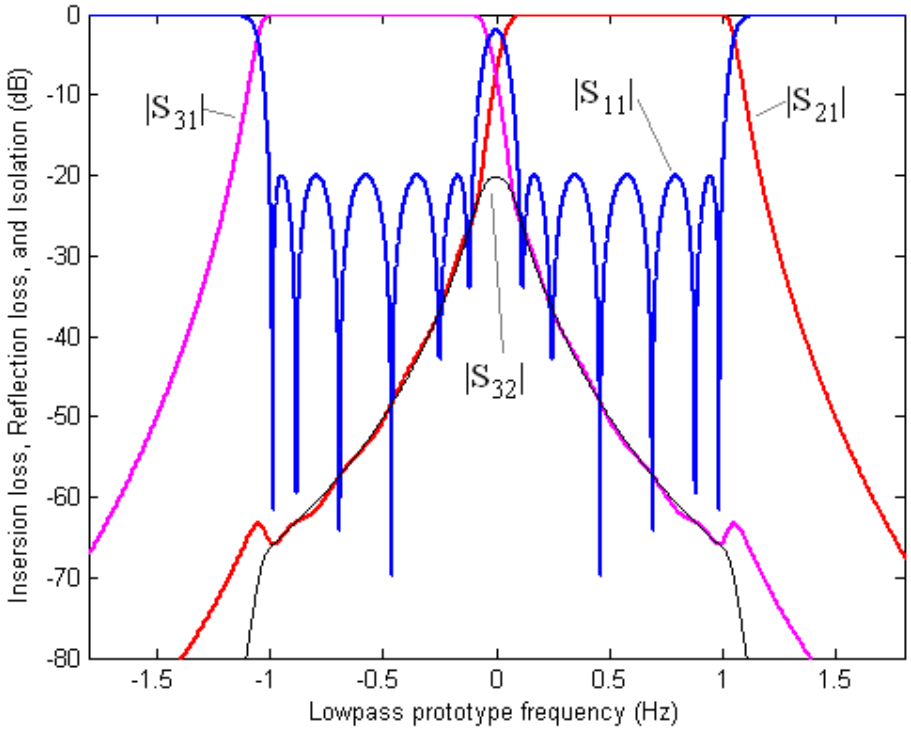

Figure 4.18: Response of diplexer E

4.5.1.6 Example F: Non-contiguous band diplexer with *n*=8, x=0.5

Example F is the conventional diplexer in figure 4.4 without a three port junction, so the common port is composed by shunt connection of the inputs of the two bandpass filters forming the diplexer. The synthesis of diplexer F is presented in this section and its performance will be compared with other coupled-resonator diplexers with T-topologies in the next section.

Diplexer F has a total number of resonators of *n*=8, inner edges for both channels of ±0.5 Hz, and a return loss of 20 dB for both channels. The topology of the diplexer is shown in figure 4.19.

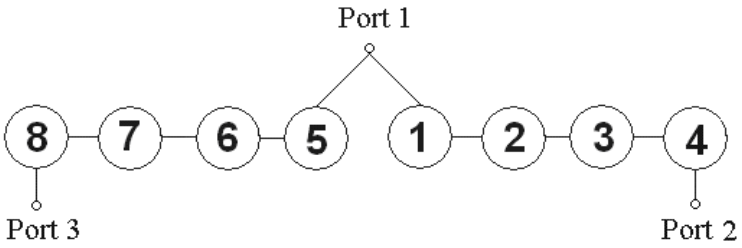

Figure 4.19: Response of diplexer F

The synthesis starts by firstly finding the coupling matrices of the individual bandpass filters formed from the resonators (1,2,3,4) and (5,6,7,8), then using the resulting matrices as initial values in the synthesis of the whole diplexer, so that the common port is integrated in the design.

The normalized external quality factors of the filters are calculated using equation (4.19) as $q_{e1}=q_{e4}= q_{e5}=q_{e8}=3.726$. The locations of the reflection zeros were initially equally spaced, and the coupling matrices of the individual filters have been found using a filter optimization technique presented in [31]. The algorithm converged after 46 iterations with final error of 6.247×10^{-12}.

The resulting normalized coupling matrices of the filters are as follows,

$$M_1 = \begin{bmatrix} 0.750 & 0.2239 & 0 & 0 \\ 0.2239 & 0.750 & 0.1748 & 0 \\ 0 & 0.1748 & 0.750 & 0.2239 \\ 0 & 0 & 0.2239 & 0.750 \end{bmatrix}, \quad M_2 = \begin{bmatrix} -0.750 & 0.2239 & 0 & 0 \\ 0.2239 & -0.750 & 0.1748 & 0 \\ 0 & 0.1748 & -0.750 & 0.2239 \\ 0 & 0 & 0.2239 & -0.750 \end{bmatrix}$$

where M_1 is that for the filter consisting of resonators (1,2,3,4) and M_2 is that for the filter consisting of resonators (5,6,7,8). The coupling matrix of the diplexer has been synthesised by unconstrained optimization with the coefficients of the matrices M_1 and M_2 used as initial values. The cost function that has been used in optimization is as follows,

$$\Omega = \sum_{i=1}^{R} \left| S_{11}(s_{ri}) \right|^2 + \sum_{v=1}^{R-2} \left| \left| S_{11}(s_{pv}) \right| - 10^{\frac{L_R}{20}} \right|^2 \tag{4.20}$$

where R is the total number of return zeros, s_{ri} are the frequency locations of return zeros, L_R is the desired return loss in dB (L_R<0), and s_{pv} are the peaks' frequency values of $|S_{11}|$ in the passband. S_{11} is evaluated from equations (4.1)-(4.4), where S_{11}^{TX} and S_{11}^{RX} are as follows,

$$S_{11}^{TX} = 1 - \frac{2}{q_{e4}} [A]_{44}^{-1}, \qquad S_{11}^{RX} = 1 - \frac{2}{q_{e8}} [A]_{88}^{-1} \tag{4.21}$$

The normalized optimized coupling matrix of the diplexer is shown below, and the response of the diplexer is shown in figure 4.20. The algorithm converged after 34 iterations with final error of 9.766 x 10^{-7}.

$$M = \begin{bmatrix} 0.7500 & 0.2279 & 0 & 0 & 0 & 0 & 0 & 0 \\ 0.2279 & 0.7500 & 0.1750 & 0 & 0 & 0 & 0 & 0 \\ 0 & 0.1750 & 0.7511 & 0.2242 & 0 & 0 & 0 & 0 \\ 0 & 0 & 0.2242 & 0.7976 & 0 & 0 & 0 & 0 \\ 0 & 0 & 0 & 0 & -0.7500 & 0.2279 & 0 & 0 \\ 0 & 0 & 0 & 0 & 0.2279 & -0.7500 & 0.1750 & 0 \\ 0 & 0 & 0 & 0 & 0 & 0.1750 & -0.7511 & 0.2242 \\ 0 & 0 & 0 & 0 & 0 & 0 & 0.2242 & -0.7976 \end{bmatrix}$$

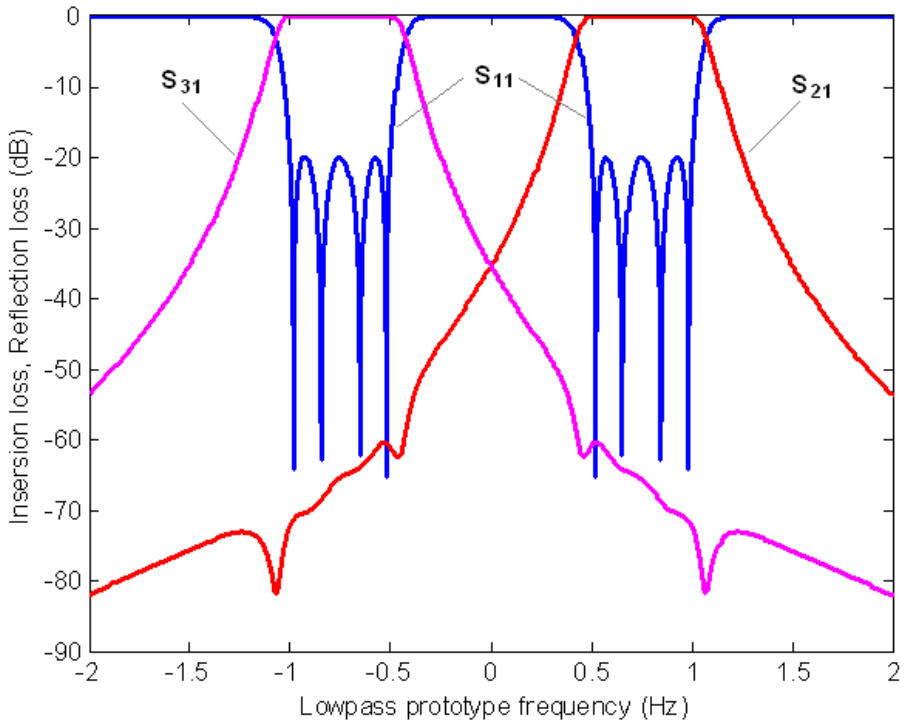

Figure 4.20: Response of diplexer F

4.6 Comparison between Diplexers

In the T-topology in figure 4.8, different values of r make it possible to realise many topologies with n coupled resonators. It has been found from optimization results that possible solutions for r that achieve a non-distorted diplexer response are between $r = \lceil \frac{n}{4} \rceil$ and $r = \left(\frac{n}{2} - 1\right)$. These solutions have been demonstrated in the examples of diplexers A-E.

In this section, a comparison between three diplexers with the same number of resonators and different topologies is presented. The diplexers under comparison are those in examples A (T-topology, n=8, r=2), B (T-topology, n=8, r=3) and F (conventional diplexer, n=8), which were synthesized in this chapter, and their topologies are shown in figure 4.21. These diplexers were synthesised with non-contiguous bands with n=8 and x=0.5 and a return loss of 20 dB at both bands for all diplexers.

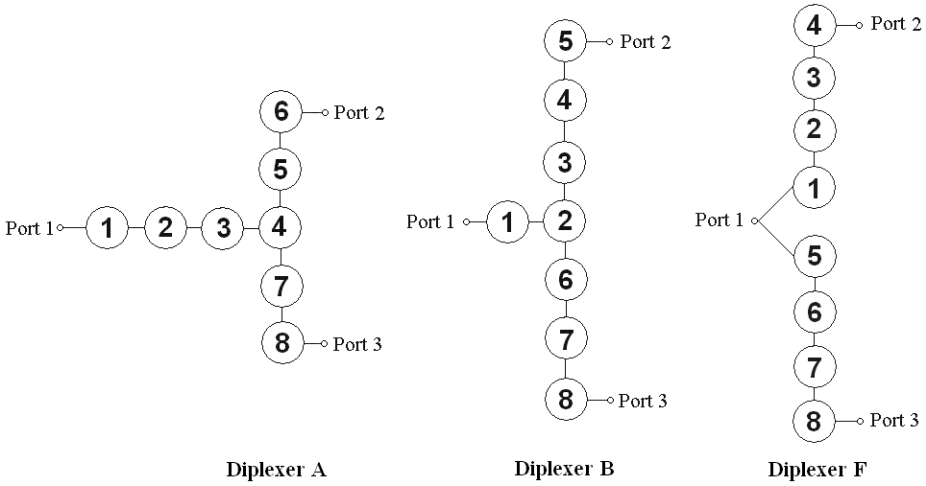

Figure 4.21: Diplexers A, B, and F topologies

The responses of the diplexers in figure 4.21 are shown in figure 4.22 for comparison. It is noticed that diplexer F has better isolation than diplexer B, and that diplexer B has better isolation than diplexer A. In other words, the higher the number of resonators between ports 2 and 3, the better the isolation. However, far out of band, the response is better for diplexers A and B.

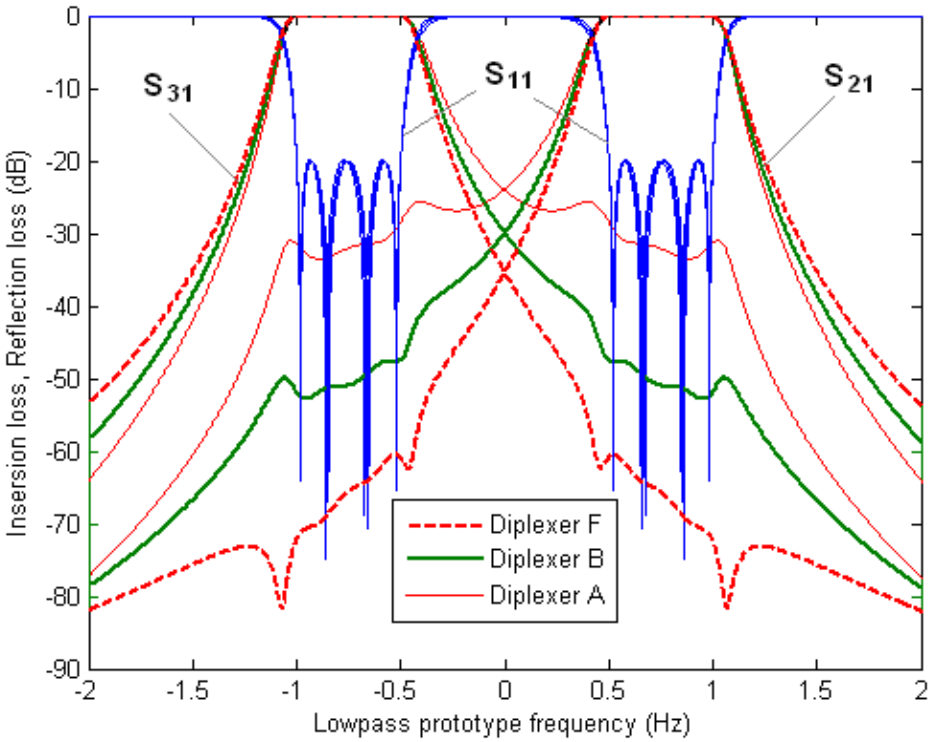

Figure 4.22: Responses of diplexers in figure 4.21

Accordingly, in the proposed general T-topology in figure 4.8, the value of r that gives the best isolation performance is $r = \left(\frac{n}{2} - 1\right)$, where n is the total number of resonators. This is due to existence of (n-1) resonators between the output ports.

4.7 Diplexers with Canonical Topology

A proposed general canonical topology for a symmetrical diplexer is shown in figure 4.23, where n is the total number of resonators and $\pm x$ define the inner edges of the two channels. In this topology, solid lines represent direct coupling, and dashed lines represent cross coupling, and Quasi-Elliptic filter responses can be achieved. The resonators (3,4,…, n/2+1) should have positive frequency offsets (M_{ii}>0) for the upper channel to be at port 2, and the resonators (n/2+2, n/2+3,…, n) should have negative frequency offsets (M_{ii}<0) for the lower channel to be at port 3.

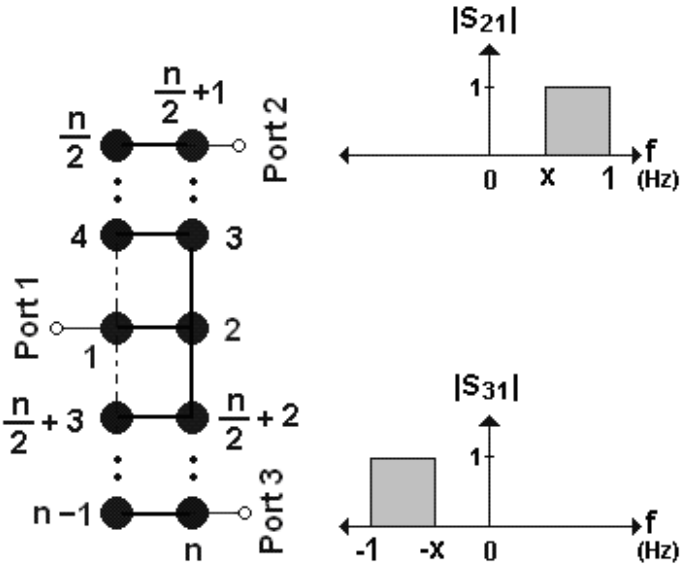

Figure 4.23: Diplexer canonical topology

To achieve symmetrical channels, the following conditions for coupling coefficients should apply,

$$m_{2,\frac{n}{2}+2} = m_{23},\ m_{\frac{n}{2}+2,\frac{n}{2}+3} = m_{34}, \ldots \quad = m_{\frac{n}{2},\frac{n}{2}+1}$$

$$m_{\frac{n}{2}+2,\frac{n}{2}+2} = -m_{33},\ m_{\frac{n}{2}+3,\frac{n}{2}+3} = -m_{44}, \ldots \quad = -m_{\frac{n}{2},\frac{n}{2}}, m_{n,n} = -m_{\frac{n}{2}+1,\frac{n}{2}+1}$$

Enforcing the topology of the symmetrical diplexer in the optimization algorithm along with the conditions given above simplifies the synthesis of the coupling matrix and reduces the convergence time.

4.7.1 Examples of diplexers with canonical topology

This section presents examples of diplexers with the proposed canonical topology with Quasi-Elliptic responses. Both non-contiguous and contiguous bands have been successfully achieved.

4.7.1.1 Example G: Non-contiguous band diplexer with *n*=12, *x*=0.3

Diplexer G has non-contiguous symmetrical bands and a Quasi-Elliptic response. It has the topology in figure 4.23 with a total number of resonators of n=12 and inner edges of ±0.3 Hz. The specified lowpass prototype transmission zeros are -0.2i Hz and -1.1i Hz for the lower channel, and 0.2i Hz and 1.1i Hz for the upper channel, and the return loss for both channels is 20 dB. The diplexer topology is shown in figure 4.24.

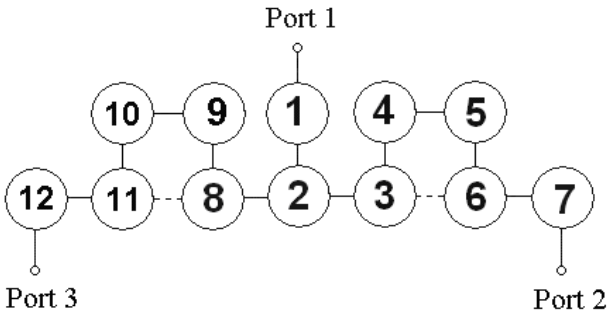

Figure 4.24: Topology of diplexers G and H

The normalized external quality factors and the initial values of the reflection zeros are the same as those of diplexer D, since both diplexers D and G have the same order of filtering functions (n=12) and the same inner edges (±0.3 Hz). In a similar way to the previous examples, some conditions for coupling coefficients have been forced in the optimization algorithm to achieve symmetrical channels. These conditions are: $m_{28}= m_{23}$, $m_{89}= m_{34}$, $m_{9,10}= m_{45}$, $m_{10,11}= m_{56}$, $m_{11,12}= m_{67}$, $m_{8,11}= m_{36}$, $m_{88}= -m_{33}$, $m_{99}= -m_{44}$, and $m_{10,10}= -m_{55}$, $m_{11,11}= -m_{66}$, $m_{12,12}= -m_{77}$.

The optimization has been done in two stages. In the first stage, an unconstrained optimization is carried out by using the first three terms in the cost function in (4.18) without cross coupling and with equally spaced reflection zeros. The initial values of the coupling coefficients m_{ij} are set to 0.5, and to 0.6 for the coefficients m_{ii} (i=3,...,7). In the second stage, the locations of reflections zeros are allowed to move, and the resulting coupling coefficients from the first stage are used as initial values, and the initial values of the cross couplings m_{36} and $m_{8,11}$ are set to 0. A constrained optimization technique has been used in the second stage, and the variables in the optimization algorithm are:

$$\{m_{12}, m_{23}, m_{34}, m_{45}, m_{56}, m_{67}, m_{36}, m_{33}, m_{44}, m_{55}, m_{66}, m_{77}, s_{r1}, s_{r2}, s_{r3}, s_{r4}, s_{r5}, s_{r6}\}$$

where $s_{r1},\ldots,s_{r6}$ represent the reflection zeros of the upper band, and the reflection zeros of the lower band are equal to $-s_{r1},\ldots,-s_{r6}$. The lower and upper bounds of the variables are set as follows,

$$\begin{cases} 0.5,\ 0.0,\ 0.0,\ 0.0,\ 0.0,\ 0.0,\ -\infty,\ 0.5,\ 0.5,\ 0.5,\ 0.5,\ 0.5,\ 0.300,\ 0.382,\ 0.534,\ 0.676,\ 0.798,\ 0.940, & \textit{lower bounds} \\ 1.0,\ 1.0,\ 1.0,\ 1.0,\ 1.0,\ 1.0,\ \infty,\ 1.0,\ 1.0,\ 1.0,\ 1.0,\ 1.0,\ 0.380,\ 0.502,\ 0.634,\ 0.776,\ 0.938,\ 0.990, & \textit{upper bounds} \end{cases}$$

The optimized normalized coupling matrix is given in table 4.3, and the response of diplexer G is shown in figure 4.25. The algorithm converged after 117 iterations with final error of 5.115×10^{-8} in the first stage. In the second stage, it has been found useful for optimization to

weight the first three terms in the cost function (4.18), and the algorithm converged after 37 iterations. The realised reflection zeros are ±0.31i, ±0.394i, ±0.565i, ±0.766i, ±0.92i, ±0.992i Hz, and realised transmission zeros are ±1.1i and ±0.19i Hz.

Table 4.3: Coupling matrix of diplexer G

	1	2	3	4	5	6	7	8	9	10	11	12
1	0	0.7932	0	0	0	0	0	0	0	0	0	0
2	0.7932	0	0.3538	0	0	0	0	0.3538	0	0	0	0
3	0	0.3538	0.5757	0.2015	0	-0.0748	0	0	0	0	0	0
4	0	0	0.2015	0.6384	0.2618	0	0	0	0	0	0	0
5	0	0	0	0.2618	0.6514	0.1964	0	0	0	0	0	0
6	0	0	-0.0748	0	0.1964	0.6475	0.2921	0	0	0	0	0
7	0	0	0	0	0	0.2921	0.6482	0	0	0	0	0
8	0	0.3538	0	0	0	0	0	-0.5757	0.2015	0	-0.0748	0
9	0	0	0	0	0	0	0	0.2015	-0.6384	0.2618	0	0
10	0	0	0	0	0	0	0	0	0.2618	-0.6514	0.1964	0
11	0	0	0	0	0	0	0	-0.0748	0	0.1964	-0.6475	0.2921
12	0	0	0	0	0	0	0	0	0	0	0.2921	-0.6482

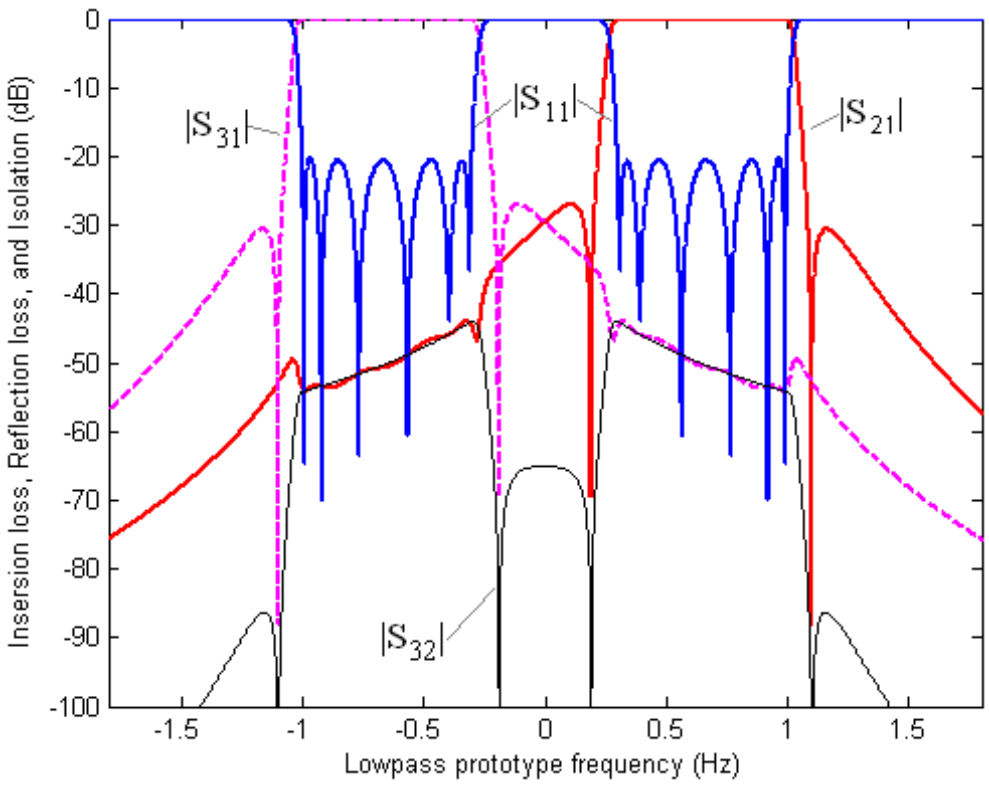

Figure 4.25: Response of diplexer G

4.7.1.2 Example H: Contiguous band diplexer with *n*=12

Diplexer H has contiguous symmetrical bands with x=0.03 Hz and a Quasi-Elliptic response. The specified lowpass prototype transmission zeros are -1.24i Hz and 0.2i Hz for the lower channel, and 1.24i Hz and -0.2i Hz for the upper channel and the specified reflection loss is 20 dB for both channels. The diplexer topology is the same as diplexer G, which is shown in figure 4.24.

The normalized external quality factors are evaluated using equation (4.19) as $q_{e7}=q_{e12}=2.05$ and $q_{e1}=1.025$. The same conditions for coupling coefficients that were applied in diplexer G to achieve symmetrical channels are used in this example, since both diplexers G and H have the same topology. The variables in the optimization algorithm are:

$$\{m_{12}, m_{23}, m_{34}, m_{45}, m_{56}, m_{67}, m_{36}, m_{33}, m_{44}, m_{55}, m_{66}, m_{77}, s_{r1}, s_{r2}, s_{r3}, s_{r4}, s_{r5}, s_{r6}\}$$

where $s_{r1},\ldots,s_{r6}$ are the frequency locations of the return zeros of the upper channel, and those of the lower channel are equal to $-s_{r1},\ldots,-s_{r6}$. The optimized coupling coefficients of diplexer E have been used as initial values in this example, and the initial values of the cross couplings m_{36} and $m_{8,11}$ have been set to 0. The initial values of the frequency locations of reflection zeros are as follows,

$$\pm 0.05i,\ \pm 0.236i,\ \pm 0.422i,\ \pm 0.608i,\ \pm 0.794i,\ \pm 0.98i$$

The cost function in (4.18) has been used in a constrained optimization technique with the lower and upper bounds of the variables are as follows,

$$\begin{cases} 0.6,\ 0.0,\ 0.0,\ 0.0,\ 0.0,\ 0.0,\ -\infty,\ 0.4,\ 0.4,\ 0.4,\ 0.4,\ 0.4,\ 0.01,\ 0.14,\ 0.32,\ 0.52,\ 0.71,\ 0.93, & \textit{lower bounds} \\ 1.0,\ 1.0,\ 1.0,\ 1.0,\ 1.0,\ 1.0,\ \infty,\ 1.0,\ 1.0,\ 1.0,\ 1.0,\ 1.0,\ 0.10,\ 0.30,\ 0.50,\ 0.66,\ 0.92,\ 0.996, & \textit{upper bounds} \end{cases}$$

The optimized normalized coupling matrix is shown in table 4.4, and the response of diplexer H is given in figure 4.26. The algorithm converged after 31 iterations with final error of 6.109 x 10^{-6}.

The realised reflection zeros are: ±0.036*i*, ±0.168*i*, ±0.414*i*, ±0.684*i*, ±0.89*i*, ±0.989*i* Hz, and realised transmission zeros are ±1.244*i* and ±0.213*i* Hz.

Table 4.4: Coupling matrix of diplexer H

	1	2	3	4	5	6	7	8	9	10	11	12
1	0	0.8143	0	0	0	0	0	0	0	0	0	0
2	0.8143	0	0.4132	0	0	0	0	0.4132	0	0	0	0
3	0	0.4132	0.4612	0.2768	0	-0.0623	0	0	0	0	0	0
4	0	0	0.2768	0.5140	0.3293	0	0	0	0	0	0	0
5	0	0	0	0.3293	0.5169	0.2882	0	0	0	0	0	0
6	0	0	-0.0623	0	0.2882	0.5145	0.4081	0	0	0	0	0
7	0	0	0	0	0	0.4081	0.5144	0	0	0	0	0
8	0	0.4132	0	0	0	0	0	-0.4612	0.2768	0	-0.0623	0
9	0	0	0	0	0	0	0	0.2768	-0.5140	0.3293	0	0
10	0	0	0	0	0	0	0	0	0.3293	-0.5169	0.2882	0
11	0	0	0	0	0	0	0	-0.0623	0	0.2882	-0.5145	0.4081
12	0	0	0	0	0	0	0	0	0	0	0.4081	-0.5144

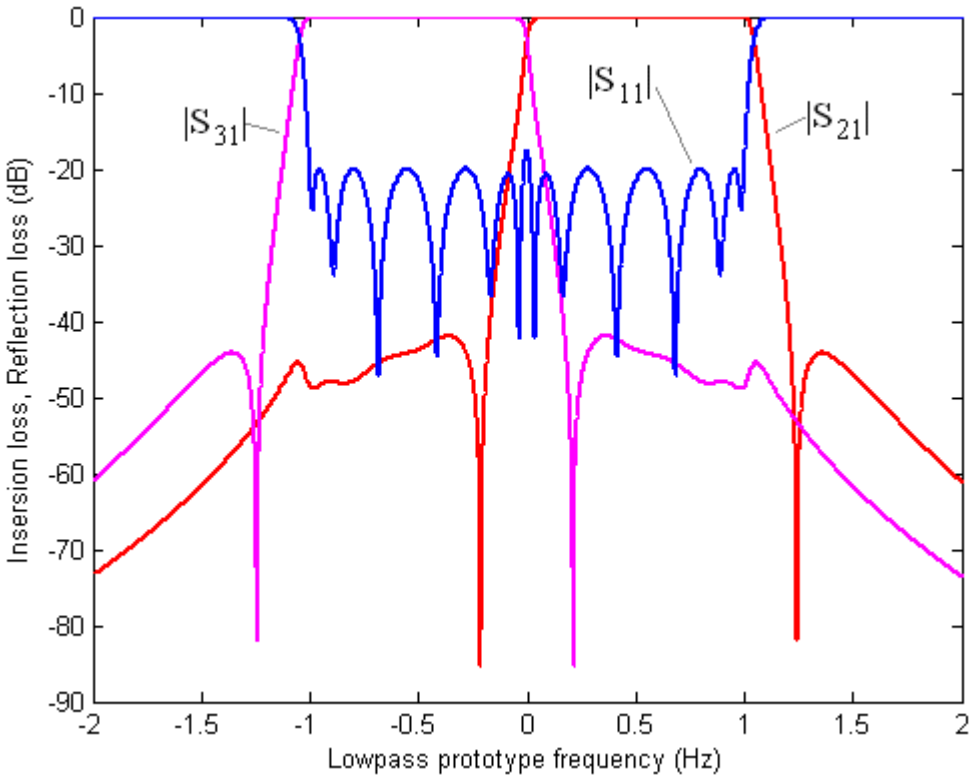

Figure 4.26: Response of diplexer H

4.8 Conclusion

Diplexers with novel topologies have been proposed. The design procedure is based on optimization of coupling matrix for multiple coupled resonators in a three-port network. These diplexers can be implemented using any type of resonators, and they do not involve energy distribution networks in their structures, unlike the conventional diplexers. This enables miniaturizing the diplexer structure.

A cost function has been formulated to be minimized in the optimization algorithm, and diplexers with different topologies with both contiguous and non-contiguous bands have been successfully synthesised. A comparison between diplexers with the same specification and different topologies has been presented. It has been found that the higher the number of resonators between output ports, the better the isolation. The implementation of coupled-resonator diplexers using waveguide cavity resonators will be presented in Chapters 5 and 6.

References

[1] R. Cameron, C. Kudsia, and R. Mansour, Microwave filters for communication systems. Wiley, 2007.

[2] I. Carpintero, M. Padilla-Cruz, A. Garcia-Lamperez, and M. Salazar-Palma,"Generalized multiplexing network," U.S. Patent 0114082 A1, Jun. 1, 2006.

[3] J. A. Ruiz-Cruz, J. R. Montejo-Garai, J. M. Rebollar, and S. Sobrino, "Compact full ku-band triplexer with improved E-plane power divider," *Progress In* Electromagnetics Research, Vol. 86, pp. 39-51, 2008.

[4] J. Dittloff, J. Bornemann, and F. Arndt, "Computer aided design of optimum E- or H-plane N-furcated waveguide power dividers," in *Proc. European Microwave Conference*, Sept. 1987, pp. 181-186.

[5] R.R. Mansour, et al., "Design considerations of superconductive input multiplexers for satellite applications," *IEEE Transactions on Microwave Theory and Techniques*, vol. 44, no. 7, pt. 2, pp. 1213-1229, 1996.

[6] J. D. Rhodes and R. Levy, "Design of general manifold multiplexers," IEEE *Transactions on Microwave Theory and Techniques*, vol. 27, no. 2, pp. 111-123, 1979.

[7] D. J. Rosowsky and D. Wolk, "A 450-W Output Multiplexer for Direct Broadcasting Satellites," *IEEE Transactions on Microwave Theory and Techniques*, vol. 30, no. 9, pp. 1317-1323, Sept. 1982.

[8] M.S. Uhm, J. Lee, J.H. Park, and J.P. Kim, "An Efficient Optimization Design of a Manifold Multiplexer Using an Accurate Equivalent Circuit Model of Coupling Irises of Channel Filters," in *proc. IEEE MTT-S Int. Microwave Symp.*, Long Beach, CA, 2005, pp. 1263-1266.

[9] R.J. Cameron and M. Yu, "Design of manifold coupled multiplexers," *IEEE Microwave Mag*., vol. 8, no. 5, pp. 46–59, Oct. 2007.

[10] M.J. Lancaster, "Radio frequency filter," W.I.P.O patent WO/01/69712, 2001.

[11] A. Garcia-Lamperez, M. Salazar-Palma, and T.K. Sarkar, "Compact multiplexer formed by coupled resonators with distributed coupling," *IEEE Antennas and Propagation Society International Symposium*, USA, 2005, pp. 89-92.

[12] A. Garcia-Lamperez, M. Salazar-Palma, and T.K. Sarkar, "Analytical synthesis of microwave multiport networks," *IEEE MTT-S International Microwave Symposium digest*, USA, June 2004, pp 455-458.

[13] F. Loras-Gonzalez, S. Sobrino-Arias, I. Hidalgo-Carpintero, A. García-Lampérez, M. Salazar-Palma, "A novel Ku-band dielectric resonator triplexer based on generalized multiplexer theory," *IEEE MTT-S International Microwave Symposium digest*, USA, May 2010, pp.884-887.

[14] M. Guglielmi, "Optimum CAD Procedure for Manifold Diplexers" in *proc. IEEE MTT-S Int. Microwave Symp.*, USA, 1993, pp. 1081-1084 vol.2.

[15] Y. Isota, M. Miyazaki, O. Ishida, and T. Hashimoto "Wideband Contiguous-Band Diplexer Using Interpolated Coupling Coefficient Bandpass Filters," *The Transactions of the Institute of Electronics, Information and Communications*, vol. 85-C, no. 3, pp. 158-165, March 2002.

[16] H. Zhang and G. James, "A broadband T-junction diplexer with integrated iris filters," *Microwave and Optical Technology letters*, vol. 17, no. 1, pp. 69-72, Dec. 1998.

[17] M. Wagner, D. Stanelli, P. Nuechter, and U. Goebel, "Compact 60 GHz Diplexer in Metallized Plastic Technology for Gigabit Wireless Links," in *Proc. European Microwave Conference*, Amsterdam, The Netherlands, Oct. 2004, pp. 1009-1012.

[18] J.M. Rebollar, J.R. Montejo-Garai, and A. Ohoro, "Asymmetric H-plane T-junction for broadband diplexer applications," *IEEE Antennas and Propagation Society International Symposium,* USA, 2000, vol. 4, pp.2032-2035.

[19] S. Bastioli, L. Marcaccioli and R. Sorrentino, "An original resonant Y-junction for compact waveguide diplexers," *IEEE MTT-S International Microwave Symposium Digest*, Boston, USA, June 2009, pp. 1233-1236.

[20] C. E. Saavedra, "Diplexer using a Circulator and Interchangeable Filters," in *Proc. of the 7th International* Caribbean Conference on Devices, Circuits and Systems, Mexico, Apr. 2008, pp. 1-5.

[21] G. Macchiarella and S. Tamiazzo, "Novel approach to the synthesis of microwave diplexers," *IEEE Transactions on Microwave Theory and Techniques*, vol. 54, no. 12, pp. 4281-4290, 2006.

[22] G. Macchiarella and S. Tamiazzo, "Synthesis of diplexers based on the evaluation of suitable characteristic polynomials," *IEEE MTT-S International Microwave Symposium*, USA, 2006, pp. 111 – 114.

[23] J. Konpang, "A Compact Diplexer Using Square Open Loop with Stepped Impedance Resonators," in Proc. Radio and Wireless Symposium, USA, Jan. 2009, pp. 91-94.

[24] C. Chi-Feng, H. Ting-Yi, C. Chi-Ping, and W. Ruey-Beei, "Microstrip diplexers design with common resonator sections for compact size, but high isolation," *IEEE Transactions on Microwave Theory and Techniques*, vol. 54, no. 5, pp. 1945-1952, 2006.

[25] C. Collado, J. Pozo, J. Mateu, and J.M. O'Callaghan, "Compact duplexer with miniaturized dual loop resonator," in *Proc. European Microwave Conference*, Paris, France, Oct. 2005, pp. 109-111.

[26] T. Yang, P.L. Chi, and T. Itoh, "High Isolation and Compact Diplexer Using the Hybrid Resonators," IEEE *Microwave and Wireless Components letters*, vol. PP, no. 99, pp. 1-3, 2010.

[27] W. Xi, W. Qing-Yuan, Z. Yuan-Hong, and L. Hong, "Design of a Compact Diplexer," *IEEE MTT-S International Microwave Workshop Series on Art of Miniaturizing RF and Microwave Passive Components*, pp.170-172, Dec. 2008.

[28] C. Tomassoni, L. Marcaccioli, M. Dionigi, M. Mongiardo, R. Vincenti Gatti, and R. Sorrentino, "A Procedure for Computer-Aided Design of Compact Diplexers with Folded Filters," in *Proc. European Microwave Conference*, Amsterdam, The Netherlands, Oct. 2004, pp. 1233-1236.

[29] N. Marcuvitz, Waveguide Handbook. NewYork: Dover, 1965.

[30] I. Hunter, Theory and Design of Microwave Filters, the IEE, London, UK, 2001.

[31] A. B. Jayyousi and M. J. Lancaster, "A gradient-based optimization technique employing determinants for the synthesis of microwave coupled filters," *IEEE MTT-S International Microwave Symposium*, USA, 2004, pp 1369-1372.

Chapter 5

Implementation of Power Dividers and Diplexers

5.1 Introduction

In the previous Chapters, a design methodology of coupled resonator power dividers and diplexers has been presented with numerical examples. This Chapter exhibits design, realization and measurement of some components with bandpass Chebyshev filtering response: X-band 3-dB power divider, X-band unequal power divider, X-band 4-resonator diplexer, X-band 12-resonator diplexer, and E-band 12-resonator diplexer. The implementation of these devices has been done using waveguide cavity resonators that are suitable for low-cost mass fabrication. Also, they have advantages in microwave frequencies due to their high unloaded quality factors and their ability to handle large amounts of power.

The theory of rectangular waveguide cavities relevant to the design process of waveguide cavity components is first discussed in this chapter. The calculation of the unloaded quality factor and the frequencies of resonant modes of a rectangular cavity will be presented, as well as the effect of finite unloaded quality factors on the insertion loss of the filtering response. The extraction of coupling coefficients and external quality factors from physical structure will be discussed. Different coupling structures involving inductive/capacitive irises will be shown. Design, fabrication and measurement of the proposed devices will be discussed throughout this chapter.

5.2 Rectangular Cavity

A rectangular cavity may be considered as a section of a rectangular waveguide terminated at both sides with conducting plates. Figure 5.1 depicts a rectangular cavity of width *a*, height *b*, and length *d*.

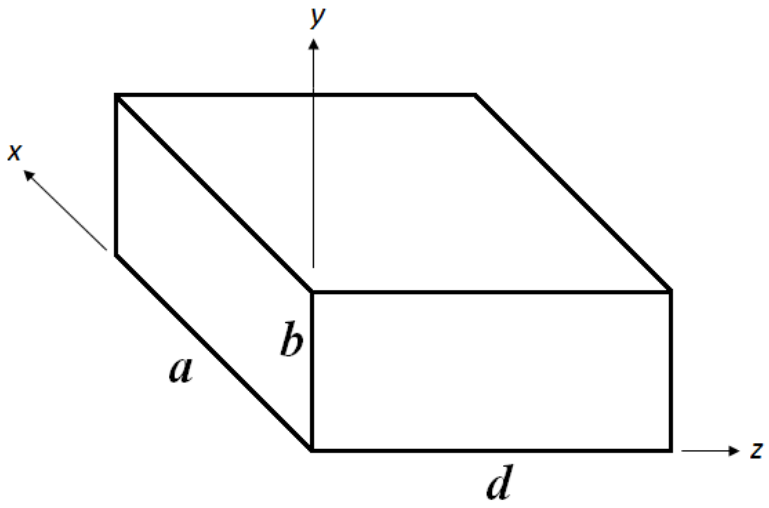

Figure 5.1: A Rectangular Cavity

For a rectangular waveguide, the transverse Electric fields (E_x,E_y) of the TE_{mn} or TM_{mn} mode can be written as [1],

$$\overline{E}_t(x,y,z) = \vec{e}(x,y)[A^+ e^{-j\beta_{mn}z} + A^- e^{j\beta_{mn}z}] \tag{5.1}$$

where $\vec{e}(x,y)$ represents the transverse variations in the *x* and *y* directions, A^+ and A^- are the arbitrary amplitudes of the travelling waves in the +*z* and –*z* directions. The propagation constant β_{mn} is given by

$$\beta_{mn} = \sqrt{k^2 - \left(\frac{m\pi}{a}\right)^2 - \left(\frac{n\pi}{b}\right)^2} \tag{5.2}$$

where $k = 2\pi f_0\sqrt{\mu\varepsilon}$, and μ and ε are the permeability and permittivity of the material filling the waveguide.

The boundary conditions of the waveguide cavity at z=(0,d) require that $\overline{E}(x,y,z)=0$. Applying the condition $\overline{E}_t=0$ at z=0 to equation (5.1) yields $A^+=-A^-$, and applying the condition $\overline{E}_t=0$ at z=d yields $\beta_{mn}d=l\pi$, where l=1,2,3… This means that the cavity length must be an integer multiple of a half-guide wavelength at the resonant frequency. The cut-off wavenumber of the rectangular cavity can be defined as

$$K_{mnl}=\sqrt{\left(\frac{m\pi}{a}\right)^2+\left(\frac{n\pi}{b}\right)^2+\left(\frac{l\pi}{d}\right)^2} \tag{5.3}$$

where the indices m,n,l correspond to the number of half wavelength variations in the x,y,z directions, respectively. The TE_{mnl} or the TM_{mnl} mode will have a resonant frequency,

$$f_{mnl}=\frac{ck_{mnl}}{2\pi\sqrt{\mu_r\varepsilon_r}}=\frac{c}{2\pi\sqrt{\mu_r\varepsilon_r}}\sqrt{\left(\frac{m\pi}{a}\right)^2+\left(\frac{n\pi}{b}\right)^2+\left(\frac{l\pi}{d}\right)^2} \tag{5.4}$$

where c is the velocity of light. If $b < a < d$, the mode with the lowest resonant frequency, known as the dominant mode, will be TE_{101} mode. The field configuration of the dominant TE_{101} mode is shown in figure 5.2, where the dashed lines represent the magnetic field, and the solid lines and the circles represent the electric field [2].

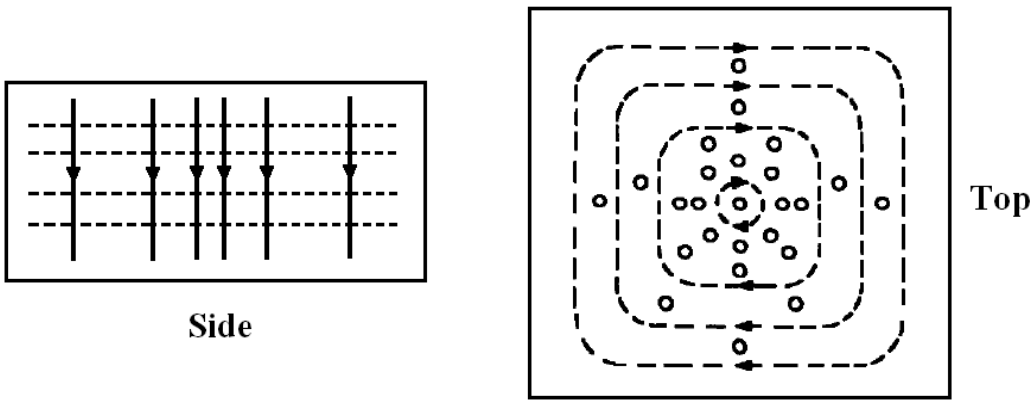

Figure 5.2: Field configuration of dominant TE_{101} mode

5.2.1 Unloaded quality factor

The unloaded quality factor Q_u is a figure of merit for a resonator. It describes the quality of the resonator in terms of losses and energy storage. For example, a high Q resonator implies low energy loss and good energy storage, whereas a low Q cavity implies higher losses. A general definition for the Q_u that applies to any type of resonator is [3],

$$Q_u = \omega \frac{\text{Time - average energy stored in the resonator}}{\text{Average power lost in the resonator}} \tag{5.5}$$

The losses in a resonator can generally be associated with the conductor, dielectric material, and radiation. The total Q_u may be defined by adding these losses together as follows [3],

$$\frac{1}{Q_u} = \frac{1}{Q_c} + \frac{1}{Q_d} + \frac{1}{Q_r} \tag{5.6}$$

where Q_c, Q_d and Q_r are the quality factors associated with losses from conductor and dielectric making up the cavity and radiation from the cavity. The loaded quality factor Q_L may be defined in terms of the unloaded quality factor Q_u and the external quality factor Q_e as follows [1],

$$\frac{1}{Q_L} = \frac{1}{Q_u} + \frac{1}{Q_e} \tag{5.7}$$

where Q_e is the quality factor associated with effective losses through the external coupling circuit, and it is defined as the ratio of the energy stored in the resonator to the energy coupled to the external circuit. The extraction of the external quality factor from the physical structure will be described in the next section.

Considering an air-filled waveguide cavity resonator, for the TE_{101} mode, the unloaded quality factor due to the losses in the conducting walls is given by [1],

$$Q_c = \frac{(k_{101}ad)^3 b\eta}{2\pi^2 R_s \left(2a^3b + 2bd^3 + a^3d + ad^3\right)} \tag{5.8}$$

where $\eta = \sqrt{\mu/\varepsilon}$ is the wave impedance, and R_s is the surface resistance of the conductive walls (with conductivity of σ), and it is calculated by [1]:

$$R_s = \sqrt{\frac{\omega\mu}{2\sigma}} \tag{5.9}$$

In coupled-resonator circuits with a filtering response, resonators with finite unloaded quality factors result in passband insertion loss. As the Q_u values of the resonators decrease, not only the passband insertion loss of the filtering response increases, but also the selectivity becomes worse. Hence, it is crucial for the designer to choose resonators with high Q_u values so that insertion loss specification is met. Generally, the insertion loss is proportional to the number of resonators, and inversely proportional to the fractional bandwidth FBW of the bandpass filter. The increase in (dB) in insertion loss ΔIL at the centre frequency of the filtering response is given by [3],

$$\Delta IL = 4.343 \sum_{i=1}^{n} \frac{\Omega_c}{FBW.Q_{ui}} g_i \quad dB \tag{5.10}$$

where Ω_c is the lowpass cut-off frequency, and g_i represents the lowpass prototype element value of resonator i, as in equation (1.3).

5.3 Coupling in Physical Terms

After determining the normalised coupling matrix [m] for a coupled resonator topology, the actual coupling matrix [M] of a coupled resonator device with given specification can be calculated by prototype de-normalisation of the matrix [m] at a desired bandwidth and a centre frequency, as follows,

$$M_{i,j} = m_{i,j} \cdot FBW \tag{5.11}$$

where FBW is the fractional bandwidth. The actual external quality factor Q_e is related to the normalised quality factor q_e by,

$$Q_e = \frac{q_e}{FBW} \tag{5.12}$$

The next step is to construct a structure of coupled resonators and implement the required coupling coefficients of the matrix [*M*] physically. The extraction of the coupling coefficient M_{ij} of two coupled resonators and the external quality factor Q_e from the physical structure is presented in the next subsections.

5.3.1 Extraction of coupling coefficient from physical structure

In coupled resonator circuits, the coupling coefficient for a selected resonator pair can be obtained from the physical structure using EM simulation. To extract the coupling coefficient of two asynchronously coupled resonators, a general formula that applies to any type of resonators is used [4],

$$M = \pm\frac{1}{2}\left(\frac{\omega_{02}}{\omega_{01}} + \frac{\omega_{01}}{\omega_{02}}\right)\times\sqrt{\left(\frac{\omega_2^2 - \omega_1^2}{\omega_2^2 + \omega_1^2}\right)^2 - \left(\frac{\omega_{02}^2 - \omega_{01}^2}{\omega_{02}^2 + \omega_{01}^2}\right)^2} \tag{5.13}$$

where ω_{01} and ω_{02} are the resonant frequencies of the two coupled resonators, ω_1 and ω_2 are the lower and higher frequencies in the magnitude of S_{21} response of the two coupled resonator structure with the ports are very weakly coupled to the resonators. The characteristic parameters ω_{01}, ω_{02}, ω_1 and ω_2 can be determined using full-wave EM simulations. Figure 5.3 shows an example of a structure of two inductively coupled waveguide cavities that are weakly coupled to the ports, and figure 5.4 depicts the simulated $|S_{21}|$ response showing the frequency peaks ω_1 and ω_2.

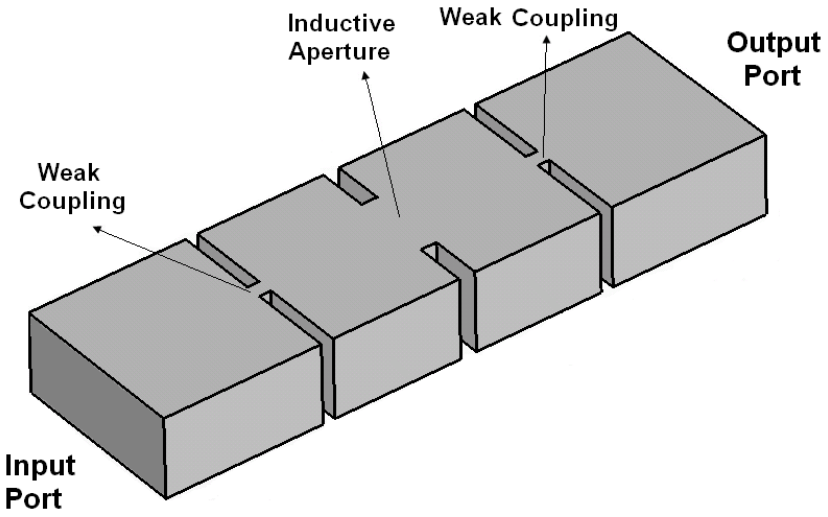

Figure 5.3: Two inductively coupled waveguide cavity resonators

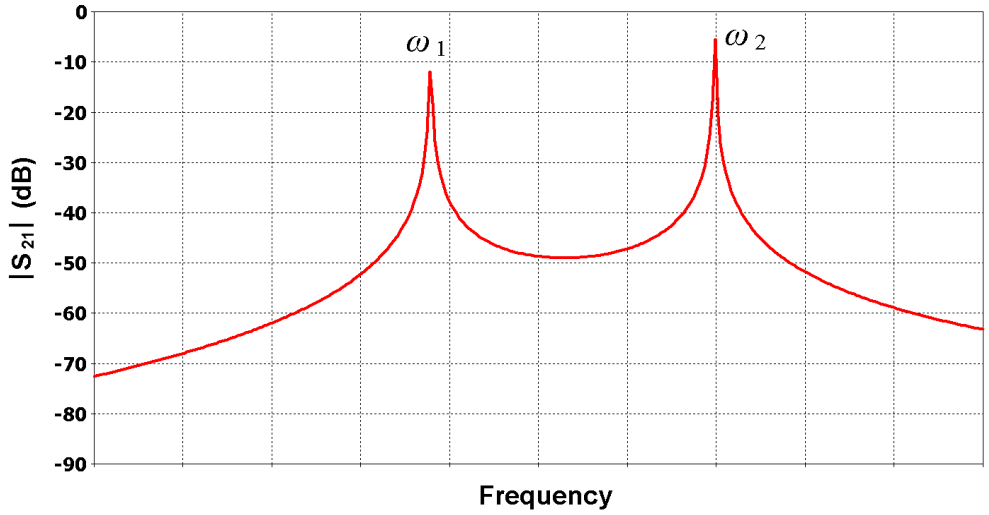

Figure 5.4: $|S_{21}|$ of two coupled resonators showing two frequency peaks.

The formula in equation (5.13) is applicable for synchronously coupled resonators, and in this case it is simplified to [4],

$$M = \pm \frac{\omega_2^2 - \omega_1^2}{\omega_2^2 + \omega_1^2} \tag{5.14}$$

The coupling coefficient usually corresponds to a magnetic coupling or an electric coupling. These two types of coupling exhibit opposite signs for the coupling coefficient.

The self-coupling coefficient M_{ii} in the principal diagonal in the coupling matrix [M] that accounts for asynchronous tuning is related to the self-resonant frequency of resonator i by,

$$M_{ii} = 2 \times \left(\frac{\omega_{0i}^2 - \omega_0^2}{\omega_{0i}^2 + \omega_0^2} \right) \tag{5.15}$$

where ω_0 is the desired centre frequency of the coupled-resonator device and ω_{0i} is the resonant frequency of resonator i.

5.3.2 Extraction of external quality factor from physical structure

The external quality factor of a single resonator can be found by simulating $|S_{21}|$ response with one port weakly coupled. Figure 5.5 shows an example of a waveguide cavity that is externally coupled to the output port via inductive iris, and weakly coupled to the input port. The external quality factor Q_e can then be calculated from the simulated $|S_{21}|$ response using the following formula [3],

$$Q_e = \frac{\omega_0}{\Delta\omega_{\pm 3dB}} \tag{5.16}$$

where ω_0 is the resonant frequency of the loaded resonator and $\Delta\omega_{\pm 3dB}$ is the 3 dB bandwidth, as shown in figure 5.6.

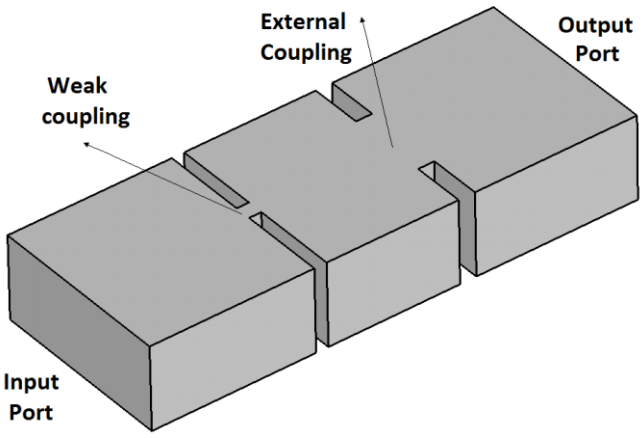

Figure 5.5: Externally coupled waveguide cavity resonator

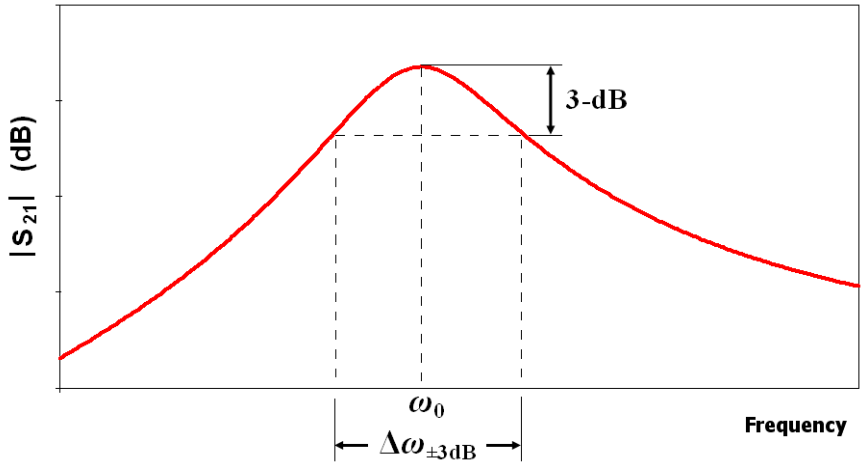

Figure 5.6: Response of $|S_{21}|$ for loaded resonator.

5.4 Implementation of Power dividers and Diplexers

Coupled resonator power dividers and diplexers have been implemented using waveguide cavity resonators. The first step in the design of these components is to synthesize a lowpass prototype by determining an appropriate coupling matrix using optimization, as presented in the previous Chapters. The next step is to construct a structure of cavity resonators coupled together by inductive or capacitive irises or both, depending on the required response. The cavities used in all the devices presented in this work operate in the fundamental mode, the TE_{101} mode, in which its resonant frequency can be calculated from equation (5.4). Figure 5.7 shows different coupling structures for two waveguide cavities coupled together using capacitive or inductive irises. Half wavelength cavities that resonate at the fundamental TE_{101} mode are commonly used in rectangular waveguide filters. In cross-coupled filters, where the coupling matrix contains positive and negative coupling coefficients, inductive irises may be employed to implement the positive couplings, and capacitive irises may be used to implement negative couplings. This has been reported in literature to produce an elliptic/quasi-elliptic filtering response [5-7]. Elliptic function responses have also been realised by waveguide cavity structures that exclusively exhibit inductive iris couplings as

reported in [8]. This has been achieved by using configurations combining TE_{101} cavities with higher order mode (overmoded) cavities. The overmoded cavities also provide higher unloaded quality factors in comparison to the TE_{101} mode cavities which may result to improvement in the insertion loss of the filtering response [9].

The initial dimensions of the coupling irises can be determined for the required coupling coefficients by following the procedure explained in section 5.3.

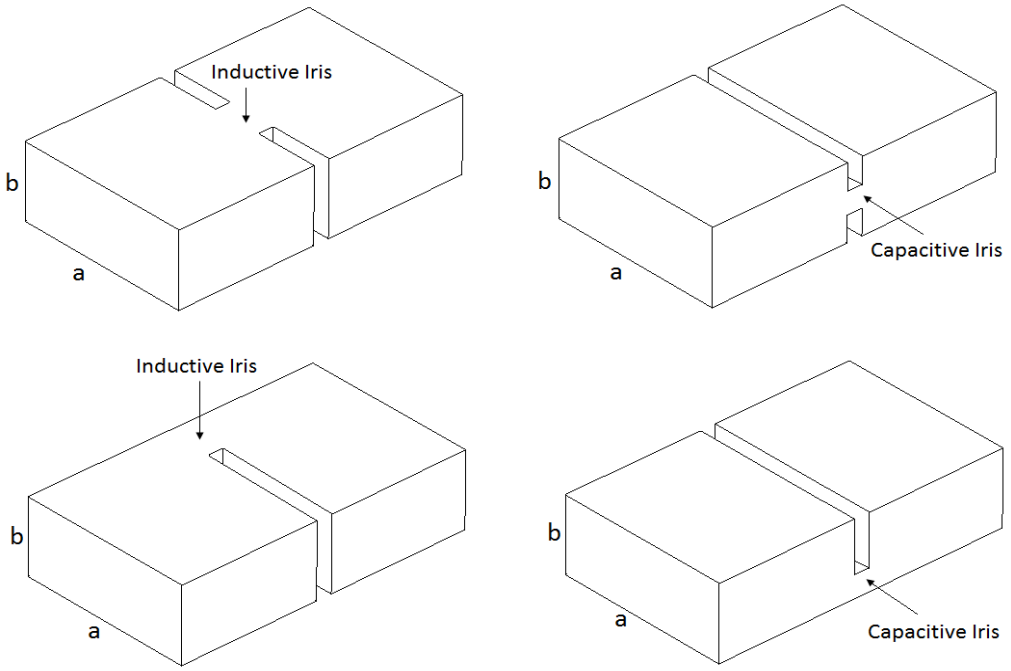

Figure 5.7: Different coupling structures for inductive and capacitive irises

Once the initial geometries of the structure are known, a full-wave EM simulator such as CST [10] is then used to obtain the optimum dimensions of the structure to meet the target response.

H-plane and E-plane power dividers and H-plane diplexers have been implemented in the X-band frequency range to verify the proposed design methodology presented in Chapters 3 and 4, and also an E-band diplexer has been designed for the use in a wireless point-to-point communications system. The X-band devices have been made of copper, with two mirror-

image blocks joined together using screws. Tuning screws have been used to compensate for the degradation of performance resulted from manufacturing errors, and the cavity rounded-corners cased by the finite radius of the milling tool. Metal screws have been used to finely tune both the resonant frequencies of the cavity resonators, as well as the coupling coefficients and external quality factors. The tuning screws are located at the centres of the cavities where the electric field is maximum and the current density is minimum.

5.4.1 X-band 3-dB power divider

5.4.1.1 Power divider design

A 4 resonator 3-dB power divider has been designed, fabricated and tested. The divider has been designed according to the coupled-resonator design methodology proposed in Chapter 3. It is designed at the X-band with a centre frequency of 10 GHz, bandwidth of 570 MHz, and reflection loss of 20 dB at the passband. The divider topology and the synthesized normalized coupling matrix are shown in figure 5.8, and the prototype response of the power divider is shown in figure 5.9. The input and output external quality factors and the coupling coefficients are computed for FBW=5.7% and found to be M_{12}= 0.0590, M_{23}=M_{24}= 0.0417, and Q_e=14.94. The divider has been implemented using waveguide cavity resonators, and its 3D structure is shown in figure 5.10.

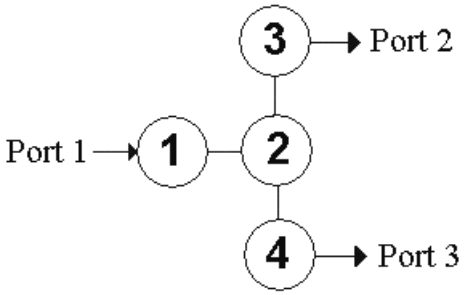

$$\begin{bmatrix} 0 & 1.0356 & 0 & 0 \\ 1.0356 & 0 & 0.7323 & 0.7323 \\ 0 & 0.7323 & 0 & 0 \\ 0 & 0.7323 & 0 & 0 \end{bmatrix}$$

$q_e = 0.8516$

(b)

Figure 5.8: 3-dB power divider (a) Divider topology, (b) Normalized coupling matrix

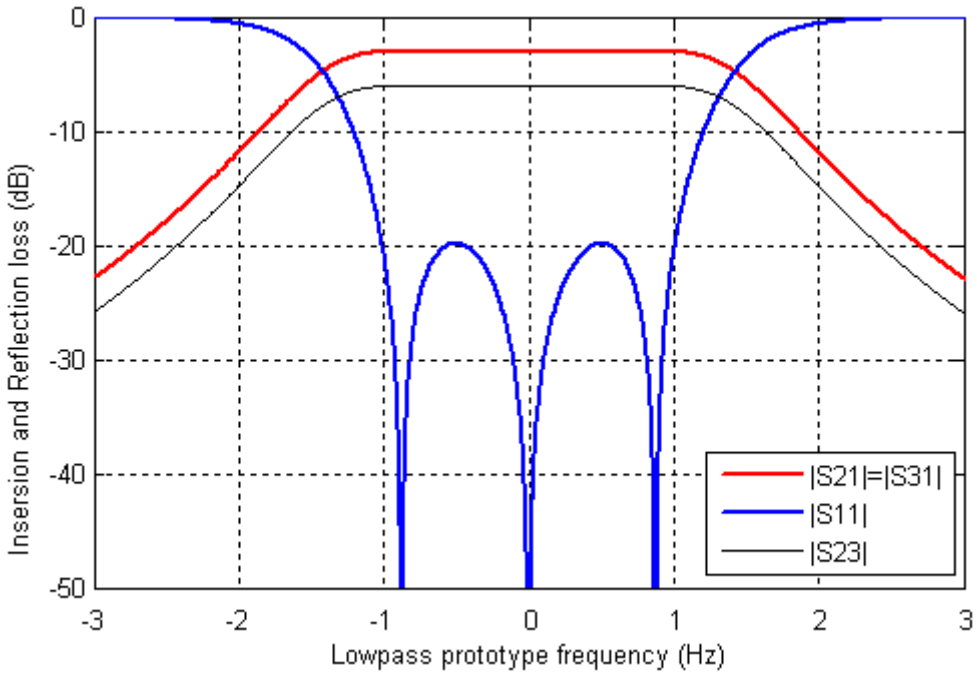

Figure 5.9: Prototype response of power divider

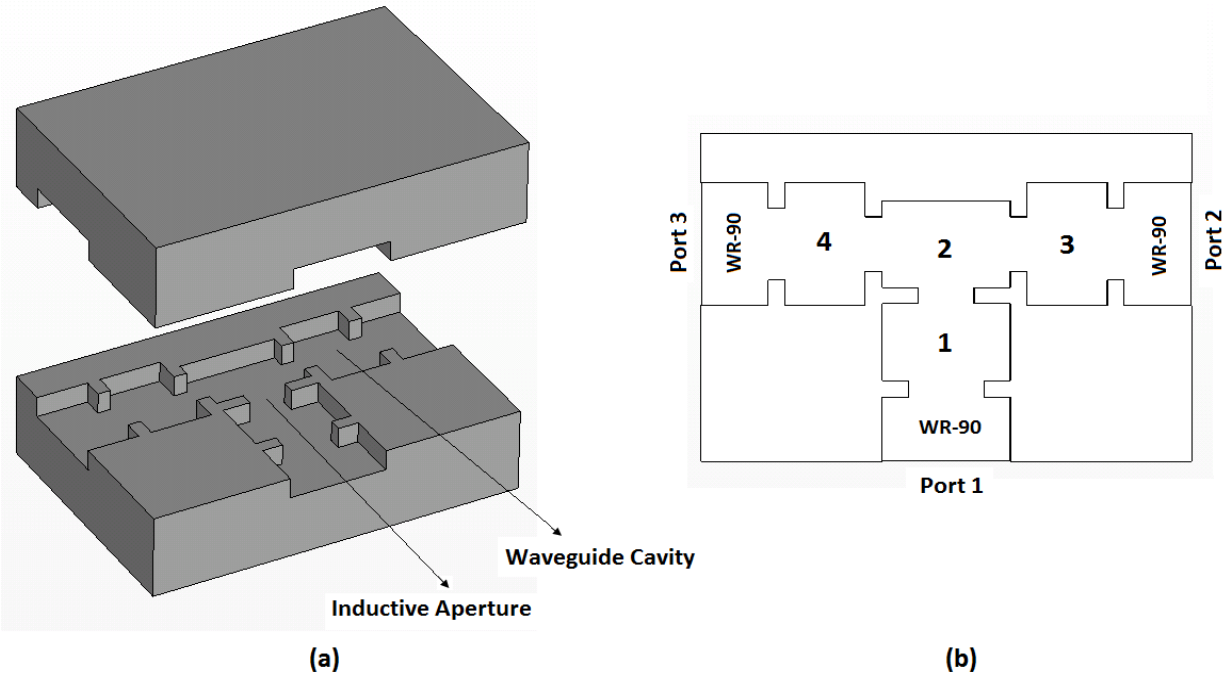

Figure 5.10: (a) 3-dB Power divider 3D structure, (b) Top View

CST has been utilised to find the initial dimensions of the cavities and the coupling irises. Each pair of coupled resonators has been simulated separately to find the dimensions of the coupling iris corresponding to the required coupling coefficient by following the procedure in section 5.3.1. The dimensions of coupling irises corresponding to external quality factors have been found from EM simulation by following the procedure in section 5.3.2. The whole structure of the power divider is initially designed with the obtained initial values, and the CST simulation response of the initial structure is depicted in figure 5.11. Starting from the initial response, the power divider has been tuned using CST frequency domain solver to satisfy the required specifications. The lengths of the cavity resonators and the widths of the coupling irises have been tuned to arrive to the final simulated response given in figure 5.11.

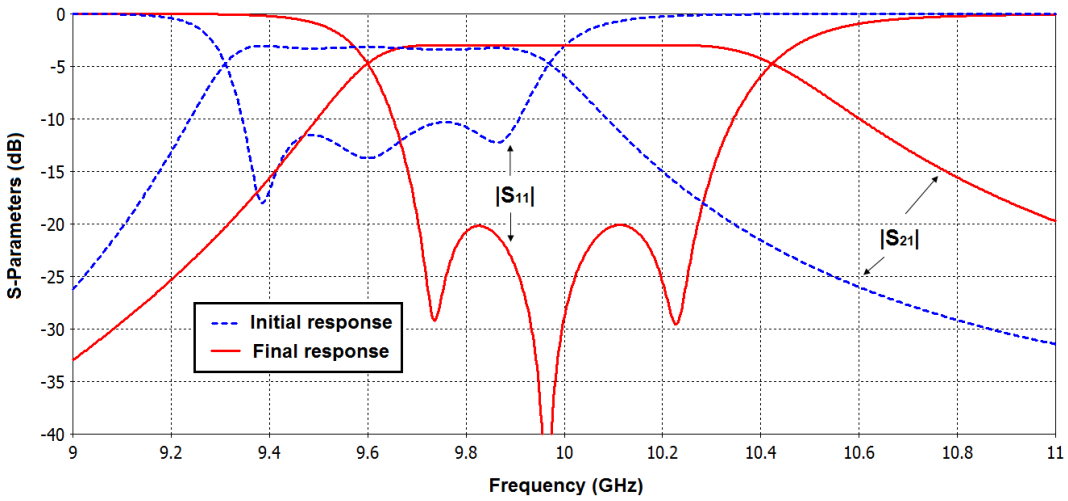

Figure 5.11: Simulated initial and final response of power divider

5.4.1.2 Fabrication and measurement

The power divider has been implemented using waveguide cavity resonators coupled together using inductive apertures. A photograph of the divider is shown in figure 5.12. A 2 mm radius milling tool has been used in manufacturing and this resulted in forming round corners in the rectangular waveguide cavities. However, the effect of these corners on the performance is small. The device has been made of two mirror-image pieces of copper; the top piece has

extra threaded holes for tuning screws. Metal screws of 1.6 mm diameter have been used to tune both the resonant frequencies of the cavity resonators and the internal and external coupling coefficients. The screws are located at the centres of the cavity resonators and the apertures.

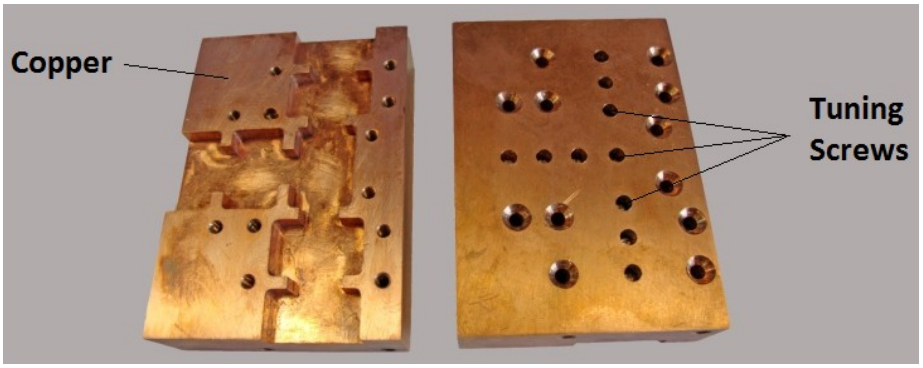

Figure 5.12: Photograph of the 3-dB power divider

A cross sectional view of the power divider with parameters for the dimensions of cavities and coupling irises is shown in figure 5.13. The dimensions of cavities and irises of both copper pieces forming the device have been measured using a microscope, and they are shown in table 5.1 along with design values. The measured dimensions show that the maximum fabrication error is around 416 μm. The device has been measured firstly without tuning, and the response exhibited a return loss of around 15 dB, and then it has been tuned using the metal screws. The simulated and measured results of the power divider are depicted in figure 5.14 for $|S_{11}|$, $|S_{21}|$ and $|S_{31}|$ and in figure 5.15 for the isolation $|S_{23}|$. The measured response is in good agreement with the simulated response. The experimental results show that the maximum return loss within the passband is 20 dB and the minimum insertion loss is 3.3 dB. The bandwidth of the measured response is slightly narrower than the simulated response. This might have been caused since the irises in the fabricated device are smaller than the design, as indicated in table 5.1. The measurements also show that the isolation $|S_{23}|$ within the passband is around 6 dB.

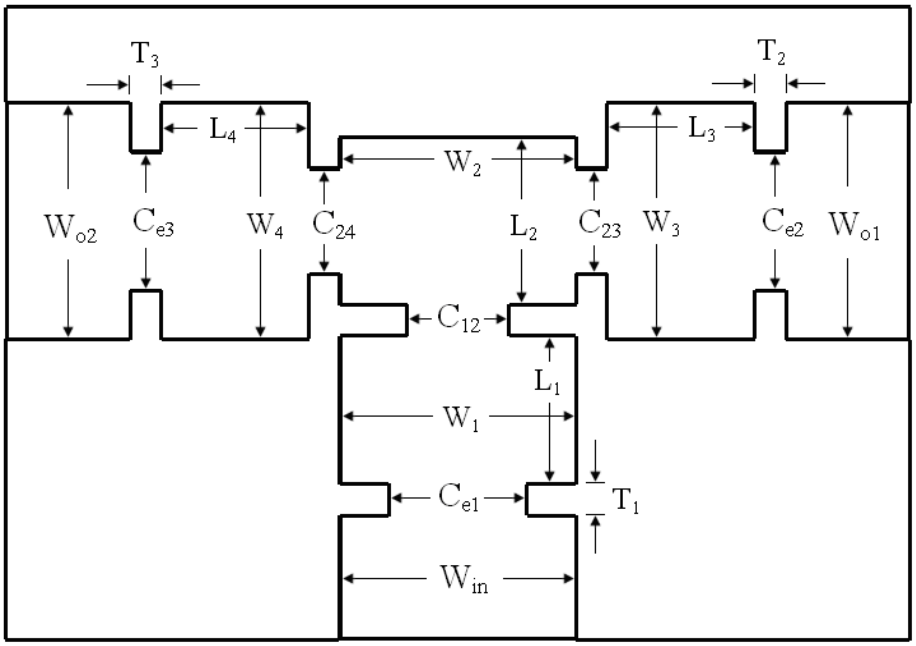

Figure 5.13: Cross sectional top view of the power divider

Table 5.1: Power divider dimensions corresponding to the parameters in figure 5.13

Parameter	Design (mm)	Top block (mm)	Bottom block (mm)
W_1	22.860	22.822	22.812
W_2	22.860	22.807	22.805
W_3	22.860	22.803	22.807
W_4	22.860	22.803	22.822
W_{in}	22.860	22.816	22.828
W_{o1}	22.860	22.810	22.823
W_{o2}	22.860	22.818	22.829
L_1	14.315	14.267	14.261
L_2	16.158	16.112	16.127
L_3	14.331	14.299	14.305
L_4	14.331	14.332	14.303
C_{12}	9.944	9.920	9.911
C_{23}	10.124	10.077	10.084
C_{24}	10.124	10.074	10.080
C_{e1}	13.384	13.335	13.357
C_{e2}	13.384	12.968	12.977
C_{e3}	13.384	12.991	12.984
T_1	3	3.034	3.041
T_2	3	3.005	3.005
T_3	3	3.019	3.008

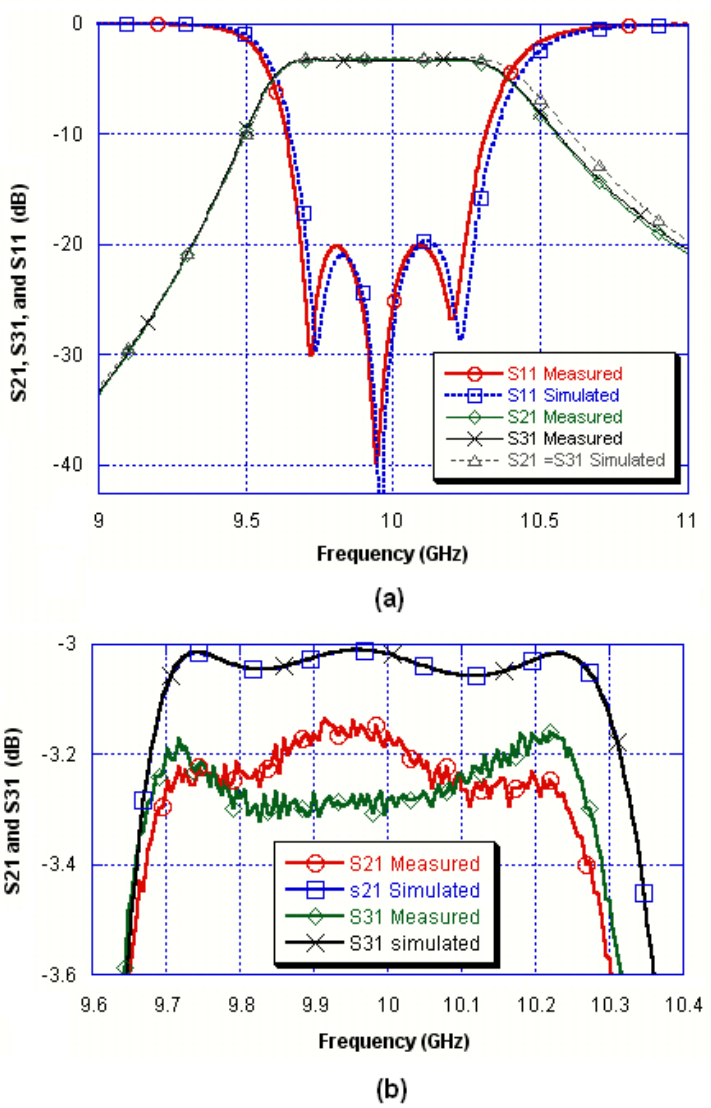

Figure 5.14: (a) Measured and simulated results of the power divider, (b) passband details

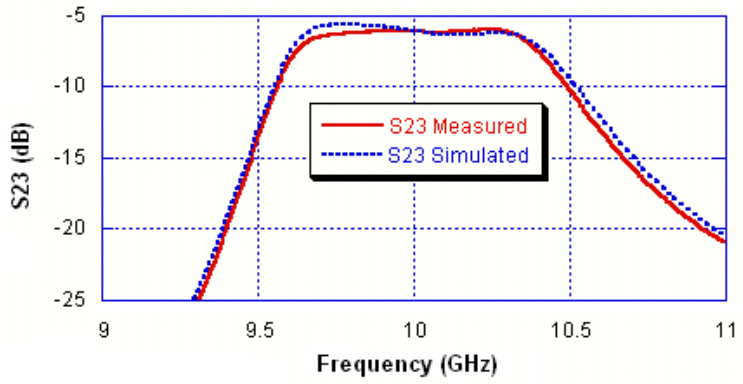

Figure 5.15: Measured and simulated $|S_{23}|$

5.4.2 X-band unequal power divider

5.4.2.1 Power divider design

A 5 resonator unequal power divider has been designed, fabricated and tested. The divider has been designed according to the coupled-resonator design procedure presented in Chapter 3. It is designed at the X-band with a centre frequency of 10.15 GHz, bandwidth of 925 MHz, a reflection loss of 20 dB at the passband, and α=1.5. The divider topology and the normalized optimized coupling matrix are shown in figure 5.16, and the prototype response of the divider is shown in figure 5.17. The 3D structure of the unequal power divider is shown in figure 5.18.

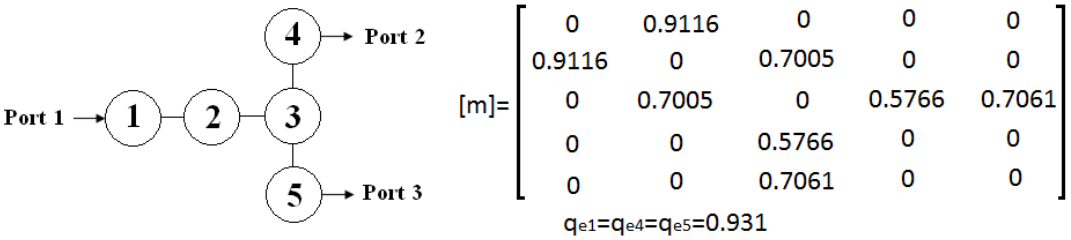

Figure 5.16: Unequal power divider topology and normalized coupling matrix

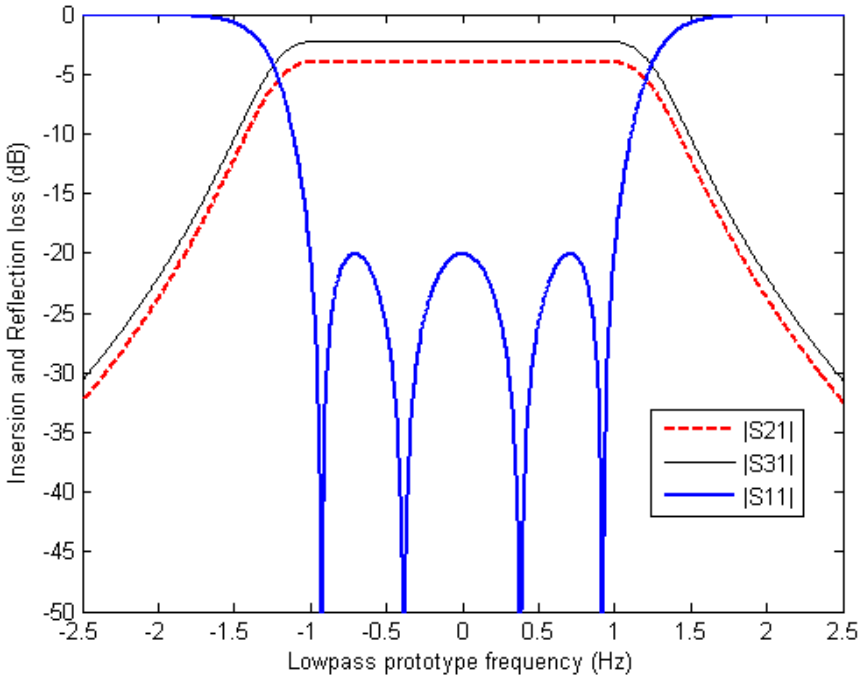

Figure 5.17: Prototype response of unequal power divider

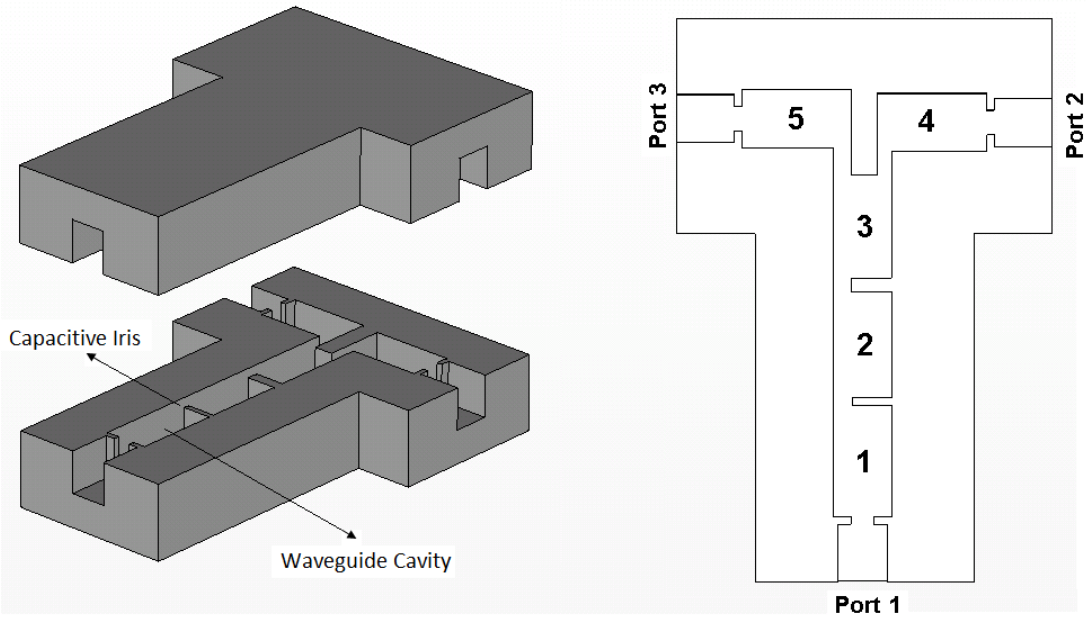

Figure 5.18: (a) Unequal Power divider 3D structure, (b) Top View

5.4.2.2 Fabrication and measurement

The power divider has been implemented using waveguide cavity resonators coupled together using capacitive irises. A photograph of the divider is shown in figure 5.19. The device has been made of two mirror image pieces of copper, and metal screws of 1.6 mm diameter have been used to tune its response.

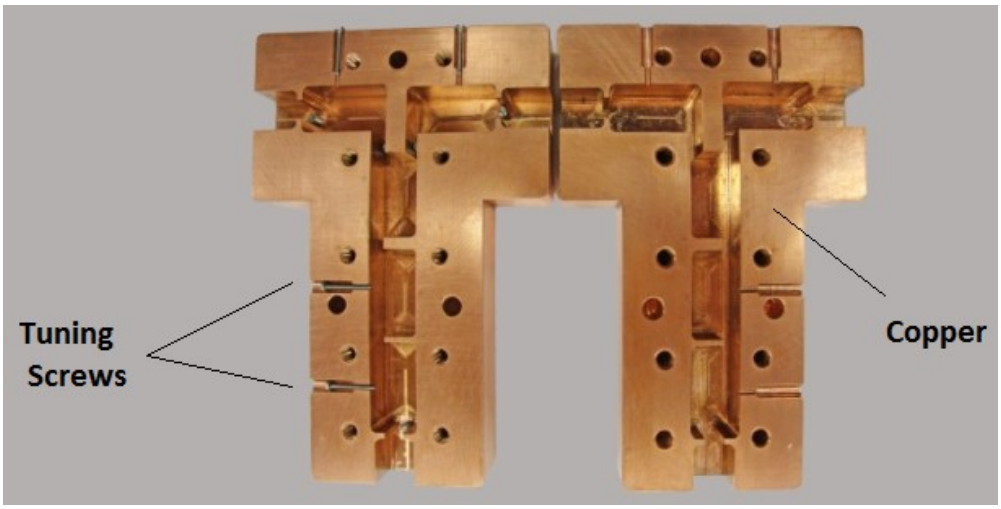

Figure 5.19: Photograph of the unequal power divider

The simulated and measured results of the power divider are depicted in figure 5.20. The measured response has been tuned using metal screws and it is in good agreement with the simulated response. The experimental results show that the maximum return loss within the passband is 20 dB and the minimum insertion loss is 2.28 dB for $|S_{31}|$ and 4.29 dB for $|S_{21}|$. The measured isolation between the output ports is more than 4.4 dB in the passband.

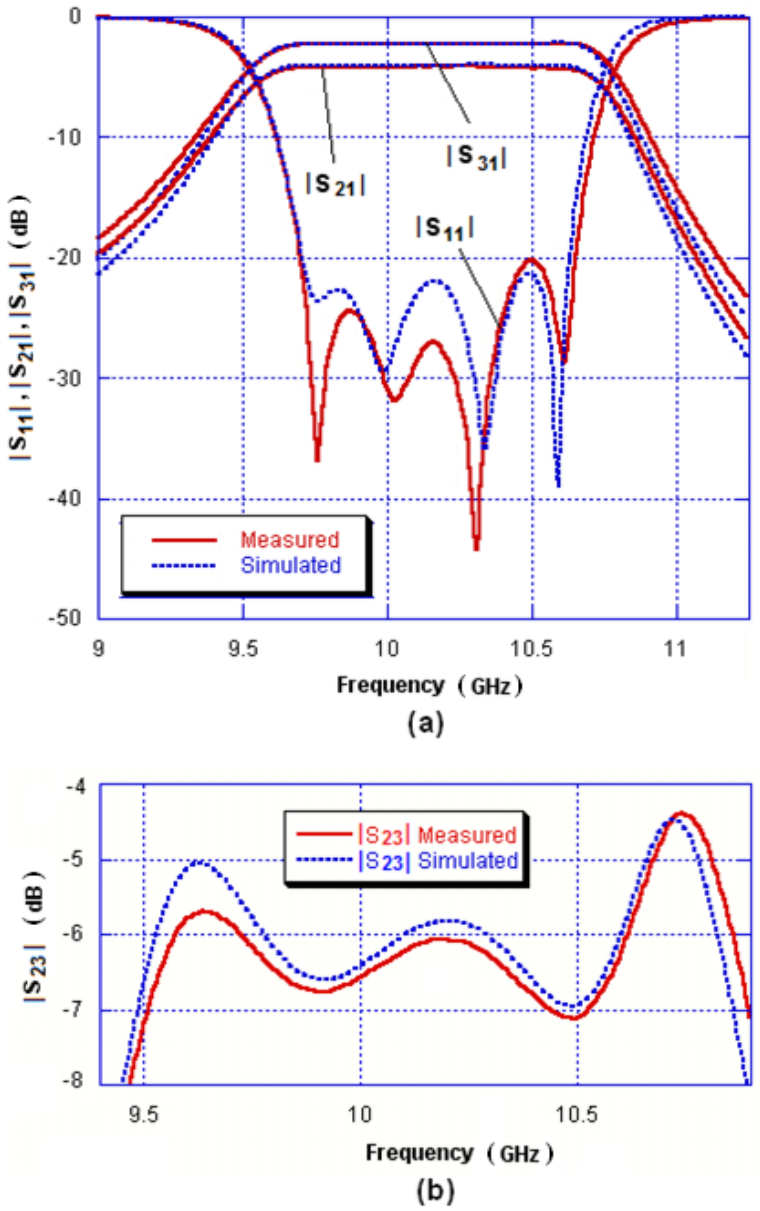

Figure 5.20: (a) Measured and simulated results of the divider, (b) Isolation

5.4.3 X-band 4-resonator diplexer

5.4.3.1 Diplexer design

A simple X-band non-contiguous diplexer has been designed using the new methodology presented in Chapter 4 and has been implemented using waveguide cavity resonators. The following specifications have been selected to implement the diplexer: passband centre frequency of 9.5 GHz for channel 1 and 10.5 GHz passband centre frequency for channel 2, bandwidth of each channel is 52 MHz, and desired return loss at the passband of each channel is 20 dB.

The diplexer topology is the same as the power divider T-topology in figure 5.8(a). The optimized normalized coupling matrix is shown below and the prototype response of the diplexer is shown in figure 5.21.

$$M = \begin{bmatrix} 0 & 1.3044 & 0 & 0 \\ 1.3044 & 0 & 0.1666 & 0.1666 \\ 0 & 0.1666 & 1.2894 & 0 \\ 0 & 0.1666 & 0 & -1.2894 \end{bmatrix}$$

$$q_{e1} = 4.651, \quad q_{e3} = q_{e4} = 9.302$$

The coupling matrix of the diplexer is computed by multiplying the normalized coupling coefficients by (FBW/Ω_c), where FBW is the fractional bandwidth and Ω_c is the low-pass prototype cut-off frequency. The coupling coefficients and the external quality factors are computed for FBW=10.52% and Ω_c=1.3711 and found to be M_{12}= 0.1, M_{23}=M_{24}=0.0128, M_{33}= -M_{44}=0.0989, Q_{e1}=60.62 and Q_{e3}= Q_{e4}=121.24. The 3D structure of the diplexer is shown in figure 5.22.

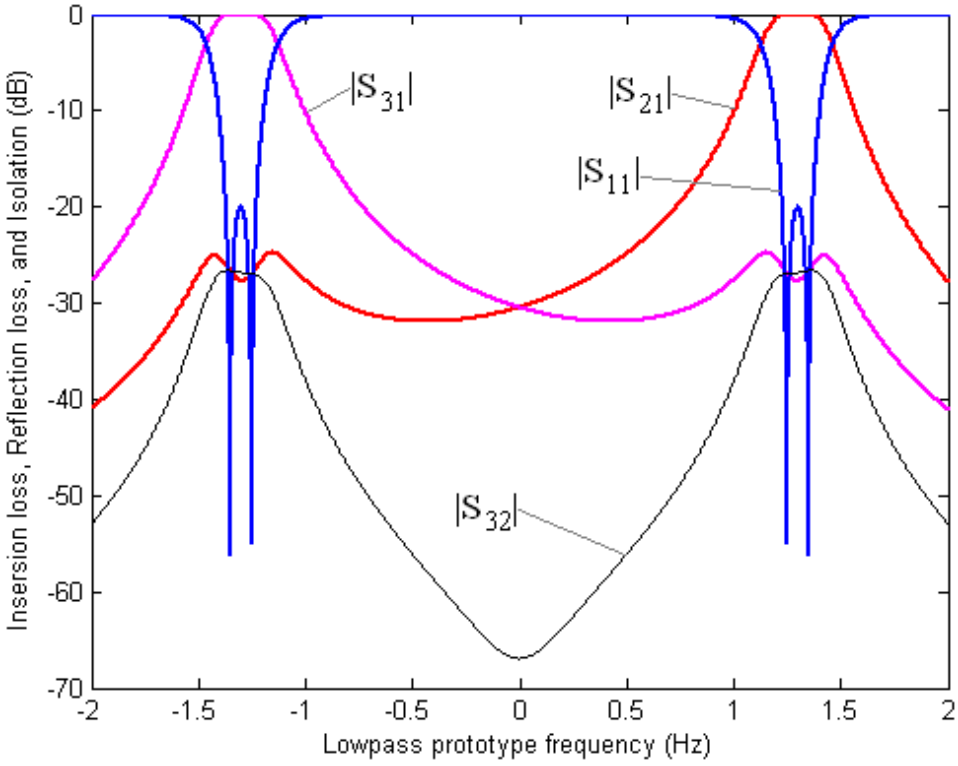

Figure 5.21: Prototype response of diplexer

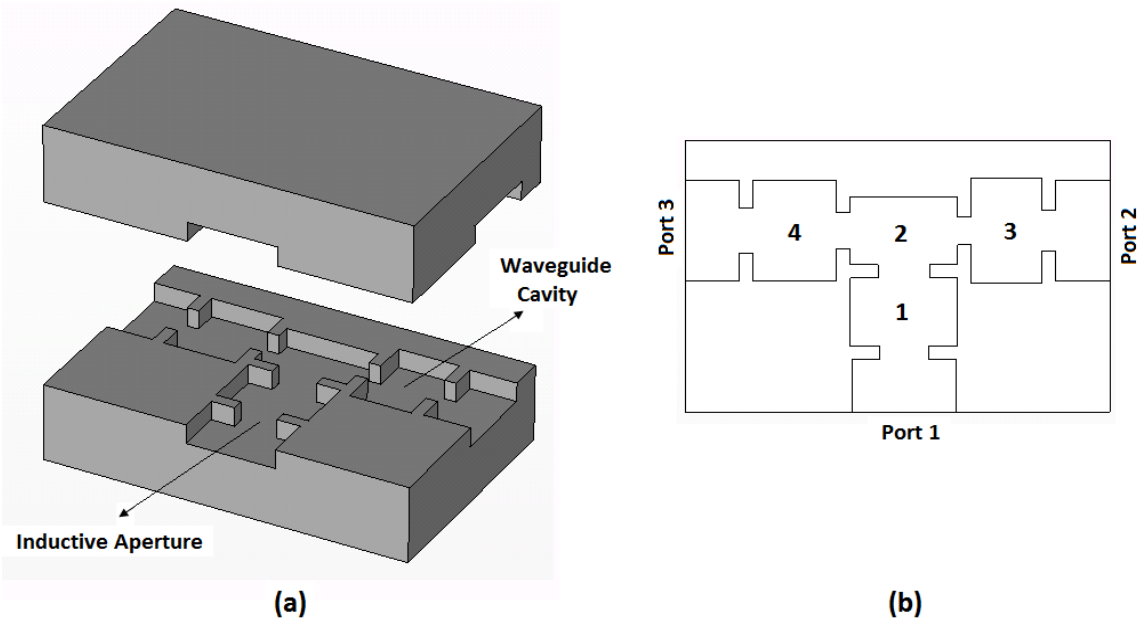

Figure 5.22: (a) Diplexer 3D structure, (b) Top View

5.4.3.2 Fabrication and measurement

The diplexer has been implemented using waveguide cavity resonators. A photograph of the physical diplexer is shown in figure 5.23. It consists of two pieces of copper and metal screws similar to those used in the power divider. The metal screws are used to tune both the resonant frequencies of the cavities and the coupling coefficients.

The simulated (CST) and measured results of the diplexer are depicted in figure 5.24. The tuned measured response is in very good agreement with the simulated response. The measurements show that the passband of channel 1 has maximum return loss of 22 dB and minimum insertion loss of 0.38 dB, and that the passband of channel 2 has maximum return loss of 22 dB and minimum insertion loss of 0.43 dB.

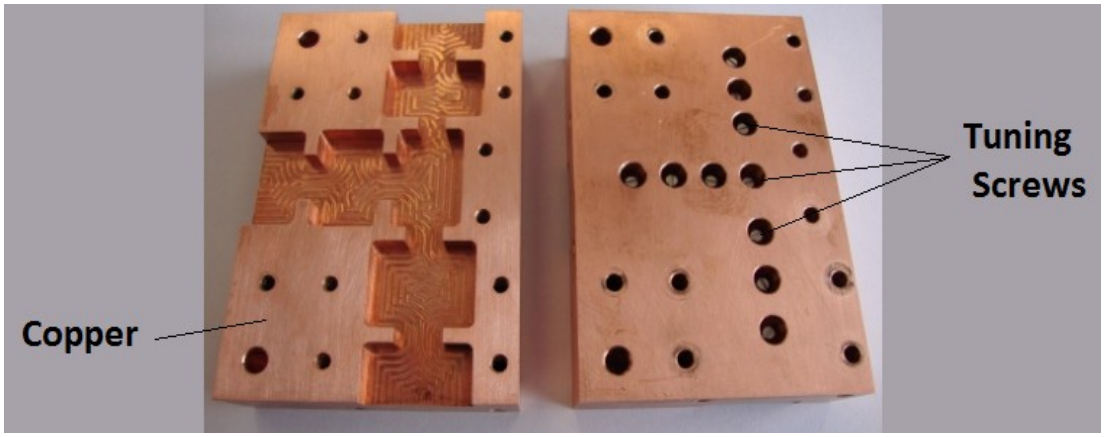

Figure 5.23: Photograph of the diplexer

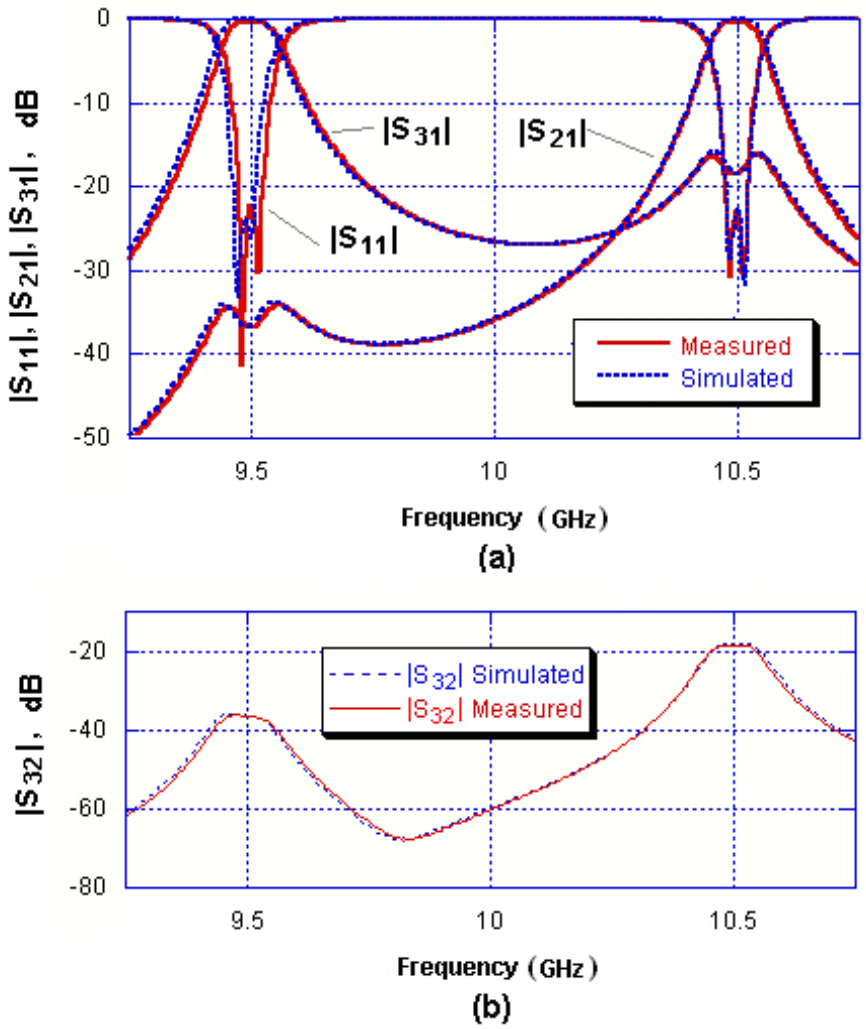

Figure 5.24: (a) Measured and simulated results of the diplexer, (b) Diplexer isolation

5.4.4 X-band 12-resonator diplexer

5.4.4.1 Diplexer design

An X-band 12-resonator non-contiguous diplexer has been designed and implemented using waveguide cavity resonators. The diplexer has passband centre frequency of 10 GHz for channel 1 and 11.35 GHz for channel 2, and a desired return loss at the passband of each channel of 20 dB. The diplexer topology is shown in figure 5.25, and the optimized normalized coupling matrix is shown in table 5.2.

The normalized external quality factors are q_{e1}=1.4903, q_{e7}= q_{e12}=2.9806, and the diplexer coupling matrix [*M*] has been computed from the normalized matrix [*m*] for a fractional bandwidth of FBW=18%. The prototype response of the diplexer is shown in figure 5.26, and the 3D structure of the diplexer is shown in figure 5.27. The diplexer has been designed with waveguide cavity resonators coupled together using inductive irises, and its structure is folded for miniaturization.

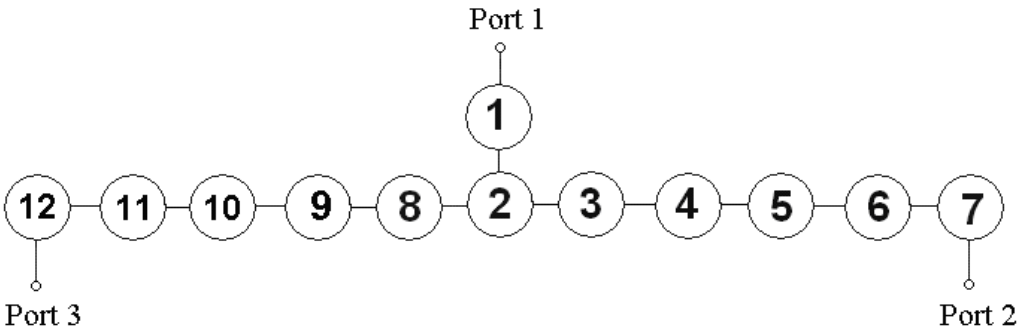

Figure 5.25: Diplexer topology

Table 5.2: Normalized coupling matrix of 12-resonator diplexer

	1	2	3	4	5	6	7	8	9	10	11	12
1	0	0.7963	0	0	0	0	0	0	0	0	0	0
2	0.7963	0	0.3466	0	0	0	0	0.3466	0	0	0	0
3	0	0.3466	0.5942	0.2101	0	0	0	0	0	0	0	0
4	0	0	0.2101	0.6552	0.1956	0	0	0	0	0	0	0
5	0	0	0	0.1956	0.6635	0.2035	0	0	0	0	0	0
6	0	0	0	0	0.2035	0.6652	0.2814	0	0	0	0	0
7	0	0	0	0	0	0.2814	0.6643	0	0	0	0	0
8	0	0.3466	0	0	0	0	0	-0.5942	0.2101	0	0	0
9	0	0	0	0	0	0	0	0.2101	-0.6552	0.1956	0	0
10	0	0	0	0	0	0	0	0	0.1956	-0.6635	0.2035	0
11	0	0	0	0	0	0	0	0	0	0.2035	-0.6652	0.2814
12	0	0	0	0	0	0	0	0	0	0	0.2814	-0.6643

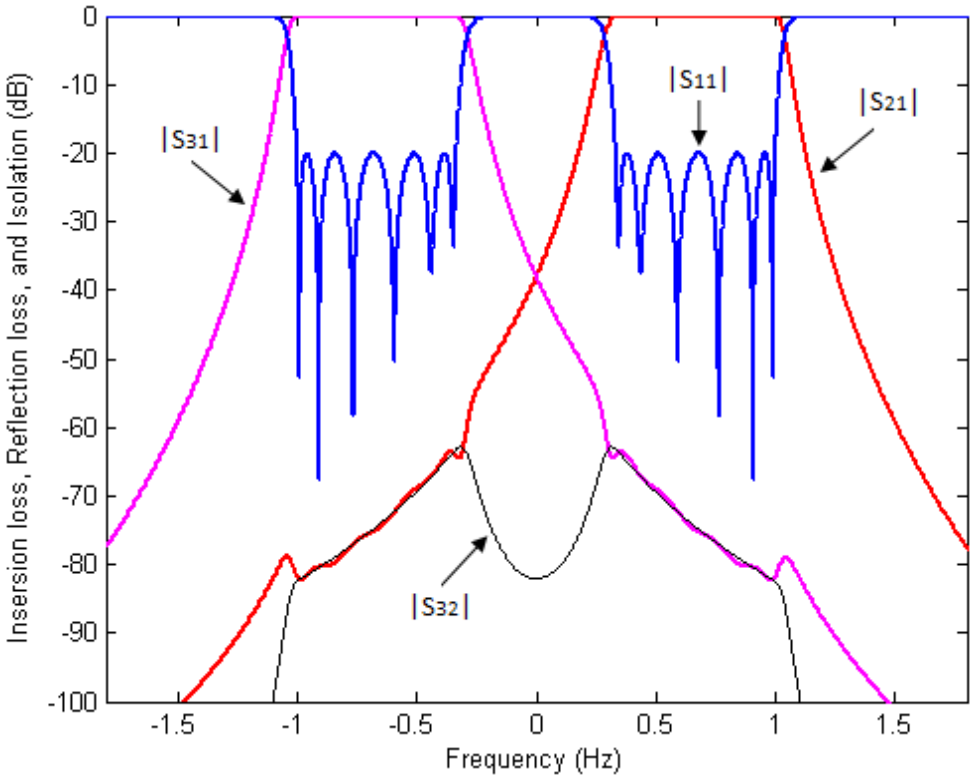

Figure 5.26: Diplexer prototype response

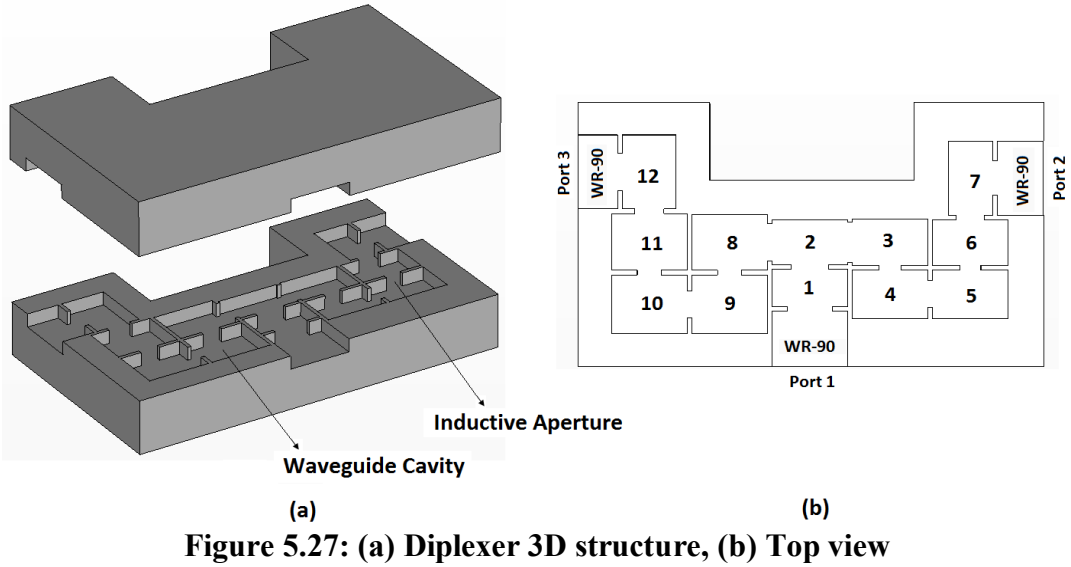

Figure 5.27: (a) Diplexer 3D structure, (b) Top view

5.4.4.2 Fabrication and measurement

The diplexer has been implemented of two mirror-image pieces of copper, and a photograph of the physical structure of the diplexer is shown in figure 5.28. Metal screws have been used to tune both the resonant frequencies of the cavities and the coupling coefficients.

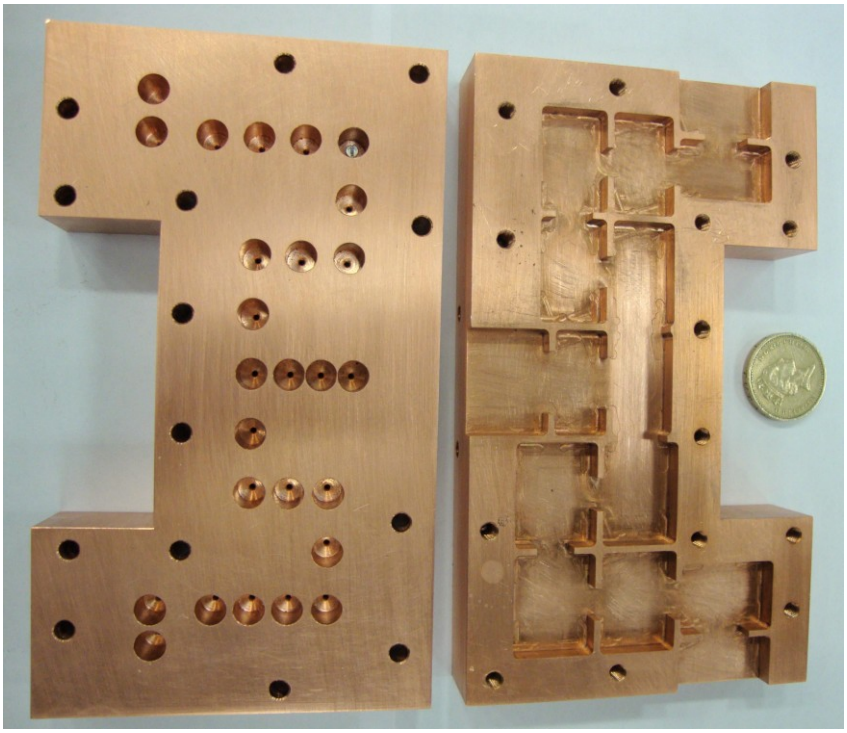

Figure 5.28: Photograph of the 12-resonator diplexer

The simulated and measured results of the diplexer are depicted in figures 5.29 and 5.30. The tuned measured response is in very good agreement with the simulated response. The measurements show that the passband of channel 1 has maximum return loss of ~18 dB and minimum insertion loss of 0.42 dB, and that the passband of channel 2 has maximum return loss of 22 dB and minimum insertion loss of 0.4 dB. The measured isolation within the passbands is 64 dB or better.

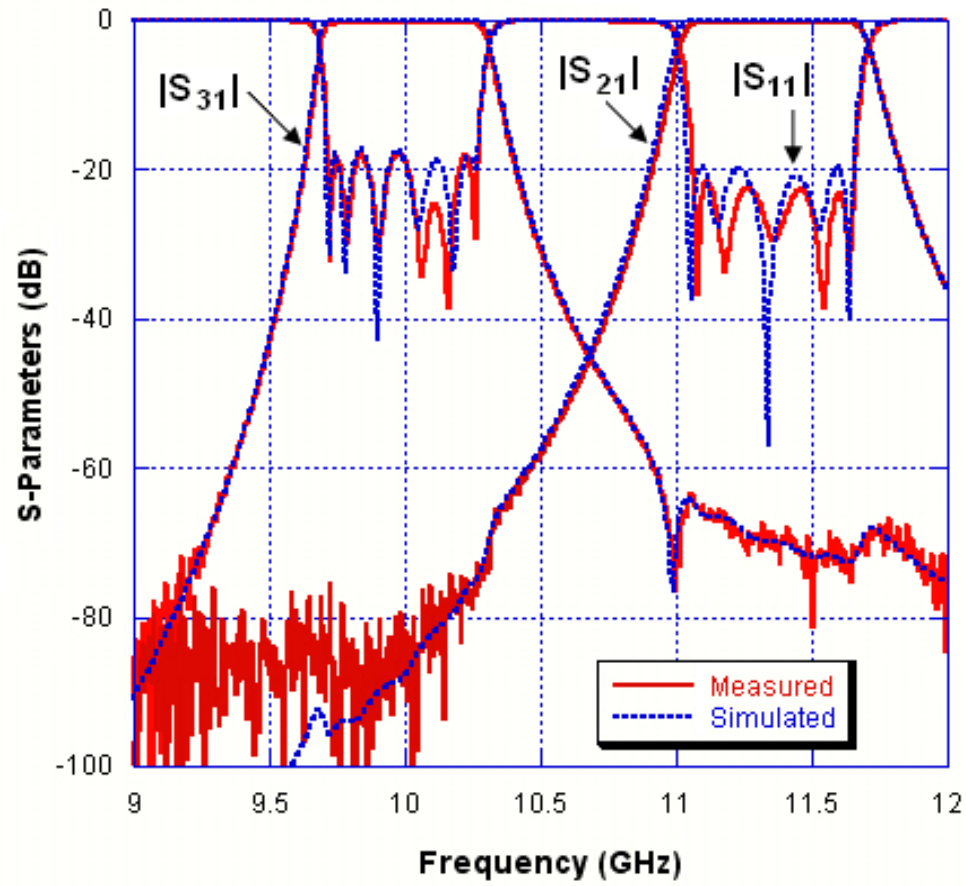

Figure 5.29: Measured and simulated results of the 12-resonator diplexer

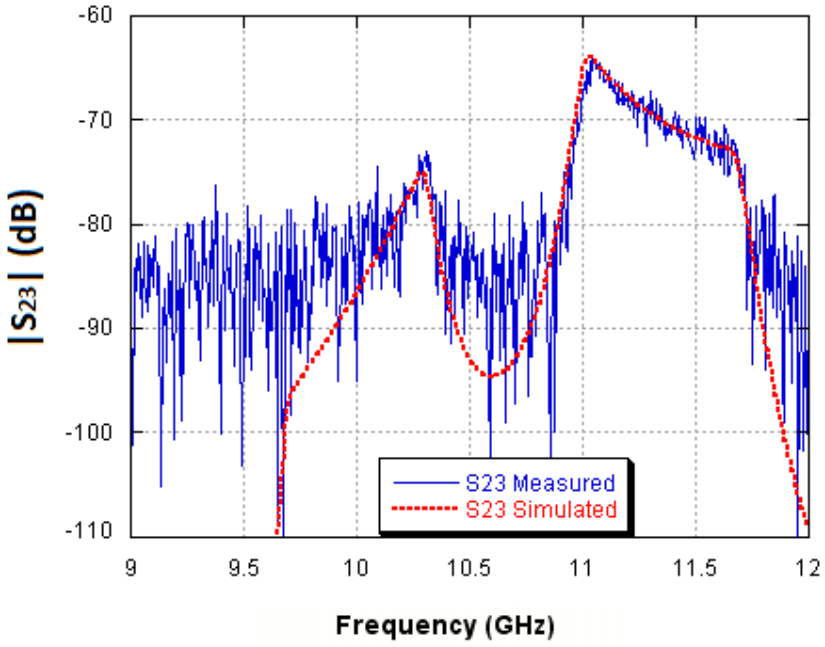

Figure 5.30: Measured and simulated $|S_{23}|$

5.4.5 E-band 12-resonator diplexer

An E-band diplexer has been designed to be used as a front-end component in the transceiver of a point-to-point broadband wireless communications system that offers Gigabit Ethernet connectivity over a distance of a mile or more. It is specified to work at the frequency bands 71-76 GHz and 81-86 GHz. The full specifications of the diplexer are given in table 5.3.

The synthesis procedure of diplexers proposed in Chapter 4 has been adopted here. A structure of 12 resonators, with the topology shown in figure 5.25, has been chosen to meet the required specifications of sharp transitions and high isolation.

Table 5.3: Specification of the E-band diplexer

Band	Frequency Range	Specification	
Low Guard Band	0-69.5 GHz	Rejection	20 dB Minimum
Channel 1	71-76 GHz	Insertion Loss	0.5 dB Maximum
		Reflection Loss	14 dB Minimum
		Isolation	60 dB Minimum
Mid Guard Band	77.5-79.5 GHz	Rejection	20 dB Minimum
Channel 2	81-86 GHz	Insertion Loss	0.5 dB Maximum
		Reflection Loss	14 dB Minimum
		Isolation	60 dB Minimum
High Guard Band	87.5-96.7 GHz	Rejection	20 dB Minimum

The normalised optimised coupling matrix is that shown in table 5.2 and the lowpass prototype response is that shown in figure 5.26. The normalized external quality factors are q_{e1}=1.4903, q_{e7}= q_{e12}=2.9806.

A structure of 12 waveguide cavity resonators coupled together using inductive apertures has been designed. The 3D structure of the designed diplexer is shown in figure 5.31, and the

simulated response is shown in figure 5.32. The diplexer does not involve any external junctions for distribution of energy, and the cavity resonators have been arranged so that the whole device is miniaturised. The overall dimensions of the designed device are 19.05 mm x 19.05 mm x 20 mm. In comparison to a conventional E-band diplexer currently in the market, the proposed design provides a compact structure, since there is no T-junction, in addition to its folded structure. The overall length of the proposed diplexer is miniaturised by 59% when compared to an E-band diplexer made by K&L Microwave Company [11] that has an overall size of 19.05 mm x 19.05 mm x 48.77 mm. The datasheet of K&L Microwave Company diplexer is given in Appendix B.

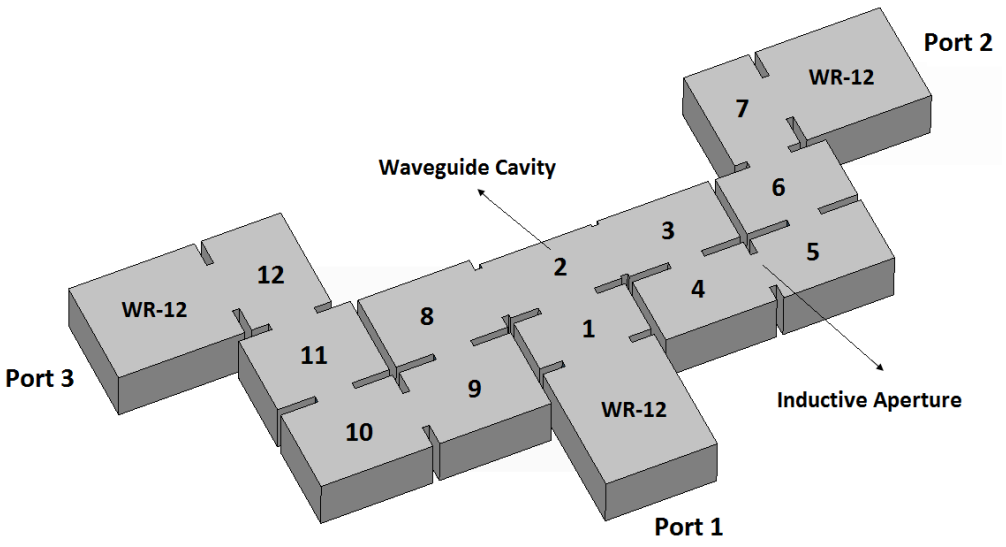

Figure 5.31: E-band diplexer structure

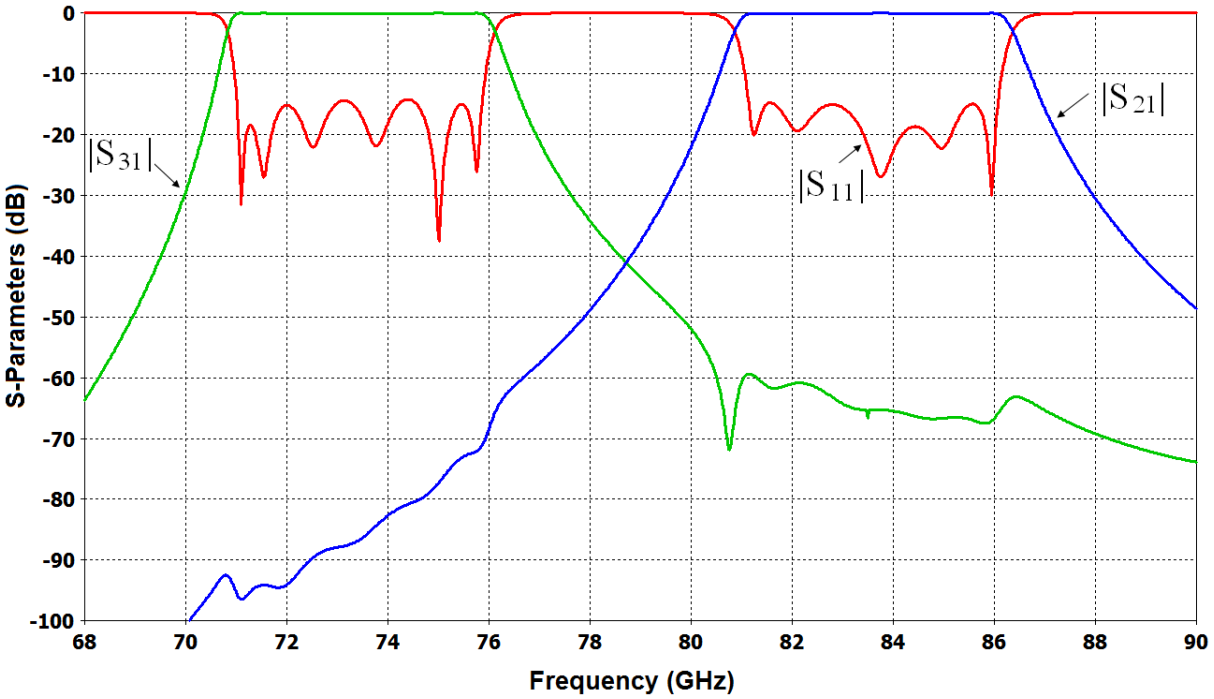

Figure 5.32: Simulated response of the E-band diplexer

5.5 Conclusion

The implementation of coupled-resonator power dividers and diplexers using waveguide cavity resonators has been presented. The devices are: X-band 3-dB power divider, X-band unequal power divider, X-band 4-resonator diplexer, X-band 12-resonator diplexer, and E-band diplexer. The X-band devices have been designed, fabricated, and tested. Metal screws have been used for tuning the filtering response of these devices, and the measurements showed a good agreement with the simulation results. The design of E-band diplexer has been presented for the use as a front-end component in the transceiver of a wireless point-to-point communications system for Ethernet connectivity. 12 resonators were needed in the E-band diplexer to fulfil the requirements of selectivity and high isolation.

References

[1] D.M. Pozar, Microwave Engineering. 2nd edition, Wiley, 1998.
[2] I. Bahl and P. Bhartia, Microwave Solid State Circuit Design. 2nd edition, Wiley, 2003.
[3] J.S. Hong and M.J. Lancaster, Microstrip filters for RF/microwave applications. New York: Wiley, 2001.
[4] J.-S. Hong, "Couplings of asynchronously tuned coupled microwave resonators," *IEE Proceedings Microwaves, Antennas and Propagation*, vol.147, no.5, pp.354-358, Oct. 2000.
[5] T. Shen, K.A. Zaki, A.E. Atia, "Full-wave design of canonical waveguide filters by optimization," *IEEE MTT-S International Microwave Symposium*, USA, May 2001, pp 1487-1490.
[6] J.A. Ruiz-Cruz, K.A. Zaki, J.R. Montejo-Garai and J.M. Rebollar," Rectangular Waveguide Elliptic Filters with Capacitive and Inductive Irises and Integrated Coaxial Excitation," *IEEE MTT-S International Microwave Symposium*, USA, June 2005, pp 269-272.
[7] J.A. Ruiz-Cruz, J.R. Montejo-Garai, J.M. Rebollar, and K.A. Zaki, "Waveguide Filters with Elliptical Function Response: Overview and Results of Different Implementations," International Journal of RF and Microwave Computer-Aided Engineering, vol. 17, no. 1, pp. 63-69, January 2007.
[8] U. Rosenberg, "New 'planar' waveguide cavity elliptic function filters," *in Proc. 25th European Microwave Conference*, Italy, Sept. 1995, pp. 524–527.
[9] U. Rosenberg, W. Hagele, "Consideration of parasitic bypass couplings in overmoded cavity filter designs," *IEEE Transactions on Microwave Theory and Techniques*, vol.42, no.7, pp.1301-1306, Jul. 1994.
[10] CST Microwave Studio. CST GmbH, Darmstadt, Germany, 2006.
[11] http://www.klmicrowave.com/

Chapter 6

Micromachined H-band (220-325 GHz) Diplexer with Embedded Bends

6.1 Introduction

The design methodology of coupled resonator diplexers has been presented in Chapter 4, and the implementation of diplexers at the X-band has been presented in Chapter 5. In this Chapter, a coupled-resonator diplexer working in the H-band (220-325 GHz) frequency range is exhibited. The diplexer has been constructed with innovative structure using micromachining technology that achieves good dimensional accuracy in the micron scale. It is formed by bonding four layers of metal coated SU-8 photoresist fabricated using photolithography technique. The diplexer configuration has been designed so that it is compatible with layered structures formed by micromachining technology. It consists of waveguide cavity resonators coupled together using capacitive irises, and its structure contains relatively long waveguides and embedded matched right-angle bends. The long waveguides allow fair separation between the test flanges that have relatively large size, and the bends have been integrated in the structure to satisfy the measurement requirement of secure and accurate connection between the device and the test ports' flanges.

Figure 6.1 depicts a measurement configuration for micromachined waveguide devices. Bends are utilized to allow the flange to be in the same plane of the SU-8 layers, and hence, the connection between the flange and the micromachined device can be secured by screws. Moreover, the configuration allows precise alignment between the test flange and the micromachined device by alignment pins. The alignment pin holes in the micromachined

structure are defined by photolithography, and hence, the accuracy of alignment is controlled by micromachining. The locations of the holes in the micromachined device match those in the standard UG-387 test flange.

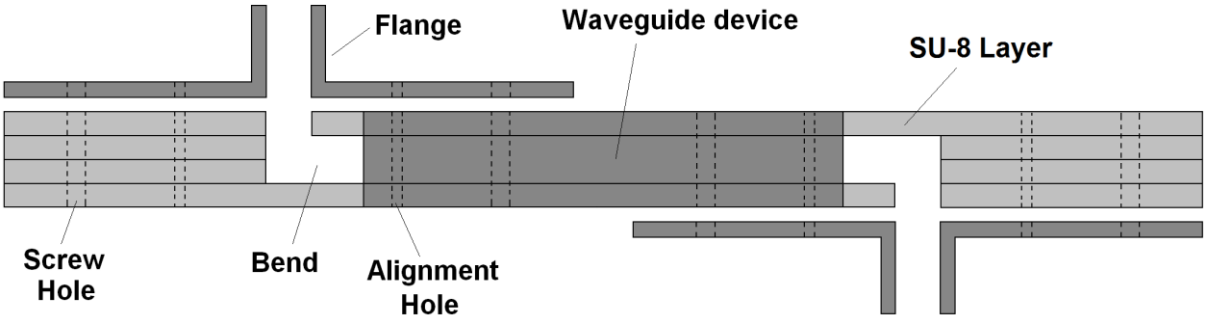

Figure 6.1: measurement setup for a micromachined waveguide device

A literature review about micromachined waveguide components working in the frequency range (220-325 GHz) will be presented first, and then a standard SU-8 micromachining process will be outlined. The design of a micromachined bend that is matched over the H-band will be presented. The design, fabrication, and measurement of a micromachined structure of two back-to-back matched bends with a straight through WR-3 (220-325 GHz) waveguide section are presented. Finally, design, realization and testing of the H-band micromachined diplexer with embedded matched bends are presented. It has to be mentioned that the author has been involved in the design and measurement stages, and that Dr. Mao Ke has been involved in fabricating the components using micromachining technology.

6.2 Review of H-band waveguide components

The growing demand for higher bandwidths in communications systems and for higher resolution imaging has increased the interest in components working in the millimetre (30 GHz to 300 GHz) and the terahertz (300 GHz to 3 THz) frequency ranges. Rectangular waveguides are popular transmission media at these high frequencies due to their low loss and

their ability to handle high power. Waveguide components that operate at the H-band frequency range (220 GHz – 325 GHz) are of interest in the current work. Conventional machining techniques are typically utilised to fabricate waveguides from metals such as brass and copper. However, at frequencies higher than a few hundred GHz, the fabrication of high precision waveguide components using standard metal machining is very expensive. Alternatively, micromachining can be used to produce millimetre/sub-millimetre wave components with good dimensional accuracy, high performance and reduced cost. For example, silicon and SU-8 micromachining techniques can be utilised to produce waveguides with critical dimensions defined through photolithography.

Micromachining techniques have been reported in literature as practical means of producing H-band waveguide components. The fabrication of various SU-8 based waveguide sections and the measurement using a specially designed metal block have been demonstrated in [1]. The measured WR-3 waveguide showed an insertion loss between 0.625 dB/mm and 1.125 dB/mm over the range 220-325 GHz. A straight SU-8 based WR-3 waveguide has also been reported in [2]. The waveguide exhibited normalized insertion loss between 0.09 dB/mm and 0.44 dB/mm over the range 220-325 GHz, and reflection response with many undesirable spikes. This was attributed to a loose connection between the test port flange and the device under test. In [3], an SU-8 micromachined WR-3 waveguide has been reported, and a photonic bandgap structure that is patterned on the test flange face has been proposed to mitigate the loss resulting from loose connection between the SU-8 micromachined waveguide and the standard test flange. The configuration proposed in figure 6.1 provides a good solution for a secure connection between the test flange and the micromachined device.

6.3 Fabrication Process

An SU-8 micromachining technique has been utilised in the fabrication of the proposed waveguide structures. SU-8 photoresist is a very attractive material for MEMS and micromachined circuits. It is highly sensitive to UV light and suitable for construction of high aspect ratio structures [4]. Since SU-8 is a photosensitive material, standard photolithography process can be utilized to define prescribed micro-patterns accurately by selective exposure to UV radiation through a mask. The basic steps of the fabrication process involve [5]: spin coating, soft bake, exposure, post-exposure baking, development, hard baking, substrate removal, and metallization. Once the SU-8 is processed by these steps, it becomes a strong and resilient structural material. The fabrication steps are detailed in the subsections below.

6.3.1 Spin coating

Spin coating process is commonly used to distribute a photoresist with a required thickness on a flat silicon substrate. A measured amount of the SU-8 resist is dispensed onto the centre of the Si substrate that is mounted to the chuck of a spinner. The thickness of SU-8 films normally depends on viscosity, solids concentration, spinner speed and time of the spinning process. The resist thickness is inversely proportional to the square root of the spin rate [6], and spin speed curves provide a useful guide about the appropriate speed required to achieve the desired film thickness. The layer thickness required for the micromachined waveguide devices in this thesis is 432 μm. Spin coating is carried out here by uniformly dispersing an amount of SU-8 2050 photoresist onto a silicon wafer, and precision weight control has been employed in order to have more accurate control on the final thickness.

6.3.2 Pre-baking

A soft bake, or a pre-exposure bake, is used to evaporate the solvents from resist and to improve resist-substrate adhesion. It is typically performed on either an oven or a level hot plate with good thermal control. The Plate is levelled in order for the SU-8 layer to have a uniform thickness. The SU-8 is baked above the glass transition temperature (Tg) of the unexposed resist. The mobility of the SU-8 at temperatures higher than its Tg, and the force of gravity and surface tension allow the SU-8 to self-planarize to a film with good flatness. The solvent contained in the SU-8 evaporates during the pre-bake process, and this causes the viscosity of the SU-8 to increase. The pre-bake process is carried out here on a level hotplate in a two-step temperature ramp, as the resist is initially baked at 65^{o} C for 30 min and then the temperature is raised to 95^{o} C for 4-5 h.

6.3.3 Exposure

After soft baking, the resist-coated substrate is moved to an exposure system (a mask aligner), where the photoresist is exposed to UV light through a photomask. The mask is usually made of glass that is transparent to UV light, with a chromium pattern applied on the glass that is opaque to UV light [7]. A mask aligner is used to shine UV light on the photoresist through the mask. It contains an UV lamp that is used to deliver light to the photoresist film with the proper exposure dose. The dose, or incident energy (J/cm^2), is defined by the incident light intensity (in W/cm^2) multiplied by the exposure time (in seconds) [8]. The optimal exposure dose depends on the required thickness of the photoresist film [9]. There are two basic types of photoresists: positive resists and negative resists. In positive resists, when exposed to light, the chemical bonds are weakened and the exposed parts become more soluble in the development stage. In negative resists, the chemical bonds are strengthened when exposed to light, and the exposed areas become insoluble [7,10]. Hence, positive resists will have a

positive image of the mask after development, whereas negative resists will have a negative image of the mask. SU-8 is a negative photoresist, and it has a photoacid produced upon exposure to light. This photoacid acts as a catalyst in the cross-linking reactions taking place during the postbake stage [11].

6.3.4 Postbake

After exposure of the SU-8, a post-bake process is carried out to enhance the cross-linking of the exposed areas and stabilize them against the solvents action in the development stage. Although the catalyst formed during the exposure process induces reactions at room temperature, the rate of these reactions increases by post-exposure bake at 60-100^{o} C [8], and therefore increases the cross-linking degree. The bake can be performed in a convention oven or on a hot plate. Precise control of the post-bake times is crucial for the quality of the final structure, as extended bake times introduce large amounts of stress in the resist that is likely to cause bending of the structure and peeling form the substrate. Moreover, reduced bake times result to structures that are not fully cross-linked with higher chance of being attacked by solvents in the development step [8]. Post-bake has been carried out here on a two-step temperature ramp process. Initially, the resist is baked at temperature of 65^{o} C for 5 minutes, and then the temperature is ramped up to 95^{o} C for 30 minutes, and then the hotplate is switched off and the resist is cooled down naturally to room temperature.

6.3.5 Development

The resist is then developed with Ethyl lactate solvent to remove the non-cross-linked SU-8 regions. The development is performed by immersing the resist-coated substrate in the developer solution at room temperature. Development rate can be increased by stirring the developer solution that enhances diffusion of developer molecules into the non-cross linked

SU-8 areas [12]. The time of development can vary based on temperature and agitation rate during development, geometry of the pattern, and resist processing parameters. The development is carried out here for about 30 minutes, followed by rinsing with isopropanol and drying with a stream of air or nitrogen. After the completion of this stage, a negative image of the mask is produced, and the pattern of the waveguide device is formed.

6.3.6 Hardbake and substrate removal

After development, a hard-bake step is useful to further strengthen the cross-linking bonds. This makes the resist strong and resistant to most known acids and alkalis, and also resilient to subsequent processing such as metal evaporation that would subject the SU-8 to temperatures higher than 100^{o} C. Skipping the hardbake step makes the SU-8 layers susceptible to bending during metallization [13]. The hardbaking is carried out here on a hot plate at 150^{o} C for 30 minutes. The hotplate is then switched off and the substrate is left on the hotplate to allow gradual cooling down to reduce the stress.

To release the SU-8 from silicon substrate, the resist-coated substrate is immersed in a 10% sodium hydroxide solution at 60^{o} C for more than 7 hours to etch the silicon away.

6.3.7 SU-8 Metallization

Evaporation and sputtering are common types of physical vapour deposition (PVD) that are used to add a metal to the surface of the substrate to be coated [9]. In evaporation, a material is vaporized from a source by heating and the vapour is transported in vacuum to condense on the surface of the substrate to be coated. In sputtering, argon ions from plasma hit the sputtering material and the ejected atoms from the material are transported in vacuum to the surface of the substrate to be coated [10]. Adhesion intermediate layers are commonly used when depositing PVD films to form strong chemical bonds at the interfaces [9]. Chromium

(Cr) and Titanium (Ti) are commonly used as adhesion layers. The metal coating is carried out here by firstly sputtering 5 nm of Cr adhesion layer, then evaporating just over 1μm thick silver and a thin protection layer of 20 nm gold. The coating is carried out here on all the surfaces of the SU-8 pieces, including the inner walls. The evaporation is done in an evaporator that can continuously rotate the substrate holder at any required angle in order to make sure the walls of the waveguide structure are well coated.

6.4 Micromachined WR-3 Waveguide with Bends

The design, fabrication and measurement of a structure of WR-3 rectangular waveguide section with two back-to-back matched right angle bends are presented (see figure 6.1). The device is made of four layers of metal coated SU-8 using photolithography to produce the micromachined circuit. A theoretical review about a rectangular waveguide and its conductor loss will be presented first in this section, followed by the design of a micromachined waveguide and a right angle bend, and then the measured results will be shown.

6.4.1 Rectangular waveguide review

A rectangular waveguide with width **a** and height **b** is illustrated in figure 6.2, where it is assumed that the material filling the waveguide has a permittivity of ε and permeability μ. This guide can propagate TM and TE modes that have cut-off frequencies in which propagation is not possible below.

The fields of the TE modes are characterised by E_z=0 and $H_z(x,y,z)=h_z(x,y)e^{-j\beta z}$, where β is the propagation constant, given by [14],

$$\beta = \sqrt{k^2 - k_c^{\,2}} \tag{6.1}$$

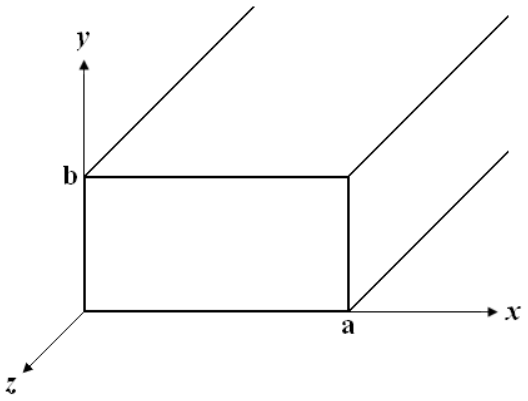

Figure 6.2: Rectangular waveguide geometry

where $k = \omega\sqrt{\mu\varepsilon}$ is the wavenumber and k_c is the cut-off number, given by,

$$k_c = \sqrt{\left(\frac{m\pi}{a}\right)^2 + \left(\frac{n\pi}{b}\right)^2} \tag{6.2}$$

The cut-off frequency $f_{c,mn}$ of the mnth mode is given by,

$$f_{c,mn} = \frac{k_c}{2\pi\sqrt{\mu\varepsilon}} = \frac{1}{2\pi\sqrt{\mu\varepsilon}}\sqrt{\left(\frac{m\pi}{a}\right)^2 + \left(\frac{n\pi}{b}\right)^2} \tag{6.3}$$

Assuming a>b, the dominant mode occurs for the TE_{10} mode, and it has a cut-off frequency $f_{c,10}$,

$$f_{c,10} = \frac{1}{2a\sqrt{\mu\varepsilon}} \tag{6.4}$$

The guided wavelength of the TE_{10} mode in a rectangular waveguide is a function of frequency and it is calculated by,

$$\lambda_g = \frac{2\pi}{\beta} = \frac{2\pi}{\sqrt{\omega^2\mu\varepsilon - \left(\frac{\pi}{a}\right)^2}} \tag{6.5}$$

The group velocity (v_g) in which the energy propagates within a rectangular waveguide is given by,

$$v_g = \frac{\sqrt{\omega^2 \mu\varepsilon - \left(\frac{\pi}{a}\right)^2}}{\omega\mu\varepsilon} \tag{6.6}$$

The attenuation due to conductor loss for the dominant TE_{10} mode in (Np/m) is given by,

$$\alpha_c = \frac{R_s}{a^3 b\beta k\eta}\left(2b\pi^2 + a^3 k^2\right) \qquad \text{Np/m} \tag{6.7}$$

where $\eta = \sqrt{\mu/\varepsilon}$ is the intrinsic impedance of the material that fills the waveguide, and $R_s = \sqrt{\omega\mu/2\sigma}$ is the surface resistance of the waveguide walls (with conductivity σ).

6.4.2 Micromachined waveguide structure

A cross section of the micromachined waveguide is shown in figure 6.3. It is composed of four layers of metal coated SU-8, each of a thickness of 432 μm. Two split blocks are formed, with layers 1 and 2 bonded together using conducting glue to make half of the split blocks, and layers 3 and 4 bonded to form the other half. To minimize the resistive losses, and to avoid any gaps between the SU-8 layers, a second metal evaporation is done on each of the two halves.

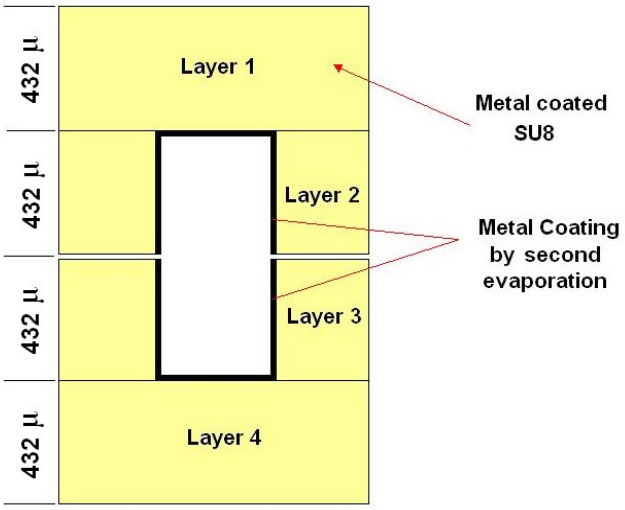

Figure 6.3: Cross sectional view of the micromachined waveguide structure.

The attenuation due to conductor loss for a section of a rectangular waveguide has been calculated using equation (6.7) in the frequency range 220-325 GHz. The insertion loss of a 16 mm waveguide is shown in figure 6.4 for different values of metal conductivity. The metal used in coating the SU-8 layers is silver, that has a conductivity of $\sigma=6.3 \times 10^7$ S/m. Figure 6.4 shows the effect of imperfection of conductivity on the insertion loss over the H-band frequency range.

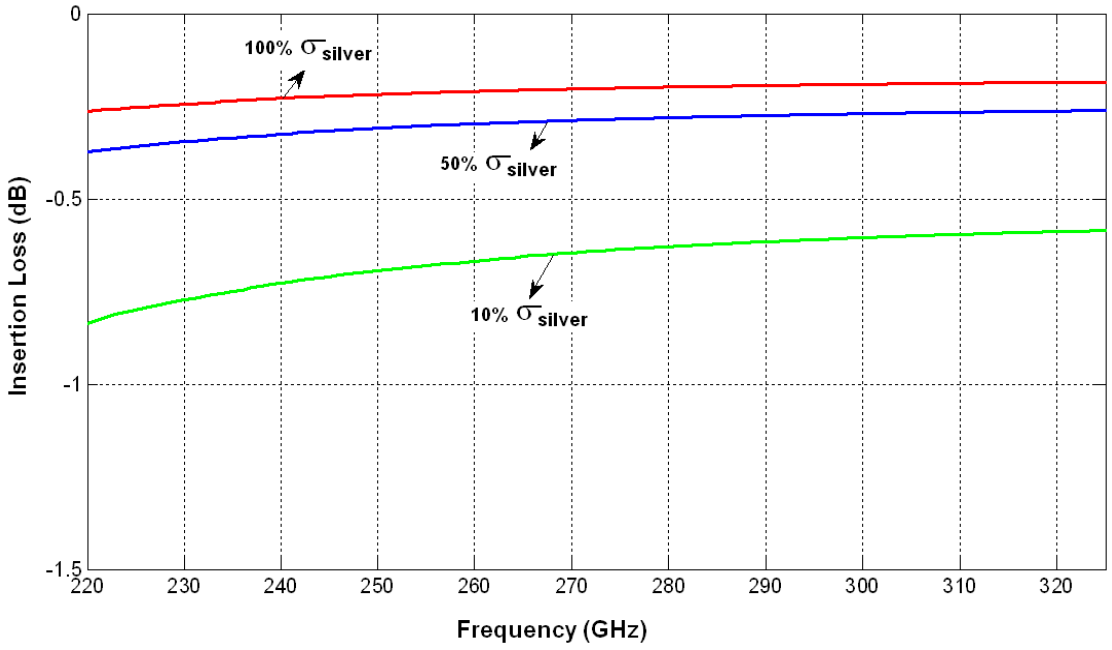

Figure 6.4: Effect of imperfection of conductivity on insertion loss

6.4.3 Bend design

Waveguide right-angle corners exhibit narrowband and mismatched response. Conventionally, a broadband matching is achieved by using a smooth transition such as multi-stepped or multi-mitred corners [15,16]. However, these configurations are not compatible with the layered structures proposed here. A modified waveguide bend that can be fabricated using the micromachining technology is therefore presented here. The bend has two ridges at the junction region; each contributes a resonance into the desired frequency band and broadens

the matched bandwidth. The bend structure, with the optimized dimensions is shown in figure 6.5, and the simulated response is given in figure 6.6. The geometries of the ridges have been adjusted by EM optimization [17] to achieve matching in the range between 250-320 GHz with a return loss of -20 dB or better. A more complicated structure would be required to achieve matching over the whole WR-3 band (220-325 GHz).

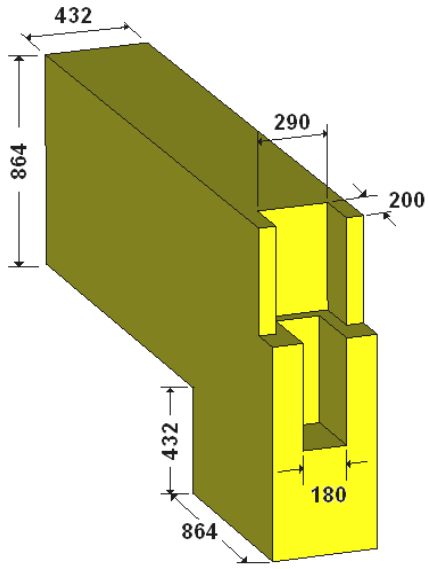

Figure 6.5: Structure of the bend. Dimensions are in micrometers.

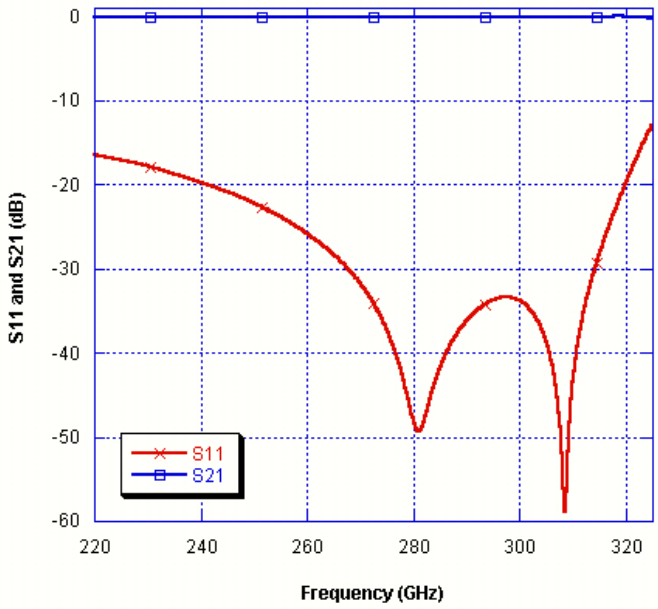

Figure 6.6: Simulated response of the bend.

To measure the bend, a structure of two back-to-back bends and a straight waveguide section is constructed. It is formed of four micromachined layers; each contains holes to allow alignment pins and screws of the test flanges to pass through. The locations and diameters of these holes match those in the standard UG-387 waveguide flange. Figure 6.7 depicts the back-to-back structure and the top view of layer 2. The waveguide length is around 16 mm excluding the bends; this is made sufficiently long to permit fair separation between the flanges so that pins and screws are not blocked from the other side. The size of each SU-8 layer is 432 μm x 48 mm x 24 mm. The bends allow the waveguide to be in the same plane as the SU-8 layers. This is distinct from the previous work [1,2] where the waveguide flange was connected laterally to the SU-8 layers. The structure in figure 6.7 allows other waveguide components such as filters to be interconnected between the bends. Moreover, it can be extended to include multiport components such as waveguide diplexers, as will be shown later in section 6.5.

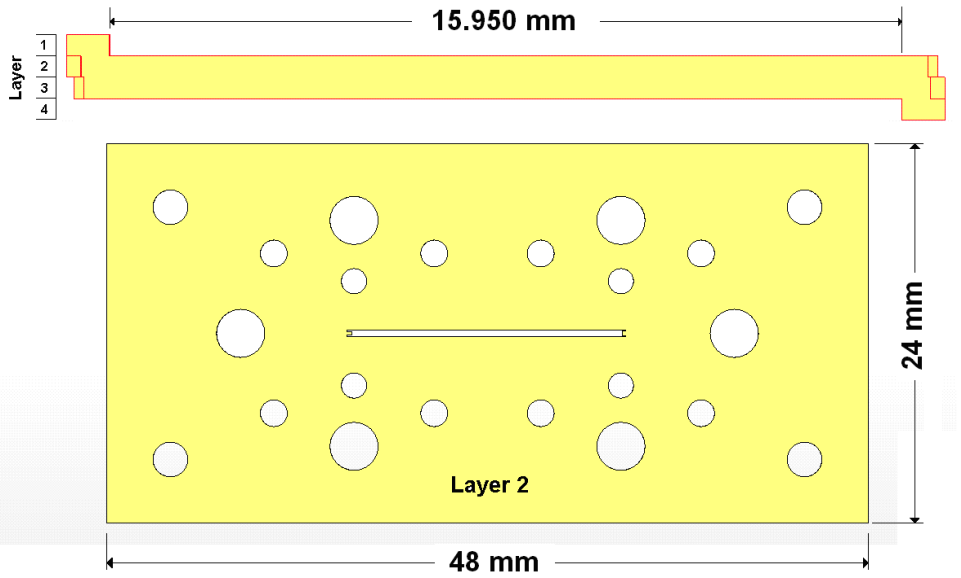

Figure 6.7: Side view of back-to-back structure and top view of layer 2.

6.4.4 Fabrication and assembly

SU-8 photolithography process has been utilized to produce the four layers of the device. The fabrication process is presented in section 6.3. Once the four metal-coated SU-8 layers were ready for assembly, layers 1 and 2 were aligned and bonded together using conducting glue, and then a second metal coating was performed to fill any gaps in the interface between the layers, as mentioned earlier. The same process was done for layers 3 and 4. Finally, the device was assembled and the pieces were aligned using pins, and then clamped together using conventionally machined metal plates made from brass. It should be noted that these brass plates bear no function for alignment, considering their inferior fabrication accuracy as compared with micromachining. A secure connection between the standard flange and the SU-8 device is realised since the flanges are directly connected to the first and the fourth layers using screws. A photograph of the assembled device is shown in figure 6.8.

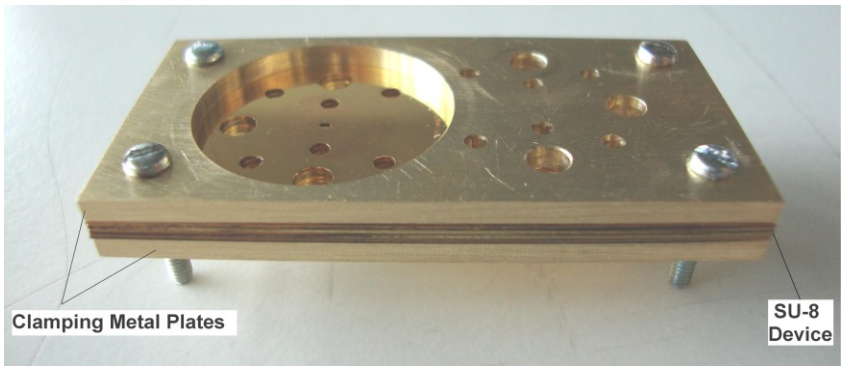

Figure 6.8: Assembled device

6.4.5 Measurement results

An Agilent E8361A network analyser with OML extension modules V03VNA2-T/R and V03VNA2-T (220-325 GHz) have been used to take measurements. The T-module is a "receive-only" and cannot provide stimulus to the device under test. Hence, a full two-port calibration is not possible, and only one transmission measurement (S_{21}) and one reflection

measurement (S_{11}) are possible by using one T/R module and one T module. The device has to be reversed to measure the parameters (S_{12}) and (S_{22}). Moreover, the return loss at any port has been measured by connecting the device to the test port of the T/R module, and connecting the other port of the device to a matched load. This is due to the poor match of the T-module (6 dB match), as the signal entering the T-module faces a mixer that has poor matching. An Enhanced-Response calibration is the most accurate for the T/T-R configuration [18,19]. It combines a one-port calibration for port-1 and a thru response calibration between ports 1 and 2. A photograph of the measurement setup showing the SU-8 device clamped between the metal plates and connected to the test ports is depicted in figure 6.9.

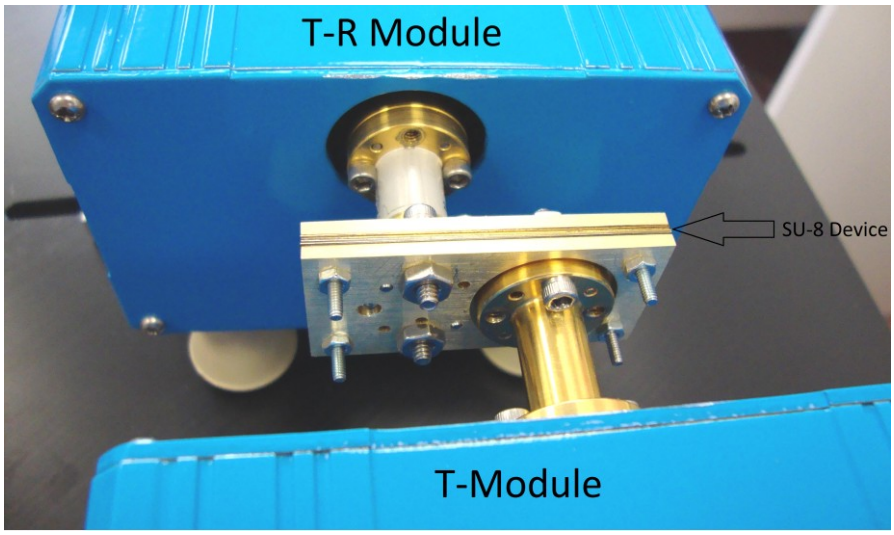

Figure 6.9: Photograph of the measurement setup

Figure 6.10 displays the simulated and the measured S-parameters of the back-to-back structure. The metal used in the lossy simulation in figure 6.10 (b) is silver, which has a conductivity of 6.3×10^7 S/m. The measured results show a return loss of better than -16 dB and insertion loss of 2.5 - 3 dB in the frequency range 240-312 GHz. The guided wavelength (λ_g) of the TE_{10} mode of the waveguide is calculated using equation (6.5) at 300 GHz, and found to be 1.224 mm. A total length of 18.542 mm (waveguide and bends) corresponds to

15.15 wavelengths, and the insertion loss per wavelength at 300 GHz is approximately 0.165 dB/λ_g (0.134 dB/mm). This is higher than the nominal value of a commercial metallic waveguide, that has insertion loss of ~0.02 dB/mm. The losses in the micromachined device could be attributed to the imperfection of metal conductivity, and also the possibility of existence of gaps in the interface between the layers, which caused the higher-than-simulated insertion loss.

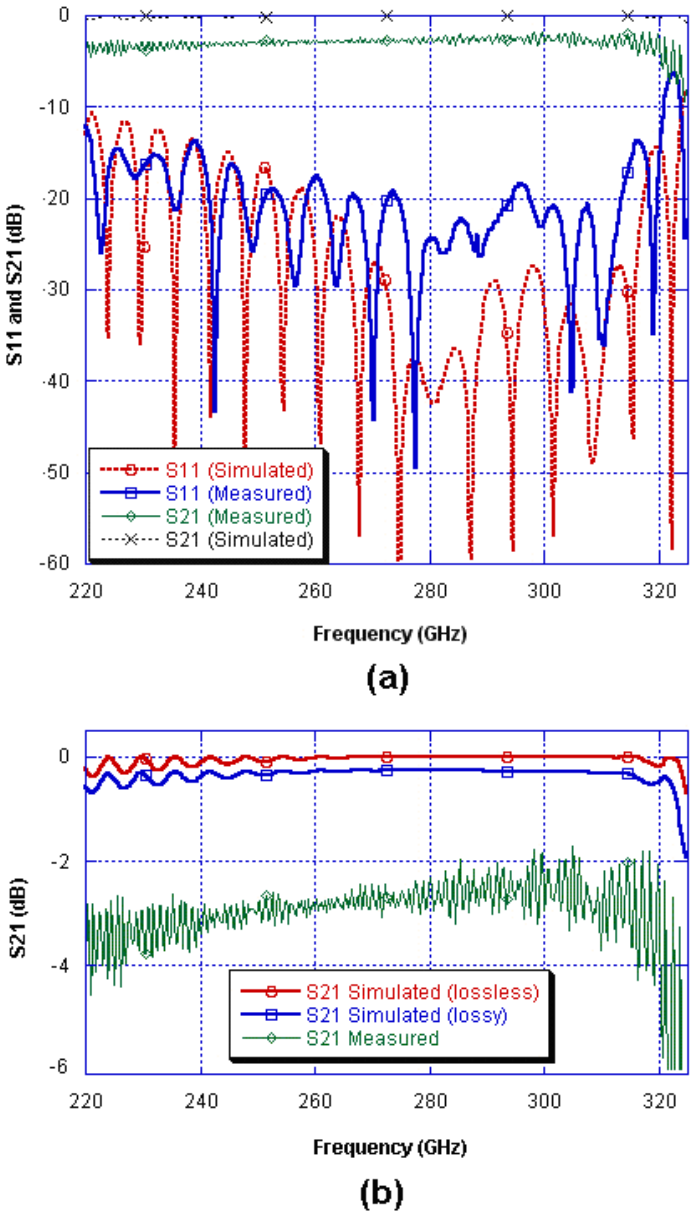

Figure 6.10: (a) Measured and simulated results, (b) passband details

The multiple nulls in the S_{11} response are due to signal reflections at the end of the waveguide sections. Using equation (6.6), the group velocity (v_g) is 1.8441 x 10^8 m/s at 220 GHz, and 2.5342 x 10^8 m/s at 325 GHz. The group delay for a wave to make one trip between the ends of the 16 mm long waveguide varies from 63 ps at 325 GHz to 87 ps at 220 GHz.

The measurements have shown good repeatability. This, together with the measured low return loss, indicates a reliable flange connection.

6.5 Micromachined H-band Diplexer

6.5.1 Diplexer design

A micromachined 8-resonator non-contiguous diplexer that works at the H-band has been designed, fabricated and tested. The diplexer channels have passband centre frequencies of 265 GHz and 300 GHz, and a desired reflection loss of 20 dB. It has been synthesized according to the procedure presneted in Chapter 4 for T-topology diplexers. The diplexer topology is shown in figure 6.11, and the optimised normalised coupling matrix is given next. The normalised external quality factors are q_{e1}=1.63, q_{e5}=q_{e8}=3.26, and the fractional bandwidth is *FBW*=17%. The prototype response of the synthesized diplexer is shown in figure 6.12.

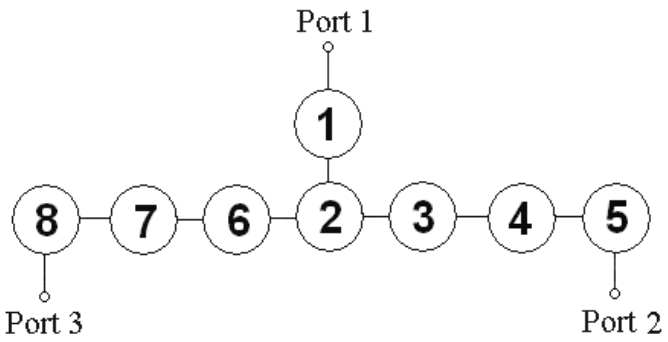

Figure 6.11: H-band Diplexer topology

$$M = \begin{bmatrix} 0 & 0.8159 & 0 & 0 & 0 & 0 & 0 & 0 \\ 0.8159 & 0 & 0.3308 & 0 & 0 & 0.3308 & 0 & 0 \\ 0 & 0.3308 & 0.6482 & 0.2051 & 0 & 0 & 0 & 0 \\ 0 & 0 & 0.2051 & 0.7044 & 0.2613 & 0 & 0 & 0 \\ 0 & 0 & 0 & 0.2613 & 0.7092 & 0 & 0 & 0 \\ 0 & 0.3308 & 0 & 0 & 0 & -0.6482 & 0.2051 & 0 \\ 0 & 0 & 0 & 0 & 0 & 0.2051 & -0.7044 & 0.2613 \\ 0 & 0 & 0 & 0 & 0 & 0 & 0.2613 & -0.7092 \end{bmatrix}$$

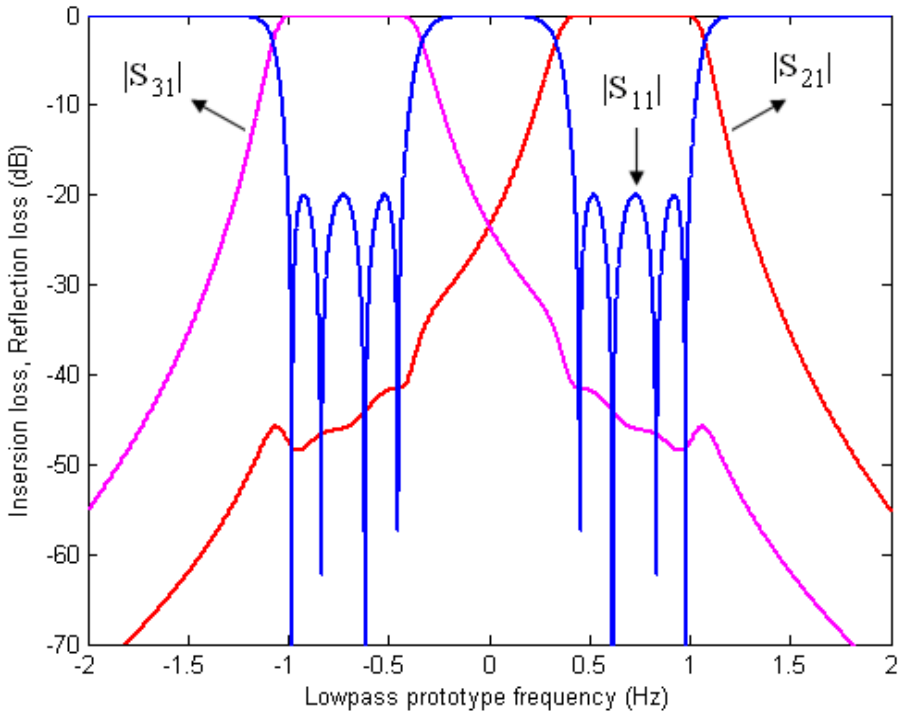

Figure 6.12: Prototype response of H-band diplexer.

The diplexer has been implemented using waveguide cavity resonators coupled together using capacitive irises. A top view of the diplexer structure is depicted in figure 6.13. The diplexer configuration has been designed so that it is compatible with layered structures produced by micromachining technology.

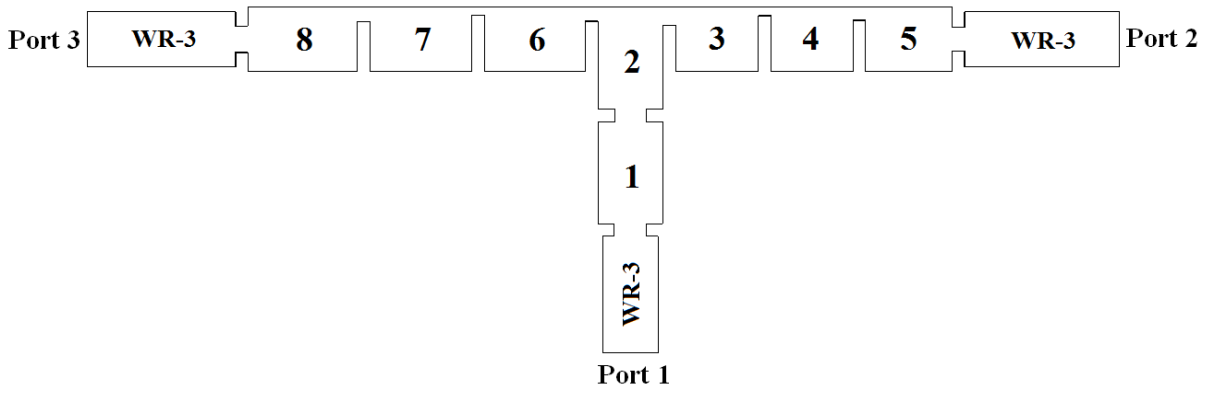

Figure 6.13: Top view of the diplexer structure

For measurement purposes, it is necessary to design the diplexer in a way that allows three test port flanges to be securely and accurately connected to the device considering their relatively large size. This is achieved by constructing the structure shown in figure 6.14. It consists of the 8-resonator diplexer, 4 matched bends, and relatively long waveguides to allow fair separation between the test flanges. The bends at the terminals of the device generally have the structure depicted in figure 6.5, with some dimensions optimized to improve matching over certain frequency bands. The right-band bend has been individually optimized so that matching is achieved at the higher frequency channel, which is centered at 300 GHz. Similarly, the left-band bend has been optimized to achieve matching at the lower frequency channel that is centered at 265 GHz. The input bend has been separately optimized so that matching is achieved over the largest possible range of frequencies in the H-band.

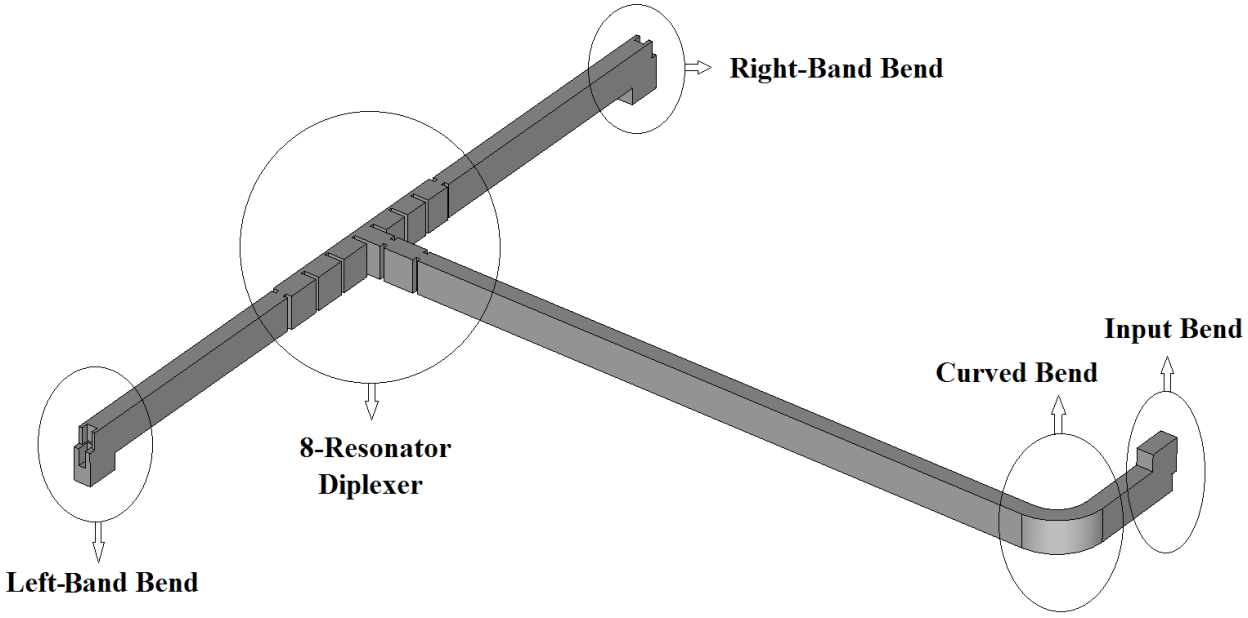

Figure 6.14: Diplexer structure

The additional curved bend is employed in the structure in order for the waveguide at the common port to have the same orientation as the waveguides at the other ports. This is necessary since the test ports have the same waveguide orientation. Figure 6.15 shows the simulation performance of $|S_{11}|$ of the optimized bends. The 8-resonator diplexer and the bends have been designed individually and then they were interconnected together. The addition of the bends to the diplexer resulted in small degradation in its performance, and hence final optimization for the whole structure has been carried out to improve the performance. This has been done for all the bends without altering the dimensions of the diplexer. Figure 6.16 depicts the simulation results of the diplexer before adding the bends, and the performance after optimizing the whole structure with the bends. CST has been used for simulation and it took around 29 minutes on a computer that has 3.47 GHz processor (4 CPUs) and 24 GB RAM. It is noticed that the addition of the bends has affected the smoothness of the transitions in the low guard band (below 260 GHz) and the high guard band

(above 315 GHz). This may have been caused due to the imperfection in matching performance of the input bend below 260 GHz and above 315 GHz.

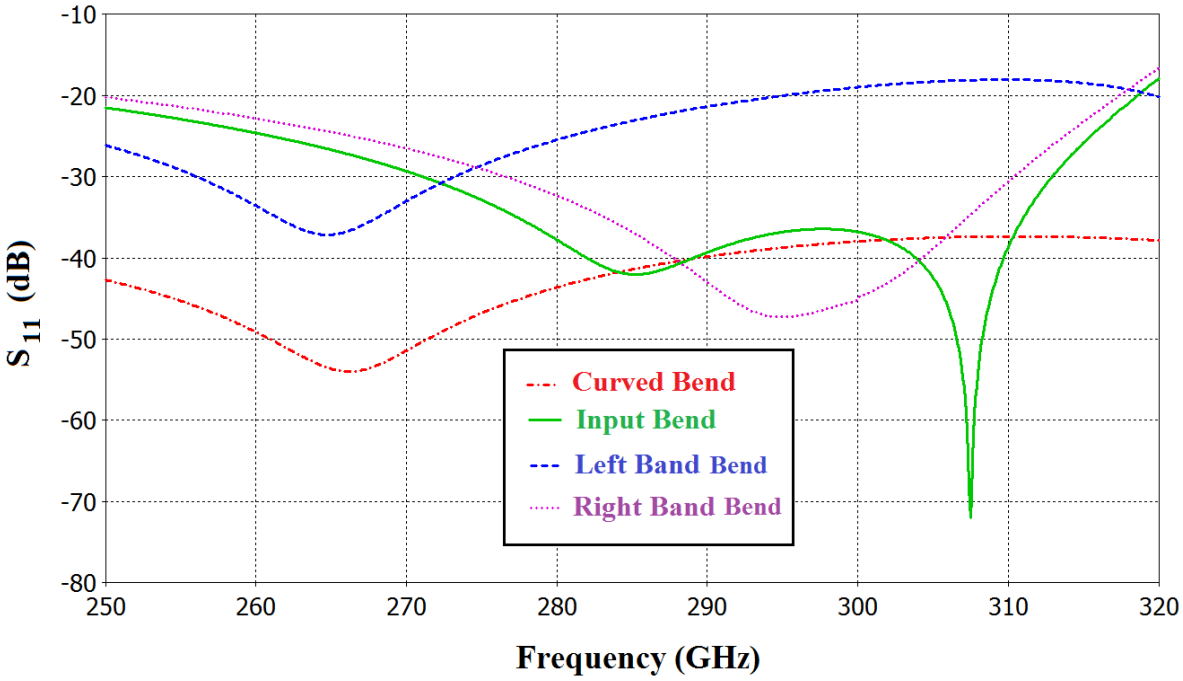

Figure 6.15: simulations results of the bends

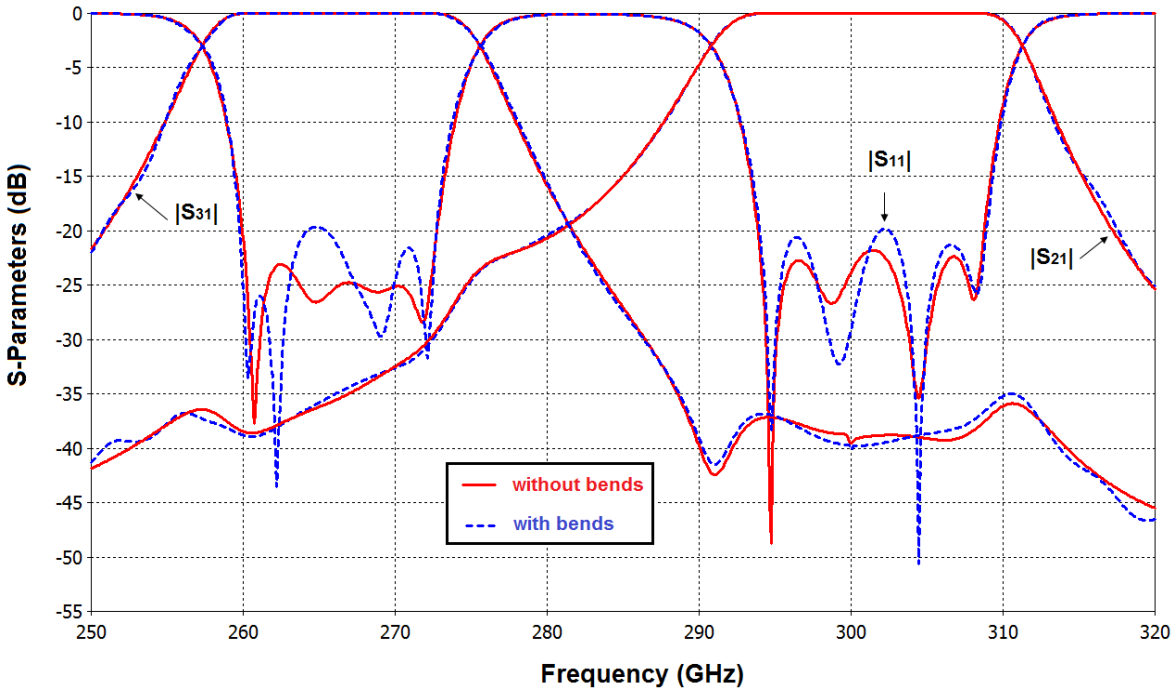

Figure 6.16: Simulation results of the diplexer with and without the bends

6.5.2 Fabrication and assembly

The device has been fabricated using the SU-8 micromachining technique presented in section 6.3. Four layers of metal coated SU-8, each of thickness of 432 µm, have been made to form the diplexer structure. The size of each layer is 50.224 mm x 43.9 mm x 432 µm, and the layouts of the top views of the layers forming the device are shown in figure 6.17. The holes in each layer match those in the standard UG-387 waveguide flanges to allow alignment pins and screws to pass through.

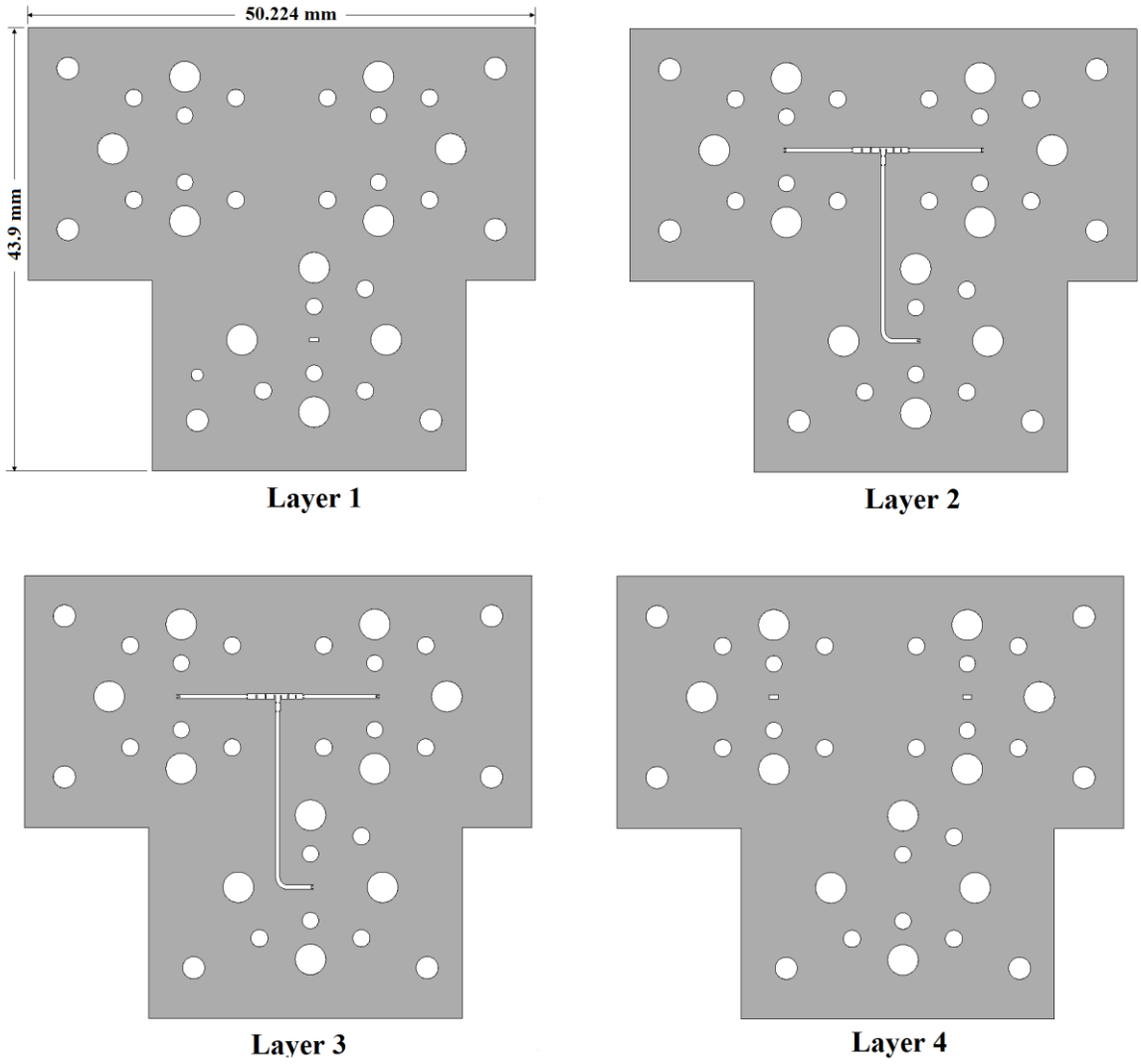

Figure 6.17: Layers layouts of the micromachined diplexer.

Figure 6.18 depicts a microscope photo of the centre part of the diplexer. It proves that good dimensional accuracy has achieved for the thickness of the irises, where the measured dimensions of iris thickness of 103.7 µm and 100.3 µm are in good agreement with the designed values of 100 µm. However, the measured dimensions of the gaps corresponding to the couplings between the cavities have shown inferior accuracy, where the measured values of 225.8 µm, 103.7 µm, and 133.8 are smaller than the designed values of 242 µm, 112 µm, and 144 µm respectively.

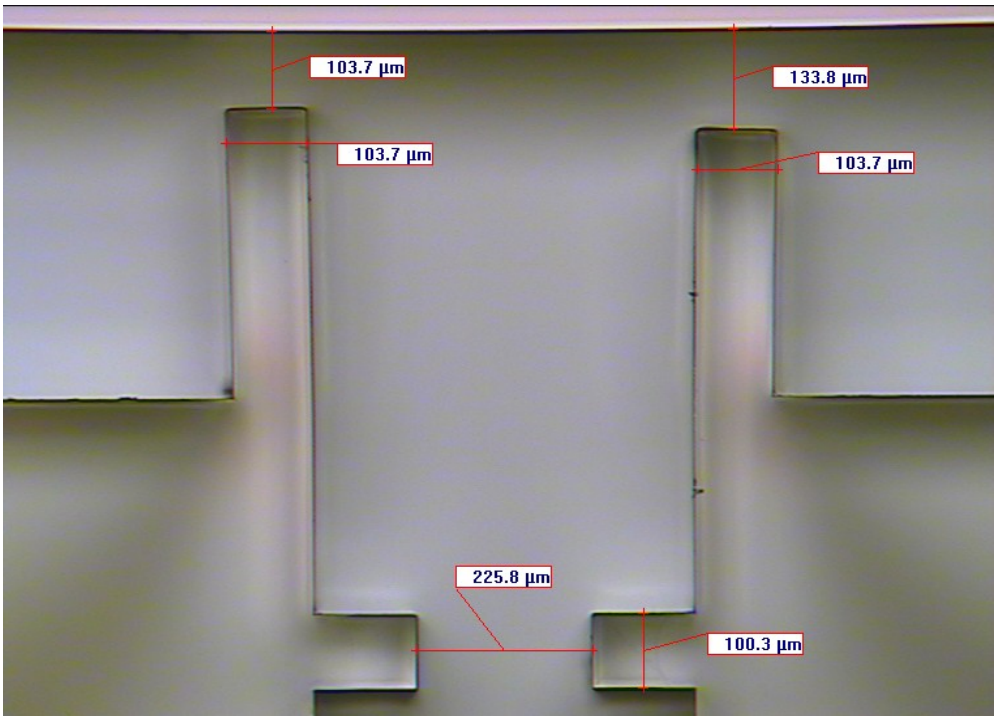

Figure 6.18: Microscope photo for layer 3 at the centre part of the diplexer.

Two split blocks have been made of the metalized layers; the first was formed by aligning and bonding layers 1 and 2 using conducting glue, and similarly, the second split block was formed from layers 3 and 4. Second metal evaporation has been done for each of the split blocks to fill any gaps between the SU-8 layers. Finally, the two blocks have been aligned

using pins, and clamped together using conventionally made brass plates. A photograph of the assembled device is shown in figure 6.19.

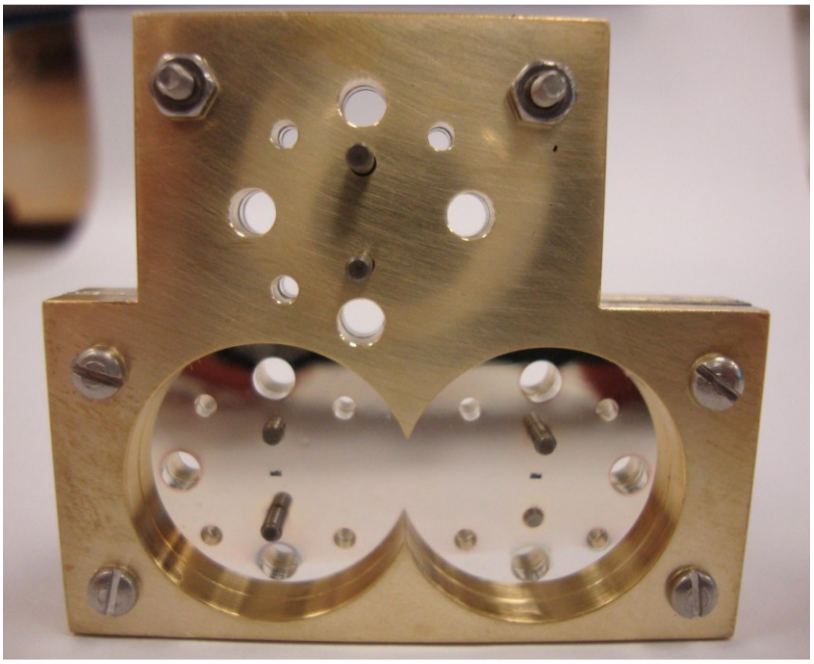

Figure 6.19: Assembled diplexer.

6.5.3 Measurement

The device has been measured using an Agilent E8361A network analyser with OML extension modules V03VNA2-T/R and V03VNA2-T (220-325 GHz). It is the same measurement equipment used to test the back-to-back bends presented earlier. Since 2-port network analyser is used here to test a 3-port device, a matched load is used in the measurement of the transmission parameters S_{21} and S_{31}. Consequently, S_{21} is measured by connecting the test ports of the T/R and T modules with ports 1 and 2 of the diplexer, respectively, and connecting a matched load to port 3. Similarly, S_{31} is measured with the test ports of T/R and T modules connected to ports 1 and 3 of the diplexer, respectively, and a matched load connected to port 2. Due to the poor match of the T-module (6 dB match), the reflection parameters at any particular port of the diplexer are measured by connecting that

port to the test port of the T/R module, and loading the other ports of the diplexer by matched loads.

An enhanced response calibration has been performed first. The measurement setup is depicted in figure 6.20 showing the micromachined device clamped between the two brass plates. The connection of a 6 dB attenuator between the device under test and the T-module reduces the reflection from port-2 (T-module) back to port-1 (T-R Module), since the reflected signal from the poorly matched T-module is damped by the attenuator. Moreover, the use of the attenuator has been found useful to reduce the periodical ripples in transmission measurements.

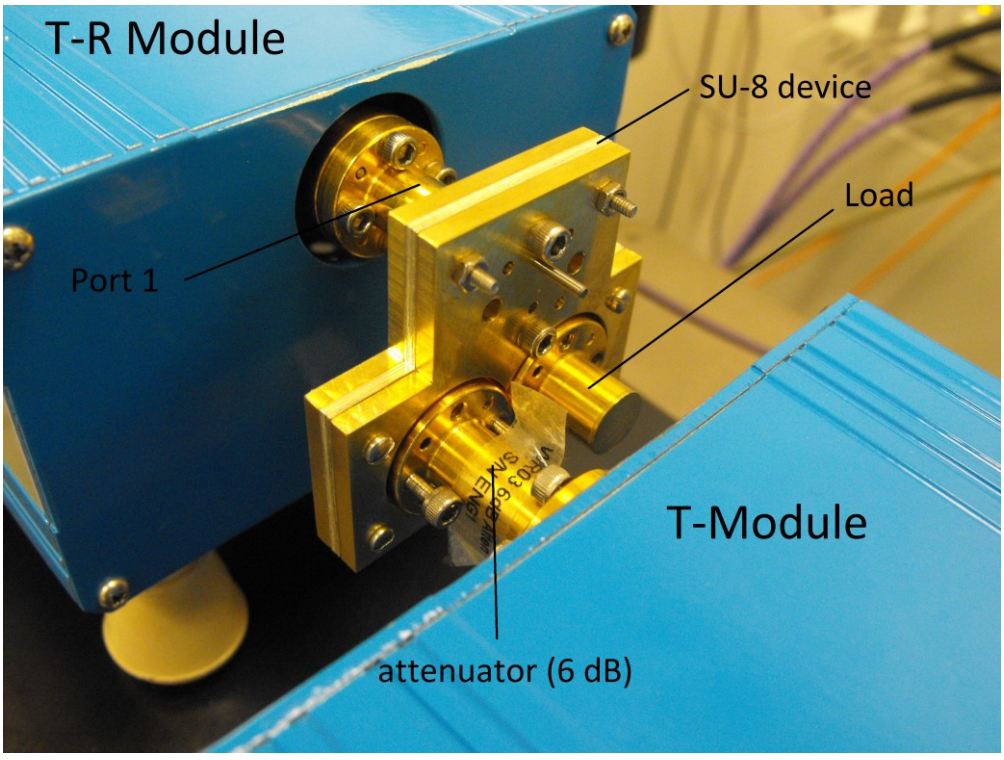

Figure 6.20: Measurement setup.

Figure 6.21 depicts the measured and simulated S_{21} and S_{31} of the diplexer, and figure 6.22 shows the measured and simulated reflection parameters S_{22} and S_{33}. The measured response of S_{11} presented unwanted ripple in the guard bands and it is depicted in figure 6.23.

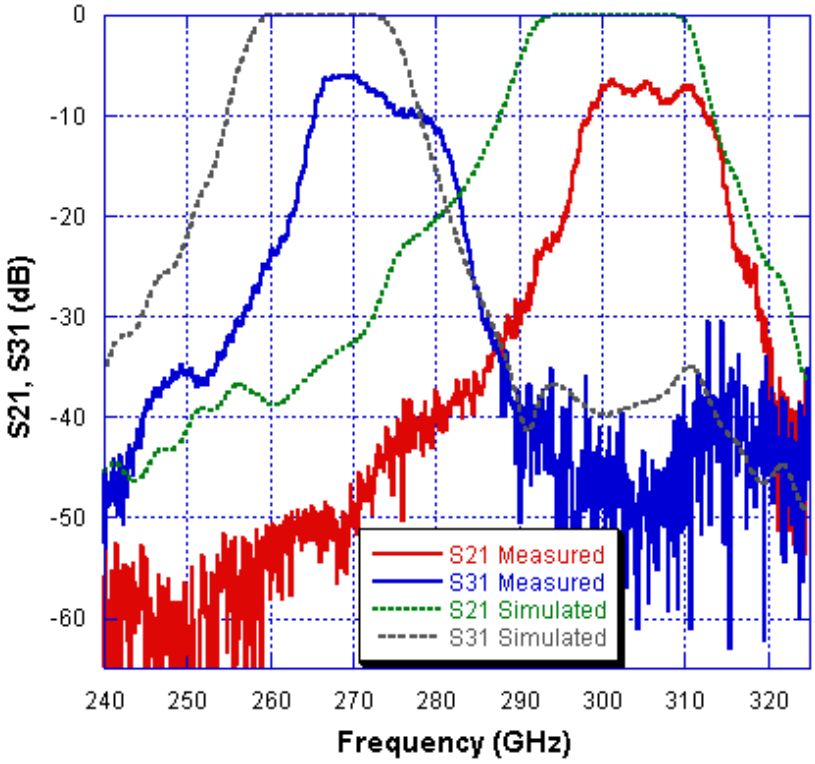

Figure 6.21: Measured and simulated S_{21} and S_{31}

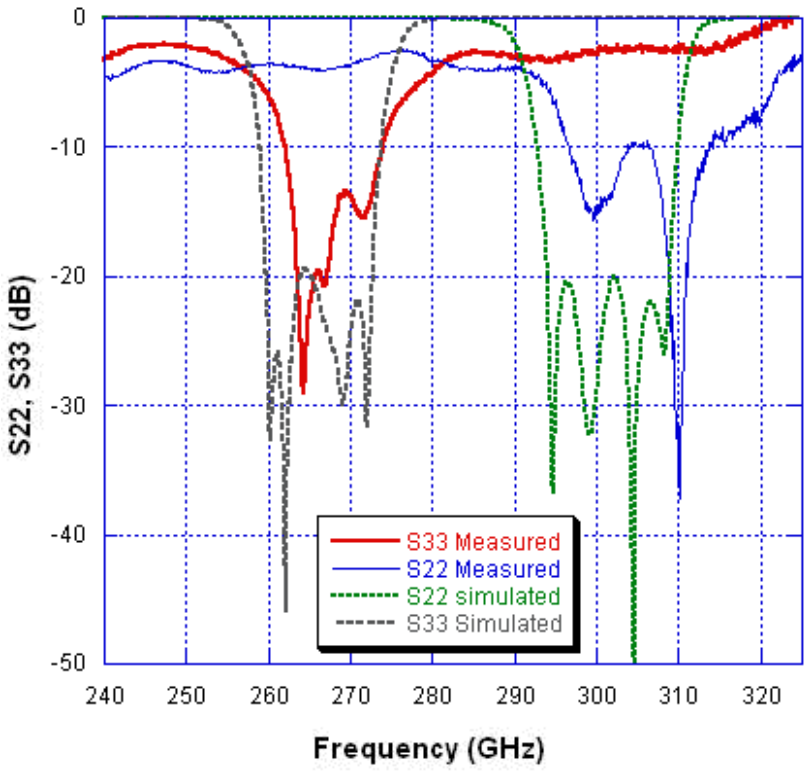

Figure 6.22: Measured and simulated S_{22} and S_{33}

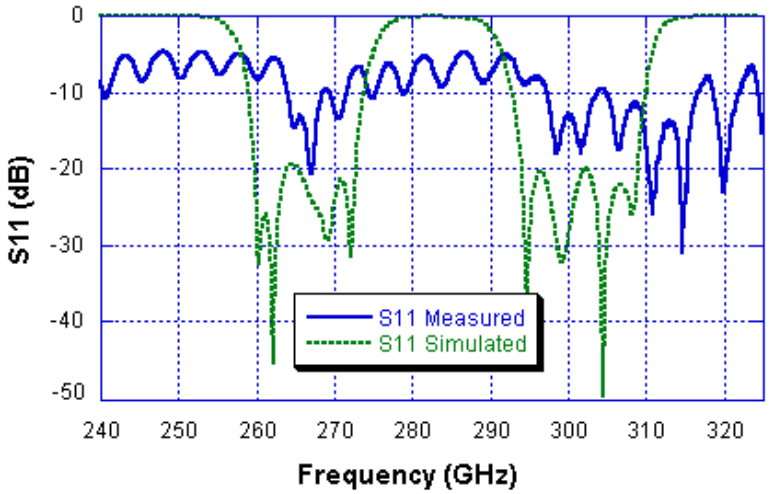

Figure 6.23: Measured and simulated S_{11}

The measured results show that the average insertion loss is 7.6 dB for $|S_{21}|$ and 8 dB for $|S_{31}|$, and that the maximum return loss at ports 2 and 3 is 10 dB and 13.4 dB, respectively. The high losses could have been attributed to the imperfection in coating the walls, especially at the narrow gaps corresponding to couplings between cavities. It is particularly difficult to access the walls at these gaps through metal evaporation even with rotating the SU-8 layers. The possibility of existence of air gaps in the interface between the SU-8 layers could have also caused more losses.

The effect of the finite conductivity of the metal walls on the insertion loss can be evaluated by considering the conductor losses of the waveguide sections, the bends, and the coupled resonator diplexer. Table 6.1 shows the insertion loss at different values of metal conductivity for the coupled resonator diplexer, the waveguide sections, and the bends. The insertion loss of the diplexer has been found from simulation results at 265 GHz and 300 GHz, and the conductor loss of the waveguide sections has been calculated using equation (6.7) at 265 GHz and 300 GHz for an overall length of waveguide sections of 29 mm. The conductor losses associated with the bends have been obtained from simulation results of each bend individually at 265 GHz and 300 GHz. Assuming that the degradation in the insertion loss is

mainly due to conductor losses in the whole structure, the calculations indicate that the effective conductivity that has been achieved is around 1% σ_{silver}. The quality of metal coating may be improved by carrying out the evaporation process several times to increase the thickness of the evaporated silver.

Table 6.1: Insertion loss at different conductivities

Conductivity	Diplexer *IL* (dB)		Waveguide sections (dB)		Bends loss (dB)		Total loss (dB)	
	265 GHz	300 GHz	265 GHz	300 GHz	265 GHz	300 GHz	265 GHz	300 GHz
$\sigma_{silver}=6.3x10^7$	0.23	0.23	0.377	0.347	0.144	0.186	0.751	0.763
10% σ_{silver}	0.727	0.756	1.192	1.097	0.426	0.568	2.345	2.421
1% σ_{silver}	2.26	2.34	3.768	3.471	1.312	1.79	7.34	7.601
0.5% σ_{silver}	3.18	3.29	5.329	4.9	1.854	2.571	10.363	10.761

The measured results also show that the bandwidth of each channel is narrower than the simulated results. This has been caused due to the significant insertion loss, and also due to the reduction in size of the coupling irises in the fabricated device in comparison to the design as shown earlier in section 6.5.2.

6.6 Conclusion

An SU-8 micromachined waveguide bend working in the H-band frequency range (220-325 GHz) has been presented. Such a bend provides a direct and accurate connection interface with standard waveguide flanges and allows interconnecting waveguide components such as cavity filters and diplexers. A 4-layer SU-8 structure of two back-to-back bends and straight WR-3 waveguide has been fabricated and tested and the measured results show better performance than micromachined SU-8 waveguides elsewhere in literature. The

measurements showed a return loss of -20 dB and a normalized insertion loss of 0.134 dB/mm at 300 GHz. Two brass plates have been used to clamp the metal coated SU-8 pieces together.

An H-band micromachined diplexer has also been designed, fabricated and tested. The diplexer structure consists of waveguide cavity resonators, relatively long waveguides, and matched bends, and it has been made of four layers of metal coated SU-8. Second metal evaporation has been done to fill any gaps in the interface between the layers and minimize the losses, and two brass plates have been used to clamp the SU-8 layers together. The measured response of the diplexer exhibited an average insertion loss of 7.6 dB for $|S_{21}|$ and 8 dB for $|S_{31}|$, and a bandwidth narrower that the desired. The imperfection of metal coating could have caused the high losses, in addition to the possibility of existence of gaps between the SU-8 layers. The coupling irises in the fabricated device are smaller than the design. This, in addition to the significant insertion loss, may have caused the bandwidth of each channel to be narrower than the specified bandwidth.

References

[1] W. H. Chow, A. Champion, and D. P. Steenson, "Measurements to 320 GHz of millimetre-wave waveguide components made by high precision and economic micro-machining techniques," *in Proc. 8th Freq. Postgrad. Stud. Colloq*., Sep. 8–9, 2003, pp. 90–93.

[2] C. H. Smith, A Sklavonuos, and N. S. Barker, "SU-8 Micromachining of Millimeter and Submillimeter Waveguide Circuits," *IEEE MTT-S International Microwave Symposium*, vols 1-3, pp. 961-964, 2009.

[3] C. H. Smith and N. S Barker," SU-8 Micromachining process for Millimeter and Submillimeter-wave Waveguide Circuit Fabrication," *in 33rd International Conference on Infrared, Millimeter and Terahertz Waves*, 15-19 Sept. 2008, pp. 1-2.

[4] S.G. Serra, A. Schneider, K. Malecki, S.E. Huq, and W. Brenner: "A simple bonding process of SU-8 to glass to seal a microfluidic device", *in Third International Conference on multi-material micro manufacture*, Borovets, Bulgaria Oct. 2007, pp. 43-46.

[5] M. Ke, Y. Wang, and M. J. Lancaster, "Design and realisation of low loss air-filled rectangular coaxial cable with bent quarter-wavelength supporting stubs," *Microw. Opt. Technol. Lett.*, vol. 50, pp. 1443–1446, May 2008.

[6] K. Suzuki and B. W. Smith, *Microlithography: Science and Technology*. 2nd edition, New York: CRC Press, Taylor & Francis Group, 2007.

[7] D. Banks , *Microengineering, MEMS, and Interfacing, a practical guide*. New York: CRC Press, Taylor & Francis Group, 2006.

[8] S. Chakraborty, *Microfluidics and microfabrication*. springer 2010.

[9] S-J Lee and N. Sundararajan, *Microfabrication for microfluidics*. Artech house, 2010.

[10] S. Franssila, *Introduction to Microfabrication*. John Wiley & Sons, 2004.

[11] J. Liu, B. Cai, J. Zhu, G. Ding, X. Zhao, C. Yang, and D. Chen,"Process research of high aspect ratio microstructure using SU-8 resist, " *Microsystem Technologies*, vol. 10, no.4, pp.265–268, May 2004.

[12] A. Del Campo and C. Greiner, "SU-8: a photoresist for high-aspect ratio and 3D submicron lithography," *J. Micromech. Microeng*., vol.17, no.6, pp. 81–95, 2007.

[13] M. Ke, Y. Wang, M. J. Lancaster, "Micromachined Rectangular Coaxial Line and Cavity Resonator for 77 GHz Applications using SU8 Photoresist", *Asia Pacific Microwave Conference*, Hong Kong , Dec. 2008, pp. 1-4.

[14] D.M. Pozar, *Microwave Engineering*. 2nd edition, John Wiley & Sons, 1998.

[15] W. B.W. Alison, *A Handbook for the Mechanical Tolerancing of Waveguide Components.* Artech House, 1972.

[16] A. Casanueva, J. A. Pereda, and A. Mediavilla, "Optimum compact H and E-plane corners in rectangular waveguide," *Microwave and Optical Technology Letters*, vol. 42, pp. 494-497, 2004.

[17] CST Microwave Studio. CST GmbH, Darmstadt, Germany, 2006.

[18] http://na.tm.agilent.com/pna/help/latest/S3_Cals/Select_Cal.htm

[19] http://ena.tm.agilent.com/e5071c/manuals/webhelp/eng/measurement/calibration/basic_ calibrations/enhanced_response_calibration.htm

Chapter 7

Conclusions and Future Work

7.1 Conclusions

The thesis has looked into coupled resonator circuits with multiple outputs. Design techniques used for coupled resonator filters have been extended here to multiple output circuits, and three-port coupled resonator power dividers and diplexers have been demonstrated in particular. The design approach allows synthesis of power dividers with arbitrary power division, as well as diplexers with novel topologies, and the realization of these components is possible using waveguide cavities, microstrip resonators or other types of resonators.

The coupling matrix of a multiport circuit with multiple coupled resonators has been derived. Magnetic and Electric couplings have been considered separately in the derivation, and then a unified solution has been generalized for both types of coupling. Transmission and reflection scattering parameters of a three-port coupled resonator circuit have been found in terms of the derived coupling matrix. The derived equations have been fundamental to the work in this thesis and they have formed a basis for the synthesis procedure. A gradient based optimization technique has been employed here to produce coupling matrices for the coupled resonator power dividers and diplexers.

Starting with power dividers, optimization has been successful in producing coupling matrices for power dividers with Chebyshev and Quasi-Elliptic filtering responses and with different power division ratios. Different topologies have been demonstrated, with large number of resonators shared in the signal paths between the input and output ports. Three-port *n*-coupled

resonator structures without cross-coupling have produced Chebyshev filtering responses with order of (n-1). Moreover, topologies of n-coupled resonators with cross coupling have produced Quasi-Elliptic filtering responses with order of (n-2). Polynomial characteristics have been formulated for the filtering coupled resonator power dividers. The proposed divider is not matched at output ports, and also the output ports are not isolated. This is a known drawback of 3-port junctions that can never be lossless, reciprocal, and matched at all ports at the same time.

Coupled resonator diplexers with novel topologies have been successfully synthesised using optimization. Unlike conventional diplexers, the proposed diplexers do not involve any external junctions for distribution of energy, such as waveguide manifolds, or T-junctions, or circulators. Thus, the proposed diplexers can be miniaturized, and the space of the external junction can be used to add resonator/resonators that contribute to the filter transfer function. However, the avoidance of the external junction is traded against reduction in isolation between diplexer channels. T-topologies that produce Chebyshev response and canonical topologies that produce Quasi-Elliptic response have been proposed. Both constrained and unconstrained local optimization techniques have been utilised to synthesise the coupling matrix, and a formula has been introduced to calculate the external quality factors of diplexers with symmetrical channels. Setting the values of the external quality factors at the outset of the optimization algorithm enhances the convergence time. It has been found that by using local optimisation techniques for relatively large structures, the optimisation algorithm may converge to a local minimum. To solve this problem, the optimisation has been done in two stages. The first stage assumed equally spaced reflection zeros and the resulting coupling coefficients have been used as initial values for the second stage. The frequency locations of the reflection zeros are then allowed to move in the second stage until equiripple level at the

specified insertion loss is achieved. Moreover, assigning different weights to the terms of the cost function has been found useful for convergence, especially for large structures.

A comparison between diplexers with the same specification (channels bandwidth, channels separation, return loss) and different topologies has been carried out. A conventional diplexer has been included in the comparison with the proposed diplexers in this thesis. It has been found that the higher the number of resonators in the path between output ports, the better the isolation. In consequence, the isolation performance of the proposed coupled resonator diplexers degrades in comparison to the conventional diplexers. However, an advantage of the proposed diplexers is that the source is directly coupled to the input resonator in the diplexer structure. This is distinct from the diplexers reported in the literature, since there is no need to use an external junction (T-junction, manifold, etc...) as in conventional diplexers, or to add a resonant junction (an extra resonator in addition to the channel filters) or to directly connect the common port to one terminal of each of the channel filters, which may have practical difficulties in implementation. Thus, the proposed coupled resonator diplexers exhibit a trade-off between design complexity and isolation performance.

Coupled resonator power dividers and diplexers have been implemented to verify the design approach. They have been realized using waveguide cavity resonators coupled together using either capacitive or inductive irises. The devices are: X-band 3-dB power divider, X-band unequal power divider, X-band 4-resonator diplexer, X-band 12-resonator diplexer, and E-band diplexer. The X-band devices have been made of two mirror-image blocks of copper, and metal screws have been used to tune the filtering response of these devices. The measured results are in good agreement with the simulated results. The E-band diplexer has been designed to be used as a front end component in the transceiver of a wireless point-to-point communication system that offers Ethernet gigabit connectivity. It is specified to work at the

frequency bands 71-76 GHz and 81-86 GHz. The diplexer has been designed with twelve resonators to fulfil the stringent requirements of selectivity and high isolation. In comparison to the conventional E-band diplexers currently in the market, the proposed diplexer is miniaturised since it is designed of a folded structure of coupled resonators without any external junctions.

A micromachined coupled resonator diplexer with embedded bends working in the H-band (220-325 GHz) has also been designed, fabricated and tested. The micromachining work started with the design of a structure of two back-to-back matched bends with a 16 mm straight through WR-3 (220-325 GHz) waveguide. The bend is matched over the H-band, and it has been designed to be interconnected with waveguide components (filters, diplexers…etc) to provide secure and accurate connection between the device and the test ports' flanges. The back-to-back bends structure has been constructed by bonding four layers of metal coated SU-8 photoresist that were fabricated using a micromachining technique. It has been tested and the measurements showed a return loss of -20 dB and a normalized insertion loss of 0.134 dB/mm at 300 GHz. The device has been measured many times and the results were repeatable.

The designed bend has then been integrated in the design of the structure of the micromachined coupled resonator diplexer. The diplexer structure consists of waveguide cavity resonators, relatively long waveguides, and matched bends. The whole structure has been made of four layers of metalized SU-8. Second metal evaporation was a necessary step to minimize the losses by filling the gaps in the interface between the aligned and bonded layers. Two brass plates have been used to clamp the SU-8 pieces together. The diplexer has been tested, and the measurement showed an average insertion loss of 7.6 dB for $|S_{21}|$ and 8 dB for $|S_{31}|$. The possibility of existence of gaps between the SU-8 layers, and the

imperfection of metal coating could have caused the high losses. The measurement also showed that the achieved bandwidth is narrower than the desired. This has been caused due to the significant insertion loss and also since the coupling irises in the fabricated device were smaller than the design.

7.2 Future Work

The work on coupled resonator diplexers can be further developed for more complicated coupling structures. Increasing the number of cross-couplings between resonators in the structure of the diplexer results to more transmission zeros, and hence selectivity can be improved. Further work can also be conducted on coupled resonator diplexers with asymmetrical channels, so that channels bandwidths are different, or channels have different filtering functions. This, together with the symmetrical channel diplexers presented in this thesis, would provide a general solution of coupled resonator diplexers that satisfies the specifications of many practical applications. Further work can also be conducted to improve the isolation between the diplexer channels, as it has been shown that the isolation performance of the proposed coupled resonator diplexers degrades in comparison with the conventional diplexers. This may be tried by adding couplings between non-adjacent resonators.

An analytic solution may be sought to find the coupling matrix entries of the proposed coupled resonator power dividers and diplexers. This would provide an alternative way to using optimization techniques in the synthesis process, and would give an insight and better understanding of the synthesis.

The synthesis of coupled resonator circuits with multiple outputs can be pursued further for more output ports. This enables more passive components to be made of coupled resonators

such as *N*-way power dividers, hybrid couplers and multiplexers, which are key devices in microwave communication systems. The design procedure presented in this thesis for coupled resonator three-port power dividers and diplexers can be generalised to multi-port coupled resonator components, and the general coupling matrix derived in this thesis can be employed as a basis for the synthesis. The level of complexity of synthesis increases for coupled resonator structures if the number of coupled resonators and the number of output ports increase. Hence, efficient optimisation techniques are required to produce the coupling matrices.

Appendix A

Cameron's Recursive Technique

For a two port lossless filter composed of N coupled resonators, the Nth degree filtering function is defined as a ratio between two polynomials,

$$C_N(\omega) = \frac{F_N(\omega)}{P_N(\omega)} \tag{A.1}$$

where the roots of $F(\omega)$ correspond to the reflection zeros, and the roots of $P(\omega)$ correspond to the prescribed transmission zeros. The polynomial $P(\omega)$ is constructed from the prescribed transmission zeros, and the polynomial $F(\omega)$ is found using Cameron's technique that is presented here.

The filtering function $C_N(\omega)$ has a form of general Chebyshev characteristic,

$$C_N(\omega) = \cosh\left(\sum_{k=1}^{N} \cosh^{-1}(x_k)\right) \tag{A.2}$$

where

$$x_k = \frac{\omega - 1/\omega_k}{1 - \omega/\omega_k}$$

and $j\omega_k = s_k$ is the position of the kth transmission zero in the complex frequency domain. If all the transmission zeros are at infinity, the filtering function C_N degenerates to the pure Chebyshev function,

$$C_N(\omega)\big|_{\omega_k \to \infty} = \cosh\left(N \cosh^{-1}(\omega)\right) \tag{A.3}$$

In order to find the roots of $F_N(\omega)$, the expression of $C_N(\omega)$ in (A.2) will be rearranged in a form of numerator and denominator, so that the numerator zeros will be equal to the roots of $F_N(\omega)$ as in (A.1).

The synthesis proceeds by replacing the $\cosh^{-1}$ in equation (A.2) with its identity, that is $\cosh^{-1}(x) = \ln\left(x + \sqrt{x^2 - 1}\right)$, which yields to,

$$C_N(\omega) = \cosh\left[\sum_{k=1}^{N} \ln\left(a_k + b_k\right)\right] \tag{A.4}$$

where $a_k = x_k$, and $b_k = \sqrt{x_k^2 - 1}$. Using the identity $\cosh(x) = \frac{1}{2}\left(e^x + e^{-x}\right)$, equation (A.4) may be re-written as,

$$C_N(\omega) = \frac{1}{2}\left[\exp\left(\sum_{k=1}^{N} \ln\left(a_k + b_k\right)\right) + \exp\left(-\sum_{k=1}^{N} \ln\left(a_k + b_k\right)\right)\right] \tag{A.5}$$

Thus

$$C_N(\omega) = \frac{1}{2}\left[\prod_{k=1}^{N}\left(a_k + b_k\right) + \frac{1}{\prod_{k=1}^{N}\left(a_k + b_k\right)}\right] \tag{A.6}$$

Multiplying the numerator and denominator of the second term in equation (A.6) by $\prod_{k=1}^{N}\left(a_k - b_k\right)$ yields,

$$C_N(\omega) = \frac{1}{2}\left[\prod_{k=1}^{N}\left(a_k + b_k\right) + \prod_{k=1}^{N}\left(a_k - b_k\right)\right] \tag{A.7}$$

Equation (A.7) may be rewritten in its final form by substitution of a_k, b_k, and x_k as follows,

$$C_N(\omega) = \frac{1}{2}\left[\frac{\prod_{k=1}^{N}\left(c_k + d_k\right) + \prod_{k=1}^{N}\left(c_k - d_k\right)}{\prod_{k=1}^{N}\left(1 - \frac{\omega}{\omega_k}\right)}\right] \tag{A.8}$$

Where $c_k = \omega - \frac{1}{\omega_k}$, $d_k = \omega'\left(1 - \frac{1}{\omega_k^2}\right)^{\frac{1}{2}}$, and $\omega' = \sqrt{\omega^2 - 1}$, a transformed frequency variable.

Comparing equations (A.8) and (A.1), it is noticed that the numerator of $C_N(\omega)$ is $F_N(\omega)$, whose zeros correspond to the reflection zeros, and that the denominator of $C_N(\omega)$ is $P(\omega)$, whose zeros correspond to the prescribed transmission zeros.

The numerator in equation (A.8) can be rewritten as follows,

$$num\left[C_N(\omega)\right]=\frac{1}{2}\left[G_N(\omega)+G'_N(\omega)\right]=F_N(\omega) \tag{A.9}$$

Where

$$G_N(\omega)=\prod_{k=1}^{N}\left[c_k+d_k\right]=\prod_{k=1}^{N}\left[\left(\omega-\frac{1}{\omega_k}\right)+\omega'\left(1-\frac{1}{\omega_k^2}\right)^{\frac{1}{2}}\right] \tag{A.10}$$

$$G'_N(\omega)=\prod_{k=1}^{N}\left[c_k-d_k\right]=\prod_{k=1}^{N}\left[\left(\omega-\frac{1}{\omega_k}\right)-\omega'\left(1-\frac{1}{\omega_k^2}\right)^{\frac{1}{2}}\right] \tag{A.11}$$

The polynomial $G_N(\omega)$ can be rearranged as a sum of two polynomials $U_N(\omega)$ and $V_N(\omega)$,

$$G_N(\omega)=U_N(\omega)+V_N(\omega)$$

where $U_N(\omega)$ polynomial has its coefficients in terms of ω only, whereas $V_N(\omega)$ polynomial has its coefficients multiplied by the transformed variable ω' as follows,

$$U_N(\omega)=u_0+u_1\omega+u_2\omega^2+\cdots \tag{A.12}$$

$$V_N(\omega)=\omega'\left(v_0+v_1\omega+v_2\omega^2+\cdots\right) \tag{A.13}$$

The coefficients of these polynomials are found through a recursive process. It starts by setting k=1 into equation (A.10), which corresponds to the first prescribed transmission zero ω_1, as follows,

$$\begin{aligned} G_1(\omega) &= \left(\omega-\frac{1}{\omega_1}\right)+\omega'\left(1-\frac{1}{\omega_1^2}\right)^{\frac{1}{2}} \\ &= U_1(\omega)+V_1(\omega) \end{aligned} \tag{A.14}$$

The recursive process continues with k=2, which corresponds to the second prescribed transmission zero ω_2, by multiplying $G_1(\omega)$ from the previous iteration by $[c_2+d_2]$, as follows,

$$\begin{aligned} G_2(\omega) &= G_1(\omega)\cdot[c_2+d_2] \\ &= \left[U_1(\omega)+V_1(\omega)\right]\cdot\left[\left(\omega-\frac{1}{\omega_2}\right)+\omega'\left(1-\frac{1}{\omega_2^2}\right)^{\frac{1}{2}}\right] \\ &= \left[U_2(\omega)+V_2(\omega)\right] \end{aligned} \tag{A.15}$$

The formulae for $U_2(\omega)$ and $V_2(\omega)$ are,

$$\begin{aligned} U_2(\omega) &= \omega U_1(\omega)-\left(\frac{1}{\omega_2}\right)\cdot U_1(\omega)+\left(1-\frac{1}{\omega_2^2}\right)^{\frac{1}{2}}\cdot\omega' V_1(\omega) \\ V_2(\omega) &= \omega V_1(\omega)-\left(\frac{1}{\omega_2}\right)\cdot V_1(\omega)+\left(1-\frac{1}{\omega_2^2}\right)^{\frac{1}{2}}\cdot\omega' U_1(\omega) \end{aligned} \tag{A.16}$$

The process continues for k=3,…,N (including the zeros at infinity) by multiplying $[c_k+d_k]$ by $G_{k-1}(\omega)$, found in the previous iteration, to find $G_k(\omega)=U_k(\omega)+V_k(\omega)$.

The general formulae for $U_k(\omega)$ and $V_k(\omega)$ are,

$$\begin{aligned} U_k(\omega) &= \omega U_{k-1}(\omega)-\left(\frac{1}{\omega_k}\right)\cdot U_{k-1}(\omega)+\left(1-\frac{1}{\omega_k^2}\right)^{\frac{1}{2}}\cdot\omega' V_{k-1}(\omega) \\ V_k(\omega) &= \omega V_{k-1}(\omega)-\left(\frac{1}{\omega_k}\right)\cdot V_{k-1}(\omega)+\left(1-\frac{1}{\omega_k^2}\right)^{\frac{1}{2}}\cdot\omega' U_{k-1}(\omega) \end{aligned} \tag{A.17}$$

Repeating the same process for $G'_N(\omega)=U'_N(\omega)+V'_N(\omega)$, it is found that $U'_N(\omega)=U_N(\omega)$, and $V'_N(\omega)=-V_N(\omega)$. Substitution the results into equation (A.9) shows that the numerator of $C_N(\omega)$ is $U_N(\omega)$, and the reflection zeros can be found by rooting $U_N(\omega)$. The roots of $V_N(\omega)$ correspond to the N-1 in-band reflection maxima.

Appendix B : K&L Microwave diplexer datasheet

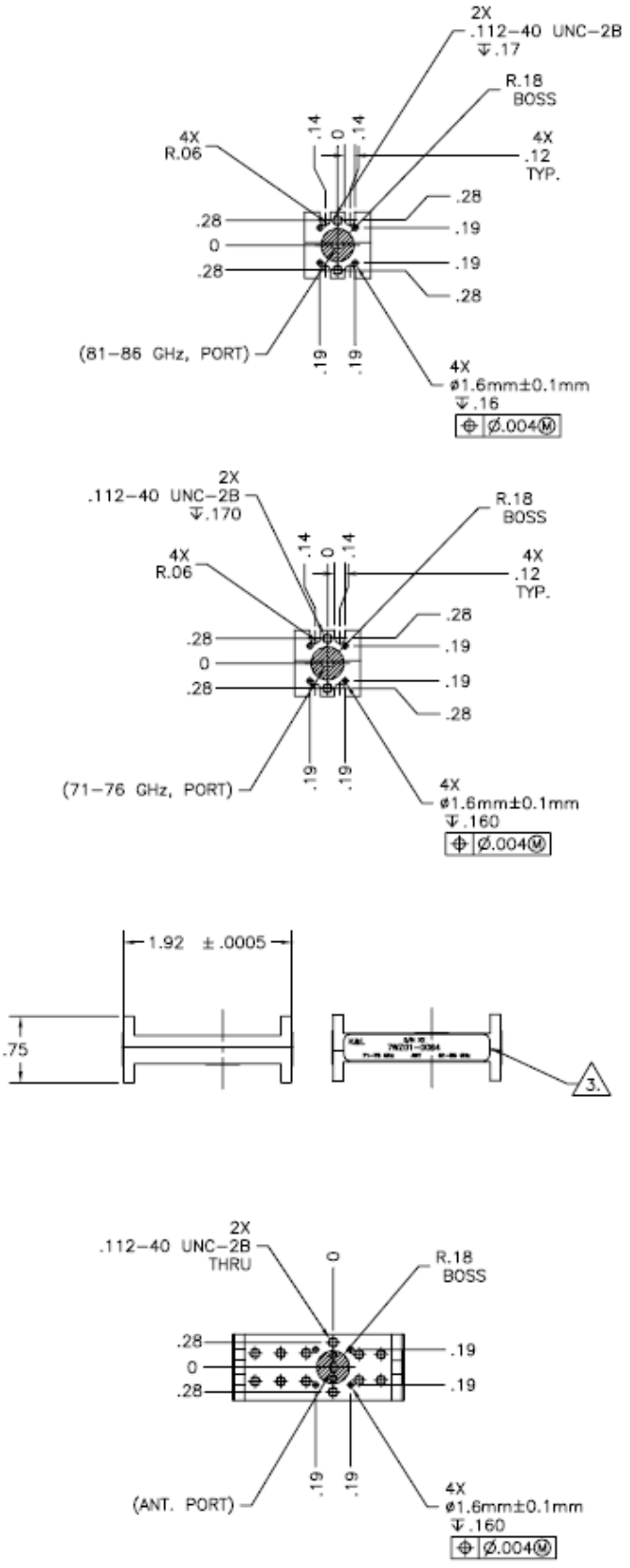

Appendix C

Publications

- **T. Skaik**, M. Lancaster, and F. Huang, "Coupled-Resonator 3-dB Power Divider," *Proceedings of the IET seminar on Passive RF and Microwave Components*, Birmingham UK, April 2010, pp. 21-36.

- **T. Skaik**, Y. Wang, M. Ke, S. Qian, and M. Lancaster, "A Micromachined WR-3 Waveguide with Embedded Bends for Direct Flange Connections," *Proceedings of the 40th European Microwave Conference,* Paris, Sep. 2010, pp. 1225-1228.

- **T. Skaik**, M. Lancaster, and F. Huang, "Synthesis of multiple output coupled resonator microwave circuits using coupling matrix optimization," *IET Journal of Microwaves, Antennas and Propagation,* 2011. **Accepted**

- **T. Skaik**, M. Lancaster, "Coupled Resonator Diplexer without External Junctions," **submitted *to*** *IEEE Microwave and Wireless Components letters*.

Coupled-Resonator 3-dB Power Divider

Talal Skaik, Michael Lancaster, Frederick Huang

School of Electronic, Electrical and Computer Engineering, University of Birmingham, B15 2TT, U.K

Email: tfs655@bham.ac.uk, m.j.lancaster@bham.ac.uk, f.huang@bham.ac.uk

Power dividers are passive devices used to divide an input signal into two or more signals of lower power. T-junctions and Wilkinson dividers are examples of widely used power dividers. Here we present a technique to synthesise a coupled-resonator power divider. The synthesis of multiport microwave coupled-resonator networks has been presented in [1]. N-port devices formed from magneto-inductive waveguides based on coupled loop resonators have been reported in [2]. The design of the power divider proposed here is based on coupling matrix optimization for multiple coupled resonators with multiple outputs. The synthesis employs coupling matrix optimisation techniques similar to those developed for coupled resonator filters. The realisation of such dividers is possible using microstrip resonators, waveguide cavities, or other types of resonators.

Fig. 1 (a) depicts a proposed structure of the power divider. It consists of *n* coupled resonators arranged in a T-topology; it is a 3-port network and will be designed with a Chebyshev filter response for S_{12} and S_{13}. The order of the filtering function at each output is equal to *(n*-1), where *n* is the total number of resonators. The coupling coefficients $m_{(n-2),(n-1)}$ and $m_{(n-2),n}$ determine the power division ratio. These coefficients will have equal values in case of 3-dB power division, and different values for arbitrary power division. An X-band 3-dB power divider has been realized using 4 waveguide cavity resonators to demonstrate the approach.

The coupling matrix of *n* coupled resonators in an *N*-port network has been derived from the equivalent circuit by formulation of impedance matrix for magnetically coupled resonators or admittance matrix for electrically coupled resonators in a similar way to the two port formulation in [3]. Each type of coupling has been considered separately and then a solution has been generalized for both types of coupling. A general normalized coupling matrix [*A*] in terms of coupling coefficients, and external quality factors, for any coupled resonator structure with multiple outputs, has been derived as shown in equation (1).

$$[A]=\begin{bmatrix} 1/q_{e1} & \cdots & & 0 \\ \vdots & \vdots & \vdots & \vdots \\ 0 & \cdots & & 0 \\ & & & \\ 0 & \cdots & & 1/q_{en} \end{bmatrix} + P\begin{bmatrix} 1 & \cdots & & \\ \vdots & \vdots & \vdots & \vdots \\ 0 & \cdots & & \\ 0 & \cdots & & \end{bmatrix} - J\begin{bmatrix} m_{11} & \cdots & & m_{1n} \\ \vdots & \vdots & \vdots & \vdots \\ m_{(n-1)1} & \cdots & & m_{(n-1)n} \\ m_{n1} & \cdots & & m_{nn} \end{bmatrix} \quad (1)$$

where q_{ei} is the scaled external quality factor of resonator *i*, *P* is the complex lowpass frequency variable, m_{ij} is the normalized coupling coefficient between resonators *i* and *j*, and the diagonal entries m_{ii} represent the self coupling coefficients for asynchronously tuned filter. The scattering parameters have been also derived as a function of the general coupling matrix as shown in (2).

$$S_{11}=1-\frac{2}{q_{e1}}[A]^{-1}_{11},\quad S_{21}=\frac{2}{\sqrt{q_{e1}q_{e(n-1)}}}[A]^{-1}_{(n-1)1},\quad S_{31}=\frac{2}{\sqrt{q_{e1}q_{en}}}[A]^{-1}_{n1} \quad (2)$$

The synthesis procedure of coupling matrices of the proposed coupled-resonator power divider using optimization is based on minimization of a cost function that is evaluated at frequency locations of reflection zeros. The derived equations (1) and (2) have been utilized in the optimization algorithm. A gradient-based local optimization technique that is used in coupled resonator filters synthesis has been employed here similar to the two port method described in [4].

A 4 resonator 3-dB power divider has been designed, fabricated and tested to evaluate the techniques. It is designed at X-band with a centre frequency of 10 GHz, a bandwidth of 570 MHz, and a reflection loss of 20 dB at the passband using waveguide cavity resonators coupled together using inductive irises. Fig. 1 (b) shows the synthesized coupling matrix (normalized), and Fig. 1(c) depicts the divider structure. The input and output external quality factors ($Q_{ei}=q_{ei}/FBW$) and the coupling coefficients ($M_{ij}=m_{ij}.FBW$), where FBW is the fractional bandwidth, are computed for a FBW =5.7% and found to be M_{12}= 0.0590, $M_{23}=M_{24}$= 0.0417, and $Q_{e1}= Q_{e3}= Q_{e4}$=14.94.

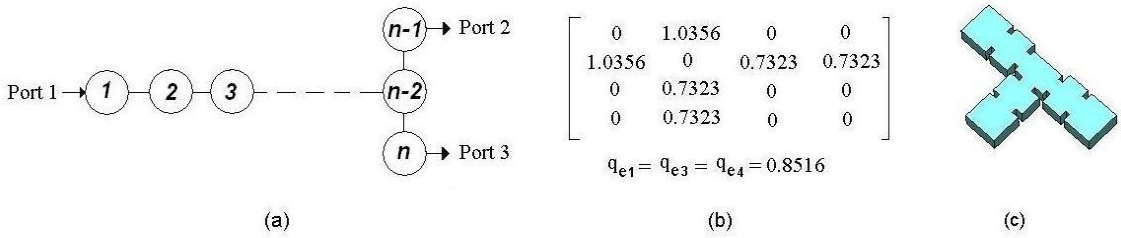

Fig. 1 (a) Resonator topology, (b) Normalized coupling matrix, n=4, (c) Divider structure, n=4.

The simulated and measured results of the power divider are given in Fig. 2. The measured response has been tuned using the metal screws and the result is in good agreement with the simulated response. The experimental results show that the maximum return loss within the passband is 20 dB and the minimum insertion loss is 3.3 dB. The bandwidth of the measured response is 1.23% narrower than the simulated response and the measured isolation S_{23} within the passband is around 6 dB as expected. The proposed divider is not matched at all ports, and the output ports are not isolated, which is typical for lossless reciprocal 3-port junctions.

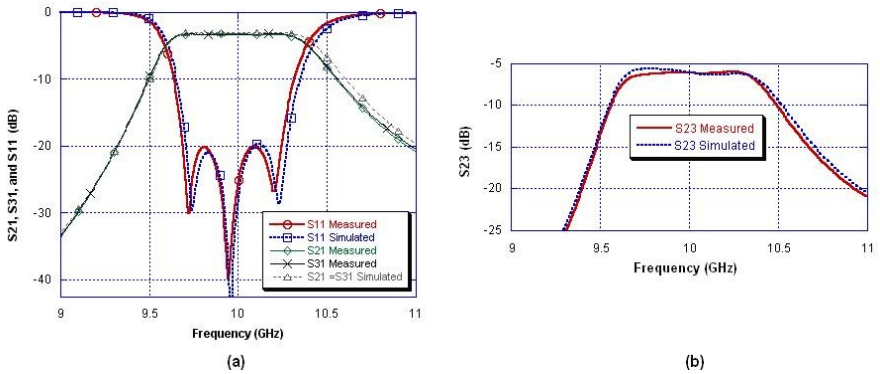

Fig. 2. Measured and Simulated results, (a) S_{11}, S_{21}, S_{31} (dB), (b) S_{23} (dB).

To conclude, a Coupled-Resonator 3-dB power divider has been synthesised using coupling matrix optimization. An X-band power divider has been designed, fabricated and tested to demonstrate the new approach.

References

[1] A. Garcia-Lamperez, M. Salazar-Palma, and T.K. Sarkar, "Analytical synthesis of microwave multiport networks," IEEE MTT-S International Microwave Symposium digest, vol. 2, pp. 455-458, 2004.

[2] R.A. Syms, E. Shamonina and L. Solymar, "Magneto-inductive waveguide devices", IEE Proc.-Microw. Antennas Propag., vol. 153, No. 2, April 2006

[3] Hong, J.S. and M.J. Lancaster, Microstrip filters for RF/microwave applications. 2001, New York: Wiley.

[4] A.B. Jayyousi, and M.J. Lancaster, "A gradient-based optimization technique employing determinants for the synthesis of microwave coupled filters," IEEE MTT-S International Microwave Symposium, USA, vol. 3, pp. 1369-1372, June 2004.

A Micromachined WR-3 Waveguide with Embedded Bends for Direct Flange Connections

Talal Skaik[*1], Yi Wang[*2], Maolong Ke[*3], Shilong Qian[*4], Michael Lancaster[*5]

[*]*School of Electronic, Electrical and Computer Engineering, University of Birmingham, B15 2TT, U.K*

[1]
[2]
[3]m.l.ke@bham.ac.uk
[4]
[5]m.j.lancaster@bham.ac.uk

***Abstract*— A novel micromachined waveguide bend operating in the frequency range 220-325 GHz is presented. It provides for a direct and accurate connection with standard waveguide flanges. A structure of two back-to-back right angle bends and a straight 16mm long WR-3 rectangular waveguide has been fabricated and tested using a UG-387 flange. The structure is made of four layers of metallised SU-8 pieces using a micromachining technique. The measurements show a return loss of -20dB and a normalized insertion loss of 0.134 dB/mm at 300 GHz.**

I. INTRODUCTION

The growing demand for higher bandwidths in communications systems and for higher resolution imaging has increased the interest in components working in the millimetre and the terahertz frequency ranges. The fabrication of high precision waveguide components operating at these frequencies using standard metal machining is very expensive. Alternatively, micromachining can be used to produce millimetre wave components with good dimensional accuracy, high performance and reduced cost. Here we use SU-8 as the micromachining technology.

The fabrication of various SU-8 based waveguide sections and the measurement using a specially designed metal block have been demonstrated in [1]. The measured WR-3 waveguide showed an insertion loss between 0.625 dB/mm and 1.125 dB/mm over the range 220-325 GHz. A straight SU-8 based WR-3 waveguide has also been reported in [2]. The waveguide exhibited normalized insertion loss between 0.09 dB/mm and 0.44 dB/mm over the range 220-325 GHz, and reflection response with many undesirable spikes. This was attributed to a loose connection between the test port flange and the device under test. It is particularly difficult to accurately connect to such tiny waveguides, and here we investigate one solution to the problem.

This paper presents the fabrication and measurement of a WR-3 rectangular waveguide section with two back-to-back matched bends enabling accurate positioning of the flange alignment pins and waveguide. The device is made of four layers of metal coated SU-8 using photolithography to produce the micromachined circuit. The proposed structure provides accurate and repeatable connection between the micromachined device and the flanges, and the measured results exhibit normalized insertion loss of 0.134 dB/mm at 300 GHz. To the best of the authors' knowledge, the measured results represent the best performance ever demonstrated on any micromachined waveguides at the same frequency range.

A cross section of the waveguide is shown in Fig. 1. It is composed of four layers of metal coated SU-8, each of a thickness of 432 μm. Layer 1 and 2 are bonded together using conducting glue to make half of the split blocks, and layer 3 and 4 are bonded to form the other half. To minimize the resistive losses, and to avoid any gaps between the SU-8 layers, a second metal evaporation has been done on each of the two halves.

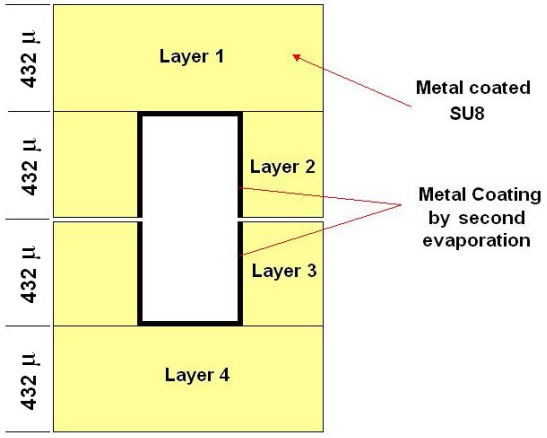

Fig. 1 Cross sectional view of the micromachined waveguide structure.

II. BEND DESIGN

Waveguide right-angle corners exhibit narrowband and mismatched response. Conventionally, a broadband matching is achieved by using a smooth transition such as multi-stepped or multi-mitred corners [3], [4]. However, these configurations are not compatible with the layered structures proposed in this paper. A modified waveguide bend that can be fabricated using the micromachining

technology is therefore presented here. The bend has two ridges at the junction region; each contributes a resonance into the desired frequency band and broadens the matched bandwidth. The bend structure, with the optimized dimensions is shown in Fig. 2, and the simulated response is given in Fig. 3. The geometries of the ridges have been adjusted by EM optimization [5] to achieve matching in the range between 250-320 GHz with a return loss of -20dB or better. A more complicated structure would be required to achieve matching over the whole WR-3 band (220-325 GHz).

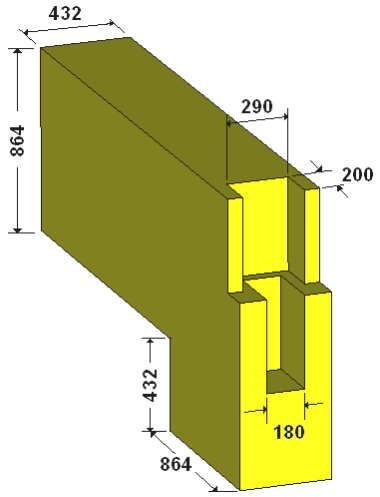

Fig. 2 Structure of the bend. Dimensions are in micrometers.

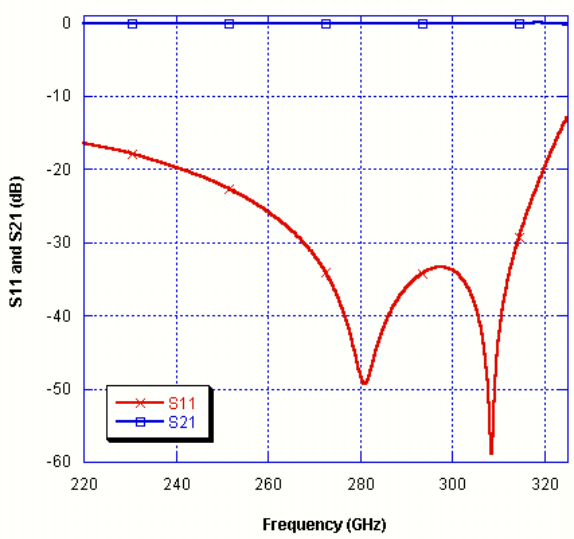

Fig. 3 Simulated response of the bend.

To measure the bend, a structure of two back-to-back bends and a straight waveguide section is constructed. It is formed of four micromachined layers; each contains holes to allow alignment pins and screws of the test flanges to pass through. The locations and diameters of these holes match those in the standard UG-387 waveguide flange. Fig. 4 depicts the back-to-back structure and the top view of layer 2. The waveguide length is around 16mm excluding the bends; this is made sufficiently long to permit fair separation between the flanges so that pins and screws are not blocked from the other side. The size of each SU-8 layer is 432 µm x 48 mm x 24 mm. Crucially the alignment pin holes and waveguide are now formed by the micromachining process, this enables the micromachining process to control the accuracy of the alignment. The bends allow the waveguide to be in the same plane as the SU-8 layers. This is distinct from the previous work [1, 2] where the waveguide flange was connected laterally to the SU-8 layers. The proposed structure will eventually allow other waveguide components such as filters to be interconnected between the bends. Moreover, it may be extended to include multiport components such as waveguide multiplexers.

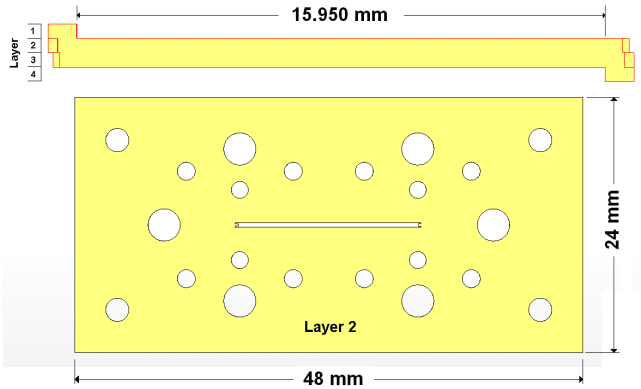

Fig. 4 Side view of back-to-back structure and top view of layer 2.

III. FABRICATION AND ASSEMBLY

SU-8 photolithography process has been utilized to produce the device. A more detailed description can be found in [6], [7]. Firstly, an amount of SU-8 was dispersed onto a 4-in silicon wafer for spinning, then the resist was pre-baked to evaporate the solvents, then the sample was exposed under UV light to define the right patterns by photolithography. Post-baking was then carried out to strongly cross-link the defined patterns, and then the wafer was developed in Ethyl lactate solvent and hard baked. The SU8 pieces were then released from silicon and metallised. The metal coating was done by firstly sputtering 5 nm of Cr adhesion layer, then evaporating just over 1µm thick silver and a thin protection layer of 20nm gold. The evaporation was done using an off-axis rotation in order to make sure the metal walls of the waveguide were well coated.

Once the four SU-8 layers were ready for assembly, layers 1 and 2 were aligned and bonded together using conducting glue, and then a second metal coating was performed to fill any gaps in the interface between the

layers, as mentioned earlier. The same process was done for layers 3 and 4. Finally, the device was assembled and the pieces were aligned using pins, and then clamped together using conventionally machined metal plates made from brass. It should be noted that these brass plates bear no function for alignment, considering their inferior fabrication accuracy as compared with micromachining. A secure connection between the standard flange and the SU-8 device is realised since the flanges are directly connected to the first and the fourth layers using screws. A photograph of the assembled device is shown in Fig. 5.

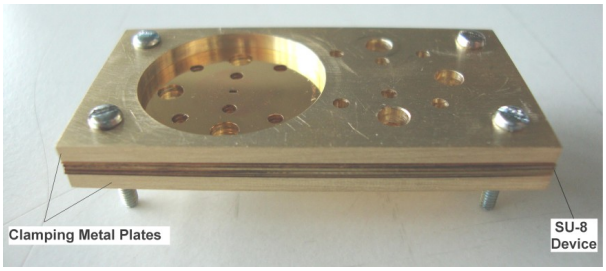

Fig 5 Assembled device

IV. MEASUREMENT RESULTS

An Agilent E8361A Network Analyser with OML extension modules V03VNA2-T/R and V03VNA2-T (220-325 GHz) have been used to take measurements. Only one transmission measurement (S_{21}) and one reflection measurement (S_{11}) are possible by using one T/R module and one T module. The device has to be reversed to measure the parameters (S_{12}) and (S_{22}). Moreover, the return loss at any port has been measured with the other port connected to load. An Enhanced-Response calibration that combines a one-port calibration and a response calibration was performed first. A photograph of the measurement setup showing the SU-8 device clamped between the metal plates and connected to the test ports is depicted in Fig. 6.

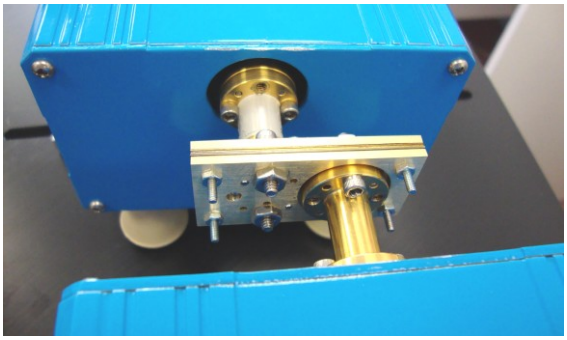

Fig. 6 Photograph of the measurement setup

Fig. 7 displays the simulated and the measured S-parameters of the back-to-back structure. The metal used in the lossy simulation in Fig.7 (b) is silver, which has a conductivity of 6.3×10^7 S/m. The measured results show a return loss of better than -16dB and insertion loss of 2.5 - 3 dB in the frequency range 240-312 GHz. We believe that the imperfection of metal conductivity, and also the possibility of existence of gaps in the interface between the layers may have caused the higher-than-simulated insertion loss.

The measurements have shown good repeatability. This, together with the measured low return loss, indicates a reliable flange connection. The multiple nulls in the S_{11} response are due to signal reflections at the end of the waveguide sections.

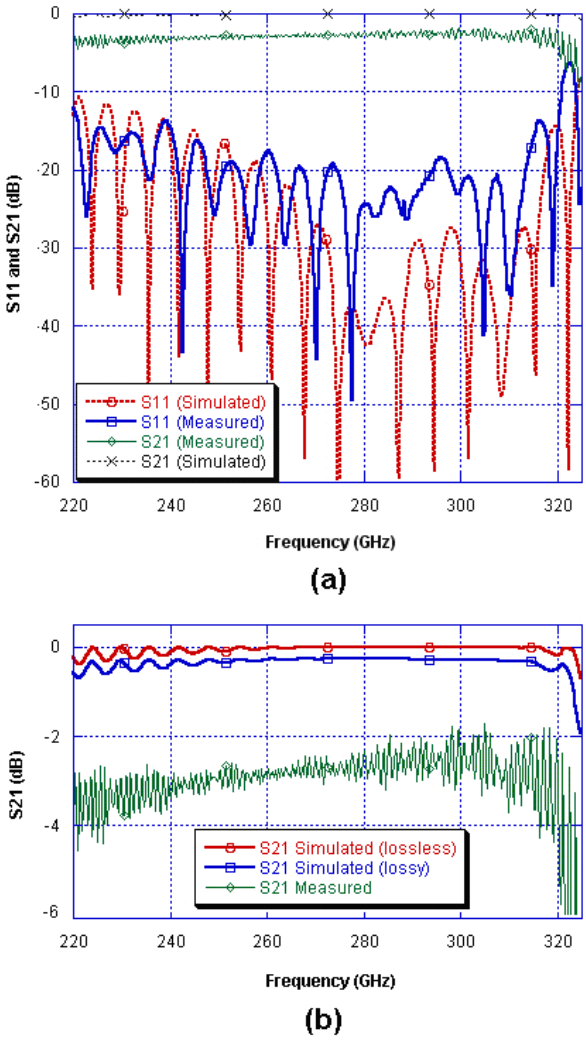

Fig. 7 (a) Measured and simulated results, (b) passband details

V. CONCLUSIONS

An SU-8 micromachined waveguide bend has been presented. Such a bend provides a direct and accurate connection interface with standard waveguide flanges and will allow interconnecting waveguide components such as cavity filters. A 4-layer SU-8 structure of two back-to-back bends and straight WR-3 waveguide has been fabricated and tested and the measured results show better

performance than micromachined SU-8 waveguides elsewhere in literature. Two brass plates have been used to clamp the metal coated SU-8 pieces together. In the near future, 300 GHz devices such as filters and diplexers will be fabricated and tested by employing the designed waveguide bends in the measurement.

ACKNOWLEDGMENT

This work has been funded by the UK Engineering and Physical Science Research Council (EPSRC).

REFERENCES

[1] W. H. Chow, A. Champion, and D. P. Steenson, "Measurements to 320 GHz of millimetre-wave waveguide components made by high precision and economic micro-machining techniques," in Proc. 8th Freq. Postgrad. Stud. Colloq., Sep. 8–9, 2003, pp. 90–93.

[2] C. H. Smith, A Sklavonuos, and N. S. Barker, "SU-8 Micromachining of Millimeter and Submillimeter Waveguide Circuits," IEEE MTT-S International Microwave Symposium, vols 1-3, pp. 961-964, 2009.

[3] W. B.W. Alison, "A Handbook for the Mechanical Tolerancing of Waveguide Components." Artech House, 1972.

[4] A. Casanueva, J. A. Pereda, and A. Mediavilla, "Optimum compact H- and E-plane corners in rectangular waveguide," Microwave and Optical Technology Letters, vol 42, pp. 494-497, 2004.

[5] CST Microwave Studio. CST GmbH, Darmstadt, Germany, 2006.

[6] M. L. Ke, Y. Wang, S. Wei, K. Jiang, and M. J. Lancaster, "Precision Micrfabrication of Millimetre Wave Components," 9th International Conference and Exhibition on Laser, Machine Tool, CMM and Robotic Performance, LAMDAMAP 2009.

[7] M. Ke, Y. Wang, and M. J. Lancaster, "Design and realisation of low loss air-filled rectangular coaxial cable with bent quarter-wavelength supporting stubs," Microw. Opt. Technol. Lett., vol. 50, pp. 1443–1446, May 2008.

Synthesis of multiple output coupled resonator circuits using coupling matrix optimization

Talal F. Skaik, Michael J. Lancaster, Frederick Huang
School of Electronic, Electrical and Computer Engineering, University of Birmingham, B15 2TT, U.K
Email:

Abstract: Coupled resonator circuits are the basis for the design of many bandpass microwave filters. Design techniques used for two port coupled resonator circuits are extended here to multiple output circuits such as power dividers and diplexers. The design approach is based on synthesis of coupling matrix for multiple coupled resonators with multiple outputs using gradient based optimization. It allows the synthesis of power dividers with arbitrary power division, as well as diplexers and multiplexers with novel topologies. Since there is no need to use separate energy distribution networks such as circulators, manifolds or other junctions, the components can be miniaturised. An X-band unequal power divider and diplexer have been designed and realised using waveguide cavity resonators to confirm the new design methodology.

Keywords: Coupling matrix optimization, coupled resonator circuits, diplexers, power dividers.

1 Introduction

In communications systems, microwave filters are used as individual components, as well as parts of multiplexers [1]. Coupled resonator filters have been extensively presented in literature for many applications. There is a general technique for designing these filters that can be applied to any type

of resonator regardless of its physical structure [2]. Such a technique is based on coupling coefficients for coupled resonators arranged in a topology representing a two-port network. Optimization techniques are employed to synthesise the coupling matrix by minimisation of a scalar cost function [3]-[5].

Coupled resonator circuits with multiple ports were first presented in [6]. The synthesis of multiport microwave coupled-resonator networks using a procedure analogous to filters has been presented in [7] and [8]. *N*-port devices such as power splitters and directional couplers formed from magneto-inductive waveguides based on coupled loop resonators have been reported in [9].

In the current work, a general coupling matrix for *n* coupled resonators with multiple ports is presented. Three-port microwave components such as power dividers with arbitrary power division and diplexers with novel topologies are demonstrated in particular. The synthesis of these devices employs similar coupling matrix optimization techniques to those of coupled resonator filters.

Power dividers are passive microwave components used to divide an input signal into two or more signals of less power [10]. Examples of widely used power dividers are T-junctions [10], and Wilkinson divider [11]. An approach to design 3-port filtering power dividers with arbitrary power division is proposed here. It is based on coupled resonator T-topology, and realisation is possible using microstrip resonators or waveguide cavities or other types of resonators. The synthesis of polynomials and coupling matrices of the proposed power divider are presented. In [12], we presented a 3-dB power divider, and here we present an unequal power divider realised using waveguide cavity resonators to demonstrate the approach.

The common approach to synthesise multiplexers is to design each channel filter individually and then to design a distribution network. The most commonly used distribution configurations are multiple-way or cascaded dividers, circulators [13] and manifold structures [14]. These configurations have drawbacks of large volume and footprints, high cost, and time-consuming

optimization. Diplexers without distribution networks have also been reported in [7], [15], and [16]. In [7], a diplexer is designed with the common port directly connected to two resonators. However, this may have practical difficulties in implementation. In [15], miniaturised microstrip diplexers designed using stepped impedance resonators by integrating two bandpass filters with common resonator sections have been proposed. In [16], the synthesis of diplexers employing a resonant junction (an extra resonator in addition to the channel filters) has been reported.

In this paper, we present diplexers with novel topologies that can be implemented using any type of resonators. The synthesis of the diplexers is based on optimization of coupling matrices for topologies without using any external junctions for distribution of energy. This gets rid of the drawbacks mentioned earlier. A simple X-band waveguide diplexer has been designed, fabricated, and tested to verify the proposed approach.

2 General Coupling matrix for multiple coupled resonators with multiple outputs

A similar approach to the derivation of coupling matrix of coupled resonator filters in [2] has been adopted in the current work to derive general coupling matrix of n coupled resonators circuit with multiple ports. Both electric and magnetic coupling have been considered separately and later a solution has been generalised for both types of coupling.

The equivalent circuit considered for each type of coupling assumes each resonator can be connected to one port, with the input port connected to resonator 1. In the case of magnetically coupled resonators, using Kirchoff's voltage law, the loop equations are derived and represented in impedance matrix form. Similarly, for electrically coupled resonators, using Kirchoff's current law, node equations are derived and represented in admittance matrix form. The derivations show that the normalised admittance matrix has identical form to the normalised impedance matrix [2]. Accordingly, regardless of the type of coupling, a general normalised matrix [A] in terms of coupling coefficients and external quality factors is derived as shown in (1).

$$[A]=\begin{bmatrix} 1/q_{e1} & \cdots & & 0 \\ \vdots & \vdots & \vdots & \vdots \\ 0 & \cdots & & 0 \\ & & / q_{e(n-1)} & \\ 0 & \cdots & & 1/q_{en} \end{bmatrix} + P\begin{bmatrix} 1 & \cdots & & \\ \vdots & \vdots & \vdots & \vdots \\ 0 & \cdots & & \\ 0 & \cdots & & \end{bmatrix} - j\begin{bmatrix} m_{11} & \cdots & & m_{1n} \\ \vdots & \vdots & \vdots & \vdots \\ m_{(n-1)1} & \cdots & & m_{(n-1)n} \\ m_{n1} & \cdots & & m_{nn} \end{bmatrix} \tag{1}$$

where q_{ei} is the scaled external quality factor ($q_{ei}=Q_{ei}.FBW$) of resonator i, P is the complex lowpass frequency variable, m_{ij} is the normalised coupling coefficient ($m_{ij}=M_{ij}/FBW$), FBW is the fractional bandwidth, and the diagonal entries m_{ii} account for asynchronous tuning, so that resonators can have different self-resonant frequencies. Considering a 3-port network with n coupled resonators, with port 1 at resonator 1, port 2 at resonator a and port 3 at resonator b, the S-parameters will have the form:

$$S_{11}=1-\frac{2}{q_{e1}}[A]^{-1}_{11}, \qquad S_{21}=\frac{2}{\sqrt{q_{e1}q_{ea}}}[A]^{-1}_{a1}$$
$$S_{31}=\frac{2}{\sqrt{q_{e1}q_{eb}}}[A]^{-1}_{b1} \tag{2}$$

3 Power Divider Synthesis

3.1 Power Divider Polynomials Synthesis

Since the proposed divider is based on filtering functions, its response can be described by polynomial transfer functions. Therefore, for a 3-port power divider consisting of n coupled resonators, the reflection and transmission functions may be defined as ratio of two polynomials as follows:

$$S_{11}(\omega)=\frac{F(\omega)}{E(\omega)}, \qquad S_{21}(\omega)=\frac{P(\omega)/\varepsilon_1}{E(\omega)}, \qquad S_{31}(\omega)=\frac{P(\omega)/\varepsilon_2}{E(\omega)} \tag{3}$$

where ω is the real frequency variable, the polynomials $F(\omega)$, $P(\omega)$ and $E(\omega)$ are assumed to be normalised so that their highest degree coefficients are unity. $F(\omega)$ and $E(\omega)$ are N^{th} order polynomials, where N is the order of the filtering function, whereas $P(\omega)$ has an order equal to the number of prescribed transmission zeros. The maximum number of transmission zeros that can be realised in the suggested network is N-2. The roots of $F(\omega)$ correspond to the reflection zeros of the filtering function and can be found by a recursive technique [17], whereas the roots of $P(\omega)$ correspond to the positions of transmission zeros of the filtering function. For a Chebyshev function, the constants ε_1 and ε_2 normalise $S_{21}(\omega)$ and $S_{31}(\omega)$ respectively to the specified insertion loss levels at ω=±1. The polynomial $E(\omega)$ has its complex roots corresponding to the filter pole positions and can be constructed if the polynomials $F(\omega)$, $P(\omega)$ and the constants ε_1 and ε_2 are known.

Expressions for ε_1 and ε_2 will be derived next, followed by a discussion on determining $E(\omega)$. If the input power is to be divided such that $|S_{31}(\omega)|^2=\alpha|S_{21}(\omega)|^2$, then for a lossless system,

$$|S_{11}(\omega)|^2+(1+\alpha)|S_{21}(\omega)|^2=1 \tag{4}$$

From (3) and (4), the constant ε_1 is evaluated as:

$$\varepsilon_1=\left|\frac{S_{11}(\omega)}{S_{21}(\omega)}\right|.\left|\frac{P(\omega)}{F(\omega)}\right|=\frac{\sqrt{1+\alpha}\,|S_{11}(\omega)|}{\sqrt{1-|S_{11}(\omega)|^2}}.\left|\frac{P(\omega)}{F(\omega)}\right|$$

When ω=±1, $|S_{11}(\omega)|$ is equal to the maximum passband reflection coefficient, whose value is known from the specification. ε_1 can be expressed in terms of the polynomials $F(\omega)$ and $P(\omega)$, and the prescribed return loss level in dB, RL, in the passband as follows,

$$\varepsilon_1=\sqrt{\frac{1+\alpha}{10^{RL/10}-1}}.\left|\frac{P(\omega)}{F(\omega)}\right|_{\omega=\pm1} \tag{5}$$

Similarly, ε_2 can be expressed as,

$$\varepsilon_2=\sqrt{\frac{1+\alpha}{\alpha\left(10^{RL/10}-1\right)}}.\left|\frac{P(\omega)}{F(\omega)}\right|_{\omega=\pm1} \tag{6}$$

Once the polynomials F and P, and the constants ε_1 and ε_2 are known, the denominator polynomial E can be derived by substitution of $F(s)$, $P(s)$ and $E(s)$, where $s=j\omega$ is the complex frequency variable, into the conservation of energy formula, as follows:

$$F(s)F(s)^{*}+\frac{P(s)P(s)^{*}}{\varepsilon_1^2}+\frac{P(s)P(s)^{*}}{\varepsilon_2^2}=E(s)E(s)^{*} \tag{7}$$

$E(s)E(s)^*$ is constructed by polynomials multiplications in the left hand side of (7), which must be polynomial of the order $2N$ with real coefficients. The roots of $E(s)E(s)^*$ will be symmetric about the imaginary axis in the complex plane, and they can be found using numerical analysis software such as MATLAB [18]. Since $E(s)$ is strictly Hurwitz, then its roots are those in the left half plane, whereas the roots of $E(s)^*$ are those in the right half plane. The polynomial $E(s)$ is then constructed by choosing the N roots in the left half plane.

3.2 Power Divider Coupling Matrix Synthesis

The synthesis procedure of the coupling matrix of the proposed power divider is similar to that of a filter with n coupled resonators. It is based on minimisation of a cost function that is evaluated at frequency locations of reflection and transmission zeros. The formulation of the cost function used here is similar in principle to that in [5], that is used to optimise coupling matrices for coupled resonator filters. Here the cost function has an extra term to satisfy the power division ratio requirement. The initial cost function is written in terms of the polynomials F and P and is evaluated at critical frequencies as follows,

$$\Omega=\sum_{i=1}^{T}\left|P(s_{ti})\right|^{2}+\sum_{j=1}^{R}\left|F(s_{rj})\right|^{2}+\sum_{j=1}^{R}\left(\left|\frac{P(s_{rj})}{\varepsilon_1 E(s_{rj})}\right|-\sqrt{\frac{1}{1+\alpha}}\right)^{2} \tag{8}$$

where T is the number of transmission zeros, R is the number of reflection zeros, s_{ti} and s_{rj} are the complex lowpass prototype transmission and reflection zeros respectively. The lowpass prototype frequency positions of reflection zeros are found using Cameron's recursive technique [17]. The last

term in the cost function is used to achieve the required power division ratio, and is evaluated at the peaks of $|S_{21}|$, where α is the power ratio as given earlier. This cost function does not involve the ripple in the optimization parameters, and hence the external quality factors have to be calculated analytically at the desired return loss. The calculations of the external quality factors and the right locations of the return zeros enforce the peaks of $|S_{11}|$ to be at the required return loss level.

The polynomials P and F can be evaluated in terms of the coupling matrix by equating the scattering parameters in equations (2) to their equivalent in equations (3). In (2), the inverse of the matrix $[A]$ can be described in terms of the adjoint and determinant as $[A]^{-1}=adj(A)/\Delta_A$, where $adj(A)$ is the adjoint of the matrix $[A]$, and Δ_A is its determinant. Using this, and noting that the adjoint is the transpose of the matrix cofactors, the cost function can be re-written as given in (9), where $[A]$ is the matrix derived and given in (1), $\Delta_A(S_{rj})$ is the determinant of the matrix $[A]$ evaluated at the frequency variable S_{rj}, and $cof_{kh}([A(s=x)])$ is the cofactor of matrix $[A]$ evaluated by removing the k^{th} row and the h^{th} column of $[A]$ and finding the determinant of the resulting matrix at the frequency variable $s=x$.

$$\begin{aligned}\Omega = \sum_{i=1}^{T}\left|\frac{2}{\sqrt{q_{e1}q_{ea}}}.cof_{1a}([A(S_{ti})])\right|^2 \\ + \sum_{j=1}^{R}\left|\Delta_A(S_{rj}) - \frac{2.cof_{11}([A(S_{rj})])}{q_{e1}}\right|^2 \\ + \sum_{j=1}^{R}\left|\frac{2}{\sqrt{q_{e1}q_{ea}}}.\frac{cof_{1a}([A(S_{rj})])}{\Delta_A(S_{rj})} - \sqrt{\frac{1}{1+\alpha}}\right|^2\end{aligned} \tag{9}$$

The external quality factors are analytically evaluated at specific order and ripple using the equations of a coupled resonator filter [2], and their values are set at the outset of optimization.

A gradient based optimization technique has been used to synthesise the coupling matrix of the proposed power divider, whereby the coupling matrix elements are the optimization variables. A proposed topology for a 3-port power divider with n coupled resonators with Chebyshev filtering

response is shown in figure 1. Although there are many possible topologies, the topology shown has been suggested since it has large number of shared resonators, so that the order of the filtering function at each output is equal to (n-1), where n is the total number of resonators. This is due to the existence of two signal paths with (n-1) resonators in each; the first contains the resonators (1,2,3,…,n-2,n-1) and the second contains the resonators (1,2,3,…,n-2,n). The coupling coefficients $m_{(n-2),(n-1)}$ and $m_{(n-2),n}$ will have equal values in case of 3-dB power division, and differing values for arbitrary power division. The initial guess of all coupling coefficients that exist in the divider topology was 0.5, and those that do not exist were set to zero.

It should be noted that the proposed divider is not matched at all ports, and the output ports are not isolated. In consequence, matching is only achieved at port 1, and the output return loss $|S_{22}|$ and $|S_{33}|$ and the isolation $|S_{23}|$ are around 6 dB in the passband. This is a typical problem of lossless reciprocal 3-port junctions [19].

3.3 Power divider example

Power dividers with different power division ratios and different number of resonators have been synthesised successfully with the proposed method. An example of 3-dB power divider is presented here. The divider has a return loss of 20 dB and it has the topology in figure 1 with n=12. Both the reflection zeros and the external quality factors have been evaluated for 11th order filter, which is the order of the filtering function at each output, and their values have been set in the optimization algorithm. The reflection zeros have been calculated using Cameron's recursive technique as follows, s_{rj}=0, ±0.2817j, ±0.5406j, ±0.7557j, ±0.9096j and ±0.9898j Hz. The values of external quality factors are q_{e1}=q_{e11}=q_{e12}=1.0331. The synthesised normalised coupling coefficients are m_{12}=0.8103, m_{23}=0.5817, m_{34}=0.5419, m_{45}=0.5289, m_{56}=0.5245, m_{67}=0.5244, m_{78}=0.5290, m_{89}=0.5418, $m_{9,10}$=0.5817, and $m_{10,11}$=$m_{10,12}$=0.5730, and the power divider ideal response is shown

in figure 2. The response shows that the output ports are not isolated as expected, with $|S_{23}|$ of 5.3 dB or better in the passband.

4 Diplexer Synthesis

4.1 Coupling Matrix Synthesis of Diplexer

A similar approach to the power divider cost function formulation has been followed to derive a cost function for diplexers. Assuming that the polynomials $F(s)$, $P_1(s)$, $P_2(s)$, and $E(s)$ along with ripple constant ε completely define the response of the diplexer, where the roots of $F(s)$ correspond to the reflection zeros, the roots of and $P_1(s)$, $P_2(s)$ correspond to the transmission zeros of the filter frequency response at ports 2, and 3 respectively, and the roots of $E(s)$ correspond to the pole positions of the filtering function, the initial cost function may be written in terms of the characteristic polynomials as follows,

$$\Omega = \sum_{i=1}^{T_1} \left| P_1(s_{ti}) \right|^2 + \sum_{k=1}^{T_2} \left| P_2(s_{tk}) \right|^2 + \sum_{j=1}^{R} \left| F(s_{rj}) \right|^2 + \sum_{v=1}^{R-2} \left| \left| \frac{F(s_{pv})}{E(s_{pv})} \right| - 10^{\frac{L_R}{20}} \right|^2 \tag{10}$$

where s_{ti}, s_{tk} are the frequency locations of transmission zeros of S_{21}, S_{31} respectively, T_1, T_2 are the numbers of the transmission zeros of S_{21}, S_{31} respectively, R is the total number of resonators in the diplexer, L_R is the desired return loss in dB (L_R<0), and s_{rj} and s_{pv} are the reflection zeros and the peaks' frequency values of $|S_{11}|$ in the passband. The last term in the cost function is used to set the peaks of $|S_{11}|$ to the required return loss level.

Assuming the common port of the diplexer is connected to resonator 1, port 2 is connected to resonator *a*, and port 3 is connected to resonator *b*, the cost function in (10) may be re-written in terms of determinants and cofactors of the matrix [*A*] in a similar way to the cost function of power divider as follows,

$$\begin{aligned}\Omega = &\sum_{i=1}^{T_1}\left|\frac{2}{\sqrt{q_{e1}q_{ea}}}.cof_{1a}([A(s_{ti})])\right|^2 \\ &+\sum_{k=1}^{T_2}\left|\frac{2}{\sqrt{q_{e1}q_{eb}}}.2.cof_{1b}([A(s_{tk})])\right|^2 \\ &+\sum_{j=1}^{R}\left|\Delta_A(s_{rj})-\frac{2.cof_{11}([A(s_{rj})])}{q_{e1}}\right|^2 \\ &+\sum_{v=1}^{R-2}\left|\left|1-\frac{2.cof_{11}([A(s_{pv})])}{q_{e1}.\Delta_A(s_{pv})}\right|-10^{\frac{L_R}{20}}\right|^2\end{aligned} \tag{11}$$

where q_{e1}, q_{ea}, and q_{eb} are the external quality factors at ports 1, 2 and 3 respectively. The first two terms in the cost function are used if the diplexer characteristics contain transmission zeros. However, for a Chebyshev response, these terms may be used to minimise the transmission of each channel at the passband of the other channel, thus increasing the isolation between channel ports. The frequency locations s_{ti} are chosen to be the band edges of the channel at port 3, and similarly the frequency locations s_{tk} are chosen to be the band edges of the channel at port 2.

The lowpass frequency positions of the reflection zeros of the diplexer are initially set to be equally spaced in the optimization algorithm, and later these positions are moved until equiripple level at specified insertion loss is achieved. The variables in the optimization algorithm are the coupling matrix elements and the frequency locations of the reflection zeros.

The external quality factors are numerically calculated, and their values are set at the beginning of the algorithm. This reduces the optimization parameters set and decreases the convergence time. To find the normalised external quality factors of the proposed diplexer, assume we have two lowpass prototype filters with the same order and filtering function but different bandwidth, the first with frequency edges of ±1 Hz and a bandwidth of $BW_{\pm1}$, and the second with frequency edges of x and 1 Hz and a bandwidth of BW_{x1}. The normalised external quality factors of these filters are related by:

$$q_{ex1} = \frac{BW_{\pm1}}{BW_{x1}} q_{e\pm1} = \frac{2}{1-x} q_{e\pm1} \tag{12}$$

where q_{ex1} is the normalised external quality factor of the second filter, and $q_{e\pm1}$ is the normalised external quality factor of the first filter, which is known for lowpass prototype filters [2]. Accordingly, for a symmetrical diplexer with channel edges of (-1,-x) and (x,1), the normalised external quality factors at ports 2 and 3 are calculated from equation (12), and the normalised external quality factor at the common port is equal to $q_{ex1}/2$. This works for all the examples of symmetrical diplexers presented throughout this paper.

Coupling matrices of symmetrical diplexers have been successfully optimised using gradient based technique for possible topologies shown in figure 3, where n is the total number of resonators, and $\pm x$ define the inner edges of the two channels.

In the T-Topology in figure 3(a), r is the number of resonators located between either output port, and the junction resonator (n-$2r$). These resonators should have different self-resonant frequencies to separate the diplexer channels from each other. Different values of r make it possible to realise many topologies with n coupled resonators. The optimization algorithm has been successful in producing non-distorted diplexer responses for the T-topology in figure 3(a) with $r = \left\lceil \frac{n}{4} \right\rceil$ and $r = \left(\frac{n}{2} - 1\right)$. A comparison between diplexers with T-topology, with the same number of resonators n, and different value of r will be shown in the next section.

All the resonators in the T-topology shown in figure 3(a) are directly coupled (no cross coupling), and hence only Chebyshev response can be obtained. The resonators in the vertical branch apart from the junction resonator should have different self-resonant frequencies; this is to achieve disjoint frequency bands at the ports 2 and 3. Consequently, for the high frequency channel to be at port 2, the resonators above the junction resonator should have positive frequency offsets (M_{ii}>0), and for the low frequency channel to be at port 3, the resonators below the junction resonator should have negative frequency offsets (M_{ii}<0).

In the canonical topology shown in figure 3(b), solid lines represent direct coupling, and dashed lines represent cross coupling, and a Quasi-Elliptic filter response can be achieved. The resonators (3,4,…, n/2+1) have positive frequency offsets (M_{ii}>0), and the resonators (n/2+2, n/2+3,…, n) have negative frequency offsets (M_{ii}<0).

It has been found that by using local optimization techniques for relatively large structures, the optimization algorithm may converge to a local minimum. To solve this problem, the optimization has been done in two stages. In the first stage, the optimization is carried out by using the cost function in (11) without the last term, and with equally spaced reflection zeros. In the second stage, the full cost function in (11) is used, and the resulting coupling coefficients from the first stage are used as initial values, and the locations of the reflections zeros are allowed to move until equiripple insertion loss is achieved. This has been successful for symmetrical diplexer topologies up to 12 resonators. Moreover, assigning different weights to the terms of the cost function has been found useful for convergence, especially for large structures.

4.2 Diplexer examples

Coupling matrices of diplexers with the same specification and different topologies have been synthesised. Shown in figure 4 are three topologies for diplexers with non-contiguous bands with n=8, x=0.5. The structures in figures 4(a) and 4(b) are examples of the general T-topology in figure 3(a) with r=2 and r=3, respectively, and the structure in figure 4(c) is a conventional diplexer with the common port assumed as a shunt connection of the inputs of the two filters composing the diplexer (the addition of a frequency-invariant susceptance representing three-port junction is possible). The synthesis of the third diplexer is presented in [16].

In both examples in figure 4 (a) and figure 4 (b), the initial values of the lowpass prototype frequency locations of the zeros of $|S_{11}|$ have been set with equal spacing, and the required return loss has been taken to be 20 dB. The external quality factors are numerically calculated as

previously described and the frequency locations of $|S_{11}|$ peaks at the passbands are evaluated by numerical differentiation at each iteration in the optimization algorithm. The initial reflection zeros are s_{rj}= ±0.52j, ±0.6733j, ±0.8267j, and ±0.98j, and the external quality factors are 1.863 at port 1, and 3.726 at both ports 2 and 3. The optimised normalised coupling coefficients for the structure in figure 4(a) are: m_{12}=0.8218, m_{23}=0.4224, m_{34}=0.7117, m_{45}=m_{47}=0.2553, m_{56}=m_{78}=0.2315, m_{55}= -m_{77}=0.7112 and m_{66}= -m_{88}=0.7414, whereas the optimised normalised coupling coefficients for the structure in figure 4(b) are: m_{12}=0.8256, m_{23}= m_{26}=0.2981, m_{34}= m_{67}=0.1786, m_{45}=m_{78}=0.2284, m_{33}= -m_{66}=0.6963, m_{44}= -m_{77}=0.7428 and m_{55}= -m_{88}=0.7462.

In the example in figure 4(c), the return loss is set to 20 dB, and each channel filter is initially designed individually, and then the full coupling matrix of the diplexer is synthesised by integrating the common port in the optimization. The optimised normalised coupling coefficients for the structure in figure 4(c) are: q_{e1}=q_{e4}= q_{e5}=q_{e8}=3.7258, m_{12}=m_{56}=0.2279, m_{23}=m_{67}=0.1750, m_{34}= m_{78}=0.2242, m_{11}=m_{22}= -m_{55}= -m_{66}=0.75, m_{33}= -m_{77}=0.7511 and m_{44}= -m_{88}=0.7976.

The responses of the diplexers in figure 4 are shown in figure 5. Comparing these responses, it is noticed that the diplexer in figure 4(c) has better isolation than the diplexer in figure 4(b), and that the diplexer in figure 4(b) has better isolation than the diplexer in figure 4(a). In other words, the higher the number of resonators between ports 2 and 3, the better the isolation is. However, far out of band, the response is better for structures in figure 4(a) and figure 4(b). Accordingly, in the proposed general T-topology in figure 3(a), the value of r that gives the best isolation performance is $r = \left(\frac{n}{2} - 1\right)$, where n is the total number of resonators. This is due to existence of more resonators between the output ports.

Although the isolation performance degrades in comparison to the conventional diplexers, an advantage of the proposed diplexers is that the source is directly coupled to the input resonator (number 1). This is distinct from the diplexers reported in the literature, since there is no need to use

an external junction (T-junction, manifold, etc...) as in conventional diplexers, or to add a resonant junction (an extra resonator in addition to the channel filters) as in [16], or to directly connect the common port to one terminal of each of the channel filters, which may have practical constraints in implementation, as in [7]. Thus, the proposed diplexer exhibits a trade-off between design complexity and isolation performance.

A contiguous band diplexer has also been synthesised. The structure of the diplexer is shown in figure 6 and it is an example of the general topology in figure 3(b) with cross coupling, n=12, and x=0. The cross coupling (dashed line) between resonators 3 and 6, and resonators 8 and 11 generate transmission zeros to obtain a quasi-elliptic response.

The optimised normalised coupling coefficients are: m_{12}=0.8224, m_{23}=m_{28}=0.4150, m_{34}=m_{89}=0.2785, m_{45}=$m_{9,10}$=0.3304, m_{56}=$m_{10,11}$=0.2865, m_{67}=$m_{11,12}$=0.4136, m_{36}=$m_{8,11}$= -0.0652, m_{33}= -m_{88}=0.4638 and m_{44}= -m_{99}=0.5148, m_{55}= -$m_{10,10}$=0.5154, m_{66}= -$m_{11,11}$=0.5088, m_{77}= -$m_{12,12}$=0.5024, and the normalised external quality factors are 0.994 at port 1 and 1.9881 at both ports 2 and 3. The response of the diplexer is shown in figure 7.

5 Implementation of Unequal Power Divider

5.1 Power Divider Design and Fabrication

A 5 resonator unequal power divider has been designed, fabricated and tested. The divider has been designed according to the coupled-resonator design methodology proposed here. It is designed at the X-band with a centre frequency of 10.15 GHz, bandwidth of 925 MHz, a reflection loss of 20 dB at the passband, and α=1.5. The divider topology is that shown in figure 1 with n=5, and the synthesised normalised coupling coefficients using optimization are as follows: m_{12}=0.9116, m_{23}=0.7005, m_{34}=0.5766, m_{35}=0.7061 and q_{e1}=q_{e4}=q_{e5}=0.931.

The power divider has been implemented using waveguide cavity resonators coupled together using capacitive irises. A photograph of the divider is shown in figure 9 (a). The device has been made of two mirror image pieces of copper, and metal screws have been used to tune its response.

5.2 Power Divider Measurement

The simulated and measured results of the power divider are depicted in figure 8. The measured response has been tuned using metal screws and it is in good agreement with the simulated response. The experimental results show that the maximum return loss within the passband is 20 dB and the minimum insertion loss is 2.28 dB for S_{31} and 4.29 dB for S_{21}. The measured isolation between the output ports is more than 4.4 dB in the passband.

6 Implementation of X-band Diplexer

6.1 Diplexer Design and Fabrication

An X-band non-contiguous diplexer has been designed using the new methodology presented with the following specifications: passband centre frequency of 9.5 GHz for channel 1 and 10.5 GHz passband centre frequency for channel 2, bandwidth of each channel is 52 MHz, and desired return loss at the passband of each channel is 20 dB.

The diplexer topology is that given in figure 3 (a) with n=4 and r=1. The optimised normalised coupling coefficients are: m_{12}=1.3044, m_{23}=m_{24}=0.1666, m_{33}=-m_{44}=1.2894 and the calculated normalised external quality factors are q_{e1}=4.651, q_{e3}=q_{e4}=9.302.

The diplexer has been implemented using waveguide cavity resonators coupled together using inductive apertures. A photograph of the physical diplexer is shown in figure 9(b).

6.2 Diplexer Measurement

The simulated and measured results of the diplexer are depicted in figure 10. The tuned measured response is in very good agreement with the simulated response. The measurements show that the

passband of channel 1 has maximum return loss of 22 dB and minimum insertion loss of 0.38 dB, and that the passband of channel 2 has maximum return loss of 22 dB and minimum insertion loss of 0.43 dB. The losses in diplexer channels are mainly due to the conductor loss in small fractional bandwidth of each channel.

7 Conclusion

The synthesis of multiple output coupled resonator circuits is presented in this study. Coupled resonator power dividers with arbitrary power division and diplexers with novel topologies have been synthesised using coupling matrix optimization technique. An X-band unequal power divider and diplexer have been designed, fabricated and tested to verify the design approach. More devices like triplexers and multiplexers will be designed in the future using the same methodology.

Acknowledgement

The authors would like to thank Clifford Ansell for fabrication of devices. The UK Engineering and Physical Science Research Council supported part of this work.

References

[1] Cameron R., Kudsia C., and Mansour R.: 'Microwave filters for communication systems' (Wiley, 2007).

[2] Hong J.S. and Lancaster M.J.: 'Microstrip filters for RF/microwave applications' (Wiley, 2001).

[3] Amari S.: 'Synthesis of cross-coupled resonator filters using an analytical gradient-based optimization technique', *IEEE Trans. Microw. Theory Tech*., 2000, 48, (9), pp. 1559-1564.

[4] Atia W.A., Zaki K.A., and Atia A.E.: 'Synthesis of general topology multiple coupled resonator filters by optimization', IEEE MTT-S Int. Microw. Symp., Baltimore, USA, 1998, pp. 821-824.

[5] Jayyousi A.B. and Lancaster M.J.: 'A gradient-based optimization technique employing determinants for the synthesis of microwave coupled filters', IEEE MTT-S Inter. Microw. Symp., USA, June 2004, pp 1369-1372.

[6] Lancaster M.J.: 'Radio frequency filter'. W.I.P.O patent WO/01/69712, 2001.

[7] Garcia-Lamperez A., Salazar-Palma M., and Sarkar T.K.: 'Analytical synthesis of microwave multiport networks', IEEE MTT-S Inter. Microw. Symp. digest, USA, June 2004, pp 455-458.

[8] Garcia-Lamperez A., Salazar-Palma M., and Sarkar T.K.: 'Compact multiplexer formed by coupled resonators with distributed coupling', IEEE Antennas and Propagation Society Intern. Symp., USA, 2005, pp. 89-92.

[9] Syms R.R.A., Shamonina E., and Solymar L.: 'Magneto-inductive waveguide devices', IEE Proceedings-Microwaves, Antennas and Propagation, 2006, 153, (2), pp. 111-121.

[10] Pozar D.M.: 'Microwave Engineering' (Wiley, 1998, 2nd ed.)

[11] Wilkinson E.J.: 'An N-way hybrid power divider', *IRE Trans. Microw. Theory and Techn*., 1960, 8, (1), pp. 116-118.

[12] Skaik T., Lancaster M., and Huang F.: 'Coupled-Resonator 3-dB Power Divider', Proc. IET seminar on Passive RF and Microwave Components, Birmingham UK, April 2010.

[13] Mansour R.R., et al.: 'Design considerations of superconductive input multiplexers for satellite applications', *IEEE Trans. Microw. Theory Techn*., 1996, 44, (7), pp. 1213-1229.

[14] Rhodes J.D. and Levy R.: 'Design of general manifold multiplexers', *IEEE Trans. Microw. Theory Techn.*, 1979, 27, (2), pp. 111-123.

[15] Chi-Feng C., Ting-Yi H., Chi-Ping C., and Ruey-Beei W.: 'Microstrip diplexers design with common resonator sections for compact size, but high isolation', *IEEE Trans. Microw. Theory Techn*., 2006, 54, (5), pp. 1945-1952.

[16] Macchiarella G. and Tamiazzo S.: 'Novel approach to the synthesis of microwave diplexers', *IEEE Trans. Microw. Theory Techn*., 2006, 54, (12), pp. 4281-4290.

[17] Cameron R.J.: 'General coupling matrix synthesis methods for Chebyshev filtering functions', *IEEE Trans. Microw. Theory Techn*., 1999, 47, (4), pp. 433-442.

[18] Mathworks Inc. MATLAB 9 user's guide (online). Available: http://www.mathworks.com.

[19] Collin R.E.: 'Foundations for Microwave Engineering' (John Wiley & Sons, 2001, 2nd ed.)

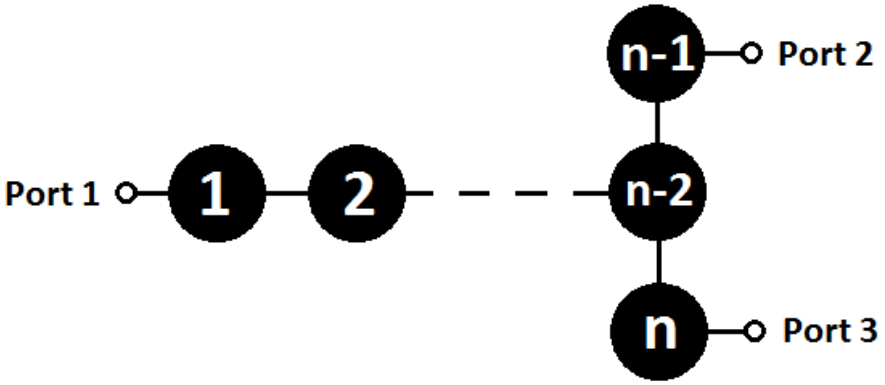

Figure 1: Power divider T-topology

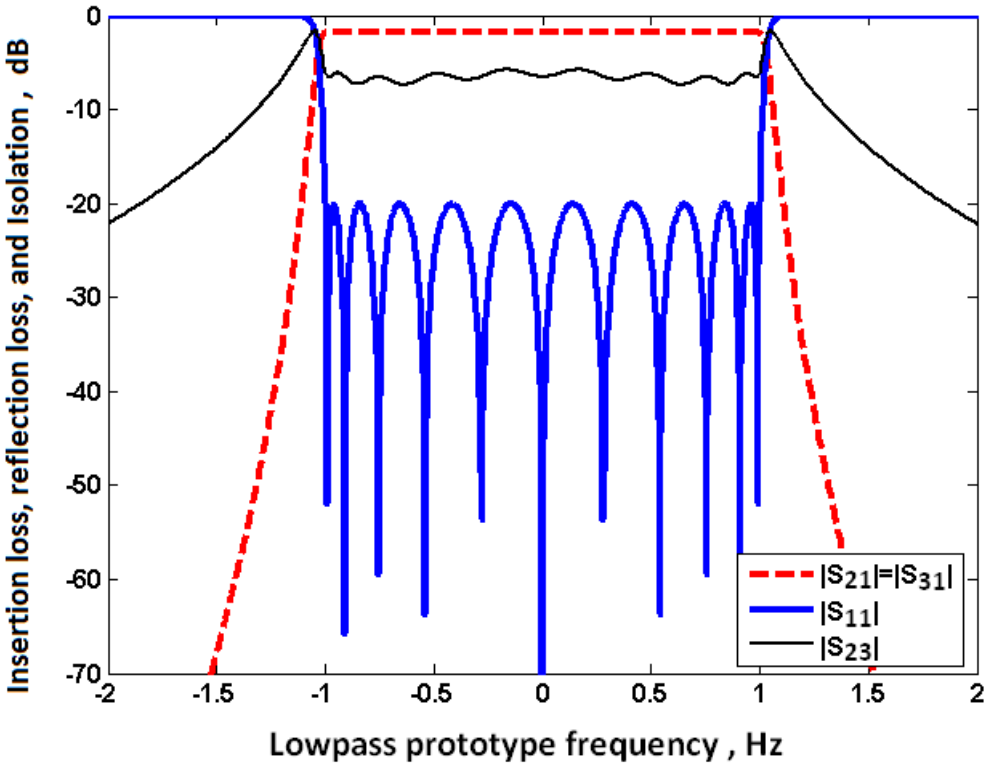

Figure 2: Filtering power divider response

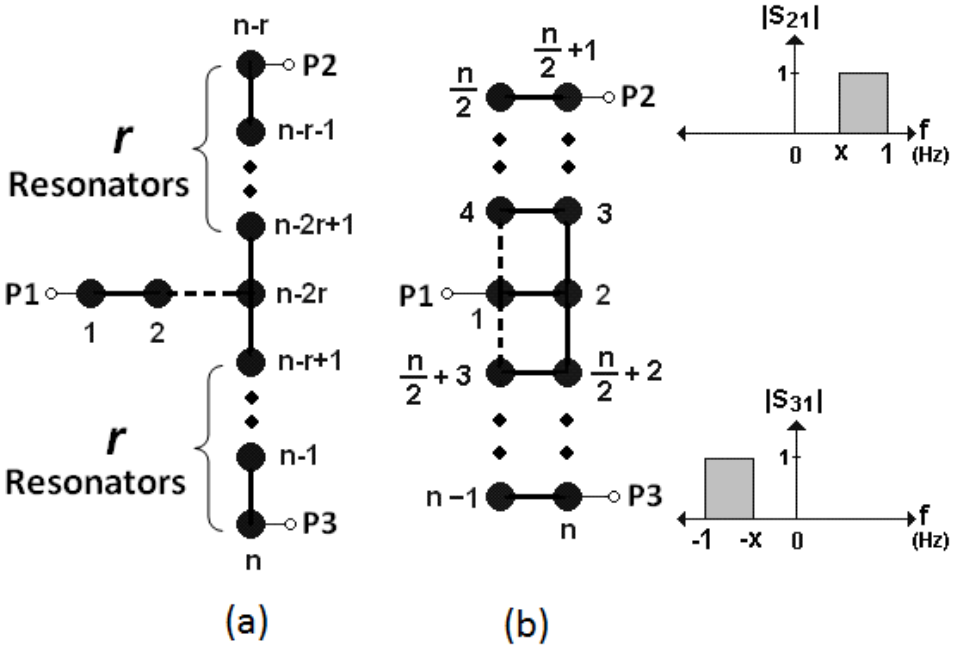

Figure 3: (a) T-Topology, (b) Canonical topology.

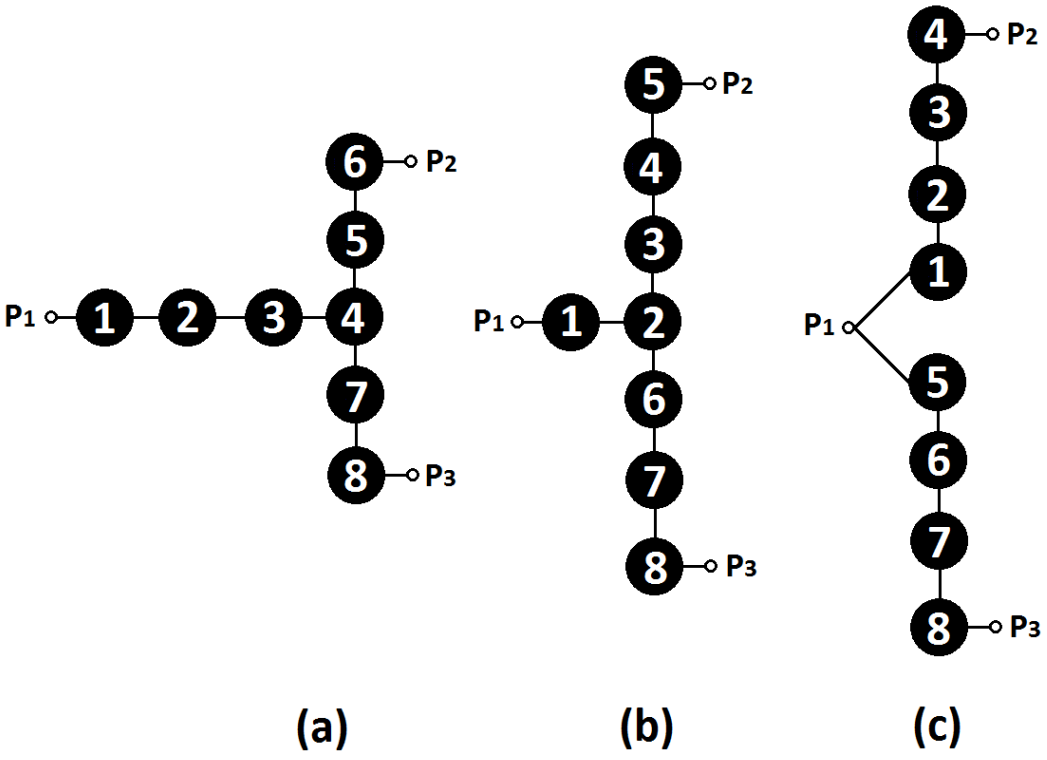

Figure 4: Topologies for diplexers

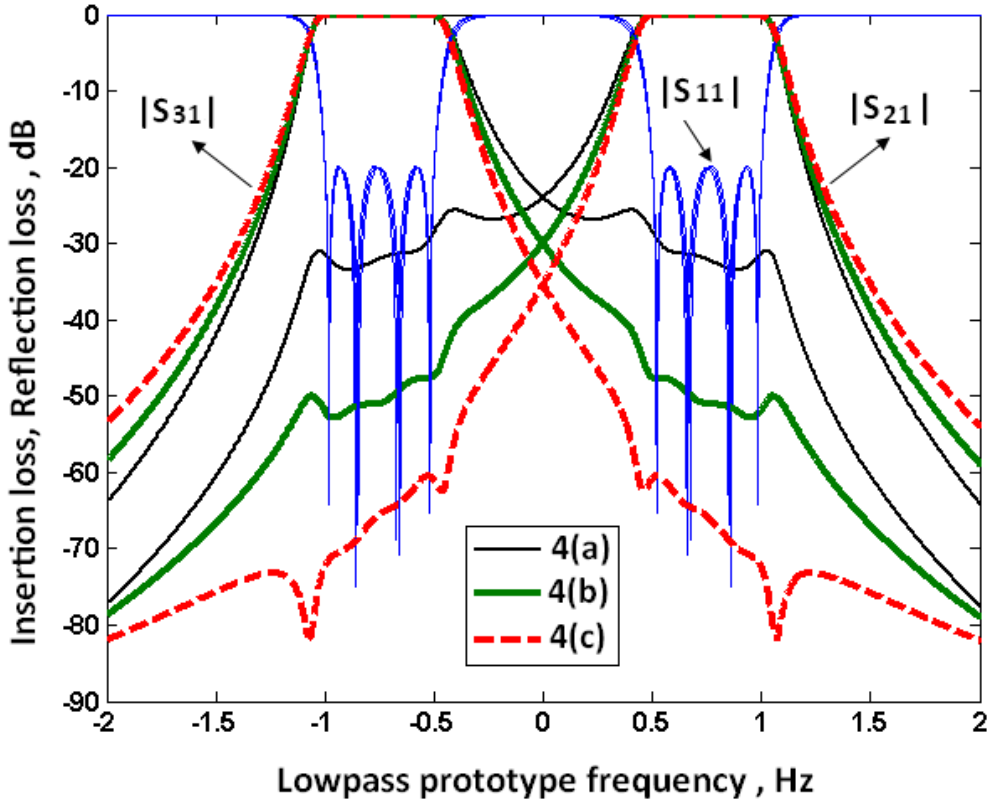

Figure 5: Responses of diplexers in figure 4.

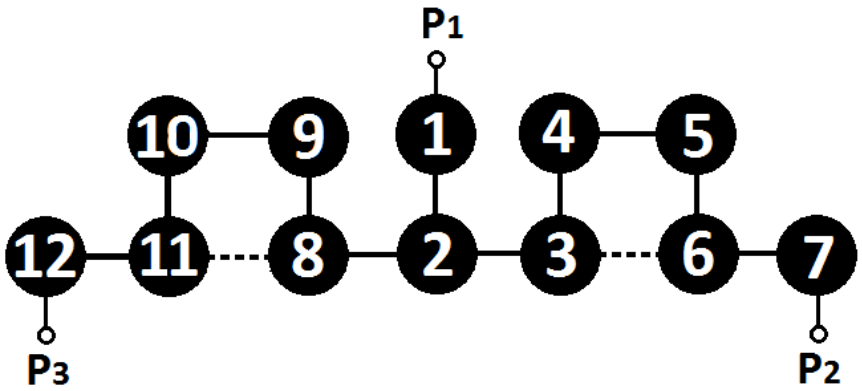

Figure 6: 12-resonator diplexer structure

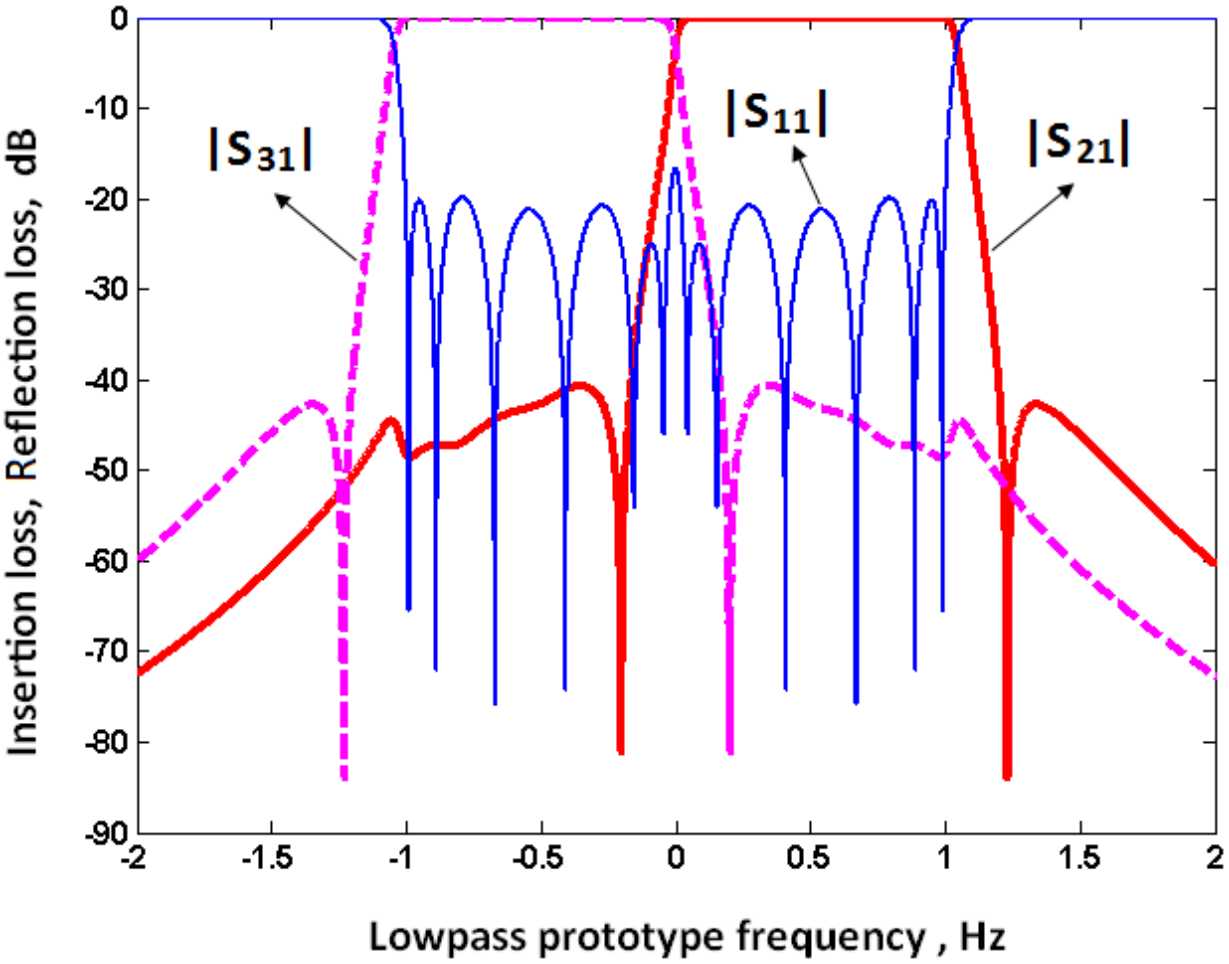

Figure 7: Response of contiguous diplexer.

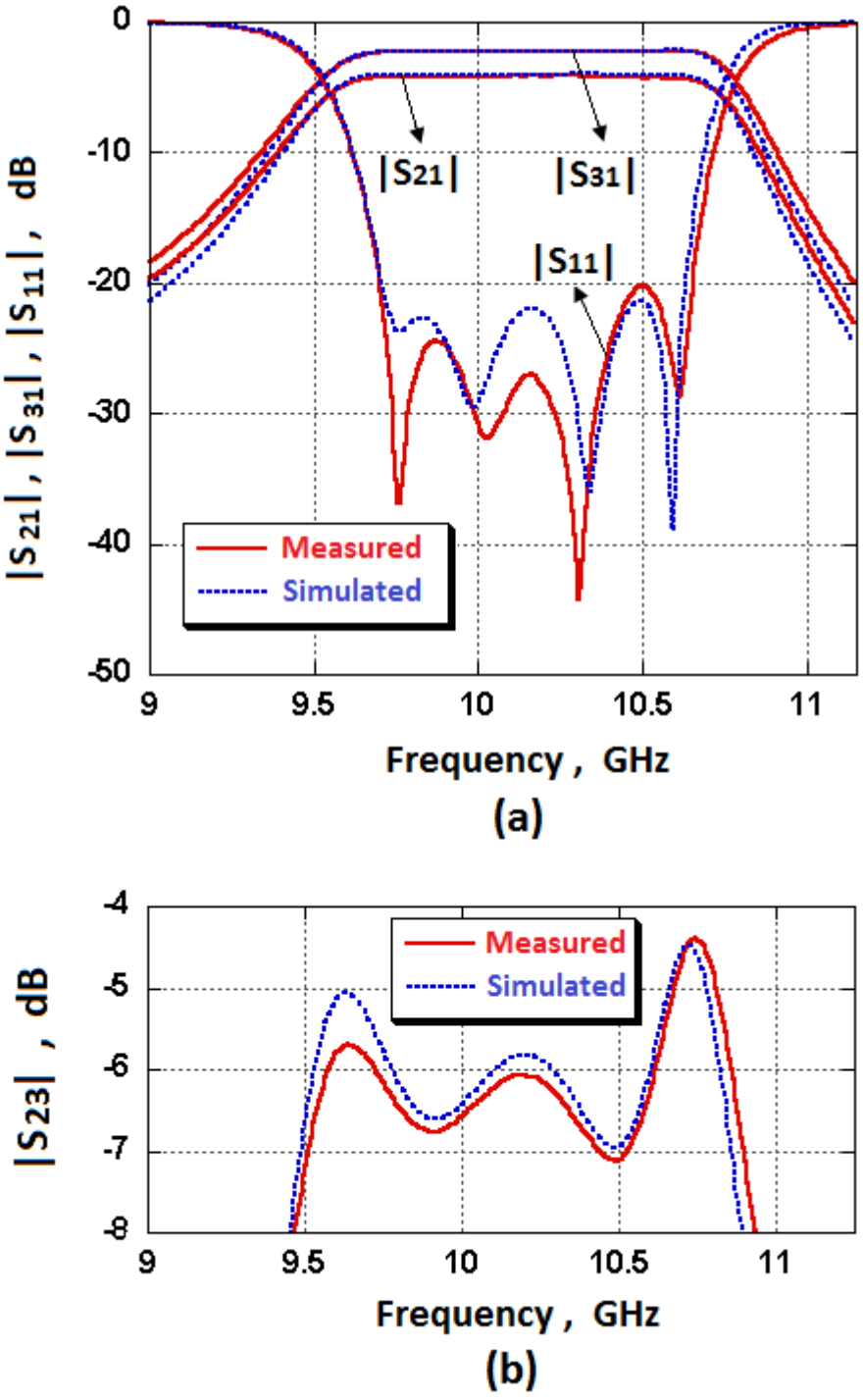

Figure 8: (a) Measured and simulated results of the power divider, (b) Power divider isolation

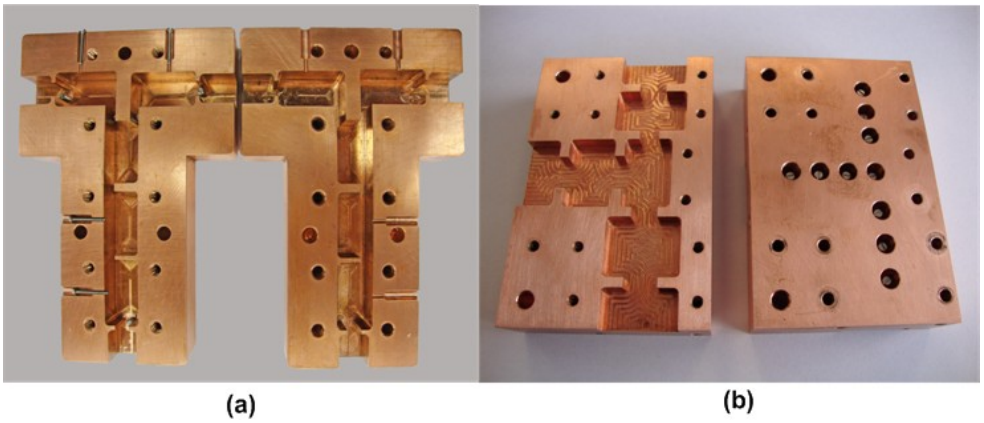

Figure 9: (a) Unequal Power Divider, (b) Diplexer

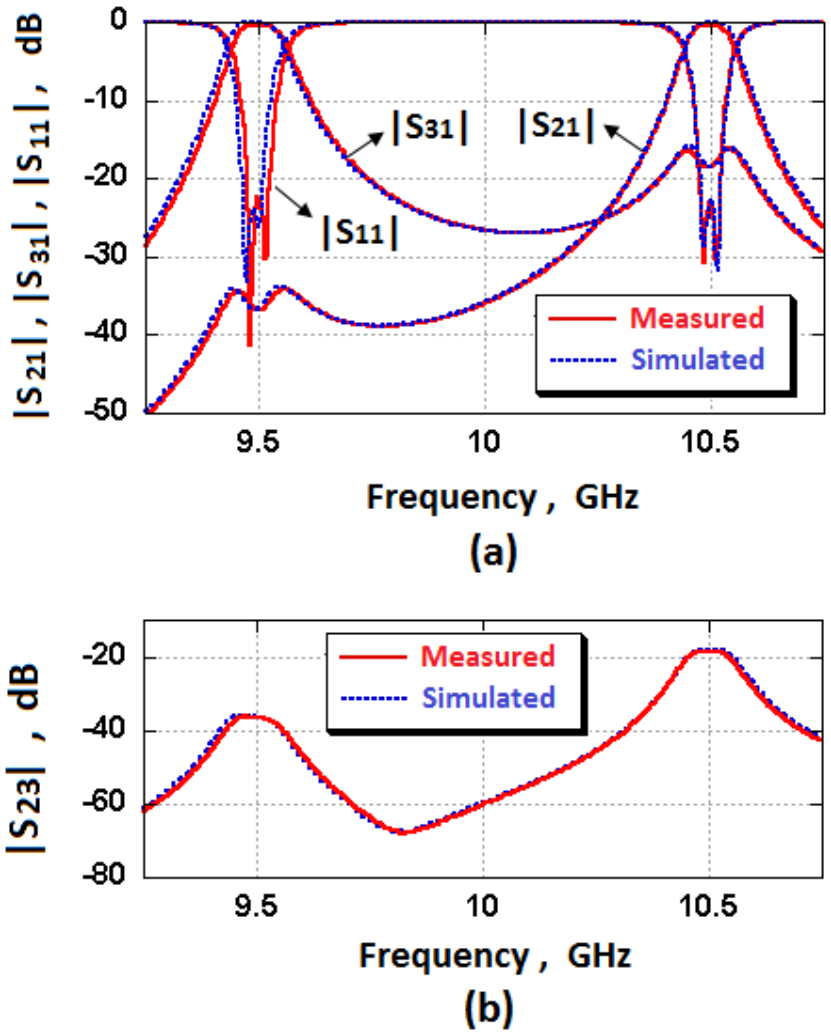

Figure 10: (a) Measured and simulated results of the diplexer, (b) Diplexer isolation

Coupled Resonator Diplexer without External Junctions

Talal F. Skaik and Michael J. Lancaster

Abstract—**A coupled resonator diplexer has been designed, fabricated, and tested. The design is based on synthesis of coupling matrix of a 3-port coupled resonator circuit using optimization. Unlike conventional diplexers, the presented diplexer configuration does not include any separate junctions for distribution of energy. The diplexer has been implemented at X-band with waveguide cavity resonators, and its measured response is in good agreement with the simulated response.**

***Index Terms*—coupling matrix, diplexer, optimization.**

I. Introduction

Microwave diplexers are widely used in communication systems to connect two networks operating at different frequencies to a common port. Conventional diplexers consist of two channel filters connected to an energy distribution network. Such a network can be a waveguide manifold [1], a T-junction [2], a Y-junction [3], or a circulator [4]. A common approach for the diplexer synthesis is based on firstly designing the channel filters independently of the diplexer, and then using numerical optimization for the whole diplexer structure. This approach can be very time consuming for large diplexer structures and the convergence of the cost function might be problematic. In [5,6], an approach to the synthesis of diplexers that takes into account a three-port junction in the initial synthesis of the two channel filters was presented. This approach provides a very good starting point for the optimization of the whole structure, so the convergence can be achieved with few iterations. Diplexers employing resonant junctions (an extra resonator in addition to the resonators of the channel filters) have also been reported in [5].

Multiplexers/diplexers based on coupled resonator circuits with multiple outputs have been reported in [7-9]. In [7], coupled resonator circuits with multiple outputs were first patented. In [8,9], the synthesis of multiport coupled resonator networks based on a procedure analogous to filters has been reported. The proposed configurations in these papers do not employ any external junctions for distribution of energy, and hence, the components can be miniaturized. The diplexer proposed in [8], however, may present difficulties in implementation, since the common port is directly coupled to two resonators.

In [10], we presented a design procedure for coupled resonator diplexers that do not employ any external junctions. The proposed diplexers have novel topologies that can be implemented by any type of resonators, and their synthesis is based on coupling matrix optimization. In this paper, we present a coupled resonator diplexer that has been synthesized using coupling matrix optimization. The diplexer has non-contiguous bands with symmetrical channels, and it is implemented at X-band using twelve waveguide cavity resonators to verify our design approach in [10]. The proposed diplexer is miniaturized when compared to the conventional diplexers, since it does not contain external junctions. In addition, miniaturization is improved by using a folded structure.

II. Diplexer Synthesis using optimization

The synthesis is based on optimization of the coupling matrix for multiple coupled resonators arranged in a 3-port network. A general matrix [*A*], derived for a multiport coupled-resonator circuit, in terms of the coupling coefficients and the external quality factors is given by [10,11],

$$[A]=\begin{bmatrix} 1/q_{e1} & \cdots & & 0 \\ \vdots & \vdots & \vdots & \vdots \\ 0 & \cdots & & 0 \\ 0 & \cdots & & 1/q_{en} \end{bmatrix} + P\begin{bmatrix} 1 & \cdots & & \\ \vdots & \vdots & \vdots & \vdots \\ 0 & \cdots & & \\ 0 & \cdots & & \end{bmatrix} - j\begin{bmatrix} m_{11} & \cdots & & m_{1n} \\ \vdots & \vdots & \vdots & \vdots \\ m_{(n-1)1} & \cdots & & m_{(n-1)n} \\ m_{n1} & \cdots & & m_{nn} \end{bmatrix} \tag{1}$$

where q_{ei} is the normalized external quality factor of resonator i, P is the complex lowpass frequency variable, m_{ij} is the normalized coupling coefficient between resonators i and j, and the diagonal entries m_{ii} account for asynchronous tuning. Considering a 3-port coupled-resonator network, and assuming that port 1 is coupled to resonator 1, port 2 is coupled to resonator a and port 3 is coupled to resonator b, the scattering parameters are related to the matrix [*A*] by [10]:

$$S_{11} = 1 - \frac{2}{q_{e1}}[A]^{-1}_{11}$$

$$S_{21} = \frac{2}{\sqrt{q_{e1}q_{ea}}}[A]^{-1}_{a1},\ S_{31} = \frac{2}{\sqrt{q_{e1}q_{eb}}}[A]^{-1}_{b1} \quad (2)$$

The optimization of the coupling matrix [*m*] is based on minimization of a cost function that is evaluated at the frequency locations of the reflection and transmission zeros. The cost function used here is given as [10],

$$\begin{aligned}\Omega = &\sum_{i=1}^{T_1}\left|\frac{2}{\sqrt{q_{e1}q_{ea}}}.cof_{1a}([A(s_{ti})])\right|^2 \\ &+\sum_{k=1}^{T_2}\left|\frac{2}{\sqrt{q_{e1}q_{eb}}}.2.cof_{1b}([A(s_{tk})])\right|^2 \\ &+\sum_{j=1}^{R}\left|\Delta_A(s_{rj}) - \frac{2.cof_{11}([A(s_{rj})])}{q_{e1}}\right|^2 \\ &+\sum_{v=1}^{R-2}\left|1 - \frac{2.cof_{11}([A(s_{pv})])}{q_{e1}.\Delta_A(s_{pv})} - 10^{\frac{L_R}{20}}\right|^2\end{aligned} \quad (3)$$

Where $cof_{kh}([A(s=x)])$ is the cofactor of matrix [*A*] evaluated by removing the *k*-row and the *h*-column of [*A*] and calculating the determinant of the resulting matrix at $s=x$. Δ_A is the determinant of the matrix [*A*]. s_{ti}, s_{tk} are the frequency locations of transmission zeros of S_{21}, S_{31} respectively. T_1, T_2 are the numbers of the transmission zeros of S_{21}, S_{31} respectively, and *R* is the total number of resonators. L_R is the specified return loss in dB (L_R<0), and s_{rj} and s_{pv} are the frequency locations of the return zeros and the peaks' frequency values of $|S_{11}|$ in the passband. The last term in the cost function is used to set $|S_{11}|$ peaks to the specified value of L_R.

III. DIPLEXER DESIGN

An X-band 12-resonator non-contiguous diplexer with symmetrical channels has been designed and implemented using waveguide cavity resonators. The diplexer has a Chebyshev response with passband centre frequency of 10 GHz for channel 1 and 11.35 GHz for channel 2, minimum isolation of 60 dB, and a desired return loss at the passband of each channel is 20 dB. The diplexer topology is shown in Fig.1. The proposed diplexer is formed of only coupled resonators, without using any external junctions for energy distribution, and the structure is folded for miniaturization. A gradient based constrained optimization technique has been utilized to synthesize the coupling coefficients, and the cost function in equation (3) has been used. To avoid convergence to a local minimum, the optimization has been carried out in two stages. In the first stage, the cost function in (3) has been used without the last term, and with equally spaced reflection zeros. In the second stage, the full cost function in (3) has been used, and the output coupling coefficients from the first stage are used as initial values, and the frequency locations of the return zeros are allowed to move until $|S_{11}|$ peaks in the passbands are equal to -20 dB. Moreover, the third term in the cost function was assigned more weight than the other terms. Although a Chebyshev response is required, the first two terms in the cost function have been used to increase the isolation between diplexer channels by minimizing the transmission of each channel at the passband of the other channel.

The optimized normalized coupling coefficients are as follows: m_{12}=0.7963, m_{23}=m_{28}=0.3466, m_{34}=m_{89}=0.2101, m_{45}=$m_{9,10}$=0.1956, m_{56}=$m_{10,11}$=0.2035, m_{67}=$m_{11,12}$=0.2814, m_{33}= -m_{88}=0.5942, m_{44}= -m_{99}=0.6552, m_{55}= -$m_{10,10}$=0.6635, m_{66}= -$m_{11,11}$=0.6652, m_{77}= -$m_{12,12}$=0.6643. The fractional bandwidth is *FBW*=18%, and the normalized external quality factors are numerically calculated as in [10] and found to be q_{e1}= 1.4903 and q_{e7}=q_{e12}=2.9806. The prototype response of the diplexer is shown in Fig.2.

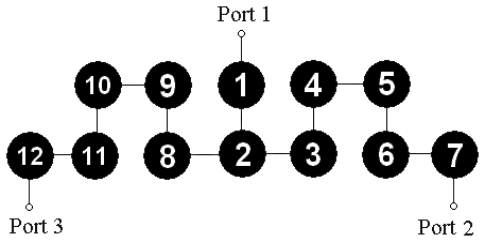

Fig.1. Diplexer Topology

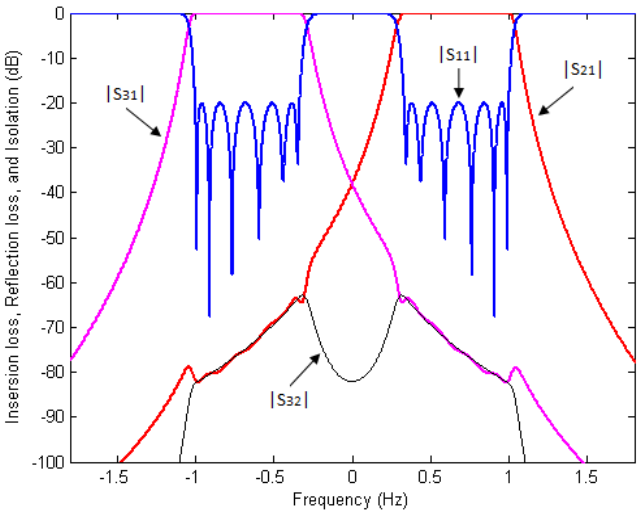

Fig.2. Diplexer ideal prototype response

The diplexer has been implemented using inductively coupled waveguide cavity resonators, and a top view of diplexer structure is shown in Fig.3.

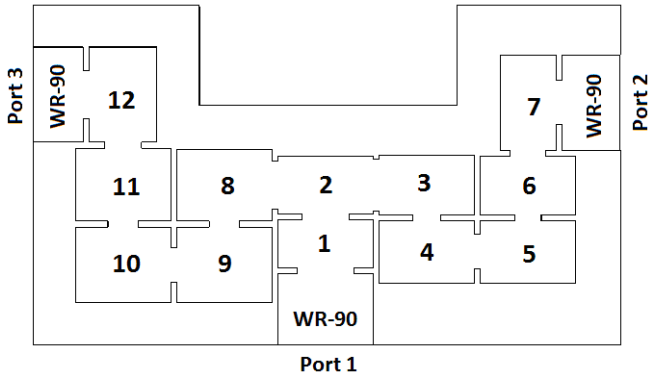

Fig.3. Top view of diplexer structure

IV. FABRICATION AND MEASUREMENT

The diplexer has been made of two mirror-image pieces of copper, and a photograph of the physical structure of the diplexer is shown in Fig.4. Metal screws have been used to tune both the resonant frequencies of the cavities and the coupling coefficients. The simulated and measured results of the diplexer are depicted in Fig.5. The tuned measured response is in very good agreement with the simulated response. The measurements show that the passband of channel 1 has maximum return loss of ~18 dB and minimum insertion loss of 0.42 dB, and that the passband of channel 2 has maximum return loss of 22 dB and minimum insertion loss of 0.4 dB.

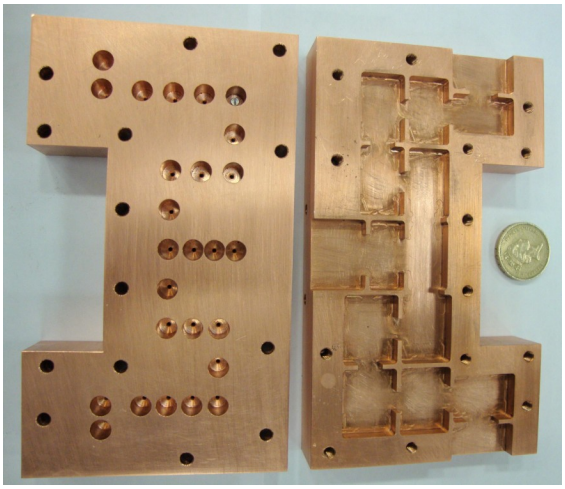

Fig.4. Photograph of the diplexer

V. CONCLUSION

An X-band coupled resonator diplexer has been presented, and its synthesis is based on coupling matrix optimization. The diplexer structure consists of resonators coupled together, and it does not involve any external junctions for distribution of energy. This enables miniaturization in comparison to the conventional diplexers. The diplexer has been implemented with waveguide cavity resonators, and the measured results showed a good agreement with the simulated results.

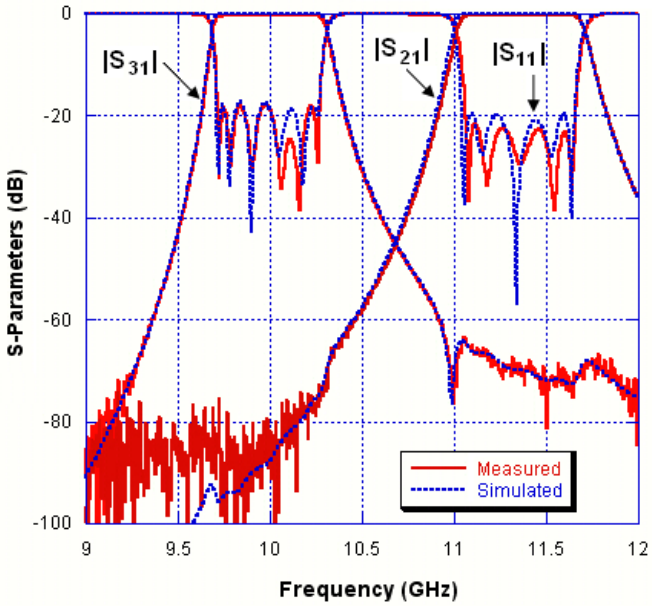

Fig.5. Measured and simulated results of the diplexer

REFERENCES

[1] M. Guglielmi, "Optimum CAD Procedure for Manifold Diplexers" *in proc. IEEE MTT-S Int. Microwave Symp.*, USA, 1993, pp. 1081-1084.

[2] H. Zhang and G. James, "A broadband T-junction diplexer with integrated iris filters," *Microwave and Optical Technology letters*, vol. 17, no. 1, pp. 69-72, Dec. 1998.

[3] S. Bastioli, L. Marcaccioli and R. Sorrentino, "An original resonant Y-junction for compact waveguide diplexers," *IEEE MTT-S International Microwave Symposium Digest*, Boston, USA, June 2009, pp. 1233-1236.

[4] C. E. Saavedra, "Diplexer using a Circulator and Interchangeable Filters," *in Proc. of the 7th International Caribbean Conference on Devices*, Circuits and Systems, Mexico, Apr. 2008, pp. 1-5.

[5] G. Macchiarella and S. Tamiazzo, "Novel approach to the synthesis of microwave diplexers," *IEEE Transactions on Microwave Theory and Techniques*, vol. 54, no. 12, pp. 4281-4290, 2006.

[6] G. Macchiarella and S. Tamiazzo, "Synthesis of diplexers based on the evaluation of suitable characteristic polynomials," *IEEE MTT-S International Microwave Symposium*, USA, 2006, pp. 111 – 114.

[7] M.J. Lancaster, "Radio frequency filter," W.I.P.O patent WO/01/69712, 2001.

[8] A. Garcia-Lamperez, M. Salazar-Palma, and T.K. Sarkar, "Analytical synthesis of microwave multiport networks," *IEEE MTT-S International Microwave Symposium digest*, USA, June 2004, pp 455-458.

[9] A. Garcia-Lamperez, M. Salazar-Palma, and T.K. Sarkar, "Compact multiplexer formed by coupled resonators with distributed coupling," *IEEE Antennas and Propagation Society International Symposium, USA, 2005, pp. 89-92.*

[10] T. Skaik, M. Lancaster, and F. Huang, "Synthesis of multiple output coupled resonator microwave circuits using coupling matrix optimization," *IET Journal of Microwaves, Antennas and Propagation*. to be published

[11] T. Skaik, M. Lancaster, and F. Huang, "Coupled-Resonator 3-dB Power Divider," *Proceedings of the IET seminar on Passive RF and Microwave Components*, Birmingham UK, April 2010, pp. 21-36.